Fabrication and characterization of ZnO-based water splitting devices by atomic layer deposition and hydrothermal synthesis

Thesis presented by

Jan Kegel

for the degree of

Doctor of Philosophy (PhD Engineering Science)

Submitted to National University of Ireland, Cork.

Tyndall National Institute, Cork

Head of School:	Prof. Justin D. Holmes, University College Cork, Cork
Supervisor:	Prof. Martyn E. Pemble, University College Cork, Cork
Co-supervisor:	Dr. Ian M. Povey, Tyndall National Institute, Cork

October 2018

Table of contents

Declaration ..... **v**

Acknowledgments ..... **vii**

Abstract ..... **ix**

List of publications ..... **xi**

Comments on my contributions ..... **xiii**

List of frequently used abbreviations and symbols ..... **xv**

1 Introduction **1**

1.1 Clean production of hydrogen 2

1.2 The chemistry and physics of the semiconductor/electrolyte interface 5

1.2.1 The semiconductor-electrolyte interface 7

1.3 Materials and devices for solar water splitting 13

1.3.1 Tandem PEC devices 16

1.3.2 Metal-insulator-semiconductor (MIS) structures 18

1.3.3 Metal-oxides for PECs 20

1.4 Zinc oxide for photo-(electro)chemical applications 24

1.4.1 PEC performance of ZnO materials having different morphologies 28

1.4.2 Facilitation of photo-(electro)chemical reactions due to defect-engineering in ZnO 33

1.4.3 Doping of ZnO for enhanced visible light absorption 40

1.4.4 Functional over-coating of ZnO 48

1.4.5 Summary of strategies designed to tailor ZnO for photo-(electro)chemical applications 55

1.5 Thesis outline 57

1.6 References 57

2 Experimental Methods **75**

2.1 Optical characterization 75

2.1.1 UV-Vis Spectroscopy (UV-Vis) 75

2.1.2 Photo-luminescence spectroscopy (PL) 78

2.1.3 Raman spectroscopy 81

2.2 Structural characterization 82

2.2.1 Scanning electron microscopy (SEM) and energy dispersive X-ray spectroscopy (EDS) 82

2.2.2 Transmission electron microscopy (TEM) 84

2.2.3 X-ray diffraction (XRD) 85

2.2.4 X-ray photo-electron spectroscopy (XPS) 87

2.3 Photo-(electro)chemical characterization 89

2.3.1 Linear sweep voltammetry (LSV) and Cyclic voltammetry (CV) ... 91
2.3.2 Chronoamperometry (CA) ... 94
2.3.3 Electrochemical impedance spectroscopy (EIS) ... 95
2.3.4 Photo-catalytic dye-degradation experiments ... 98
2.4 Growth of ZnO nanorod arrays and sample preparation ... 100
2.4.1 ZnO Seed-layer deposition ... 101
2.4.2 Hydrothermal growth of ZnO ... 104
2.4.3 Atomic layer deposition of TiO_2 over-layers ... 107
2.4.4 General sample preparation and rapid thermal annealing (RTA) ... 108
2.5 References ... 110

3 Defect-promoted photo-electrochemical performance enhancement of orange-luminescent ZnO nanorod-arrays ... 115
3.1 Abstract ... 115
3.2 Introduction ... 115
3.3 Experimental ... 117
3.4 Results and discussion ... 119
3.5 Conclusions ... 144
3.6 References ... 145

4 Effect of Surface and Defect Chemistry on the Photocatalytic Properties of Intentionally Defect-Rich ZnO Nanorod Arrays ... 151
4.1 Abstract ... 151
4.2 Introduction ... 151
4.3 Experimental Methods ... 153
4.4 Results and discussion ... 156
4.5 Conclusions ... 172
4.6 References ... 173

5 Rapid low-temperature solution growth of ZnO:Co nanorod arrays with controllable visible light absorption ... 179
5.1 Abstract ... 179
5.2 Introduction ... 179
5.3 Experimental ... 181
5.4 Results and discussion ... 183
5.5 Conclusions ... 195
5.6 References ... 196

6 One-pot synthesis of $Co(OH)_2$ and/or Co_3O_4 decorated cobalt-doped ZnO nanorod-arrays and their potential as (photo-)anode materials ... 201
6.1 Abstract ... 201
6.2 Introduction ... 201
6.3 Experimental ... 202
6.4 Results and discussion ... 205
6.5 Conclusions ... 222
6.6 References ... 223

7 ZnO nanorod-arrays as photo-(electro)chemical materials: strategies designed to overcome the material's natural limitations.....229
7.1 Abstract.....229
7.2 Introduction 229
7.3 Experimental.....233
7.4 Results and Discussion 236
7.5 Conclusions 254
7.6 References 255
8 Conclusions and future work.....261
8.1 References 268
Appendix 1: Supporting information for Chapter 3.....xix
Appendix 2: Supporting information for Chapter 4.....xxv
Appendix 3: Supporting information for Chapter 5..... xxxvii
Appendix 4: Supporting information for Chapter 6.....xxxix

Declaration

I, Jan Kegel, hereby confirm that the work I am submitting is my own and has not been submitted for another degree, either at University College Cork or elsewhere. All external references and sources are clearly acknowledged and identified within the contents. I have read and understood the regulations of University College Cork concerning plagiarism.

Jan Kegel

Date

Acknowledgments

This thesis would not have been possible without the help and support of a number of people. First and foremost, I would like to thank my supervisors Martyn and Ian, for giving me the opportunity to work on this very interesting research project. Their guidance throughout and their constant availability in relation to all the big or small questions around it were crucial to keep on track during the past years. Likewise, I am very grateful for the scientific freedom they allowed me and the trust associated with it.

I would like to acknowledge the former and current members of the AMSG group for the good time we spent together. I always felt welcome and happy to come into the office or the chemistry lab. I am very thankful for the help they offered or for cheering me up when things did not work out too well. As a trained engineer, it was a pleasure to learn about so many aspects of materials chemistry. Vitaly and Michael were very supportive in helping me to understand some physical aspects of my research project.

On the technical side of things, I would like to thank Donal from the mechanical workshop. Without his craftsmanship some of the experiments would not have been possible to perform. Similarly, I am thankful to Krimo for fixing some of the equipment when it broke.

A special thanks is directed to the Tyndall National Institute in general. The welcoming and friendly atmosphere made it easy for me to integrate and to build up many wonderful friendships over the years. Particularly the Tea-group should be mentioned in this regard. Many happy hours were spent and I really appreciate that I was able to work alongside such nice people at all times.

However, Alessandra was the greatest support over the past 4 years. She has always been there for me to share all the moments from the happiest to the saddest. She was a big help in keeping me motivated and brought me a lot of love and joy outside of the research routine.

Finally, the biggest gratitude belongs to my family. Their love was always with me despite the distance, and their endless support paved the way to this doctoral journey. Without it, all of this would not have been possible.

Abstract

The urgent need for clean and storable energy drives many currently topical areas of materials research. Metal oxides like zinc oxide (ZnO) are particularly promising materials to be used in core technologies such as batteries, photovoltaics or solar fuel production. The latter photo-(electro)chemical application is considered as the '*holy grail*' of energy research by some. This high consideration stems from the possibility to convert solar energy directly into chemical bonds and thus into a storable energy carrier. In this regard, the generation of hydrogen via solar water splitting forms a key building block related to this field of research. Governed by its low-cost, environmentally friendly and earth-abundant nature, ZnO represents a promising material for this application. However, the material possesses some natural limitations, which are hindering the use of ZnO for photo-(electro)chemical applications. Therefore, this study aims at tailoring the material properties of ZnO towards these applications by addressing the key issues of: low visible-light absorption, fast charge carrier recombination over intrinsic defects and the deterioration of the material due to photo-corrosion.

Employing a combination of atomic layer deposition (ALD) for the growth of functional layers and low-temperature hydrothermal methods for the deposition of ZnO nanorod arrays, strategies are presented as to how to use defect-engineering to enhance the photo-(electro)chemical performance and how to increase the visible-light- absorption and activity by substitutional cobalt doping.

First, a synthetic approach for the growth of ZnO nanorod arrays, which allows for the induction of strong defect-related orange luminescence upon rapid thermal annealing, is introduced. The nature of this defect center is thoroughly investigated and the oxygen vacancy–zinc interstitial defect-complex is identified as a possible origin. When used as a photo-anode for the splitting of water or as photo-catalyst material for the degradation of model pollutants, the orange luminescent nanorod arrays are shown to outperform samples that do not exhibit this emission. The mechanism leading to the defect-promoted enhancement of these key properties is discussed based on a possible charge carrier lifetime enhancement ascribed to this defect center. In regard to an improvement of the visible-light absorption of ZnO, a low temperature solution-based growth method was developed, which enables a rapid deposition (1 h) of cobalt-doped ZnO nanorod arrays with controllable visible-light absorption. Upon optimizing this

method, a one-pot synthesis is introduced, which allows for the growth of high surface-area cobalt doped ZnO nanorod-arrays decorated with catalytic cobaltic over-coatings. Control over the visible light absorption and the nature of the catalytic cobaltic over-coating ($Co(OH)_2$ and/or Co_3O_4) can be easily achieved by changing the growth parameters used during the one-pot synthesis. The proposed growth mechanism may enable the controlled deposition of functional metal-oxide based material systems for various applications. In addition to the aforementioned solution-based approaches, which aim at altering the material properties of ZnO, ultrathin ALD titanium dioxide (TiO_2) layers are investigated as chemical barriers for the protection of ZnO against photo-corrosion. The resulting core-shell structures exhibit an improved chemical stability and the photo-current obtained is sustained for a longer time when compared to unprotected ZnO nanorod arrays. Pinholes in the TiO_2 shell, particularly found at the rod tips, are identified as source for the photo-current and material degradation which nevertheless occurred after prolonged measurements.

The experimental studies presented in this thesis will potentially accelerate the incorporation of ZnO-based materials into photo-(electro)chemical applications. This is not only achieved due to the introduction of tailored synthetic approaches, but also arises from the in-depth analysis and interpretation of the resulting material properties, which will deepen our fundamental understanding of ZnO as semiconductor.

List of publications

Published works:

[1] J. Kegel, V. Z. Zubialevich, M. Schmidt, I. M. Povey, and M. E. Pemble, "Effect of Surface and Defect Chemistry on the Photo-catalytic Properties of Intentionally Defect-rich ZnO Nanorod Arrays," *ACS Applied Materials & Interfaces,* DOI: 10.1021/acsami.8b05130.

[2] J. Kegel, I. M. Povey, and M. E. Pemble, "ZnO Nanorod-Arrays as Photo-(Electro)Chemical Materials: Strategies Designed to Overcome the Material's Natural Limitations" *Journal of The Electrochemical Society,* vol. 165, pp. H3034-H3044, 2018.

[3] J. Kegel, F. Laffir, I. M. Povey, and M. E. Pemble, "Defect-promoted photo-electrochemical performance enhancement of orange-luminescent ZnO nanorod-arrays," *Physical Chemistry Chemical Physics,* vol. 19, pp. 12255-12268, 2017.

[4] J. Kegel, J. Halpin, F. Laffir, I. M. Povey, and M. E. Pemble, "Rapid low-temperature solution growth of ZnO:Co nanorod arrays with controllable visible light absorption," *CrystEngComm,* vol. 19, pp. 1938-1946, 2017.

[5] J. Kegel, I. M. Povey, and M. E. Pemble, "(Invited) Tailoring Zinc Oxide Nanorod-Arrays for Photo-(electro)Chemical Applications," *ECS Transactions,* vol. 77, pp. 43-60, April 25, 2017.

In preparation:

[6] J. Kegel, F. Laffir, I. M. Povey, and M. E. Pemble, "One-pot synthesis of $Co(OH)_2$ and/or Co_3O_4 decorated cobalt-doped ZnO nanorod-arrays and their potential as (photo-)anode materials"

Comments on my contributions

The main body of this work has been carried out at the Tyndall National Institute, Cork. Funding for this work was secured by Martyn E Pemble and Ian M. Povey. My contributions to the aforementioned publications are reflected in the design of the experimental studies, synthesis of materials using solution growth methods, characterization of the materials, data analysis/interpretation and manuscript preparation. The planning and progress of the experimental studies were monitored by Ian M. Povey and Martyn E. Pemble. Ian M. Povey was responsible for the atomic layer deposition. All authors of the individual publications contributed to the finalization of the manuscript. Individual contributions of the co-authors to the chapters are outlined below:

Chapter 3: F. Laffir carrier out and analyzed the XPS measurements. Furthermore she added valuably to the discussion of this data.

Chapter 4: V. Z. Zubialevich assisted and partly carried out the low-temperature photo-luminescence measurements. He also added valuably to the discussion of this data.

M. Schmidt carried out the transmission electron microscopy measurements and contributed valuably to the discussion of this data.

Chapter 5: J. Halpin carried out some of the growth experiments regarding the cobalt-doped zinc oxide and assisted in some of the UV-Vis spectroscopy measurements.

F. Laffir carrier out and analyzed the XPS measurements. Furthermore she added valuably to the discussion of this data.

Chapter 6: F. Laffir carrier out and analyzed the XPS measurements. Furthermore she added valuably to the discussion of this data.

Chapter 7: M. Schmidt carried out the transmission electron microscopy measurements.

List of frequently used abbreviations and symbols

NR, NRA	nanorod and nanorod array, respectively
ALD	atomic layer deposition
TCO	transparent conductive oxide
RTA	rapid thermal annealing
STHE	solar to hydrogen efficiency
ABPE	applied bias photon-to-current conversion efficiency
IPCE	incident-photon-to-current-conversion efficiency
PEC	photo-electrochemical cell; sometimes also used as photo-electrochemical
PV	photovoltaic
AM	air mass
MIS	metal-insulator-semiconductor
DMS	diluted magnetic semiconductor
$ML_{CB}CT$	metal to ligand conduction band charge transfer
$L_{VB}MCT$	ligand valence band to metal charge transfer
OER	oxygen evolution reaction
HER	hydrogen evolution reaction
RHE	reversible hydrogen electrode
SHE	standard hydrogen electrode
SCE	saturated calomel electrode
WE	working electrode
CE	counter electrode
RE	reference electrode
V_O, V_{Zn}	oxygen and zinc vacancy, respectively
O_i, Zn_i	oxygen and zinc interstitial, respectively
O_{Zn}, Zn_O	oxygen and zinc antisite, respectively
VB, VBM	valence band and valence band minimum, respectively
CB, CBM	conduction band and conduction band minimum, respectively
XPS	X-ray photo-electron spectroscopy
XRD	X-ray diffraction
TEM	transmission electron microscopy
EDS	energy dispersive X-ray spectroscopy

UV-Vis	UV-Vis spectroscopy
SEM	scanning electron microscopy
BSE	backscattered electrons
SE	Secondary electrons
LED	light emitting diode
EIS	electrochemical impedance spectroscopy
CV	cyclic voltammetry
LSV	linear sweep voltammetry
CA	chronoamperometry
PL, LT-PL	photo-luminescence and low-temperature photo-luminescence spectroscopy, respectively
NBE	near band edge emission
DLE	deep level emission
DLD	deep level defect
DA	donor-acceptor
FB	free-bound
FX_A	free exciton (A-exciton)
D_0X	exciton bound to a neutral donor
LDH	layered double hydroxide
FWHM	full width at half maximum
N_A, N_D	acceptor and donor concentration, respectively (cm^{-3})
JCPDS	Joint Committee on Powder Diffraction Standards
AC	alternating current
MB	methylene blue
MO	methyl orange
ZNH	zinc nitrate hexahydrate
ZnAc	zinc acetate dihydrate
CoAc	cobalt acetate dihydrate
MEA	monoethanolamine
HMTA	hexamethylenetetramine

τ_n, τ_p	electron and hole minority carrier lifetime, respectively (s)
μ_n, μ_p	electron and hole minority carrier mobility, respectively (s)

L_n, L_p	electron and hole minority carrier diffusion length, respectively (m)
L_D	Debye-length (m)
E_F	Fermi Energy level (eV)
w	width of the space charge region (m)
E_{FN}, E_{FP}	quasi-Fermi energy level of electrons and holes, respectively (eV)
E_C, E_V	energy of the conduction and valance band edge, respectively (eV)
E_G	bandgap energy (eV)
e	electron charge ($1.6 \cdot 10^{-19}$ C)
m_e, m_h	Mass of an electron or hole, respectively (kg)
k	Boltzman`s constant ($1.38 \cdot 10^{-23}$ J/K)
c	Speed of light ($3.0 \cdot 10^{8}$ m/s)
h	Planck`s constant ($6.625 \cdot 10^{-34}$ J s)
λ	wavelength (m)
ν	frequency of light (s^{-1})
$\bar{\nu}$	wavenumber ($1/\lambda$; m^{-1})
T	absolute temperature (K)
eV	electron volt ($1.6 \cdot 10^{-19}$ J)
φ_0	photon flux (number of photons / $s \cdot m^2$)
α	spectral absorption coefficient (m^{-1})
I, I_0	current and saturation current, respectively (A)
J, J_0	current density and saturation current density, respectively (A)
J_{Ph}, J_{SC}	photo-current density and short-circuit photo-current density, respectively (A)
η_{Far}	Faradaic efficiency (%)
V, V_{OC}	voltage and open circuit voltage, respectively (V)
$V_{redox, H20}$	voltage associated with the redox potential of water – 1.23 V (V)
V_T, V_{SC}	total voltage drop over the semiconductor electrolyte interface and voltage drop over the space charge region, respectively (V)
V_H, V_G	voltage drop over the Helmholtz layer and the Gouy layer, respectively (V)
E, E_{Appl},	potential and applied potential, repsectively (V)
E_{RHE}, E_{ref}	potential vs. RHE, potential vs. reference electrode, potential vs.
$E_{Ag/AgCl}$	silver/silver chloride electrode, respectively (V)

E_{redox}	Redox potential of a redox-couple in an electrolyte (V)
$E_{F,redox}$	Fermi Energy of the redox-couple (V); semiconductor physics equivalent to E_{redox} – reference energy is the vacuum energy
A, A_{ill}	area and illuminated area, respectively (m^2)
ε	permittivity (F/cm)
P_{Light}	Power intensity of the irradiation (W/m^2)
$\Delta G°$	Gibbs free energy (J/mol)
ϕ^{ox}	oxidation potential of a material (V)
ϕ^{red}	reduction potential of a material (V)
T	transmission (%)
R	reflection (%)
A	absorption (%)
S	scattering (%)
d	thickness (m)
E_U	Urbach Energy (eV)
θ	angle between the impinging X-ray and the normal to the sample surface (°)
d	interplanar spacing (m)
E_B	binding energy (eV)
Z	impedance (Ω)
R	resistance (Ω)
L	inductance (Henry)
C	capacitance (F)
V	volume (m^3)
C, C_0	concentration and starting concentration, respectively (M)

Chapter 1

1 Introduction

One of the big challenges mankind is facing in the 21st century is a radical change in the global energy system. Recent studies on the sudden drainage [1] and recharge [2] of subglacial lakes under the ice shield of Greenland, for example, show that the effects of the anthropogenic climate change might have bigger impact than expected. As one of the major concerns, rising sea levels has become somewhat symbolic of global warming. If the mean global temperature is stabilized around 2 °C in respect to pre-industrial levels, as set out by the Paris agreement of 2016, the median sea level is predicted to rise by ca. 1.5 m over the next centuries [3]. The effects of rising sea levels will be mostly felt by those nations less responsible for the anthropogenic climate change - namely the poor low-land nations of e.g. Bangladesh, Indonesia, Thailand or the Solomon Islands. These nations emit very little greenhouse gases as compared to western societies and in order to stay within the (probably too unambitious) targets of the Paris agreement, are urged to keep a low carbon-footprint. This is not only true for the aforementioned countries but is in fact a necessity for all so-called developing countries. However, how can these countries reach western-levels of wealth if they are asked not to avail of the key component that made western countries prosper - fossil fuels as sources of energy? Also how or perhaps more correctly why should these countries pay for necessary actions against the consequences of an anthropogenic global warming that they did not really contribute to? The potential for conflicts that is inherent to these questions is obvious and resembles the foundation of heated debates at past meetings at the United Nations Climate Change Conferences. From a moral and ethical point of view the winner of such debates is clear to the objective observer.

Seen from a global perspective a possible solution to the first question may lay in the use of renewable energies in the developing world. Indeed it would be highly desirable for these countries – and for the rest of the world – to build up an energy supply based on renewables rather than investing in an old-fashioned energy system based on limited resources and the need of expensive infrastructure in form of an extensive transmission grid. However, it is also true for western societies that the minimization of greenhouse gases emissions, which would result from switching from a centralized power generation system using fossil fuels to a de-centralized system based on renewable energies, seems necessary. Considering that renewable energies are almost

or already cost-competitive – even without incorporating the follow-up costs associated with the use of fossil fuels [4-6] – it seems surprising that these clean technologies are currently only playing a minor role in the global energy market. Why are renewable energies still lacking momentum? What is indisputable is that the growth and use of renewable energies is dependent on politics like almost no other industry [7]. To date, economic interests still carry more weight than environmental, ethical and social concerns. However, in the western world the change to renewable energy sources is also accompanied with technological issues. Two major challenges in this regard are the reconstruction of the power-grid and the storage of the generated power. These two topics are heavily discussed in the public domain as well as in the research community. It is particularly true that the efficient and cost efficient storage of renewable energies – over a long and short period of time – remains challenging [8, 9].

Here, Hydrogen (H_2) is a potential candidate for the storage of the energy produced by renewables, due to its exceptional chemical and physical properties. The value of hydrogen for modern energy systems may be manifold. Firstly, it can be compressed into vessels for later use in fuel cells (generation of electricity) – which is especially interesting for the future of the mobility sector. Secondly, the great capacity of the existing natural gas-grid could be used to store about 10 % or more of H_2 [10, 11] in order to produce heat and electricity generation from modern gas turbines. Lastly, hydrogen can be stored by forming chemical bonds to produce hydrocarbons, e.g. with CO and/or CO_2 in a Fisher-Tropsch synthesis [12]. Conventionally most hydrogen is produced via steam reforming (90 %), which uses methane as a feedstock [13]. An alternative method is the use of an electrolyzer, which splits water (into hydrogen and oxygen) electrochemically by applying an electrical potential to electrodes. However, to date the electricity needed to run the water splitting reaction is mostly generated from fossil fuels. Thus, for hydrogen to contribute significantly to satisfy future global energy needs it must arguably be generated entirely from renewable energy sources.

1.1 Clean production of hydrogen

In this regard solar energy possesses the greatest potential to meet the global energy demand. Theoretically the energy striking the surface of the earth within 2 h would be enough to generate the global energy demand for 1 year [14]. For the production of clean hydrogen the most obvious strategy would thus be to couple an electrolyzer with

a photovoltaic (PV) cell or module, as schematically depicted in Figure 1-1a. In this arrangement the electrical potential required to split water (1.23 V theoretical + ca. 0.7 V overpotential [15]) is supplied by the PV cell. The anode and cathode materials are electro-catalyst coatings on conductive substrates. These are then wired to the PV cell in order to transfer the generated charge carriers. One advantage of this device configuration is the use of somewhat mature technologies. On a lab scale, devices based on this configuration already reached over 30 % of solar to hydrogen efficiencies (STHE) [16]. Ultimately the STHE can be understood and should be measured as shown in equation (1.1) [17]:

$$STHE = \frac{Rate\ of\ hydrogen\ produced\ \cdot\ \Delta G^0}{P_{Light} \cdot A_{Ill}} \tag{1.1}$$

Here ΔG^0 is the Gibbs free energy per mole of H_2 (ΔG^0 = 237 kJ/mol at 25 °C) and P_{Light} the power intensity of the irradiation (usually 100 mW/cm^2, AM 1.5G) that illuminates the sample area A_{Ill}. An alternative and more practical expression of the STHE (in the un-assisted case e.g. no bias potential) is however presented by equation (1.2) [17, 18]:

$$STHE = \frac{j_{SC}\ \cdot\ V_{redox,H20}\ \cdot\ \eta_{Far}}{P_{Light}} \tag{1.2}$$

where j_{sc}, $V_{redox,\ H20}$ and η_{Far} are the short-circuit photo-current density, the redox potential of water (usually taken as 1.23 V at 25 °C) and the Faradaic efficiency, respectively. However, the previously-mentioned 30 % STHE were achieved using expensive materials such as a triple-junction PV cell made of group III-V materials and noble metal catalysts (platinum and iridium) [16]. Such material combinations might be interesting for extraterrestrial applications but the high costs will severely limit the use on an industrial scale. Alternatively, the use of materials like silicon, perovskites and earth-abundant metal-oxides present a route to decrease the costs while maintaining STHE of 10 % and above [19, 20]. Another advantage that the PV/electrolyzer assembly has is the de-coupling of the light absorbing material and the electrolyte. This is especially important for materials that are rather unstable in contact with water. On the other hand, the de-coupling leads to a more complex device and reactor design – and therefore significantly higher costs – when compared to a so called photo-

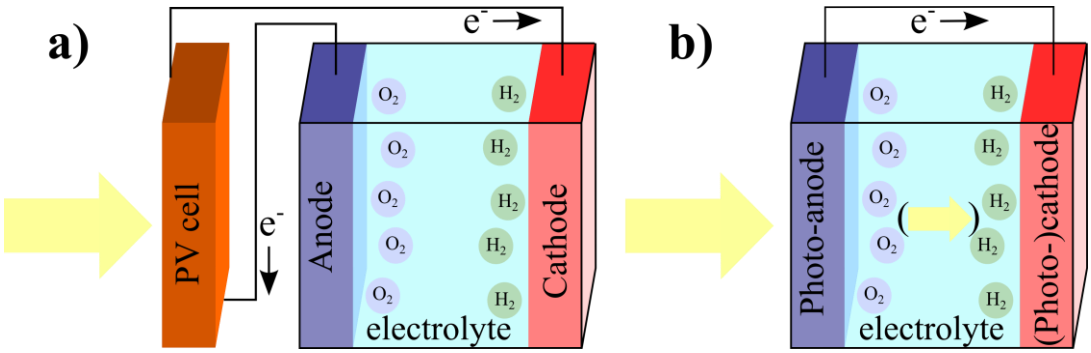

Figure 1-1: Schematic of basic device configurations for the production of clean hydrogen from sunlight. a) Photovoltaic cell coupled with an electrolyzer. b) Photo-electrochemical cell (PEC) arrangement.

electrochemical cell (PEC) [21]. In a PEC arrangement, as schematically shown in Figure 1-1b, the anode and/or cathode are photoactive themselves (i.e. photo-anode/photo-cathode). Schematically speaking this means that charge carriers are generated within those layers and directly participate in the oxygen evolution reaction (OER) or hydrogen evolution reaction (HER). Similarly to a PV cell, the materials used as photo-anode/cathode are semiconductors. Importantly, the voltage required to split water may be generated directly from the semiconductor-electrolyte interface under illumination (see section 1.2.1). Furthermore the PEC configuration may also reduce the energy losses associated with commercial electrolyzer-systems, which account for about 30 % [22]. The PEC configuration thus represents a somewhat ideal means of production of hydrogen in the form of a direct, chemical driven hydrogen generation powered by solar energy.

The first scientific demonstration of "solar water splitting" using a PEC was reported by Fujishima and Honda in 1972 [23]. Since then solar water splitting has attracted enormous attention among the research community but the industrial fabrication of efficient, stable and economical devices to run the water splitting reactions remains to be demonstrated. Many researchers focus on improving existing materials or the development of new materials/compounds to achieve the key aspects involved in the complex process of direct water splitting [17, 24-26]:

- The generated potential must exceed the theoretical voltage to split water (1.23 V) + overpotentials due to kinetic losses (≈ 0.7 V)
- A sufficiently high absorption of solar radiation is required
- The material(s) must withstand corrosion for a long time
- The device should ideally be fabricated from cheap, earth-abundant materials

Furthermore, to be economically competitive to current hydrogen production methods, the production-costs per kg H_2 should be between \$2 and \$4 [21, 27]. The solar-to-hydrogen efficiency of photo electrochemical cells – as the most cost-sensitive parameter – has to be higher than 15 % to meet this target, with laboratory efficiencies of 8 % - 18 % being achieved depending on the system used [27, 28]. Additionally the PEC configuration allows for various device designs to be employed. Most commonly coupled/tandem devices are being investigated that energetically connect the photo-active materials to capitalize on as much of the impinging solar irradiation as possible [21, 26, 29, 30]. As an example here a low-cost device based on a buried amorphous silicon PV element and a bismuth vanadate photo-anode, developed by the group of Roel van de Krol reached 4.2 % STHE and higher [31, 32].

For a PEC device the above mentioned key aspects are closely related to the chemistry and physics of the interface between water (or an electrolyte) and the water-splitting material, which are discussed in the following section.

1.2 The chemistry and physics of the semiconductor/electrolyte interface

Water (H_2O) is the chemical result of bonding between molecular hydrogen and oxygen. It can be reduced or oxidised (redox-couples: H_2O/H_2, O_2/H_2O). The two pH dependent redox half-reactions reactions can be written as equations (1.3) - (1.6) [33]:

Acid media:

$$2H_2O + 4h^+ \rightleftarrows O_2 + 4H^+ \ (O_2/H_2O) \tag{1.3}$$

and

$$2H^+ + 2e^- \rightleftarrows H_2 \ (H_2O/H_2) \tag{1.4}$$

Basic media:

$$4OH^- + 4h^+ \rightleftarrows O_2 + 2H_2O \ (O_2/H_2O) \tag{1.5}$$

and

$$2H_2O + 2e^- \rightleftarrows H_2 + 2OH^- \ (H_2O/H_2). \tag{1.6}$$

From the equations above it can be seen that the water splitting reaction is a multiple particle process. In regards to solar water splitting this means that four electron-hole pairs have to be generated to give the four holes (h^+) required to run the oxygen evolution reaction (OER; equations (1.3) and (1.5)).

The overall water splitting reaction in the presence of illumination can be written as

equation (1.7) [25]:

$$4h\nu + 2H_2O_{(liquid)} \rightleftarrows O_{2(gas)} + 2H_{2(gas)} \quad (1.7)$$

The standard Gibbs free energy $\Delta G° = 237$ kJ/mol of this reaction is indicative of a highly endothermic process [34].

The electrochemical potentials E_{redox} of the two redox couples change drastically with the pH. Applying the Nernst law (standard conditions) to the water splitting process one can express equation (1.8):

$$E_{redox} = E^{\circ}_{redox} + \frac{0.059\ V}{z} \cdot lg\frac{c(Ox)}{c(Red)} = E^{\circ} - 0.059\ V \cdot pH \quad (1.8)$$

where E°_{redox} is the electrochemical standard-potential. Therefore, equations (1.9) and (1.10) are obtained for the OER and HER reaction, respectively:

$$E_{redox}(OER) = 1.23\ V - 0.059\ V \cdot pH \quad (1.9)$$

$$E_{redox}(HER) = 0\ V - 0.059\ V \cdot pH \quad (1.10)$$

The progression of the potentials vs. the pH is plotted in Figure 1-2. The potentials in the figure are given vs. the standard hydrogen electrode (SHE). SHE defines the standard potential of hydrogen at pH = 0 (see reaction in equation (1.4)) as zero. This definition was set to make a comparison between different potentials easier. For example, the reference electrodes used in this work have a potential E_{Ref} of either + 199 mV or + 244 mV vs. SHE. Therefore, all potentials E conducted during electrochemical measurements were corrected to SHE according to equation (1.11):

$$E\ vs.SHE = E_{Appl} + E_{Ref} \quad (1.11)$$

or the reversible hydrogen electrode (RHE), which accounts for the shift of the potential with the pH, equation (1.12):

$$E\ vs.RHE = E_{Appl} + E_{Ref} + 0.059\ \cdot pH \quad (1.12)$$

The difference between the oxidation and reduction potential is the theoretically minimum potential necessary to split water E_{theo} = 1.23 V. From Figure 1-2 it can be seen that the E_{theo} does not change with pH. In contrast, the change of the position of the oxidation and reduction potential is relatively large (= 0.862 V between pH = 0 and pH = 14). This is important for solar water splitting as the position of the semiconductor energy-bands will vary with respect to the oxidation/reduction potential of water. Furthermore the energetic position of the oxidation/reduction potential is

highly important for the stability of the photo-electrode [35].

In practice, the potential required to run the water splitting reactions is much higher than the E_{theo}. Indeed, due to kinetic losses the practical potential to split water (E_{prac}) lays at ≈ 2 V or higher [29].

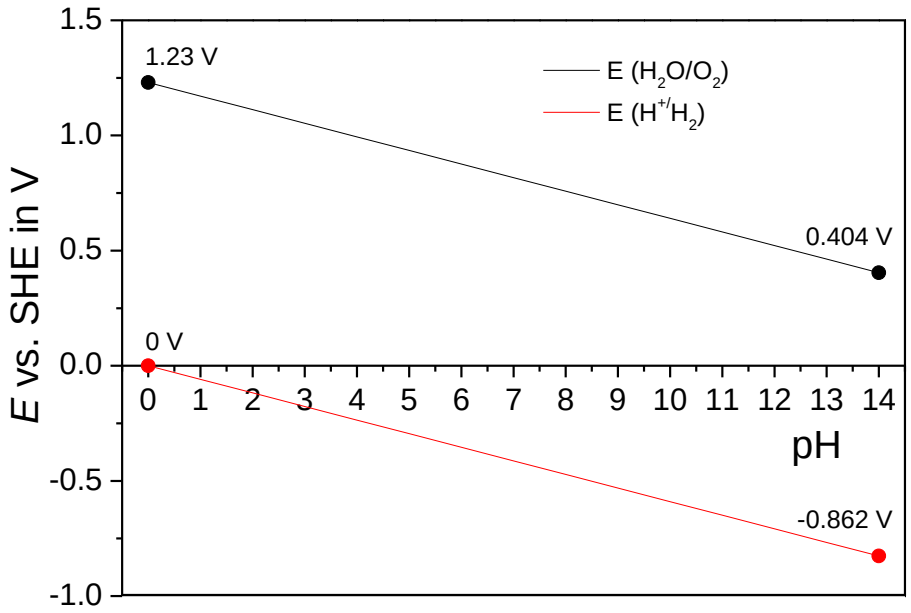

Figure 1-2: Calculated oxidation and reduction potentials of water in dependence of the pH value.

1.2.1 **The semiconductor-electrolyte interface**

Semiconducting materials offer unique properties in terms of the positions of their energy-bands. The energy levels of the conduction band E_C and valence band E_V are separated from each other by the bandgap energy E_G, equation (1.13):

$$E_G = E_C - E_V \tag{1.13}$$

For semiconductors E_G is less than 4 eV, which therefore allows these materials to absorb radiation emitted by the sun. Absorption in a semiconductor is possible if the energy of the impinging radiation E_λ is equal to or greater than E_G, equation (1.14):

$$E_G \leq E_\lambda = \frac{h \cdot c}{\lambda} \tag{1.14}$$

In equation (1.14) h is Planck's constant, c the speed of light and λ the wavelength of the impinging radiation.

Whereas semiconductors with a high bandgap energy absorb only in the ultra-violet region (UV, below 380 nm), semiconductors with a low E_G are able to absorb radiation

from the UV-region up to the near-infrared region (NIR, e.g. silicon absorbs radiation < 1100 nm). The visible spectra of irradiation (= light) ranges from ca. 380 nm to 780 nm. The standard spectrum of the sun with an air mass (AM) of 1.5 is shown in Figure 1-3. This spectrum is also the reference for the 1-sun experiments which are commonly adopted in studies of photovoltaics and photo-electrochemical water splitting. The area between the two colored, dashed lines in Figure 1-3 represents the visible region of the spectrum. As can be seen from the figure, the spectral irradiance of the sun has its highest intensity in the visible region with a distinct peak at ≈ 500 nm (green light). For solar water splitting it is therefore desirable to use materials which are able to absorb also in the visible region.

The ability to generate electrical energy upon the absorption of light (the photovoltaic effect) makes semiconductors the materials of choice for solar water splitting. To make water splitting possible the bandgap energy of the material should be at least 1.23 eV [25]. If the compensation for kinetic losses is included, E_G should be ≈ 2 eV or higher. Furthermore the valence and conduction band positions with respect to the oxidation and reduction potentials are important. Figure 1-4a shows E_G, E_C, E_V, the Fermi energy

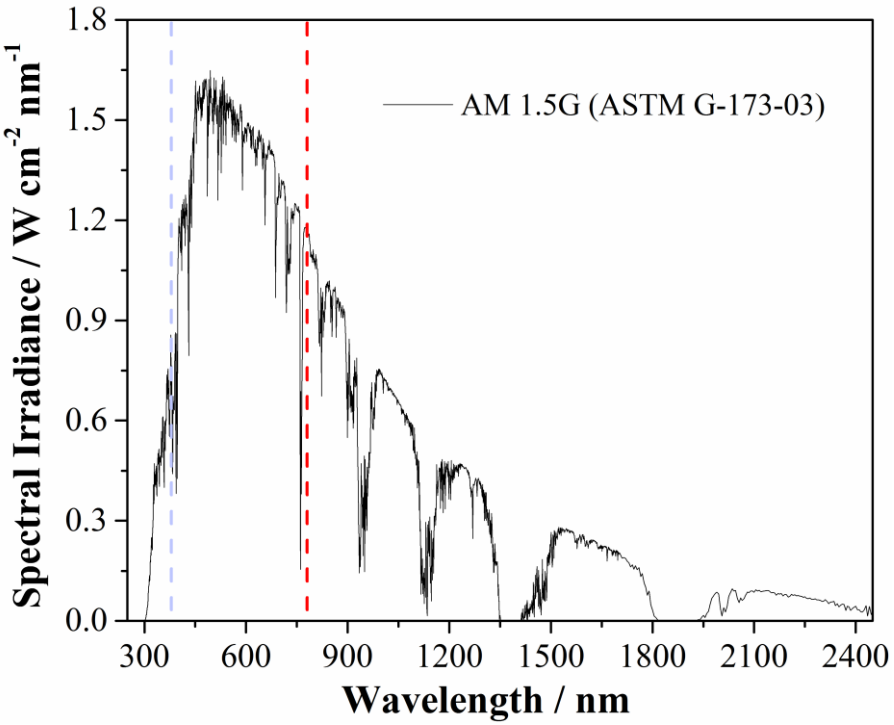

Figure 1-3: ASTM G-173-3 reference spectrum of the sun (AM 1.5 G). Data taken from Ref [36]. The colored, dashed lines represent the visible region of the spectrum.

E_F, the electron affinity E_{ea} (sometimes ⌀) and the workfunction χ of an n-type semiconductor in respect to the vacuum energy reference. A quantity with central importance in semiconductor physics is the Fermi energy. In a semiconductor E_F is the energy where the probability of occupancy $f(E)$ is exactly 0.5 [37]. This is derived from the Fermi-Dirac statistic. For the case that the energy of a state E_{state} is measured from the lowest possible state, E_F equals E_{state}. The Fermi-Dirac statistic is then given by (equation (1.15)):

$$f(E) = \frac{1}{1 + e^{\left(\frac{E_{state} - E_F}{k \cdot T}\right)}} = 0.5 \tag{1.15}$$

where k is the Boltzmann-constant and T the absolute temperature. For an intrinsic semiconductor E_F would lie in the middle of the bandgap. Doping of semiconductors leads to a shift of E_F. For the example of the n-type semiconductor in Figure 1-4b the Fermi energy is shifted towards the conduction band edge.

The concept of E_F can also be applied to an electrolyte, where the redox-potential of a redox-couple can be identified as its Fermi energy $E_{F,redox}$ [38]. This is given due to the established assumption that the states of the oxidized species of a redox-couple are empty (= acceptors) and the states of the reduced species are occupied (= donors). This is shown schematically by the distribution of the density of states of an electrolyte in Figure 1-4a (right). Where E°_{redox} has a 50 % probability of occupancy, analogous to E_F in a semiconductor. To assign $E_{F,redox}$ to the vacuum energy reference level commonly used in semiconductor physics, redox-potentials with respect to SHE can be converted using equation (1.16) [38]:

$$E_{F,redox} = 4.5\ eV - e \cdot E^{\circ}_{redox} \tag{1.16}$$

If a semiconductor and an electrolyte are put into contact without any external bias their Fermi energies will equilibrate since in every system only one Fermi energy is allowed. By analogy to a semiconductor-metal interface, the electrolyte can be seen as infinite reservoir of charge carriers. Thus the semiconductor will equilibrate to the Fermi energy of the electrolyte. The interfaces that form between an n- or p-type semiconductor and an electrolyte are depicted in Figure 1-4b and c, respectively. For the case of an n-type semiconductor E_F lies above $E_{F,redox}$, forcing the semiconductor energy-bands to bend upwards as a result of electron transfer from the semiconductor surface into the electrolyte (right schematic in Figure 1-4b). The exact opposite is the

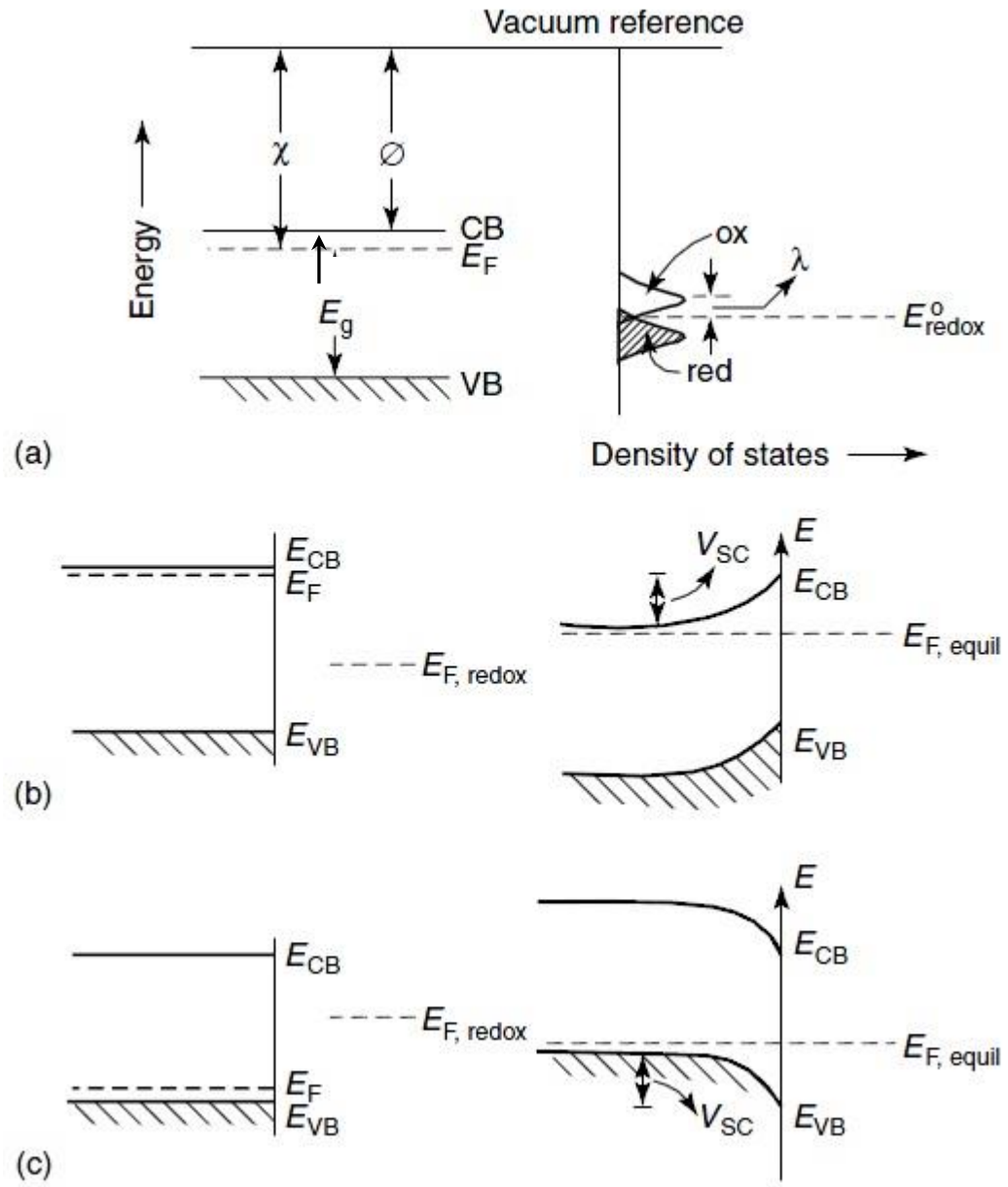

Figure 1-4: a) Left: energy band diagram of an n-type semiconductor. Right: Distribution of the density of states of an electrolyte. b) Left: Energy diagram of an n-type semiconductor prior to contact with the electrolyte. Right: energy diagram of an n-type semiconductor-electrolyte junction equilibrate in the dark. c) Left: energy diagram of a p-type semiconductor prior to contact with the electrolyte. Right: energy diagram of a p-type semiconductor-electrolyte junction equilibrate in the dark. Reproduced with permission from Ref. [38]. Copyright 2007 Wiley-VCH Verlag GmbH & Co.

case for a p-type semiconductor (right schematic in Figure 1-4c), where the energy-bands are bending downwards as a result of electrons from the electrolyte filling up empty states (= holes) in the semiconductor.

In both cases the surface layer is depleted, forming the so-called space charge region

in the semiconductor. Figure 1-5a shows a more detailed schematic of the semiconductor-electrolyte interface. Due to the band bending at the interface a potential difference V_{SC} builds up, which can be assigned to the space charge region of the semiconductor. The width w over which this space charge region is propagating is dependent on V_{SC} and the donor concentration N_D (≈ doping concentration) for an n-type semiconductor, equation (1.17):

$$w = \sqrt{\frac{2 \cdot \varepsilon_0 \cdot \varepsilon_R}{e \cdot N_D} \left(V_{SC} - \frac{k \cdot T}{e}\right)} \tag{1.17}$$

With e, ε_0 and ε_R being the electron charge, the dielectric constant of vacuum and the dielectric constant of the material, respectively.

Furthermore, the band bending is partly distributed into the electrolyte, in the so-called Helmholtz and Gouy layers, resulting in the potential differences V_H and V_G, respectively. The Gouy layer resembles the diffusion layer of the electrolyte and can be neglected most of the time, since it only becomes important if the concentration of the redox-couple is low [37, 38]. The ≈ 1 nm thick [37] Helmholtz layer is formed due to the adsorption of H^+ and/or OH^- groups (pH dependent) to the semiconductor surface and accumulation of oppositely charged ions in the solution [18]. In order to maintain a charge equilibrium over the interface, a depletion layer will form in the semiconductor (e.g. positive charge for an n-type semiconductor).

The built in voltage of a semiconductor-electrolyte junction is dictated by the difference in the Fermi energies ΔE_F [26]. This potential is dropped in the semiconductor space charge region and the electrolyte and the total potential difference V_T thus consists of V_{SC}, V_H and V_G [38], equation (1.18):

$$V_T = \frac{\Delta E_F}{e} = \frac{E_F - E_{F,redox}}{e} = V_{SC} + V_H + V_G \tag{1.18}$$

Illumination of the semiconductor-electrolyte junction leads to a flattening of the bands in the semiconductor. As in a conventional p-n junction this results in splitting of the Fermi energy into quasi-Fermi levels for electrons E_{FN} and for holes E_{FP}. The illuminated semiconductor-electrolyte interface is shown in Figure 1-5b. In the case of an n-type semiconductor the photo-generated holes will drive the OER at the interface, causing E_{FP} to equilibrate to E°_{redox}. In this photo-anode the backside of the semiconductor is conventionally connected to a metal electrode.

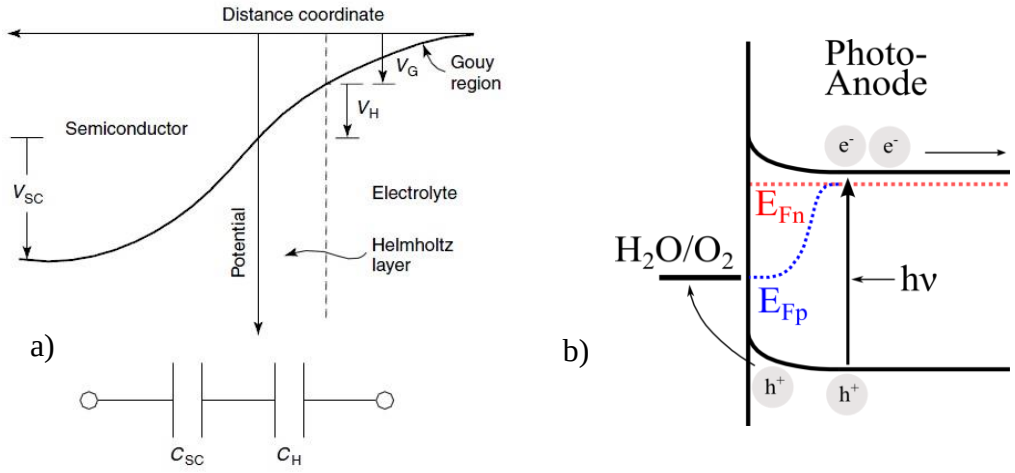

Figure 1-5: a) Detailed illustration of the semiconductor-electrolyte interface. Reproduced with permission from Ref. [38]. Copyright 2007 Wiley-VCH Verlag GmbH & Co. b) The interface of an n-type semiconductor with an electrolyte under illumination (equilibrated).

Photo-generated electrons will travel to the metal electrode and run the HER. The voltage, which is generated due to the charge carrier separation, is called the open-circuit voltage V_{OC} and is the difference between E_{FN} and E_{FP}, equation (1.19):

$$V_{OC} = E_{FP} - E_{FN} \tag{1.19}$$

Its magnitude is strongly dependent on the difference between E_F of the semiconductor and $E_{F,redox}$, When the electrical circuit is closed (e.g. the material is connected to a counter electrode where the complimentary HER/OER reactions runs and charges are transferred over the electrolyte) the impinging photon flux φ_0 may result in a photo-current I_{Ph}. A simple model for the description of the photo-current density j_{Ph} (I_{Ph} per unit area) arising at illuminated semiconductor junctions has been developed by Gärtner [39] and can be written as equation (1.20) [38]:

$$j_{Ph} = e \cdot \varphi_0 \left(1 - \frac{\exp(-\alpha \cdot w)}{1 + \alpha \cdot L_p}\right) \tag{1.20}$$

As equation (1.20) shows, j_{Ph} is influenced by the absorption coefficient α and the diffusion length of the minority charge carrier (here holes, hence L_p). L_p on the other hand is governed by the hole mobility μ_p and the hole lifetime τ_p, equation (1.21):

$$L_p = \sqrt{\frac{k \cdot T}{e} \tau_p \cdot \mu_p} \tag{1.21}$$

The diffusion length of charge carriers is a crucial parameter for the performance of a

PEC. Having in mind that charge carriers in the space charge region – and therefore within its width w – are separated by the electric field, L_p determines how far a charge carrier can diffuse through the material in order to reach the space charge region. Together these two parameters (expressed as the so called Debye-length L_D) form the upper boundary as to how deep charge carrier pairs can be generated before they simply recombine, equation (1.22) [38]:

$$L_D = L_p + w \tag{1.22}$$

Furthermore, when inserting equations (1.17) and (1.21) into equation (1.20) one can recognize some important influences on the obtainable photo-current, equation (1.23):

$$j_{Ph} = e \cdot \varphi_0 \left(1 - \frac{e^{-\alpha \cdot \sqrt{\frac{2 \cdot \varepsilon_0 \cdot \varepsilon_R}{e \cdot N_D} \cdot (V_{SC} - \frac{k \cdot T}{e})}}}{1 + \alpha \cdot \sqrt{\frac{k \cdot T}{e} \tau_p \cdot \mu_p}} \right) \tag{1.23}$$

Increasing the doping concentration N_D, for example, leads to a reduced j_{Ph}. However, N_D is also complicit in determining the position of E_F of the semiconductor and therefore the magnitude of the band bending and V_{SC} at the interface. If the band bending is too low (i.e. N_D low – E_F close to $E_{F,redox}$), then under illumination this would result in flattened bands, which is unfavourable in terms of the need to separate charge carriers and drive them towards the surface to run the OER. It becomes obvious that these two influences are thus somewhat opposing and the control over the doping concentration is very important [40]. Furthermore, equation (1.23) reveals that both an increased μ_p and τ_p would result in an increased photo-current density. While μ_p is a material constant, τ_p is crucially affected by the material quality because it is determined by the rate and kind of recombination pathways within the material. If the density of recombination centers (in the bulk, space charge region and at the surface) is low, the charge carrier lifetime increases leading to an improved photo-current. The charge carrier lifetimes – especially of charge carriers at the surface of the semiconductor as a result of recombination over surface states – were found as the most important parameter that govern the *j-V* characteristics of photo-electrodes [40].

1.3 Materials and devices for solar water splitting

A vast number of materials have been reported for their potential use in solar water splitting, ranging from bulk semiconductor materials such as silicon [41-44], over metal-nitrides and sulfides [24, 45, 46] to metal-oxides [47-49]. A number of excellent

review articles giving overviews of materials for solar water splitting have been published [24-26, 34, 45, 50].

A virtually endless number of semiconducting materials and material combinations exist. However, not all of these are suitable to be used as photo-electrodes in solar water splitting. The following section briefly summarizes the fundamental selection rules for materials used in this field, evaluates some PEC device configurations and introduces some commonly used materials to make them.

A first selection for a material to be used in solar water splitting can be done from its bandgap. Figure 1-6 summarizes the requirements associated with the bandgap energy and the position of the energy bands. Based on theoretical calculations the optimal bandgap energy for a single bandgap absorber is between 2 eV and 2.2 eV, depending on the losses included in the calculation [51]. If a 2 eV bandgap is considered then at best, a solar-to-hydrogen efficiency of about 17 % can be reached with a single semiconductor system. This theoretical calculation includes the assumption that two other requirements for effective solar water splitting are fulfilled: a) the open-circuit voltage generated by the material is greater than 1.23 V + losses and b) the energy straddles the oxygen hydrogen redox-potential. This latter consideration means that the conduction band of the semiconductor has to be energetically above (electrochemically more negative) the hydrogen-redox potential and the valence band has to be energetically below (electrochemically more positive) the oxygen redox-potential. If this requirement is not fulfilled unassisted solar water splitting cannot occur. Nevertheless, materials exhibiting only one favourable energy band position can still be used as either photo-anode or photo-cathode in connection with a (photo-)cathode or (photo-)anode to run the complimentary reaction. Another important property of a material for water splitting is the stability in aqueous media – the electrolyte. Here stability includes general resistance against corrosion in the electrolyte and light-induced degradation (photo-corrosion). The pH value of the electrolyte influences the general stability of a material in an electrolyte. A suitable material should withstand a range of H^+/OH^- ion concentrations in the electrolyte as wide as possible and therefore should not dissolve or corrode. While this criterion is already somewhat challenging, applying a bias in form of an electric potential or illumination (photo-corrosion) further complicates matters.

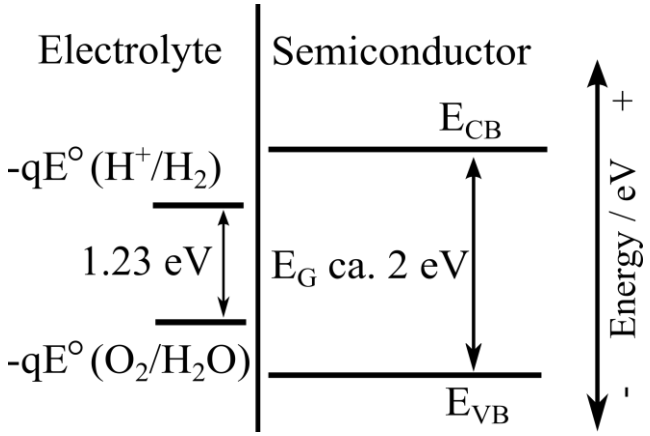

Figure 1-6: Schematic to illustrate the requirements for solar water splitting in terms of the bandgap energy and energy band positions (acidic conditions).

The schematic in Figure 1-7 shows the underlying principle of photo-corrosion. A material is sensitive to photo-corrosion if its oxidation potential ϕ^{ox} and reduction potential ϕ^{re} are misaligned in respect to the oxidation and reduction potential of water. The photoanode in Figure 1-7a will be stable as long as its oxidation potential ϕ^{ox} is below the oxidation potential of water [35]. If it lies above the water oxidation potential, photo-generated holes will oxidize the material first rather than water [35]. Similarly a photocathode (Figure 1-7b) will photo-corrode if its ϕ^{re} lies below the reduction potential of water. Photo-generated electrons will then reduce the material rather than water [35]. Recently it was shown that materials can be efficiently protected against photo-corrosion by ultrathin over-coatings with non-corroding materials [41, 52-55].

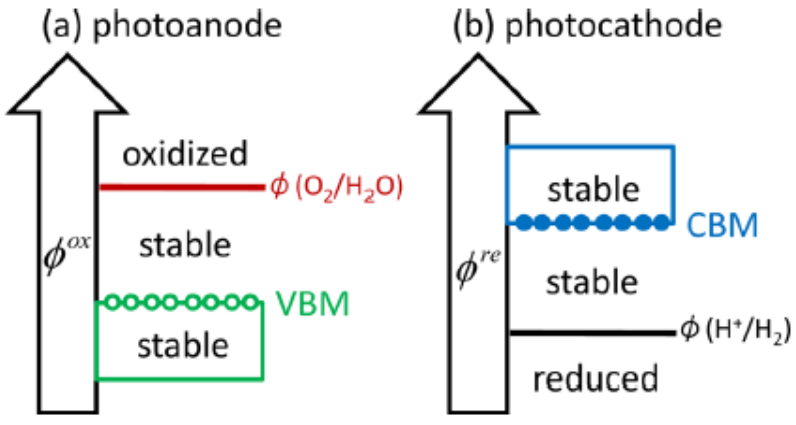

Figure 1-7: Change in resistance against photo-corrosion of photo-electrodes. a) For a photo-anode as its oxidation potential ϕ^{ox} shifts from the valence band minimum (VBM) higher. b) For a photocathode as its reduction potential ϕ^{re} shifts towards the conduction band minimum (CBM). Reprinted with permission from Ref. [35]. Copyright 2012 American Chemical Society.

Furthermore, ideally the material should be earth-abundant, cheap and non-toxic in order to be used in an industrial scale. A material which fulfils all these requirements and efficiently (> 10 % STHE) runs the water splitting reactions has not yet been found.

1.3.1 **Tandem PEC devices**

Indeed, the STHE target of > 10 % seems ambitious to reach with a single material. Thus, it appears likely that future PECs will consist of a combination of various materials in order to achieve high STHEs. Much research in this regard focuses on the development of tandem devices. In such a device a light-active photo-cathode and a light-active photo-anode may be directly connected. Here multiple device configurations are possible, including the introduction of buried PV elements to supply an extra voltage [21]. The basic principle of this configuration (without buried PV) is indicated in Figure 1-1b. If the impinging light is not fully absorbed by the photo-anode, a portion of the irradiation is transmitted through the electrolyte and can be utilized by the cathode material. A photo-active cathode then allows using the band-bending at the cathode-electrolyte interface to run/assist the HER. From an engineering point of view, the two electrodes do not have to be arranged in tandem but could also be arranged next to each other. This holds true as long as an external wire is used to connect the two electrodes. However, in a similar fashion one could also think of this arrangement without the external wire, which would allow for a fully integrated device. An advantage of this configuration – termed an "artificial leaf" by some, due to analogies in respect to the natural photosynthesis occurring in a leaf [56, 57] – could be an easier integration into later reactor designs and possible avoidance of the energy loss inherent to contacting and wiring of the individual electrodes.

A schematic and the respective energy band-diagram of such a wireless tandem PEC, consisting of a photo-anode and a photo-cathode, is shown in Figure 1-8. Both materials are connected by an ohmic contact, which in practice could be a transparent conductive oxide (TCO). Also tunnel junctions are possible, if the band alignment of the photo-anode and photo-cathode materials are chosen appropriately. As mentioned earlier, it is necessary that the front electrode (a photo-anode in Figure 1-8a) consists of a material that transmits a part of the impinging light. This requirement translates into a difference in the respective bandgap energies of the materials, in which E_{G1} >

E_{G2}. Similarly to multi-junction solar cells, an optimized material configuration enables absorbing as many of the impinging photons (of different wavelengths/energies) as possible. However, the choice of appropriate materials is not straightforward. For example the band-edge alignment of the materials needs to be arranged in such a way that energetic losses are minimized. One requirement here is that an overlap between the bandgap energies exists (i.e. the valance band of the photo-cathode is more anodic than the conduction band of the photo-anode) [58]. However, the overlap between the conduction band edge of the photo-anode and the valance band edge of the photo-cathode should be small, since otherwise the photo-voltage obtainable would be minimized [58]. Hence, a few research groups have focused on the optimization of the material combination – especially in regards to their bandgap positions and energies [29, 51, 58-60].

Currently the research regarding tandem PECs is gaining momentum due to the emergence of perovskite photovoltaics, which have shown an enormous improvement in terms of achievable efficiencies within the last decade, now (at the time of writing) reaching up to 22 % [61]. While the integration of same into PECs often resembles more a buried PV approach, these materials are of particular interest as large bandgap material. This is due to the ability to tune the bandgap and photo-voltage of the material by changing the material composition, resulting in a demonstrated STHE of 6 % when coupled with a copper chalcopyrites photo-cathode [59].

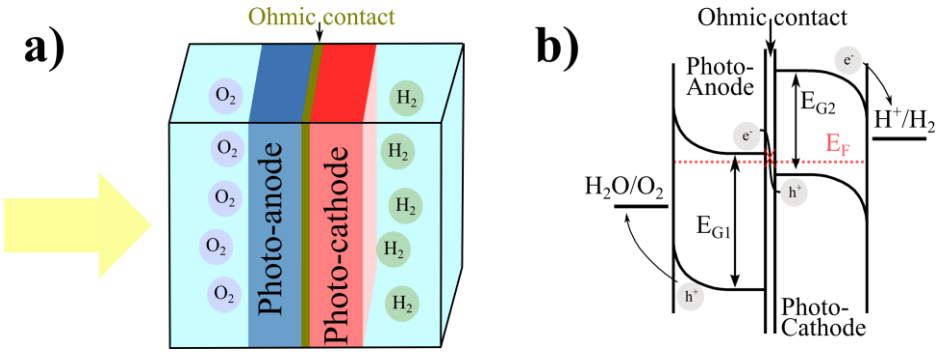

Figure 1-8: a) Schematic representation of a wireless tandem PEC device. b) Energy band-diagram of the device in a). Note that for demonstrative purposes the band-bending resembles the semiconductor-electrolyte interfaces in the dark, while the charge carrier flow resembles the illuminated case.

1.3.2 **Metal-insulator-semiconductor (MIS) structures**

However, similarly to their use in PV cells there are stability concerns regarding the use of perovskites in the presence of an aqueous medium. In order to tackle the stability issue – not only for perovskites but also for a whole range of materials that would either undergo surface transformation, corrosion and/or photo-corrosion –protective coatings in form of metal-insulator-semiconductor (MIS) structures have been studied extensively, as a recent review on the matter shows [55].

A typical layout of a MIS structure consists of a semiconducting substrate covered with an oxide and metal layer. This basic structure – shown in the schematic in Figure 1-9 – is one of the main building blocks in micro- and power electronics. However, as noted previously, recently an increased interest in MIS structures for solar water splitting could be noticed among the research community [55]. The MIS structure addresses several issues commonly experienced in solar water splitting with semiconductors:

- Use of highly absorbing materials with small bandgaps
- Stability issues for small bandgap materials
- Poor charge carrier kinetics at the semiconductor electrolyte interface

In a MIS structure an open-circuit voltage is built up as a consequence of the workfunction-difference between the metal and the semiconductor. Therefore, usually high workfunction metals (e.g. Pt or Ir) are chosen for n-type semiconductors [62]. Devices based on an improved design of a MIS have reached photo-voltages of up to 630 mV, which makes them attractive for the use as photo-electrodes [63]. Furthermore, the metal layer also has the function of promoting charge carrier transport through the oxide layer in order to catalyze the OER. To avoid compromises between charge carrier collection and band bending vs. OER catalysis it is also possible to use two metals to separate their function, as described by Esposito et al. for p-type Si [64]. Small bandgap materials such as silicon (Si) often show poor stability in aqueous

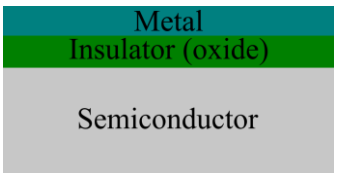

Figure 1-9: Schematic of a MIS structure.

media. On the other hand, they have the advantage of absorbing a high portion of the solar spectrum. In order to take advantage of this material characteristic one has to somehow inhibit the surface-transformation/corrosion processes that would lead to poor device performance. Here an ultra-thin insulator layer (usually an oxide) can protect the semiconductor absorber efficiently against e.g. photo-corrosion [54, 65].

Modern deposition methods, such as atomic layer deposition (ALD), allow for the deposition of ultra-thin, pin-hole free oxide layers and/or special tuning of their physical properties. Beside their protective properties, these layers also enable charge carrier transport from the absorber towards the metal layer (collector). Therefore the MIS structure decouples the stability and light-harvesting characteristics of the semiconductor photo-catalyst [64, 66].

Charge carrier transport through the oxide layer is one of the big challenges. Different transportation mechanisms, as for example transport via tunnelling or defects in the oxide layer, have been reported [54, 65]. Tunnelling or transport via defects greatly affect the oxide thickness required. Hu et al. [65] noticed only a minor dependence of photoanode power-characteristics from the thickness of their ALD deposited amorphous TiO_2 layers. The highly defective oxide was able to efficiently promote the transport from the semiconductor (Si, GaAs and GaP were tested) to the metallic collector. On the other hand, Si photo-anodes prepared by Scheuermann et al. [67] showed a strong increase of the OER overpotential with increasing TiO_2 tunnel oxide thickness (≈ about 21 mV/nm).

Novel approaches to further enhance and control charge carrier transport include the incorporation of organic molecules into the oxide layer [68]. Copper hexadecafluoro-phthalocyanine ($F_{16}CuPc$) and copper phthalocyanine (CuPc) were integrated into Al_2O_3 oxide-layers for $Si/SiO_2/Al_2O_3(F_{16}CuPc)/CuPc/Au$ MIS-structures and tested for their charge transport characteristics by Seo et al. [68]. These workers showed that direct charge carrier transport between the semiconductor and metal via the LUMO (lowest unoccupied molecular orbital) and HOMO (highest occupied molecular orbital) of the organic molecules is possible.

Another route to enhance charge carrier transport through an ITO layer (indium doped tin oxide) involves the deposition of thin metal layer as an interlayer, as for example presented in [69]. These authors sandwiched a 5 nm thin gold layer between two sputtered ITO layers (100 nm). Lower contact and film resistance as well as improved

hole transport and Si absorber stability were the result of the gold interlayer.

It is worth noting that attempts have been made to include the properties of the oxide protection layer and the metal collecting layer into one single material. Kenney et al. used electron beam evaporated nickel (≈ 2 nm) to form n-Si/SiO_2(native)/Ni/ MIS structures [41]. In contact with the electrolyte a thin NiO_x layer was formed at the surface. It was shown that the Ni/NiOx surface layer-stack efficiently catalyzed the OER while preventing the silicon absorber from corrosion.

The combination of both aforementioned device designs may present an interesting route to achieve efficient and stable solar water splitting in the future. Efficient protection of the light absorbing material using a MIS-type structure would greatly enhance the catalogue of potential materials that could be incorporated into tandem devices. However, it is obvious that materials that match the general selection criteria, mentioned at the beginning of this section, are still desirable, since they build the foundation of comparably easy PEC structures. Among the many potential candidates, metal oxides have been considered as a promising class of material for a wide range of applications in PEC and hence these are discussed in the following section.

1.3.3 **Metal-oxides for PECs**

Metal-oxides are the most studied category of materials for solar water splitting. Metal-oxides active for solar water splitting mainly contain transition-metal cations with d^0 or d^{10} electronic configurations. For these materials the conduction band is mostly formed by empty d-orbitals of the transition-metal cations (d^0) or hybridized s and p orbitals of cations (d^{10}) [70]. O2p orbitals commonly form the valence band of these systems, fixing the valence band at ≈ 3 eV vs. SHE [71]. Therefore most metal-oxides are wide-bandgap semiconductors with typical bandgap energies of ≈ 3 eV. Prominent examples for this material group are titanium dioxide (TiO_2), zinc oxide (ZnO) and tungsten trioxide (WO_3).

Since materials with bandgaps > 3 eV can only absorb less than 10 % of the radiation emitted by the sun, attempts were made to find alternative metal-oxides. A common approach to shift the bandgap towards the visible region is the incorporation of nitrogen (N) into the metal-oxide. The so formed metal(oxy)-nitrides exhibit a valence band which consists of hybridized N2p and O2p orbitals [71].

A hybridization of orbitals is also the reason for smaller bandgaps in materials like $BiVO_4$ and α-Fe_2O_3 (hematite). In $BiVO_4$ with a scheelite structure, transitions from the Bi6s or hybridized Bi6s-O2p states to the conduction band (composed of V3d states) are possible, resulting in a bandgap of 2.4 eV [72]. Similarly the valence band of α-Fe_2O_3 consists mainly of O2p and Fe3d hybrid states [73], thus, allowing the material to absorb photons with energies greater 2.2 eV [74]. Even if the bandgaps of these materials are close to the optimal bandgap for a single materials system, for both, $BiVO_4$ and α-Fe_2O_3, the efficiency is limited by the poor charge carrier transport kinetics [75, 76].

However, promising improvements were made for both materials. Kim et al. reported on a significant increase of the photocurrent density of α-Fe_2O_3 photo-anodes [77]. Their wormlike structures grown on transparent conducting oxide (TCO) coated glass reached 4.32 mA/cm² at 1.23 V vs. SHE. A stand-alone solar-to-hydrogen efficiency (STH) of 4.9 % was achieved by Abdi et al. [32]. They introduced a gradient of tungsten doping to enhance the charge carrier separation of their $BiVO_4$ photo-anodes. In connection with a double-junction solar cell the system reached a stable photocurrent of 4 mA/cm².

Oxygen evolution catalysts based on metal oxides

While the aforementioned materials could, for example, be coupled to a platinum counter-electrode and used as single material PEC to generate solar hydrogen, the overall STHE will be low. This is not only due to the low photon absorption (compared to a tandem PEC) and poor charge carrier transport kinetics but also arises to a high degree from the kinetically challenging, multiple particle OER and HER (see also section 1.2). In order to minimize the losses associated with these reactions the photo-electrode is usually coated with a co-catalyst layer.

Seen as a whole, the water splitting reaction is an energetic uphill reaction. This means that in addition to the theoretical energy needed to run the reaction (demanded by ΔG^0 = 237 kJ/mol at 25 °C; 1.23 V) an additional activation energy E_A is needed. The role of the co-catalyst is thus to minimize the magnitude of E_A [78]. For PEC devices these energetic losses (with or without co-catalyst) are represented by the overpotential needed to run the reaction in question. If a suitable co-catalyst is applied to a photo-electrode the required overpotential can thus be reduced and the obtainable photo-

current can be increased [78]. Additionally, as presented in section 1.3.2, the co-catalyst attracts the charge carriers of the photo-electrode (e.g. holes for a photo-anode) and may thus improve the charge carrier separation, reduce recombination and photo-corrosion. However, due to the need for four holes at the semiconductor-electrolyte interface to run the OER, this reaction represents a bottleneck in current catalyst research associated with PECs [79, 80].

Iridium/IrO_2 was already mentioned as an example for such a catalyst material throughout the preceding sections. Together with ruthenium these materials represent a benchmark for OER catalysts. However, since they are relatively scarce, earth-abundant alternatives are of high importance. Here (transition-) metals and their oxides again present a promising material class. Even though plain metals and their alloys can be deposited, under oxidative conditions in an aqueous electrolyte the surface of such layers can be expected to be oxidized. Among the many candidates materials based on nickel (Ni) and cobalt (Co) have attracted great attention, as low overpotentials have been reported for same [79, 80].

For the OER, nickel based materials (nickel oxide (NiO) and nickel hydroxide (α- and β-$Ni(OH)_2$)) have been the subject of many studies [81-87]. In alkaline media, the catalytic activity of $Ni(OH)_2$ materials is believed to involve the formation of nickel oxy-hydroxide (NiOOH) at the surface [81, 82, 87]. This formation goes alongside a change in the Ni oxidation state from II^+ to III^+ – the accepting of a hole from the anode material leading to the ability of the catalyst to accept an electron from the electrolyte (e.g. from a OH^- group). Similarly, a nickel oxide layer may undergo hydration in alkaline media, leading to the formation of a hydrated oxide layer with significant activity towards the OER [82]. Importantly, the overpotentials for these simple nickel based materials are reported to be around 400 mV or lower [80, 85]. In turn Mao and co-workers, for example, showed that the photo-electrochemical performance of to ZnO photo-anodes could be greatly enhanced with a NiO/$Ni(OH)_2$ over-coating [83, 84]. Furthermore, the catalytic activity of nickel based materials – and the PEC performance when these catalyst are applied – can be greatly enhanced by the incorporation of iron [88-91]. However, the exact role of iron in these materials remains to be determined [92, 93].

Similarly to nickel based materials, catalysts consisting of cobalt and its oxides/hydroxides have been extensively researched [88, 94, 95]. Jiao and Frei

reviewed the overpotentials of some literature reports investigating the OER using the mixed-valence cobalt oxide Co_3O_4 [96]. At room-temperature these values ranged between 414 mV – 235 mV [96]. In this regard nanostructuring may present an interesting approach to further reduce the overpotential, since it was shown that the overpotential of Co_3O_4 nanoparticles decreased significantly with smaller particle sizes (increase of the surface area) [97]. This appears likely to be correlated to the number of active sites able to participate in the OER, suggesting that the electrolyte does not penetrate into the bulk of the catalyst material. However, very small clusters of the Co_3O_4 catalysts have recently been shown to not improve the OER kinetics further [98]. Additionally, Co_3O_4 has gained interest due the possibility to catalyze water oxidation in neutral conditions [95, 96]. Doping of the material with silver could even further improve its stability at lower pH values [99].

One strategy to obtain Co_3O_4 is to anneal cobalt hydroxide $Co(OH)_2$ and/or cobalt oxy-hydroxide CoOOH [100, 101]. However, both $Co(OH)_2$ and CoOOH also represent known OER catalysts with reported overpotentials only slightly higher than for Co_3O_4 [101, 102]. $Co(OH)_2$ may be of particular interest, since it can also be converted to CoOOH by electrochemically cycling/scanning of an $Co(OH)_2$ electrode around/over the Co^{2+} - Co^{3+} oxidation potential in alkaline media [101, 103]. Furthermore, the different oxides/hydroxides may perform differently in connection with other materials. Zhang et al., for example, showed that the overpotential of carbon nitrides impregnated with layered $Co(OH)_2$ can be significantly lower when compared to the structures after annealing (i.e. Co_3O_4 formation) [104]. These electrodes were shown to also efficiently promote the oxygen evolution reaction under UV-Vis irradiation. Similarly, the photo-electrochemical performance of Si photo-anodes could be enhanced using $Co(OH)_2$ as a catalyst [105]. On the other hand, an increase in photo-current was reported for photo-anode materials like TiO_2 and hematite (α-Fe_2O_3) when decorated with Co_3O_4 [100, 106]. Interestingly some studies suggest that the co-existence of different cobalt phases may result in superior OER kinetics [106, 107]. The combination of Co_3O_4 with a surface layer consisting of $Co(OH)_2$ exhibited remarkable performance when coated onto Si [107]. The resulting photo-anodes showed a photo-voltage of 600 mV, a photo-current of 30.8 mA/cm^2 at 1.23 V vs. RHE and good stability over several days [107]. As is the case for Ni-based catalysts, the catalytic function for Co-based materials is reported to stem from the oxidation of cobalt to Co^{3+} and Co^{4+} [98, 107]. For both $Co(OH)_2$ and Co_3O_4, it can thus be expected

that, when applying an anodic potential and/or under solar irradiation, CoOOH (i.e. Co^{3+}) is formed at the catalyst surface with a further subsequent transformation to CoO_2 (i.e. Co^{4+}) [108]. Water oxidation may then occur due to the formation of the O-O bond at two or more catalytically active Co^{4+} sites [98, 107, 109]. In turn Co^{4+} is reduced but can be readily oxidized again under the aforementioned conditions [109].

1.4 Zinc oxide for photo-(electro)chemical applications

Another interesting metal oxide to be used in PECs but also for photo-catalytic applications is zinc oxide – the material which this thesis focuses on. The material properties and prospects shall thus be elaborated in further detail in the following sections.

Zinc oxide (ZnO) is composed of the elements zinc (2+) and oxygen (2-). In terms of abundancy of the elements in the earth`s crust, zinc is ranked as 25th (75 ppm) and oxygen as 1st (474000 ppm) [110, 111]. Estimated reserves of 230 million tonnes of zinc and mining areas spread across the world make the metal oxide therefore relatively abundant [110, 112].

Chemically, ZnO can exist in three crystal phases – zinc blende, rock salt and hexagonal wurtzite, with the latter being the most stable phase at ambient conditions [113]. In the wurtzite crystal structure, the Zn^{2+} and O^{2-} atoms are tetrahedrally coordinated and occupy alternating planes along the c-axis [114, 115]. In this structure, ZnO forms a tetrahedral unit cell, which lacks symmetry and thus leads to the emergence of piezoelectric properties [114, 115]. The unit cell is determined by the two lattice parameters *a* and *c*, which for the wurtzite structure exhibit a theoretical ratio of $c/a= (8/3)^{0.5}$ [113]. As for other metal oxides, the bonding character of ZnO can be described as highly polar [18]. This arises due to the big difference of the electronegativity of the elements (E_O = 3.44; E_{Zn} = 1.65; ΔE = 1.79). The bonding is therefore partly covalent and partly ionic. On the other hand, the big difference of the electronegativity demands that the valance band is mainly formed by the O2p orbitals. The conduction band is governed mostly by the empty 4s orbital of Zn [116] and/or a hybridization of empty s and p orbitals [70]. This leads to a wide, direct bandgap with E_G = 3.37 eV [114, 115].

So far two key properties of zinc oxide have been mentioned: its piezoelectricity and the wide, direct bandgap. These properties are of particular interest for various

applications. Motion energy can, for example, be converted into electrical energy by taking advantage of the piezoelectric effect. Since our daily life is based around motion and also because wearable technologies are becoming more and more important, much research has focused on the development of piezoelectric nanogenerators (PNGs) designed in order to convert mechanical and vibrational energy into electricity for powering nano-scale devices. In particular, ZnO has been considered as a promising material as a result of the first successful demonstration of a PNG in 2006 [117, 118]. Since then the field of energy harvesting has experienced an ever growing level of research interest especially since the realization of a triboelectric nanogenerator (TENG) in 2012 [119-121]. While this type of energy harvester does rely on the triboelectric effect, the introduction of piezoelectric ZnO has been shown to enhance the performance of TENGs [122, 123].

The wide bandgap on the other hand may lead to applications in photonics [124]. Here light emitting diodes operating in the UV or blue spectral range are example applications [124-126]. In the mentioned spectral ranges gallium nitride materials – with a comparable bandgap energy – are traditionally used for opto-electronic applications [127]. ZnO has been widely used to compliment GaN-based devices but, due to a strong improvement of the quality of the ZnO crystals that can be produced, it is also considered as possible replacement for GaN [125, 127, 128]. A big advantage in this regard is that, in contrast to GaN, large single crystal ZnO materials are relatively easy to prepare, using a wide range of deposition techniques [113, 114, 127]. High quality ZnO single crystals are also studied from the point of view of their possible use as UV laser sources [129, 130].

Apart from the wide bandgap, the high binding energy that ZnO possesses, some 60 meV at room-temperature, is an important material property in this regard. The binding energy is larger than the available thermal energy at room temperature (25 meV) and thus stable excitons can exist that enable efficient excitonic recombination at room-temperature [129, 131]. For laser applications, single crystal nanorod geometries may be particularly promising because they inherently provide the necessary lasing cavity [129, 131].

ZnO exhibits an unintentional n-type character (i.e. it exhibits a high number of electron donors). Additional doping can further increase the donor concentration. Among the most studied donor dopants for ZnO is aluminium (Al) [132].

Concentrations of 2 % - 5 % of Al in ZnO have been shown to yield low resistivities (10^{-4} Ω cm range) [132]. Paired with the large E_G, Al-doped films are established candidates for transparent conductive oxides (TCOs), which could possibly replace the less earth-abundant indium tin oxide or fluorine doped tin oxide films. Another important material property for every application where an electronic charge has to be transmitted is the mobility of charge carriers (electrons and holes). For ZnO single crystals, the electron and hole mobilities have been reported to be as high as μ_e = 200 $cm^2\ V^{-1}\ s^{-1}$ and μ_h = 180 $cm^2\ V^{-1}\ s^{-1}$, respectively [18]. Recalling equation (1.23) it is apparent that it is highly beneficial to have high charge carrier mobilities, since a positive effect on the photo-current achievable can be expected. Fortunately, ZnO exhibits relatively high charge carrier mobilities when compared to other metal oxides frequently used for solar water splitting [18, 133]

Combining the aforementioned material properties, its non-hazardous nature and the ability to deposit ZnO in good quality and in nanostructured forms using a wide range of deposition methods, it is no surprise that also the PEC and photo-catalysis research community has a keen interest in ZnO.

ZnO for PECs

As for many other materials, ZnO based PECs may show improved performance when deposited in nanostructured form [134]. Nanostructuring of photo-electrodes can have various advantageous such as a shorter carrier collection pathway (i.e. necessary charge carrier diffusion is reduced), decreased reflectance leading to enhanced absorbance and hence improved charge carrier generation, and an enhanced charge transfer at the interface due to an increased overall surface area [50]. However, since disadvantages related to the small size of these structures (e.g. increased surface recombination and a lower photo-voltage) may also occur [45], the controlled deposition of nanostructures is key to achieving good-performing devices.

In the following some of the published literature dealing with the use ZnO for PECs will be addressed but beforehand it is important to note some drawbacks when accessing those reports. Currently there are no accepted national or international standards for the evaluation of the performance of PEC/photo-electrodes. Despite the advice to researchers to try to follow the same set of general protocols and guidelines for the assessment of important material and electrode characteristics [135], literature

reports can and do vary dramatically in how the PEC performance is evaluated. For example, large differences exist in the spectrum and intensity of the light-source used. The photovoltaic community has defined the AM 1.5 G spectrum (see also Figure 1-3 and related comments) with an intensity of 100 mW/cm^2 as the research/industrial standard to report efficiencies. Solar simulators were thus developed to model the sun's spectrum as closely as possible. Each solar simulator is evaluated and categorized for its spectral match, stability and homogeneity. However, in research papers concerning PECs one can often find non-standardized illumination conditions such as UV-lights, LEDs and a broad range of intensities. Also the use of AM 1.5G filters in connection with, for example, a high-power xenon lamp is somewhat troublesome, since the parameters of the spectral match, stability and homogeneity are mostly unknown. While these light sources are indeed helpful when accessing more fundamental questions related to the material properties, it is often difficult to compare reported efficiencies. Also some variation in general measurement parameters during the reported photo-electrochemical experiments further exacerbate the problem. The (potential) scan-rate, for example, may have an influence on the magnitude of the photo-current and thus on the often-reported applied bias photon-to-current efficiency. However, an even more characteristic pitfall that exists in the literature is the use of various electrolytes. Generally, when reporting efficiencies, one should use electrolytes where the generated current solely arises from the water splitting reactions outlined in section 1.2. Metal oxide photo-anodes can be measured in an alkaline electrolyte (e.g. NaOH, KOH). Despite the pH dependence that can be corrected for, the concentration could have a major influence on the photo-current simply due to the availability of OH^- groups at the surface and improved transport characteristics for higher electrolyte concentrations. Furthermore some groups use electrolytes that potentially act as sacrificial hole scavengers (electron donor). This obscures reported photo-currents and efficiencies. A good example for a sacrificial hole scavenger is the Na_2S/Na_2SO_3 system, that may be used to inhibit material decomposition [136, 137]. In this system the photo-generated holes do not directly oxidize water but S^{2-} and SO_3^{2-} ions while photo-generated electrons still participate in the HER [136]. When such an electrolyte is used, one can nevertheless compare samples of one study in order to get insight into the charge carrier kinetics of the electrode materials. For example, this was, recently done by Yolaçan and Sankir where they investigated different ZnO morphologies and their photo-currents [138]. However, they also calculated PEC

efficiencies and compared them to other literature reports, which is somewhat misleading for real PEC applications [138]. How significant the differences in photo-current may be when using a sacrificial hole scavenger (Na_2SO_3) as compared to a more common electrolyte (Na_2So_4), was recently elucidated for ZnO nanorod arrays [139]. Unfortunately the pH values of the electrolytes were not evaluated, rendering the reported 4.5-fold improvement of the photo-current at 0.6 V vs. Ag/AgCl open to question [139]. Also stability tests are obviously affected by such electrolytes. It is also noted, that secondary-reactions of photo-generated holes with anions of an electrolyte can occur (e.g. from buffers or acids) [140, 141]. The recorded photo-currents and stabilities may well vary depending on the anion species, even at a similar pH [140]. When secondary-reactions may play a role, the oxidation products should be analysed, since the efficiency will crucially depend on the dominating reaction [141]. With these remarks in mind, the following sections focus on reported improvements and comparisons within the individual studies but do not compare reported efficiencies.

1.4.1 **PEC performance of ZnO materials having different morphologies**

Wolcott and co-workers deposited ZnO nanostructures using conventional pulsed laser deposition, pulsed laser oblique-angle deposition and electron beam glancing-angle deposition techniques [142]. The different deposition techniques/geometries led to films with different morphologies and sizes but also to different donor densities and absorption characteristics. In particular, their data suggests a trend of the resulting photo-electrochemical performance and the donor density, which was found to be closely related to the density of defects in the films [142]. The sample with the highest donor density, for example, exhibited the lowest photo-current. The authors attributed this effect to increased charge-carrier recombination over defects and thus to a worsening of the charge carrier transport. In addition to their discussion it may however be noted that when the donor density is too high this may necessarily lead to a decrease of the photo-current density for reasons discussed in section 1.2.1 and in Ref [40].

In order to avoid the influences that different deposition techniques may have on the material properties, one can use the same growth technique but change the growth properties. While even this approach may lead to different nanostructure geometries,

it is for example possible to change the aspect ratio of ZnO nanorods (NRs) during hydrothermal synthesis by varying the zinc precursor to hexamethylenetetramine (HMTA) concentration ratio [143]. The resulting ZnO NR photo-anodes showed an increased photo-current with decreasing rod-diameter as the most influential parameter [143]. However, while the authors assumed that changing the concentration ratio would mostly effect the structural properties, it has also been shown that the defect density is significantly changed by this approach [144]. This may in turn explain why the efficiencies of samples with different rod-diameters was different depending on the light-source used (UV or simulated solar irradiation). In this regard, a somewhat more appropriate approach was recently chosen by Govatsi et al., where ZnO NR-arrays with different aspect-ratios (i.e. varying rod- length and diameter) were grown by fixing the zinc precursor to HMTA ratio but changing the overall concentration during the hydrothermal growth [145]. The important structural parameters of these nanorod-arrays are shown in Figure 1-10a - d. When these different nanorod-arrays were tested for their photo-electrochemical properties, it was firstly revealed that both thin (40 nm) and thick (260 nm) nanorod-arrays lead to poor photo-anode performance. In the case of the thin NRs, the authors attributed the low photo-current obtained to the low number of NRs. On the other hand, for thicker rods (low aspect-ratio), the overall surface area is reduced and the availability of exposed surface to the electrolyte will be reduced due to very dense growth [145]. NR-arrays with medium rod-diameters showed an increase in the photo-current, with the sample exhibiting a

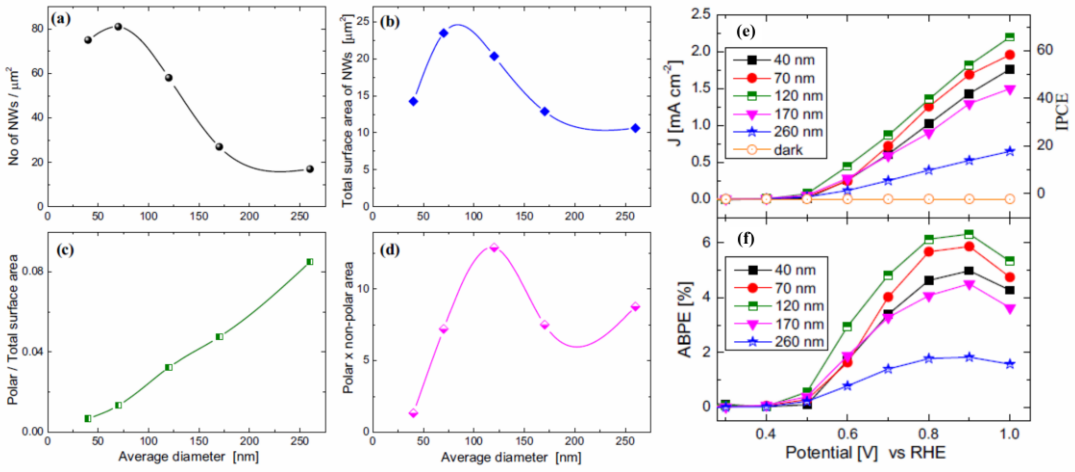

Figure 1-10: Correlation of structural ((a) - (d)) and photo-electrochemical properties ((e) and (f)) of ZnO nanorod-arrays. Reprinted with permission from Ref. [145]. Copyright 2018, Elsevier.

rod-diameter of 120 nm performing the best. Interestingly, the performance did not peak at the maximum total surface area (see Figure 1-10b and f) – which was observed at a rod-thickness of 70 nm – but at the maximum product of polar · non polar surface area (see Figure 1-10d and f) [145]. These results may confirm those from Hsu et al. which deliberately grew ZnO nanostructures with strongly varying crystal plane contributions [146]. Nanosheets with a relatively large portion of polar facets (crystallographically, the (002) plane – for aligned nanorods this resembles the plane perpendicular to the substrate and aligned along the c-axis) showed an improved photo-current, compared to nanotubes which showed a higher contribution of non-polar facets [146]. Finally, these authors reason that the polar-facets exhibit a higher activity towards the splitting of water, since they have the highest surface energy among all facets and exhibit an increased capability of adsorbing reactant ions [146]. It is important to note that this study does not address the obvious differences in relation to the donor densities and the possibly related changes in the defect chemistry, which may also impact the photo-electrochemical properties. From a theoretical point of view, the arguments in favour of a higher PEC performance with increasing exposure to the (002) planes are supported by the fact that a surface (002) plane may be Zn rich and may exhibit a dangling bond, translating into a high surface energy, as shown by Pawar et al. [147]. Using a secondary growth method, these workers were able to grow comparably flat films (i.e. the surface area should be somewhat comparable) where the surface exposed to the electrolyte consisted either of the (100), (002) or (101) plane. In addition to a higher surface energy, the sample with higher (002) plane contribution showed the lowest bandgap energy and therefore benefited from an increased absorption [147].

Nevertheless, the statement that "increased contribution of polar facets = increased PEC performance" may not be universally applicable for different ZnO morphologies, as has been shown by somewhat contradicting results obtained by Liu et al. [148]. Even though these workers obtained their results in 0.1 M Na_2S (a hole scavenging electrolyte), they found the photo-current to increase from nanodisks (high (002) contribution) over nanorods/nanowires to nanotubes and it was speculated that the increased absorbance of the nanotubes was responsible for the observed performance increase [148]. In another study, nanotubes were similarly found to be more efficient than nanorods [149]. While a reduced bandgap energy observed for the nanotubes surely increases the photo-current, the authors correctly point out that the more general

structural differences are highly important and need to be assessed appropriately [149]. Nanotubes exhibit a much larger surface porosity and active surface area to volume ratio than nanorods. In light of the semiconductor-electrolyte interface this results in an improved access and transport of the electrolyte [149]. Furthermore the smaller width of the tube-walls as compared to the rod-diameter may also lead to an increased carrier separation [149].

Other strategies to increase the PEC performance of ZnO nanostructures by changing their morphology include, for example, the deposition of branched nanostructures [150-152]. For these structures, a secondary growth method is generally applied to form e.g. nanowires or spikes branching off a bigger nanostructure. Zhang et al. used nanorods as a 'backbone' nano-structure and showed that the addition of nanowires branched thereof increased the photo-current density [151]. Various nanoforests (in essence also nanowires branching of nanorods) were thoroughly investigated by Sun and co-workers [152]. Example SEM images of their individual brush-like and willow-like nanotrees are shown in Figure 1-11a and b, respectively. Densely packed nanowire branches exhibited the best PEC performance. One positive aspect of these dense nanoforests is the increased surface area. Furthermore, light scattering events may increase the light harvesting and absorption in those samples (see optical properties and schematic representation, Figure 1-11c - f). Finally the authors find that the good PEC performance (see Figure 1-11g -h) stems from the aforementioned effects in conjunction with a small charge transfer resistance and increased charge carrier lifetime [152]. Also, nano-spikes branching of tetrapods have been found to enhance the overall light harvesting and thus resulted in a doubling of the photo-current density and the incident-photon-to-current-conversion efficiency [150]. That the deposition time – and therefore tetrapod morphology – can influence the photo-current was demonstrated in reference [153]. Doubling of the photo-current density was observed for samples that were grown for 90 min instead of 60 min during the deposition using a tube furnace. The improvement was related to a better crystallinity and lower defect density of the sample [153]. However, a possible surface area enhancement due to the longer deposition time was not correlated to the photo-current improvement.

This effect will surely have contributed to the improved photo-currents for the particular 'nanocorals' formed, which were deposited by employing a certain RF-

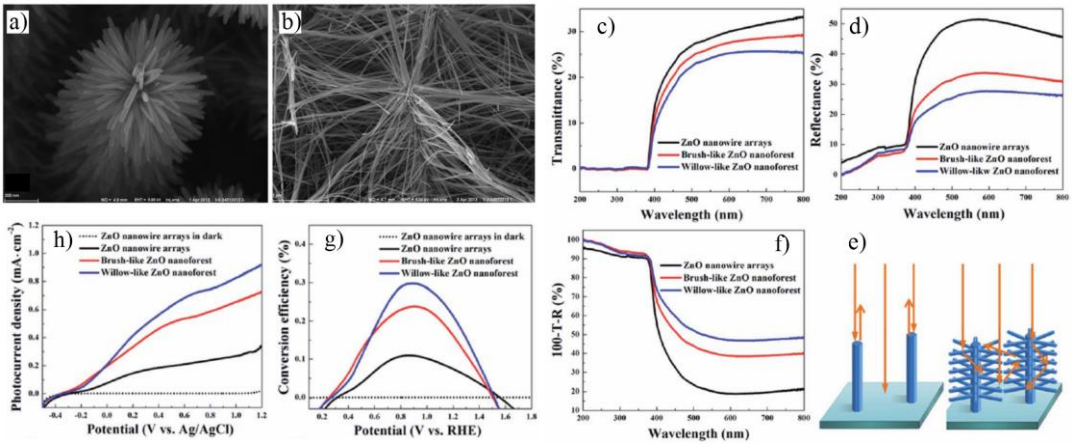

Figure 1-11: SEM images of a brush-like and willow-like nanotree (a) and b), respectively). Optical properties of ZnO nanoforests (c), d) and f)) and the schematic representation (e)) of scattering effects that underpin the optical properties. The tree-geometry increases the light-harvesting due to multiple scattering events. Applied bias photon-to-current efficiency (g)) and j-V plot (h)) of different ZnO nanoforests. Reproduced from Ref. [152] with permission from The Royal Society of Chemistry.

power during the sputtering process [154]. The nanocorals were found significantly more efficient than nanorods or compact films [154]. The same group investigated the PEC performance of different ZnO morphologies as the result of varying the gas ambient present during the sputtering process. At a substrate temperature of 500 °C, they were able to grow aligned ZnO nanorods using a mixture of argon and nitrogen as the gas ambient [155]. When only argon was used no aligned nanorods could be observed. Interestingly, the nanorod geometry exhibited a two-fold higher photo-current, probably related to an increased surface area and smaller bandgap [155].

All of the aforementioned articles focus on the structural/morphological influences on the PEC performance of ZnO nanostructures. However, sometimes the differences evaluated among e.g. the various geometries and crystal facets maybe somewhat obscured by other influences. Here defect states can crucially effect the PEC performance and a change of the defect chemistry as the result of a changed morphology needs to be expected. The following sections deal with strategies as to how to further improve the photo-(electro)chemical performance of ZnO, including the role that defects may play. Apart from PEC applications photo-catalytic studies will also be included, since these studies give valuable insight into the kinetics and activity of the material in question and are thus helpful when accessing the material properties. For a recent review on the aspects that influence the use of ZnO as a photo-catalyst the reader is referred to Kumar and Rao [156]. However, it is not necessarily

true that a material that can photo-catalytically degrade a pollutant well (e.g. a dye), exhibits equally good PEC performance.

1.4.2 Facilitation of photo-(electro)chemical reactions due to defect-engineering in ZnO

Currently it is rather difficult to deposit defect-free ZnO materials. While the traditional strategy for the deposition of devices that perform well is to avoid defects within ZnO, another route aims at engineering the defect-chemistry towards a specific application. In the following the latter route will be explored by introducing some of literature reports dealing with the subject matter, but first some more general aspects in relation to defects in ZnO shall be elaborated.

For ZnO the term ‘defect-free’ means that the crystal follows exactly the wurtzite crystal structure with no inclusion of foreign elements (i.e. extrinsic defects). Furthermore every atom within the crystal is in the correct configuration of the unit cell, without any Zn/O atoms missing (vacancies), Zn/O atoms occupying the O/Zn position in the unit cell (antisites) or additional Zn/O atoms within the crystal structure (interstitials). The aforementioned crystallographic point defects are all of intrinsic nature and are rather plentiful in ZnO. Furthermore these defects may form defect-complexes. If these defects are present in the ZnO crystal, a change of the structural properties (e.g. stress or strain) must be expected. However, since all defects also differ energetically from the usual Zn-O bonding configuration, they also have crucial influence on the resulting electronic and optical material properties. It is thus of immense importance to control the intrinsic and extrinsic defects in order to achieve the desired material properties for a specific application.

Usually ZnO exhibits an unintentional n-type character, which means that it has a high concentration of donor-defects that lift the Fermi energy close to the conduction band edge. The origin of the unintentional n-type character is still a matter for debate but it is generally agreed that it must be related to defects in the material [124, 127, 157-160]. Theoretically, all donor-type defects could be considered – intrinsically, these are oxygen vacancies V_O, zinc interstitials Zn_i and zinc antisites Zn_O in ZnO (neglecting defect-complexes with donor-character) [159]. In order for a material to exhibit n-type character at room-temperature, the defect must donate its electron(s) to the conduction band. This demands that firstly, the energetic position of the defect has to be close to the conduction band edge (shallow) and secondly, the defect is

thermodynamically stable. Historically, V_O was seen as possible origin for unintentional n-type doping of ZnO [127, 157, 158]. This defect has a low formation energy in n-type ZnO and could thus exist relatively abundantly [127]. Over the past two decades and with the emergence of computer-based atomic structure modelling the view on this defect has however changed. It is now believed that the energetic position of the thermodynamically stable neutral V_O is deep in the forbidden gap, which renders it unlikely to be ionized at room-temperature [127, 158]. Nevertheless, the electronic properties of the material can still be crucially influenced by oxygen vacancies – especially if it acts as compensation of intentional p-type doping, which may be one important reason why p-type doping still remains challenging in ZnO [158, 159]. Zinc interstitials on the other hand may contribute to the unintentional n-type doping, since they were found to be shallow defects [127, 144, 161]. A relatively high formation energy should however result in a low concentration of this point-defect [127].

As an extrinsic defect, hydrogen is now considered as a likely source for n-type doping, even though literature reports from the 1950s concluded this already [158] and references within. The introduction of hydrogen into ZnO is difficult to control since it is almost impossible to exclude it during the synthesis of the material. Similarly related to the growth method/conditions, is the fact that the formation energies of the intrinsic point defects vary depending whether the synthesis is carried out under zinc or oxygen rich conditions [127]. In turn, this leads to difficulties that are inherent to studies that compare, for example, the photo-current of different ZnO morphologies deposited using different growth methods. The use of different growth methods will impact the defect-chemistry and this in turn may, as we will see in the following, lead to rather different PEC or photo-catalytic performance.

Another problem that arises due to the abundance of intrinsic defects in ZnO is that material properties in relation to PEC or photo-catalytic applications are often difficult to assign to one specific defect. Here a first issue is often to identify the property-dictating defects. For this purpose photo-luminescence experiments are often used, since these measurements may give an idea of optical transitions caused by defects. However, the assignment of the, usually very broad, emission in the visible region is not straightforward due to the overlap of emissions caused by different defects [125, 126] and the uncertainty of electronic structure calculations in this regard [158]. Thus,

another approach is to deliberately try to induce a specific defect in order to study the effect on the material properties and the PEC or photo-catalytic performance. Often the synthesis process is changed in such a way that it would theoretically favour the formation of certain defects. Post-deposition treatments such as annealing in different atmospheres represent an additional approach to change the defect chemistry. However, it is important to note that, whichever routes are followed, the material properties need to be evaluated with as many characterization methods as possible, in order to conclusively relate a change of the PEC or photo-catalytic performance to intrinsic defects.

Probably the most studied defect for defect-engineered functional ZnO is the oxygen vacancy. For a recent review on the synthesis, properties and applications of ZnO nanomaterials with oxygen vacancies the reader is referred to Wang et al. [162]. Deliberately V_O rich ZnO films can be synthesized for example by calcination of a ZnO_2 precursor, with the V_O concentration depending on the calcination temperature [163]. A relatively moderate temperature of 400 °C led to the deposition of films with a high number of oxygen vacancies. When higher temperatures were chosen for the calcination in air, the oxygen vacancies were partly filled [163]. The V_O rich sample showed a bandgap narrowing and as result an increased absorption of visible light. A schematic representation of the variation of the bandgap/absorption in dependence of the V_O concentration is shown in Figure 1-12a and b. In turn, Figure 1-12c depicts that the highest photo-current under irradiation with $\lambda \geq 400$ nm was recorded for the sample with the highest V_O concentration/highest visible light absorption [163]. Also the degradation of 2,4-dichlorophenol was found to be significantly higher as compared to the other samples.

A visible-light activated photo-current has not been observed for ZnO single crystals deposited via a chemical vapour transport method [164], even though the authors recognized a significant shift of the absorption onset for their as-grown films. After annealing in oxygen, the absorption shifted towards the UV range and the photo-current density of their photo-anodes decreased. It was postulated that the oxygen anneal led to a filling of oxygen vacancies and thus resulted in the observed changes of the material properties [164]. However, the defect-chemistry was not investigated properly, making a conclusive statement about the role of oxygen vacancies difficult.

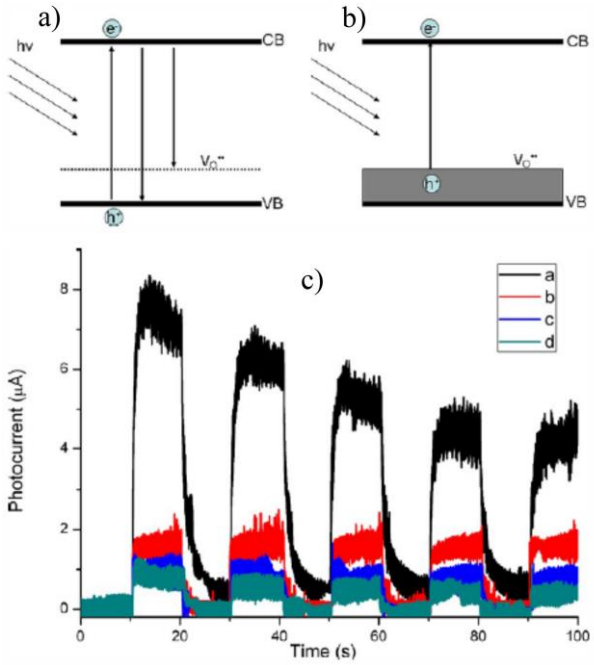

Figure 1-12: Schematic representation of ZnO with a low and high concentration of oxygen vacancies (a) and b), respectively). A high concentration of oxygen vacancies leads to delocalization of the defect states, overlap with the valence band and thus shifting its minimum upwards. c) photo-current of ZnO annealed at (a) 400 °C (high V_O concentration), (b) 600 °C, (c) 800 °C and (d) ZnO reference. Note that the V_O concentration was decreased upon annealing at temperatures > 400 °C. The photo-electrodes were measured at zero bias voltage versus Ag/AgCl in 0.2 M Na_2SO_4 aqueous solution. Reprinted with permission from [163]. Copyright 2012 American Chemical Society.

Another method of introducing V_O into ZnO may be the annealing in a hydrogen atmosphere at moderate temperature [162]. For TiO_2, this strategy has attracted considerable attention and the resulting hydrogenated photo-anodes, sometimes referred to as 'black titania', show remarkable PEC performance [47, 165]. This strategy was adapted for ZnO photo-anodes by Yao et al. [166], who showed that the hydrogenated (potentially V_O rich) ZnO photo-anodes showed the highest photo-current densities. Despite an obvious color change (milky-white to brown), significant visible light activity was not observed for these samples. On the other hand, the donor-density was found to increase by an order of magnitude for the hydrogenated samples. This was attributed to be the result of both the induction of V_O and hydrogen impurities. Thus the authors concluded that the increase of the PEC performance of the hydrogenated samples is related to an increased conductivity and improved charge carrier transport at the interface [166]. That the benefits of the hydrogen treatment may have another/additional origin was suggested following transient-absorption

experiments on ZnO nanowires [167]. Evidence was presented that hydrogen could passivate the acceptor-type defect V_{Zn} which would reduce hole-trapping and therefore enable the formation of a higher hole concentration at the surface. As an additional reason for the increased photo-current observed for hydrogenated ZnO nanowires, the authors mention an increased donor density ($2.74 \cdot 10^{21}$ cm^{-3}) [167]. However, such high donor concentrations are usually only observed for intentionally doped ZnO films used for electronic or PV applications (e.g. TCOs) [158] but might have disadvantageous effects on the photo-current in PEC applications [40]. Additionally it is important to note that annealing in a hydrogen containing atmosphere at higher temperatures (e.g. > 550 °C) can seriously damage ZnO films, which might be related to damage caused to the zinc sub-lattice [160, 168, 169].

Other annealing atmospheres can also be employed to change the defect-chemistry. Although one has to exercise caution since the effect of the annealing treatment – and the related photo-catalytic properties – may show significant differences depending on the ZnO starting material (e.g. morphology, defect density etc.) [170]. For the deliberate induction of additional defects, moderate to high temperatures are usually required, since the formation energy of the defect has to be overcome [127, 157]. If intrinsic defects are present after the growth, low-temperature annealing treatments can be used to induce mediation of defects, where the mediation of the individual defects can again be expected to be temperature dependent [127, 171]. From PL and X-ray photoelectron spectroscopy (XPS) measurements, Bora and co-workers concluded that the temperature mediated diffusion of oxygen vacancies led to a highly oxygen-deficient nanorod-surface upon annealing in air at 250 °C for 1 h [171]. These nanorod-arrays then exhibited the highest photo-catalytic degradation rates for phenol/methylene blue (as compared to lower and higher annealing temperatures) and also showed effective destruction of E.coli cells upon irradiation with simulated sunlight, which the authors attributed to improved charge carrier generation due to sub-bandgap absorption of visible light [171]. These results confirmed an earlier report by the same group that found that the photo-catalytic activity of ZnO nanorods annealed at 350 °C increased, as compared to annealing at 100 °C [172]. Also reports from the group of Uyar point towards a positive effect of oxygen vacancies in terms of the efficacy of photo-catalysis [173, 174]. In these papers the existence of V_Os was also investigated using PL measurements. Interestingly, the emission peaks attributed to the two mentioned recombination processes for V_Os are different to those described

in the aforementioned work by Bora et al.. Both papers assign the observed emissions to a), a recombination of a CB electron with a V_O^{++} state and b), a CB electron being captured at V_O^{+} site which then recombines with a hole in the VB. The emission peak centers given for a) are 585 nm, 565 nm and for b) 533 nm and 500 nm for Ref [171] and [173], respectively. While this does not exclude the possibility that these observations are indeed related to the same defect/recombination mechanism, it exemplifies a general problem in terms of the identification of intrinsic defects, since many defect emissions may overlap and literature reports find different origins for similar emissions [125].

Ranjith and Kumar studied a whole range of different ZnO morphologies grown by changing the pH value during a solution-based synthesis. They found a correlation between the resulting optical and photo-catalytic properties [175], which is presented in Figure 1-13a. In this regard it is noted that other authors have presented evidence regarding a possible interplay between the morphology, defect density and resulting photo-catalytic performance [176, 177]. In Ref [175] increasing the pH resulted in a worsening of the UV/visible PL-emission ratio (i.e. higher defect emission) but in an improvement of the photo-catalytic activity. The degradation of methylene blue, methyl orange and rhodamine B was most efficient when ZnO structures were grown at a pH of 9. It was concluded that this was the result of a synergetic effect of an increased overall surface area and a higher number of oxygen related defects [175]. The ‘nano-flowers’ which were the deposited at pH = 9, were then studied in more detail [178]. This visible-light active photo-catalyst was shown to exhibit a good reusability upon mild wet-chemical removal of adsorbed hydrocarbon groups (see Figure 1-13b). Furthermore the authors found that holes in the VB, electrons in the CB and defect states all participated in the photo-catalytic degradation of MB [178].

Other intrinsic defects are less frequently investigated for their involvement in photo-catalysis but some authors suggest that zinc and oxygen interstitials may improve the photo-catalytic performance [173, 175, 179].

However, it is important to note that some studies do not find a clear correlation between the defect-chemistry and the resulting photo-catalytic properties [180, 181]. Furthermore, the aforementioned studies by Djurisic and co-workers illustrate the important role that defects may play in the adsorption of pollutants (e.g. dyes) and/or

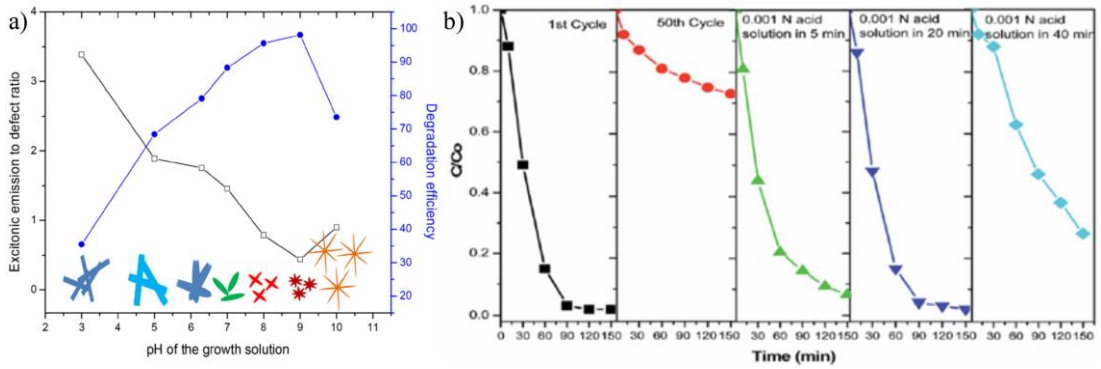

Figure 1-13: a) Correlation of the PL properties (near UV/defect emission ratio) and photo-catalytic degradation efficiency (methylene blue solution) for ZnO nanostructures of different morphology prepared from growth solutions with varying pH. Reprinted with permission from Ref. [175]. Copyright 2016, Elsevier. b) degradation of MB under UV irradiation in the presence of ZnO flowers (see also pH = 9 in a)). From left to right: 1st cycle, 50th cycle, acid treatment of 5 min on 50 times reused catalyst, acid treatment of 20 min on 50 times reused catalyst, acid treatment of 40 min on 50 time reused catalyst. 0.001 N HCl was used for the mild acid treatment. Reproduced from Ref. [178] with permission from The Royal Society of Chemistry.

functional groups. The reason behind this is that if a charged defect exists at the surface, the pollutant/functional group in solution may be attracted towards the surface. Additionally, these studies correctly point out that a low density of non-radiative defects is crucial to achieving a good-performing photo-catalyst [180, 181]. This arises because non-radiative recombination usually happens on a comparably short timescale. A high density of non-radiative defects thus usually leads to bad photo-catalytic and PEC performance. On the other hand, a high density of radiative-recombination centers does not necessarily need to result in a bad performance. Thus Djurisic and co-workers showed that it is possible to obtain good photo-catalytic activity coupled with higher dye-adsorption with samples showing a high concentration of emitting shallow donor defects, as long the non-radiative recombination is low [180].

Despite the discussion regarding possible conductivity and visible-light absorption enhancement, it was so far not discussed how intrinsic defects could possibly aid the reactions involved in PEC and photo-catalysis. In this regard the first mechanism that is postulated in the literature is the direct participation of defects in photo-(electro)chemical reactions, when the defects are present at the surface [156, 173, 175, 179]. It is believed that charge carriers (photo-generated holes and electrons alike) that are trapped at these defect-sites may be directly involved in the reaction mechanism

[173]. As an example of this, one may consider a photo-generated electron-hole pair. The hole in the valance band may be captured by a surface defect and – under the assumptions that its energetic position is proper and OH^- is adsorbed at the surface – may form an $OH^\cdot$ radical that can further participate in the PEC/photo-catalytic reaction. In this regard the PEC process and the process of photo-catalytic degradation in an aqueous solution are somewhat comparable since it is now understood that reaction intermediates (e.g. the $OH^\cdot$ radical) are crucial for both applications [182, 183]. The surface-defect can thus be considered to act as an active site [179, 183-185]. However, a consequent question is, what if the defects are not present at the surface? This question leads to a second proposed mechanism, which is particularly considered for bulk defects and where the defects are ascribed a charge carrier life time enhancing role [173, 179]. As an example here, an electron excited into the CB and subsequently trapped at a defect state shall be considered: In a PL experiment, the trapped electron can recombine with a photo-generated hole in the VB, giving rise to a visible emission. However in terms of PEC/photo-catalysis the hole may also diffuse towards the surface and – due to the electric field at the interface – be separated from the trapped electron. Obviously this mechanism can only occur if the outlined recombination mechanism is slow, which it for example could be compared to non-radiative recombination processes. This is another reason why ZnO films that exhibit high, defect-related PL emissions can still show good or even improved PEC/photo-catalytic performance [173, 175, 180].

1.4.3 **Doping of ZnO for enhanced visible light absorption**

Doping of ZnO is an important method for changing the materials properties in order to meet the requirements of a specific application. The variety of possible dopants is as broad as the range of applications [127, 131, 158, 186, 187]. If ZnO is to be used as an active absorber material in solar power applications, its large bandgap presents a major drawback, since only a very small portion of the impinging irradiation can be absorbed. As for other semiconductors, the introduction of dopants can help in terms of increasing the visible light absorption. The following section therefore introduces this strategy on the basis of some selected example dopants. For a more comprehensive discussion on extrinsic doping of ZnO, including the bandgap-engineering with MgZnO and CdZnO alloys, the reader is referred to some excellent reviews on the topic [113, 127, 132, 159, 187].

As mentioned earlier, the valance band of ZnO is formed by the O2p orbitals [116]. The VB edge is thus significantly below (electrochemically more positive) the O_2 evolution potential. One strategy designed to shift the VB further up (electrochemically more negative) is to replace significant amounts of the lattice oxygen with nitrogen (N2p orbitals are energetically more negative than O2p orbitals). This may lead – as for other metal oxides too – to the hybridization of the O2p and N2p orbitals [71]. Depending on the concentration of N in the lattice, either weakly visible light absorbing localized states or delocalized states (leading to an energetically more negative VB) are formed [71].

Assuming that nitrogen replaces oxygen in the lattice, the group V element nitrogen could act as an acceptor-type dopant leading to p-type doping [158]. However, p-type character upon N-doping was found to be hard to achieve and highly dependent on the deposition and post-deposition conditions [188]. Thus, it is rather common that researchers report similar or even higher donor densities upon N-doping in ZnO as compared to undoped ZnO, which may be related to the formation of additional defects such as N_2 occupying the O-site or hydrogen incorporation [150, 189-191]. For sputtered ZnO films, for example, incorporation of 2 %atom N during the growth was found to increase the donor density by one order of magnitude [189]. Following XPS measurements, this was attributed to N_2 occupying the O site, leading to the formation of a shallow double-donor state [189]. However, upon N-doping significant visible light absorption could be observed up to 600 nm. By using various filters, the authors were able to show that the overall improved photo-current could be mainly attributed to the light with $\lambda \geq 400$ nm [189].

Another common method of N-doping is to subject undoped samples to an annealing treatment in ammonia NH_3, which can decompose at moderate/high temperatures [71, 192]. Qui et al. used this nitridation method (530 °C, 30 min) to achieve a calculated substitutional doping-concentration of 3.5 %atom in their branched ZnO tetrapods [150]. The resulting PEC characteristics are shown in Figure 1-14. The N-doping significantly increased and shifted the incident-photon-to-current efficiency towards longer wavelengths (see Figure 1-14c). In turn, the photo-current density and applied bias photon-to-current efficiency of the N-doped tetrapods in Figure 1-14a and b, respectively, was found to be 8 times higher than for the pristine sample [150]. However, the stability of the photo-current of the tetrapods worsened upon nitridation

when the samples were biased at +0.55 V versus Ag/AgCl under illumination (Figure 1-14d). It was speculated that N-leaching may be responsible for the observed photo-current decay [150]. Similarly high N-doping concentrations in ZnO nanorod arrays were also observed by Yang et al. [191]. Also in the aforementioned study the nitridation (first 530 °C for 30 min in NH_3, then 30 min at 530 °C in N_2) resulted in a substantial improvement of the PEC performance. Furthermore, it was pointed out that increasing the doping-concentration to > 4 %atom. proved difficult, since longer annealing times led to sample damage, likely related to the presence of hydrogen [191]. It was also found that higher temperatures during annealing in hydrogen containing atmospheres may lead to this effect [160, 168]. Somewhat conflicting in this regard are the results of a more recent study by Patel et al., where nitridation temperatures of up to 700 °C were investigated for cobalt-doped ZnO nanorod arrays [190].

These authors reported seeing structural changes only for temperatures > 600 °C, with samples annealed at 600 °C for 1 h showing no damage [190]. It can only be speculated that the cobalt-doping during the hydrothermal synthesis (prior to the nitridation) may have improved the thermal stability during the annealing treatment in a hydrogen containing atmosphere. For N-doping at 600 °C, the charge carrier density was found to increase by 4 orders of magnitude (10^{22} cm^{-3}) [190]. From the XPS data presented it is difficult to judge if N_2 occupying the O-site (i.e. shallow double-donor) may contribute to this effect, similar to the observations of Ahn et al. [189]. Despite the influence of the intentional dopants Co and N, at this high temperature it must however be expected that hydrogen was unintentionally incorporated into the structure, contributing to the observed increase of the charge carrier density [127]. Whatever the reason for the high charge carrier density, the resulting N and Co co-doped ZnO nanorods showed a remarkably high visible light absorption and an estimated bandgap of 2.16 eV, which is in line with earlier studies on the variation of E_G with increasing N-concentration [193]. Paired with a very low overall charge transfer resistance, the resulting applied bias photon-to-current efficiency was reported as 1.39 % at 0.79 V vs. RHE in 0.5 M Na_2SO_4 [190]. Apart from N-doping it was also shown that the incorporation of cobalt had significant influence on the optical and photo-electrochemical properties of the ZnO nanowires in the aforementioned study. This represents another important route to alter the optical, magnetic, electronic and photo-

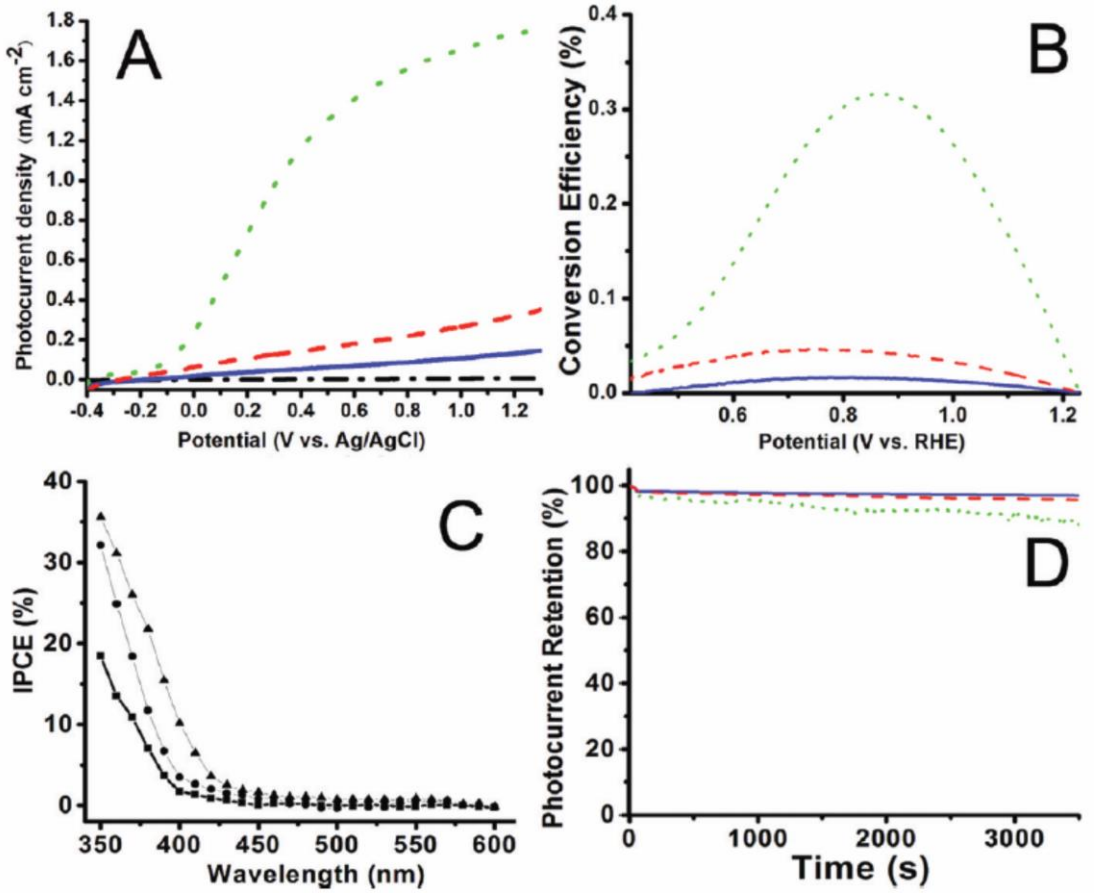

Figure 1-14: (A) *J*−*V* curves recorded for pristine ZnO nano-tetrapods (NTs) in the dark (black line), pristine ZnO NTs (blue solid line), branched ZnO NTs (red dashed line), and N-doped branched ZnO NTs (green dotted line) with a scan rate of 10 mV/s and with the AM1.5G simulated solar light at 100 mW/cm^2. (B) Applied bias photon-to-current efficiency of pristine ZnO NTs (blue solid line), branched ZnO NTs (red dashed line), and N-doped branched ZnO NTs (green dotted line). (C) IPCEs for pristine ZnO NTs (squares), branched ZnO NTs (cycles) and N-doped branched ZnO NTs (triangles), measured in the wavelength range from 350 to 600 nm at an applied potential of +0.50 V vs Ag/AgCl. (D) Photo-current retention performance over 3500 s of pristine ZnO NTs (blue solid line), branched ZnO NTs (red dashed line), and N-doped branched ZnO NTs (green dotted line) at an applied potential of +0.55 V vs. Ag/AgCl under illumination. PEC characterizations were performed in a 0.5 M Na_2SO_4 electrolyte solution buffered to pH ~ 7.0 with phosphate buffer solution. Reprinted with permission from [150]. Copyright 2012 American Chemical Society.

(electro)chemical properties of ZnO: the doping with transition-metals such as the cobalt used in the study mentioned above, manganese [194-199], nickel [197, 200, 201] or iron [202, 203]. The interest in these dopants is not only restricted to photo-(electro)chemical applications, but also arises from a possible magnetic application as diluted magnetic semiconductors (DMS). Here metal-oxides have attracted much attention as potential host materials for DMS. As metal-oxides are initially non-

magnetic, a ferromagnetic phase can be formed by "diluting" the metal-oxide via doping of magnetic impurities [204]. For this purpose the aforementioned dopants are commonly used (e.g. Fe, Ni, Co, Mn) [205, 206]. The idea behind the DMS materials is to dope the parent semiconductor with a sufficiently high concentration of these dopants in order to achieve the best of both worlds, the opto-electronic properties of the metal oxide and the ferromagnetism (possibly at room temperature) of the dopant. This would then make these materials very attractive for use in applications such as spintronics, magneto-optics and photovoltaics [204, 207]. One of the most researched DMS materials is ZnO, especially when doped with cobalt [196, 198, 199, 204, 208, 209]. However, the interpretation of the literature data dealing with ferromagnetism at room temperature for ZnO:Co is rather difficult, since many explanations for the absence or occurrence of ferromagnetism are given. A review by Ogale [204] points out some general issues related with DMS in terms of reproducibility and interpretation of results, highlighting the difficulties associated with the reliability of certain reports. A similar conclusion has been drawn by Djerdj et al. who reviewed the progress in ZnO:Co as a potential DMS system [208]. In any case, ferromagnetic behavior seems to be highly influenced by the deposition method and induced defects might play a crucial role. In general, the material properties of substitutional cobalt-doped ZnO have been studied quite extensively for its material properties. More recently it has thus also attracted the attention of photo-(electro)chemical research community.

Cobalt doped Zinc Oxide (ZnO:Co)

While the magnetic properties of this material could potentially be interesting for the control of dopant-related recombination, for photo-(electro)chemical processes the optical properties (visible light absorption) are of particular importance and are thus elaborated in more detail in the following section.

In terms of the influence that Co doping may have on the optical properties of ZnO:Co structures the literature is somewhat contradictory. For example some groups have reported seeing a blue shift of the bandgap with increasing Co-concentration [210,

211]. The Burstein-Moss[1] effect is often used to account for the broadening of the bandgap with increasing doping concentration [210, 212]. If substitutional doping is expected (Co^{2+} replaces Zn^{2+}), this would likely be related to the induction of additional intrinsic donor-type defect states. Bu et al. invoked the Burstein-Moss effect in order to explain the observed bandgap broadening for higher Co concentrations (5 atom %) [213]. For lower concentrations (1 - 3 atom %) they observed a decrease of the bandgap. The complete opposite is reported in Ref [214] where the bandgap was first found to increase with increasing Co concentration but then decreased again for higher cobalt incorporation.

In contrast, a red shift with increasing Co concentration has been observed by other groups [196, 198, 215]. This finding is supported by PL measurements [209, 216] which show a shift of radiative recombination near the band edge towards higher wavelengths, thus narrowing the bandgap. Strong semiconductor-metal (sp-d) interactions [198, 217] have been cited as a reason for the observed red shift.

However, a combination of both the Burstein-Moss effect and sp-d interactions, might also be possible. Kim and Park reported on the observation of a sudden change from a blue- to a red shift of the bandgap with increasing carrier concentration in indium doped ZnO [218]. They attributed the blue shift below a carrier concentration of $n = 5 \cdot 10^{19}$ cm^{-3} to the Burstein-Moss effect and explained the red shift above this carrier concentration to semiconductor-metal interactions.

Optical measurements can provide evidence of additional transitions in the visible region of the spectrum, but this is another area where the reports in the literature are somewhat conflicting. Where many researchers have not detected any additional features in UV-Vis or PL measurements from ZnO:Co [211, 213, 214, 216, 219] additional features have been observed by other groups [196, 198, 209, 215, 217, 220, 221]. A typical absorption spectrum of these observations is shown in Figure 1-15a. As can be seen from this spectrum, introduction of cobalt into the ZnO lattice can create additional absorption features between 500 nm and 700 nm. Generally these features (and in particular their distinct shape) are identified as originating from cobalt-

[1] The apparent bandgap of the semiconductor is increased as a result of a high density of charge carriers filling the bottom of the conduction band (i.e. the Fermi Energy lies in the conduction band). Therefore, optical transitions occur between the next higher unoccupied conduction state and not the conduction band minimum [212].

related d-d metal transitions [222]. The substitution of Zn^{2+} by Co^{2+} in the tetrahedral crystal field symmetry (wurtzite structure) of ZnO leads to the formation of triplet and doublet states within the bandgap, exhibiting sharp transitions at around 550 nm, 610 nm and 650 nm [222-224].

In addition to these prominent features, the incorporation of cobalt can lead to charge transfer (CT) between the metal (M) and the ligand (L) conduction band ($ML_{CB}CT$) and between the ligand valance band and the metal ($L_{VB}MCT$) upon photo-excitation, represented by h·ν in equations (1.24) and (1.25) [225, 226]:

$$ML_{CB}CT: Co^{2+} + h \cdot \nu \rightarrow Co^{3+} + e_{CB}^{-} \quad (1.24)$$

and

$$L_{VB}MCT: Co^{2+} + h \cdot \nu \rightarrow Co^{+} + h_{VB}^{+} \quad (1.25)$$

Importantly, the interplay between the cobalt-related d-d transitions and the aforementioned CTs plays a crucial role in relation to sub-band gap photoconductivity, which has been observed for ZnO:Co and is of high interest for solar energy related research [225, 227, 228].

Lu et al. [215] used ZnO:Co as a photocatalyst. Their cobalt doped samples were able to decompose 93 % of an alizarin red (dye) solution under illumination with λ > 420 nm within an hour, whereas undoped samples showed almost no decomposition of the dye. The charge transfer processes that were identified to be responsible for the visible light photo-activity are shown in Figure 1-15b. Most of the visible-light activity was attributed to the electronic interaction between the Co species and ZnO ($L_{VB}MCT$) and only a small contribution was found to stem from the d-d transitions [215]. These results were further confirmed by surface photo-voltage measurements, showing a — significantly increased surface photo-voltage in the range 400 – 520 nm as compared to the undoped reference sample [215]. Furthermore this study points out that the cobalt concentration in the films needs to be optimized, since increasing the Co-content from 1 % to 1.5 %atom. decreased the photo-catalytic activity [215]. A cobalt concentration of < 1 %atom. also increased the photo-catalytic activity for nanorod-arrays in the study of Li et al. [229]. Upon cobalt-doping the PL intensity was dramatically decreased when compared to pristine ZnO. It can thus be expected that non-radiative recombination is dominant for such films. However, the authors claim that apart from a higher visible-light absorption, the incorporated Co^{2+} acts as a charge

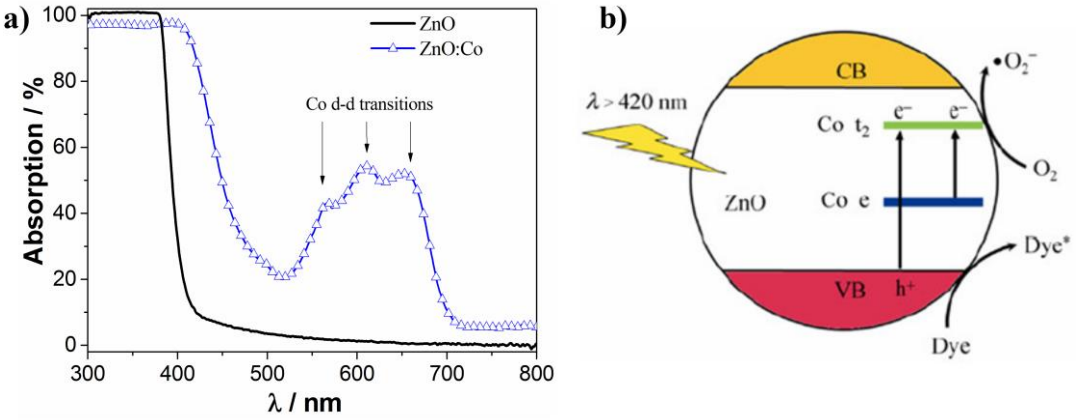

Figure 1-15: a) Absorption spectra of a cobalt-doped ZnO nanorod array comapred to a pristine ZnO nanorod-array. b) Schematic representation of ZnO:Co used as a photocatalyst for the decomposition of a dye (alizarin red) [215]. Reproduced with permission from ref. [215].

carrier trap, restraining the recombination of photo-generated electron-hole pairs [229].

Similar conclusions were also drawn by Sutka et al. [230]. Two different morphologies were investigated and cobalt-doped nanorods were found to catalyze methyl orange decomposition more efficiently than cobalt-doped nanoparticles. Also the results presented in their study show a clear dependence of the photo-catalytic activity and the cobalt concentration in the films [230]. The highest activity was found for the sample labelled $Zn_{0.95}Co_{0.05}O$ (5 %atom Co) but the Co levels noted here do not refer to the actual atom % of Co but rather to the Co concentration in the growth-solution during the hydrothermal growth. Compared to other studies, the authors observed a non-negligible Co^{3+} presence at the surface, which then raises the possibility that the catalytic function of the materials may be altered by same [230].

The PEC performance of K, Na, Ni and Co-doped ZnO was investigated by Lee et al. [201]. Using inductively coupled plasma mass spectroscopy, a Co-concentration of ca. 3%atom. was registered. This corresponded to a doping efficiency of ca. 11.8 % during the chemical bath deposition. The incorporation of Co led to a decrease of the bandgap energy but surprisingly no cobalt related d-d transitions were observed. Among all the investigated dopants, Na showed the best of the PEC performance in 1 M KOH [201]. However, it was also found that the photo-current onset potential and overall photo-current density of the cobalt-doped sample was significantly improved when compared to the undoped sample [201]. Furthermore it is important to note that no clear correlation between the dopant-induced charge carrier density and

PEC performance could be established. All dopants led to an increase of the charge carrier density compared to the undoped reference sample ($7.61 \cdot 10^{18}$ cm^{-3}). However, nickel doping, for example, resulted in the highest charge carrier concentration ($1.34 \cdot 10^{20}$ cm^{-3}) yet also showed the lowest photo-current density of all doped samples. This questions the often stated explanation that a high charge carrier density leads to an improved PEC performance. The suggestion that this reasoning is not necessarily true can be formulated by considering the negative impact of high charge carrier densities on the photo-current/Debye length and the rising importance of the fast Auger recombination [40, 231-233].

1.4.4 **Functional over-coating of ZnO**

A tremendous challenge for the use of ZnO in photo-(electro)chemical applications is to overcome its poor (photo)stability in aqueous solutions [18]. This lack of stability stems from the fact that the oxidation potential of ZnO lies above the oxidation potential of water [35]. The chemical dissolution of the material in the dark is fast in acidic solution, improves from neutral to moderately alkaline but may also occur in highly alkaline electrolytes, according to equations (1.26) and (1.27) [140, 156]:

$$ZnO + 2H^+ \rightarrow Zn^{2+} + H_2O \tag{1.26}$$

and

$$ZnO + H_2O + 2OH^- \rightarrow [Zn(OH)_4]^{2-} \tag{1.27}$$

Additionally, the excitation of the material by an electrical bias and/or irradiation with sunlight induces additional decomposition processes [140], which can be summarized in equation (1.28) [156, 234, 235]:

$$ZnO + nH_2O + 2h^+ \rightarrow [Zn(OH)_n]^{(2-n)+} + \frac{1}{2}O_2 + nH^+ \tag{1.28}$$

The pH dependent equation (1.28) thereby describes the photo-corrosion process under the formation of Zn^{2+} – which is believed to include the rapid formation of oxygen molecules under the influence of surface-trapped holes resulting in the expulsion of Zn^{2+} [156] – and the formation of a surface hydroxide layer [156]. It is thus of greatest importance to inhibit these negative reactions. Approaches designed to tackle this challenge involve the modification of ZnO itself (e.g. by changing the defect-chemistry)[156] or to apply a suitable, chemically stable over-coating to ZnO and thus avoid a direct interface of ZnO and the electrolyte. The latter strategy will be discussed

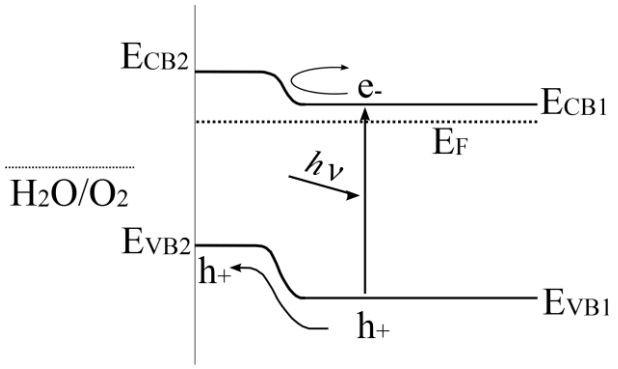

Figure 1-16 Energy-band diagram of a suitable protective over-coating to inhibit the destruction of ZnO. Note that the schematic depicts the material combination in the light with no contact to the electrolyte. The band-bending/contact of the individual materials is simplified and absorption in the over-coating (material 2) is neglected.

in further detail in the following section.

A first starting point when thinking of a suitable over-coating material is to evaluate its energy-band positions with respect to those of ZnO. A few general aspects can be described by the schematic representation in Figure 1-16. The depicted material combination consists of the core material with its energy bands E_{CB1} and E_{VB1} in contact with a thin shell material symbolized by its energy bands E_{CB2} and E_{VB2}. In Figure 1-16 E_{CB2} and E_{VB2} lie above E_{CB1} and E_{VB1}, respectively. This ensures that a suitable degree of band-bending occurs at the interface of the two materials, allowing photo-generated holes to reach the surface while photo-generated electrons may be 'reflected' back into the bulk/towards the back-contact. In order for water oxidation to occur, it is furthermore required that E_{VB2} lies below the oxidation potential of water. If the over-coating is not photo-active itself (e.g. the charge carrier lifetime is very low), the bandgap of the coating should be relatively wide and the layer-thickness thin. This would then minimize the losses due to parasitic absorption in the over-coating. A possible material combination that could resemble the band-diagram shown in Figure 1-16 is ZnO coated with TiO_2 [52, 236, 237]. However, some authors find the respective energy-band positions of this combination of materials to be the opposite of that specified in Figure 1-16 [183, 238, 239]. This uncertainty may arise from difficulties in determining the exact TiO_2 phase present (e.g. amorphous, anatase, rutile or mixed phases) and the associated related energy-band positions [240, 241]. Early work by Law et al. examined the ZnO-TiO_2 core-shell material-combination for use in dye-sensitized solar-cells (DSSC) [236]. The solar-cells improved significantly upon

a thin over-coating with TiO_2 and it was concluded that this was due to the suppression of ZnO surface recombination. This effect was further confirmed theoretically by Pazoki et al. [242]. Although the charge transfer in a DSSC (e.g. oxidation of the dye) relies on electron injection from the dye into the CB rather than oxidation by a photo-generated hole from the semiconductor (e.g. PEC), this study of the TiO_2-thickness dependency revealed that an efficiency gain could be achieved upon changing from amorphous TiO_2 to anatase for layers thicker than 7 nm [236].

Different thicknesses of TiO_2 (2 – 6 nm) were also investigated as shell-coatings for ZnO nanoparticles to be used as photo-catalysts in the study of Rakkesh and Balakumar [237]. The thickest coating (ca. 6 nm), identified as anatase, improved the degradation of acridine orange substantially. Enhanced charge carrier separation due to a suitable band alignment (as in Figure 1-16) and an increase of the active surface area were found to be responsible for the improvement [237]. An optimal TiO_2 (anatase) thickness of 3.5 nm – 5 nm was identified as being able to reduce the dark current and in turn increase the charge carrier lifetime (as estimated by analysis of the photo-current decay) for a ZnO nanowire based photo-anode [243]. The photo-current density of the core-shell structure (5 nm TiO_2) was stable in 0.1 M Na_2SO_4 for 3 h (ca. 0.55 mA/cm^2 at 0.25 V vs. SCE; this should be compared to uncoated ZnO: ca. 0.75 mA/cm^2 at 0.25 V vs. SCE) [243]. Even thinner TiO_2-shells (nominally ca. 1 nm) were investigated as over-coatings for ZnO nanowires by Liu et al. [52]. Upon depositing TiO_2 using 100 atomic layer deposition cycles (note that this is a relatively slow growth rate) the defect-related PL emission was dramatically reduced and the band-band emission increased. Since this may be taken as an indication of the passivation of surface defects, the authors suggested that the overall rate of recombination was reduced, leading to a 25 % larger photo-current as compared to uncoated ZnO [52]. Furthermore, the electrode performance was stable and no visible sample damage occurred to the structures when tested for ≥ 3h in 0.1 M KOH [52].

Hernández studied the ZnO-TiO_2 core-shell structure for PEC extensively [244-246]. Rather than employing ALD for the deposition of TiO_2, an acid-free sol-gel method was used to deposit the anatase shells [245]. Using this method, the thicknesses of the shells can be adjusted by varying the deposition time, resulting in a coverage of ca. 15 - 50 nm TiO_2 after 5 min [245]. The reflection spectra of two core-shell structures with varying thicknesses of TiO_2 are shown in Figure 1-17a. A longer deposition time of

10 min, and therefore a thicker TiO_2 layer, increases the reflection substantially with negative effects on the absorption within the ZnO cores. The ZnO-TiO_2 core-shell structures turned out to be most efficient for the OER as compared to other structures like plain TiO_2 nanoparticle-films and TiO_2 tubes as well as plain ZnO nanorods [244-246]. This is exemplified by the comparison of the chronoamperometric measurements shown in Figure 1-17b. Generally the studies by Hernández et al. reveal that upon TiO_2-overcoating, both the flat band potential and the photo-current onset potential are shifted cathodically. A better charge carrier separation paired with a lower recombination rate and an improved electron transport due to the ZnO 1D geometry can be expected from such structures [245, 246]. The core-shell structures were furthermore optimized by annealing treatments (450 °C in air or nitrogen for 30 min)

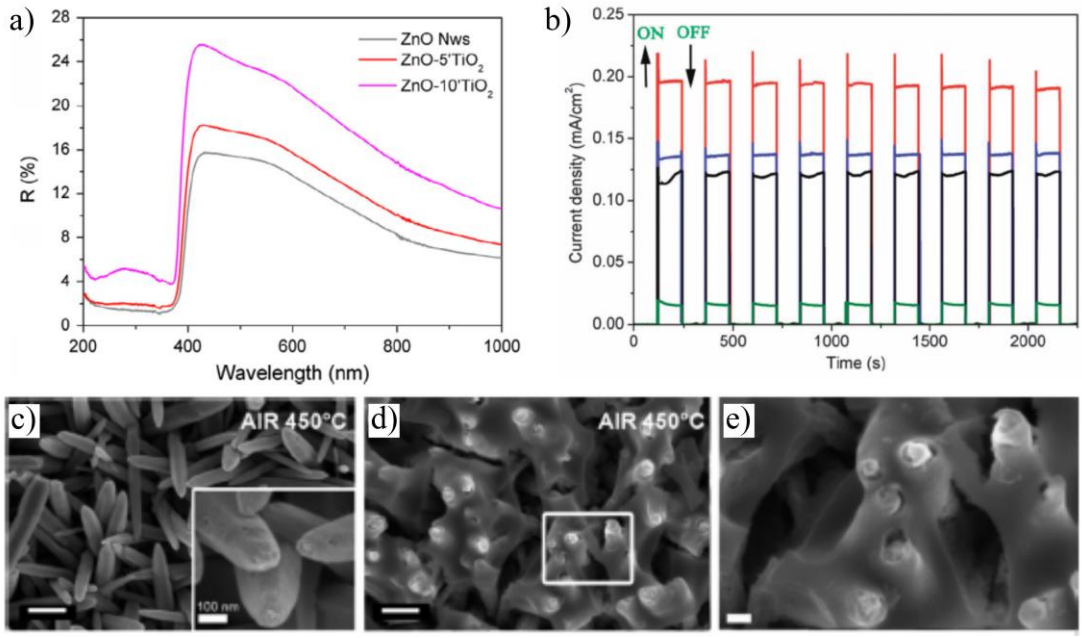

Figure 1-17: a) Reflection spectra of pristine and TiO_2 coated ZnO nanowire-arrays. Two different TiO_2 thicknesses (resulting from a sol-gel deposition time of 5 min (red curve) and 10 min (pink curve)) are shown. Reprinted with permission from Ref. [245]. Copyright 2014, Elsevier.
b) Chronoamperometric (I–t) curves at an applied potential of -0.1 V vs. Ag/AgCl under illumination (AM 1.5 G, 100 mW/cm^{-2}) with 120 s light ON–OFF cycles of the samples: TiO_2 nanoparticle film (green line), TiO_2 nanotubes (black line), ZnO nanowires (blue line) and ZnO-TiO_2 core–shell structures (red line). [246] - Published by the PCCP Owner Societies. c) – e) SEM top-view images of the c) bare ZnO nanowires and d) + e) ZnO-TiO_2 core−shell nanostructures after the PEC measurements. e) shows a higher magnification of the white square shown in d). Samples were annealed in air at 450 °C prior to the PEC characterization. The scale bars for c) and d) are 500 nm and 100 nm for e). Reprinted with permission from [244]. Copyright 2014 American Chemical Society.

[244]. Both annealing the entire structure as well as annealing the ZnO core prior to the TiO_2 deposition improved the photo-electrochemical performance. It was noted that pre-annealing of the ZnO core could prove particularly useful, since it improved the interconnection of the two materials and hence decreased the overall charge-transfer resistance and also enhanced the stability (90 min chopped-light experiments) of the structure further [244]. When the ZnO-TiO_2 core-shell structures were examined by SEM after the PEC characterization (Figure 1-17d and e), no structural changes could be observed. Uncoated ZnO nanowires, on the other hand, showed structural damage in the form of e.g. pits (Figure 1-17c) [244]. An applied bias photon-to-current efficiency of 0.36% at 0.7 V vs. RHE (0.5 M Na_2SO_4, 1-sun illumination) was achieved for a ZnO-TiO_2 core-shell structure where an additional iron oxy-hydroxide, FeOOH co-catalyst was applied (0.01% at 0.96 V. and 0.07% at 0.95 V for pristine ZnO nanorods and the ZnO/TiO_2 core-shell structure, respectively)[247]. Importantly, the FeOOH facilitates the transport of photo-generated holes towards the electrolyte interface and hence also suppresses recombination due to efficient charge carrier separation [247]. Moreover, it was found that the fast hole transport to the FeOOH significantly reduces the probability for ZnO photo-corrosion to occur. This was experimentally confirmed by chronoamperometric measurements, where the photo-anode retained its photo-current (at 1.1 V vs. RHE under illumination) as compared to the ZnO and ZnO-TiO_2 samples (42 % and 72 % retention after 2 h, respectively) [247].

The aforementioned study represents another approach to the inhibition of how photo-corrosion using over-coatings: the application of a thin co-catalyst layer for water oxidation. More generally, this strategy is governed by the same principles that underpin metal-insulator-semiconductor structures, which are being heavily researched in the field of PECs at the present time [41, 44, 54, 55, 63-67, 69]. The emphasis here lies on the use of very thin layers, as coatings made from catalytic metals (e.g. iridium, ruthenium) and also catalytic metal-(oxy-)hydroxides (e.g. Co_3O_4, $Ni(OH)_2$, FeOOH) may result in a lower light absorption in the ZnO due to parasitic absorption in the catalytic coating.

However, it is also the case that if a catalytic coating is to be used alone (e.g. without an additional chemical-barrier layer such as TiO_2), then the catalytic layer must also be pin-hole free, in order to avoid any direct ZnO-electrolyte interface. As a possible

materials combination, Co_3O_4 was investigated as a catalytic over-layer by Li et al. [248]. In order to facilitated the charge carrier separation, the structures were interlaced with carbon nanotubes (CNT) acting as an electron transport medium (see SEM images in Figure 1-18a and b). The photo-electrochemical characterization of the resulting photo-anodes – including different Co_3O_4 deposition times – is shown in Figure 1-18c - f. From this figure it may be seen that the Co_3O_4 over-coating exhibits a catalytic function as evidenced by a cathodic shift of the photo-current onset-potential and an overall increase of the photo-current density (improved charge carrier separation). As a result the prepared photo-anodes showed an incident-photon-to-current-conversion efficiency of > 50 % for $hv > E_{GZnO}$ – a 5 fold improvement as compared to pristine ZnO nanorod-arrays. However, this study also exemplified the importance of the catalyst loading, as thicker Co_3O_4 layers were found to be less efficient (see Figure 1-18e and d), partly due to reduced light absorption in the ZnO [248]. For an optimal layer thickness the photo-current of the CNT-ZnO-Co_3O_4 structures was reasonably stable for 30 LSV scans in 0.5 M Na_2SO_4 [248].

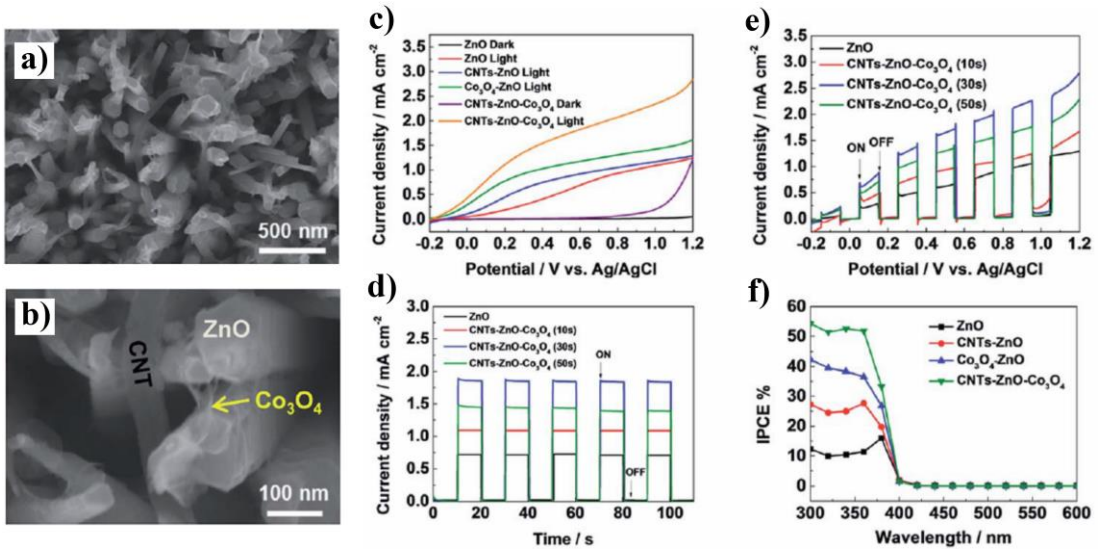

Figure 1-18: a) and b) SEM images of Co_3O_4 coated ZnO nanowires (NWs) interlaced with carbon nanotubes (CNT). c) current–voltage curves of pristine ZnO NWs, binary CNT–ZnO (0.25 mg ml^{-1}) NWs, Co_3O_4–ZnO (30 s) NWs and ternary CNT–ZnO–Co_3O_4 (30 s) NWs. (d) amperometric *I–t* curves of pristine ZnO NWs and ternary CNT–ZnO–Co_3O_4 NWs (with varying Co_3O_4 electrodeposition times) measured at 0.6 V vs. Ag/AgCl. (e) current–voltage curves of pristine ZnO NWs and ternary CNT–ZnO–Co_3O_4 NWs (with varying Co_3O_4 electrodeposition times) under chopped light illumination. (f) IPCE spectra of pristine ZnO NWs, binary CNT–ZnO NWs, Co_3O_4–ZnO NWs and ternary CNT–ZnO–Co_3O_4 NWs at 0.6 V vs. Ag/AgCl. An aqueous 0.5 M Na_2SO_4 (pH 6.8) electrolyte was used for the photo-electrochemical characterization.

Good electro-catalytic stability was also confirmed for a thin (ca. 2.4 nm) CoO over-coating that readily oxidized to form Co_3O_4 under galvanostatic conditions (1 mA/cm^2) [249]. It has also been found that so-called layered double hydroxides (LDH) can be used to improve the PEC performance and stability of ZnO, as shown by Shao et al. using electrodeposited Cobalt-Nickel-LDH shells [250]. Similarly to the findings by Li et al. [248], the IPCE was strongly increased for the core-shell structure, indicating suppressed recombination as a result of improved charge carrier separation. The catalytic function towards the OER was ascribed to the redox reaction of cobalt in the LDH [250]. However, a synergetic effect of both, the nickel and cobalt redox reactions is possible [251].

This is also due to the fact that also Ni-based materials exhibit the ability to catalyze the OER. For example, $Ni(OH)_2$ – as it is present in the mentioned CoNi-LDH – represents a versatile co-catalyst for the combination with ZnO [84]. A schematic representation of a possible ZnO-$Ni(OH)_2$ core-shell structure for the OER is shown in Figure 1-19a. The electrodeposited high-surface area $Ni(OH)_2$ structures effectively reduce the over-potential needed to oxidize water. This is exemplified by the photo-current density J_{ph} vs. voltage curves in Figure 1-19b. Interestingly, the photo-current onset potential is shifted cathodically with increasing $Ni(OH)_2$ shell thickness (20 nm, 40 nm, 100 nm and 220 nm). However, when higher anodic potentials were applied,

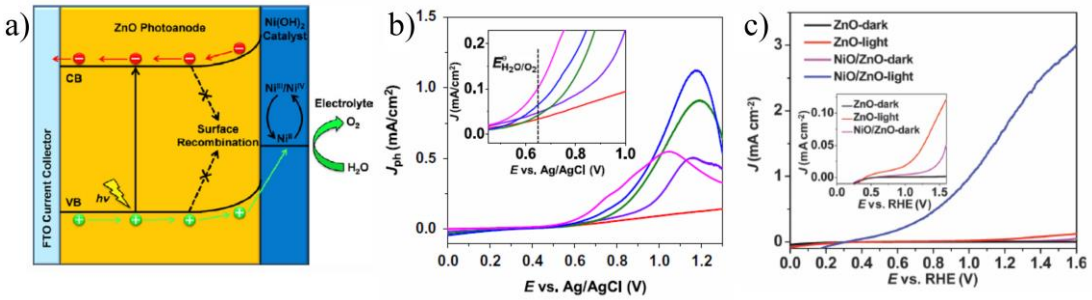

Figure 1-19: a) Schematic representation of $Ni(OH)_2$ coated ZnO photo-anode for the oxidation of water. b) Photo-current density J_{ph} of ZnO nanorod-arrays (red) and ZnO nanorod-arrays covered with $Ni(OH)_2$ over-coating; deposition time of 1 min (purple), 3 min (green), 5 min (blue) and 7 min (pink).The inset of (b) shows the magnified J_{ph} curves around the thermodynamic OER potential = 0.64 V vs. Ag/AgCl at pH = 6.62 (0.5 M Na_2SO_4). a) and b) are reprinted with permission from Ref. [84]. Copyright 2014, Elsevier. c) *J-V* curves of pristine and NiO coated ZnO nanorods measured in 0.5 M Na_2SO_4 (pH = 6.62). Reprinted with permission from Ref. [83]. Copyright 2016, Elsevier. Note that the ZnO nanorods of b) and c) were deposited using the same growth method/conditions.

the 220 nm thick $Ni(OH)_2$ exhibited fast photo-current saturation. The authors argued that thicker layers increase the catalytic activity of the shell (earlier onset and higher dark current) but may also impair the light absorption of the core-shell structure (reduced max. photo-current density) [84]. Building on these results, a further study investigated amorphous NiO shell structures as over-coatings for ZnO nanorwires [83]. Annealing at moderate temperatures (e.g. 300 °C [83]) was used to convert the nickel hydroxide to nickel oxide since, as a known electrocatalyst, it was believed that NiO may further improve the OER kinetics [86, 88]. This was confirmed for the ZnO-NiO core-shell structures, where a dramatic improvement of the photo-current (see Figure 1-19c) led to a 30 fold increase of the applied bias photon-to-current efficiency, when compared to the pristine ZnO nanorods. [83]. Despite a 260 mV cathodic shift of the photo-current onset-potential due to the improved OER kinetics, the amorphous nature of the NiO shell may help to suppress surface recombination and to increase the number of active sites for water oxidation [83]. However, it is also important to note that the parasitic light absorption within a thin NiO layer was already significant [83].

1.4.5 Summary of strategies designed to tailor ZnO for photo-(electro)chemical applications

The preceding sections introduced a few general concepts to tailor ZnO towards photo-(electro)chemical applications. Based on the presented, non-exhaustive literature reports it becomes clear that control over the structural properties and defect chemistry as well as the manipulation of the material using doping and/or over-coating strategies is of high importance to the scientific community. Synthetic approaches for the deposition of various nano-morphologies offer the possibility to precisely control important material parameters such as the surface area and the ratio of crystal planes exposed to the electrolyte. For the latter parameter, literature reports indicate that the (002) plane is reactively most active while an increased surface area can offer more active sites to run the reaction in question. Additionally, very rough 3D geometries (e.g. nano-forests) may prove advantageous for the suppression of reflection and thus increase the portion of irradiation absorbed. However, different structural properties might also lead to a changed defect chemistry for the resulting materials. The surveyed literature dealing with defect-engineering in ZnO shows that this route may prove useful to enhance the performance of ZnO in photocatalysis and PECs. This is particularly valid, if slow recombination over intrinsic defects can be used to suppress

non-radiative recombination, which acts as a fast pathway in this respect. When present as surface states, some intrinsic defects, such as for example oxygen vacancies, are furthermore found to act as active sites participating in the respective reaction. Additionally, the deliberate introduction of intrinsic defects in larger concentrations is also reported to lead to visible light- absorption and activity for the otherwise only UV-active ZnO. However, this can also be achieved when introducing extrinisc impurities into the lattice. Such doping strategies also attracted much attention and nitrogen and cobalt were discussed as prominent examples. For both elements the visible light absorption can be increased and strong improvements of the photo-catalytic and photo-electrochemical performance is evidenced from the presented literature. Further gains in this respect are shown to arise from the application of thin catalytic over-coatings. These may not only serve a catalytic purpose alone but potentially act as protective coating against ZnO`s (photo)instability. This is similar to TiO_2-ZnO core-shell structures, which some of the reviewed studies find effective to suppress same.

Despite the fact that great progress has been made to adapt ZnO for photo-(electro)chemical applications, the areas of research mentioned in the earlier sections are relatively young and demand further studies. For the material`s use in PECs its properties need to be adjusted further to effectively absorb visible light and, at the same time, hinder recombination and facilitate the charge carrier transfer. These fundamental processes are currently not as efficient as the application in PECs demands them to be. A combination of all of the preceding approaches to improve the materials properties may thus be needed to satisfy this need. Form a material synthesis point of view, a combination of atomic layer deposition (ALD) for the growth of ultra-thin functional layers paired with the rapid solution-based deposition (e.g. hydrothermal growth) of nanostructures appears as a promising combination to produce tailor-made ZnO-based photo-electrodes. Both growth techniques are characterized by their relatively low deposition temperatures, making this combination also highly desirable from an economic point of view. However, controlling the defect-chemistry and/or introducing functional dopants during the low-temperature solution-based deposition remains challenging to date. These aspects are nonetheless key to the materials potential use in PECs, particularly in light of the required high visible light absorption and low rate of recombination. Therefore, this thesis explores possible pathways to influence and control the defect- and doping-chemistry of ZnO and

evaluates the application of TiO_2 ALD over-coatings to inhibit photo-corrosion.

1.5 Thesis outline

Having introduced the research needs and current state-of-art with respect to the strategies designed to facilitate the use of ZnO in PECs in Chapter 1, Chapter 2 then presents a description of the experimental methods used. The then following chapters are broadly categorized into the use of defect-engineered ZnO for photo-(electro)chemical applications, the low-temperature synthesis of cobalt-doped ZnO and the investigation of TiO_2-ZnO core-shell structures as corrosion resistant photo-electrodes. Thus, Chapter 3 introduces a low-temperature method for the growth of intentionally defect-rich ZnO materials, which can be engineered (using rapid thermal annealing) to exhibit strong orange luminescence paired with improved photo-electrochemical performance. Building up on these results, Chapter 4 then further investigates the defect- and surface-chemistry of such defect-engineered ZnO nanorods on the basis of photo-catalytic dye-degradation experiments. Chapter 5 presents a simple, low-temperature solution based growth method enabling the deposition of cobalt-doped ZnO (ZnO:Co) with controllable visible light absorption. The potential of this method is then explored in more detail for the one-pot synthesis of visible-light active ZnO:Co over-coated with catalytic $Co(OH)_2$ and/or Co_3O_4 in Chapter 6. Among with further experimental results regarding the defect-engineered or cobalt-doped ZnO, Chapter 7 investigates the possibility to apply ultra-thin TiO_2 shells deposited by ALD to the ZnO nanorod cores. Finally, in Chapter 8 some conclusions in respect to this thesis are drawn and ideas for further work are presented.

1.6 References

[1] I. M. Howat, C. Porter, M. J. Noh, B. E. Smith, and S. Jeong, "Brief Communication: Sudden drainage of a subglacial lake beneath the Greenland Ice Sheet," *The Cryosphere*, vol. 9, no. 1, pp. 103-108, 2015.

[2] M. J. Willis, B. G. Herried, M. G. Bevis, and R. E. Bell, "Recharge of a subglacial lake by surface meltwater in northeast Greenland," *Nature*, 2015.

[3] M. Mengel, A. Nauels, J. Rogelj, and C. F. Schleussner, "Committed sea-level rise under the Paris Agreement and the legacy of delayed mitigation action," *Nat Commun*, vol. 9, no. 1, p. 601, 2018.

[4] C. Breyer and A. Gerlach, "Global overview on grid-parity," *Progress in Photovoltaics: Research and Applications*, vol. 21, no. 1, pp. 121-136, 2013.

[5] P. A. Narbel, "What is really behind the adoption of new renewable electricity generating technologies?," *Energy for Sustainable Development,* vol. 17, no. 4, pp. 386-390, 2013.
[6] H. Wirth, "Aktuelle Fakten zur Photovoltaik in Deutschland " Fraunhofer ISE, 2018.
[7] P. D. Lund, "Boosting new renewable technologies towards grid parity – Economic and policy aspects," *Renewable Energy,* vol. 36, no. 11, pp. 2776-2784, 2011.
[8] O. H. Hohmeyer and S. Bohm, "Trends toward 100% renewable electricity supply in Germany and Europe: a paradigm shift in energy policies," *Wiley Interdisciplinary Reviews: Energy and Environment,* vol. 4, no. 1, pp. 74-97, 2015.
[9] S.-i. Inage, "The role of large-scale energy storage under high shares of renewable energy," *Wiley Interdisciplinary Reviews: Energy and Environment,* vol. 4, no. 1, pp. 115-132, 2015.
[10] K. Altfeld and D. Pinchbeck, "Admissible Hydrogen Concentrations in Natural Gas Systems," *Gas Energy* vol. 12, no. 3, 2013.
[11] M. W. Melaina, O. Antonia, and M. Penev, "Blending Hydrogen into Natural Gas Pipeline Networks: A Review of Key Issues," NREL/TP-5600-51995, 2013.
[12] Y. Yao, D. Hildebrandt, D. Glasser, and X. Liu, "Fischer−Tropsch Synthesis Using H2/CO/CO2 Syngas Mixtures over a Cobalt Catalyst," *Industrial & Engineering Chemistry Research,* vol. 49, no. 21, pp. 11061-11066, 2010.
[13] J. M. Ogden, "PROSPECTS FOR BUILDING A HYDROGEN ENERGY INFRASTRUCTURE," *Annual Review of Energy and the Environment,* vol. 24, no. 1, pp. 227-279, 1999.
[14] J. Tsao, N. Lewis, and G. Crabtree, "Solar FAQs," Sandia2006.
[15] K. Zhang, M. Ma, P. Li, D. H. Wang, and J. H. Park, "Water Splitting Progress in Tandem Devices: Moving Photolysis beyond Electrolysis," *Advanced Energy Materials,* vol. 6, no. 15, p. 1600602, 2016.
[16] J. Jia *et al.*, "Solar water splitting by photovoltaic-electrolysis with a solar-to-hydrogen efficiency over 30," *Nat Commun,* vol. 7, p. 13237, 2016.
[17] H. D. Zhebo Chen, Eric Miller, *Photoelectrochemical Water Splitting Standards, Experimental Methods, and Protocols* (SpringerBriefs in Energy). Springer-Verlag New York, 2013.
[18] R. Krol, "Principles of Photoelectrochemical Cells," in *Photoelectrochemical Hydrogen Production*(Electronic Materials: Science & Technology: Springer, 2012, pp. 13-67.
[19] J. Luo *et al.*, "Water photolysis at 12.3% efficiency via perovskite photovoltaics and Earth-abundant catalysts," *Science,* vol. 345, no. 6204, pp. 1593-6, 2014.
[20] Y. Kageshima *et al.*, "A miniature solar device for overall water splitting consisting of series-connected spherical silicon solar cells," *Sci Rep,* vol. 6, p. 24633, 2016.
[21] C. Jiang, S. J. A. Moniz, A. Wang, T. Zhang, and J. Tang, "Photoelectrochemical devices for solar water splitting - materials and challenges," *Chem Soc Rev,* vol. 46, no. 15, pp. 4645-4660, 2017.
[22] N. B. S. Kaveh Mazloomi, Hossein Moayedi, "Electrical Efficiency of Electrolytic Hydrogen Production," *Electrical Efficiency of Electrolytic Hydrogen Production,* vol. 7, no. 4, pp. 3314-3326, 2012.

[23] A. Fujishima and K. Honda, "Electrochemical Photolysis of Water at a Semiconductor Electrode," *Nature,* vol. 238, no. 5358, pp. 37-38, 1972.
[24] X. Chen, S. Shen, L. Guo, and S. S. Mao, "Semiconductor-based Photocatalytic Hydrogen Generation," *Chemical Reviews,* vol. 110, no. 11, pp. 6503-6570, 2010.
[25] T. Bak, J. Nowotny, M. Rekas, and C. C. Sorrell, "Photo-electrochemical hydrogen generation from water using solar energy. Materials-related aspects," *International Journal of Hydrogen Energy,* vol. 27, no. 10, pp. 991-1022, 2002.
[26] M. G. Walter *et al.*, "Solar Water Splitting Cells," *Chemical Reviews,* vol. 110, no. 11, pp. 6446-6473, 2010.
[27] B. A. Pinaud *et al.*, "Technical and economic feasibility of centralized facilities for solar hydrogen production via photocatalysis and photoelectrochemistry," *Energy & Environmental Science,* vol. 6, no. 7, p. 1983, 2013.
[28] M. M. May, H. J. Lewerenz, D. Lackner, F. Dimroth, and T. Hannappel, "Efficient direct solar-to-hydrogen conversion by in situ interface transformation of a tandem structure," *Nat Commun,* vol. 6, p. 8286, 2015.
[29] T. J. Jacobsson, V. Fjällström, M. Edoff, and T. Edvinsson, "A theoretical analysis of optical absorption limits and performance of tandem devices and series interconnected architectures for solar hydrogen production," *Solar Energy Materials and Solar Cells,* vol. 138, pp. 86-95, 2015.
[30] J. Brillet, M. Cornuz, F. L. Formal, J.-H. Yum, M. Grätzel, and K. Sivula, "Examining architectures of photoanode–photovoltaic tandem cells for solar water splitting," *Journal of Materials Research,* vol. 25, no. 01, pp. 17-24, 2011.
[31] L. Han *et al.*, "Optimization of amorphous silicon double junction solar cells for an efficient photoelectrochemical water splitting device based on a bismuth vanadate photoanode," *Phys Chem Chem Phys,* vol. 16, no. 9, pp. 4220-9, 2014.
[32] F. F. Abdi, L. Han, A. H. Smets, M. Zeman, B. Dam, and R. van de Krol, "Efficient solar water splitting by enhanced charge separation in a bismuth vanadate-silicon tandem photoelectrode," *Nat Commun,* vol. 4, p. 2195, 2013.
[33] C. Lefrou, P. Fabry, and J.-C. Poignet, *Simplified description of electrochemical systems,* Springer, pp. 51-118, 2012.
[34] K. Maeda, "Photocatalytic water splitting using semiconductor particles: History and recent developments," *Journal of Photochemistry and Photobiology C: Photochemistry Reviews,* vol. 12, no. 4, pp. 237-268, 2011.
[35] S. Chen and L.-W. Wang, "Thermodynamic Oxidation and Reduction Potentials of Photocatalytic Semiconductors in Aqueous Solution," *Chemistry of Materials,* vol. 24, no. 18, pp. 3659-3666, 2012.
[36] PVEducation. (2018, 28.05). *Standard Solar Spectra*. Available: https://www.pveducation.org/pvcdrom/appendices/standard-solar-spectra
[37] O. K. V. Craig A. Grimes, Sudhir Ranjan, *Light, Water, Hydrogen*. Springer, 2008, p. 546.
[38] K. Rajeshwar, "Fundamentals of Semiconductor Electrochemistry and Photoelectrochemisty," in *Encyclopedia of Electrochemistry, Volume 6, Semiconductor Electrodes and Photoelectrochemistry*, M. S. Allen J. Bard, Stuart Licht, Ed.: Wiley, 2002, p. 608.

[39] W. W. Gärtner, "Depletion-Layer Photoeffects in Semiconductors," *Physical Review,* vol. 116, no. 1, pp. 84-87, 1959.
[40] Y. K. Gaudy and S. Haussener, "Utilizing modeling, experiments, and statistics for the analysis of water-splitting photoelectrodes," *J. Mater. Chem. A,* vol. 4, no. 8, pp. 3100-3114, 2016.
[41] M. J. Kenney *et al.*, "High-performance silicon photoanodes passivated with ultrathin nickel films for water oxidation," *Science,* vol. 342, no. 6160, pp. 836-40, 2013.
[42] J. Oh, T. G. Deutsch, H.-C. Yuan, and H. M. Branz, "Nanoporous black silicon photocathode for H2 production by photoelectrochemical water splitting," *Energy & Environmental Science,* vol. 4, no. 5, p. 1690, 2011.
[43] J. A. Turner, "Chemistry. A nickel finish protects silicon photoanodes for water splitting," *Science,* vol. 342, no. 6160, pp. 811-2, 2013.
[44] A. G. Scheuermann, J. P. Lawrence, M. Gunji, C. E. D. Chidsey, and P. C. McIntyre, "ALD-TiO2 Preparation and Characterization for Metal-Insulator-Silicon Photoelectrochemical Applications," *ECS Transactions,* vol. 58, no. 10, pp. 75-86, 2013.
[45] F. E. Osterloh, "Inorganic Materials as Catalysts for Photochemical Splitting of Water," *Chemistry of Materials,* vol. 20, no. 1, pp. 35-54, 2007.
[46] A. Pareek, R. Dom, and P. H. Borse, "Fabrication of large area nanorod like structured CdS photoanode for solar H2 generation using spray pyrolysis technique," *International Journal of Hydrogen Energy,* vol. 38, no. 1, pp. 36-44, 2013.
[47] G. Wang *et al.*, "Hydrogen-treated TiO2 nanowire arrays for photoelectrochemical water splitting," *Nano Lett,* vol. 11, no. 7, pp. 3026-33, 2011.
[48] C. Janáky, K. Rajeshwar, N. R. de Tacconi, W. Chanmanee, and M. N. Huda, "Tungsten-based oxide semiconductors for solar hydrogen generation," *Catalysis Today,* vol. 199, pp. 53-64, 2013.
[49] M. Trunk, A. Gorzkowska-Sobas, V. Venkatachalapathy, T. Zhang, A. Galeckas, and A. Y. Kuznetsov, "Testing ZnO based photoanodes for PEC applications," *Energy Procedia,* vol. 22, pp. 101-107, 2012.
[50] F. E. Osterloh, "Inorganic nanostructures for photoelectrochemical and photocatalytic water splitting," *Chem Soc Rev,* vol. 42, no. 6, pp. 2294-320, 2013.
[51] K. Sivula and M. Grätzel, "Tandem Photoelectrochemical Cells for Water Splitting," in *Photoelectrochemical Water Splitting : Materials, Processes and Architectures*, L. P. Hans-Joachim Lewerenz, Ed. 1 ed.,RSC Energy and Environment Series: Royal Society of Chemistry, 2013, pp. 83-108.
[52] M. Liu, C.-Y. Nam, C. T. Black, J. Kamcev, and L. Zhang, "Enhancing Water Splitting Activity and Chemical Stability of Zinc Oxide Nanowire Photoanodes with Ultrathin Titania Shells," *The Journal of Physical Chemistry C,* vol. 117, no. 26, pp. 13396-13402, 2013.
[53] L. Ji *et al.*, "A silicon-based photocathode for water reduction with an epitaxial SrTiO3 protection layer and a nanostructured catalyst," *Nat Nanotechnol,* vol. 10, no. 1, pp. 84-90, 2015.
[54] Y. W. Chen *et al.*, "Atomic layer-deposited tunnel oxide stabilizes silicon photoanodes for water oxidation," *Nat Mater,* vol. 10, no. 7, pp. 539-44, 2011.

[55] T. Zhu and M. N. Chong, "Prospects of metal–insulator–semiconductor (MIS) nanojunction structures for enhanced hydrogen evolution in photoelectrochemical cells: A review," *Nano Energy,* vol. 12, pp. 347-373, 2015.
[56] D. G. Nocera, "The Artificial Leaf," *Accounts of Chemical Research,* vol. 45, no. 5, pp. 767-776, 2012.
[57] S. Y. Reece *et al.*, "Wireless solar water splitting using silicon-based semiconductors and earth-abundant catalysts," *Science,* vol. 334, no. 6056, pp. 645-8, 2011.
[58] B. Seger, I. E. Castelli, P. C. K. Vesborg, K. W. Jacobsen, O. Hansen, and I. Chorkendorff, "2-Photon tandem device for water splitting: comparing photocathode first versus photoanode first designs," *Energy Environ. Sci.,* vol. 7, no. 8, pp. 2397-2413, 2014.
[59] J. Luo *et al.*, "Targeting Ideal Dual-Absorber Tandem Water Splitting Using Perovskite Photovoltaics and CuInxGa1-xSe2Photocathodes," *Advanced Energy Materials,* vol. 5, no. 24, p. 1501520, 2015.
[60] K. T. Fountaine, H. J. Lewerenz, and H. A. Atwater, "Efficiency limits for photoelectrochemical water-splitting," *Nat Commun,* vol. 7, p. 13706, 2016.
[61] J. S. Shaikh *et al.*, "Perovskite solar cells: In pursuit of efficiency and stability," *Materials & Design,* vol. 136, pp. 54-80, 2017.
[62] A. G. Muñoz and H. J. Lewerenz, "Model experiments on electrochemical formation of nano-dimensioned noble metal–oxide–semiconductor junctions at Si(111) surfaces," *Electrochimica Acta,* vol. 55, no. 26, pp. 7772-7779, 2010.
[63] A. G. Scheuermann *et al.*, "Design principles for maximizing photovoltage in metal-oxide-protected water-splitting photoanodes," *Nat Mater,* vol. 15, no. 1, pp. 99-105, 2016.
[64] D. V. Esposito, I. Levin, T. P. Moffat, and A. A. Talin, "H2 evolution at Si-based metal-insulator-semiconductor photoelectrodes enhanced by inversion channel charge collection and H spillover," *Nat Mater,* vol. 12, no. 6, pp. 562-8, 2013.
[65] S. Hu, M. R. Shaner, J. A. Beardslee, M. Lichterman, B. S. Brunschwig, and N. S. Lewis, "Amorphous TiO(2) coatings stabilize Si, GaAs, and GaP photoanodes for efficient water oxidation," *Science,* vol. 344, no. 6187, pp. 1005-9, 2014.
[66] A. G. Scheuermann and P. C. McIntyre, "Atomic Layer Deposited Corrosion Protection: A Path to Stable and Efficient Photoelectrochemical Cells," *J Phys Chem Lett,* vol. 7, no. 14, pp. 2867-78, 2016.
[67] A. G. Scheuermann, J. D. Prange, M. Gunji, C. E. D. Chidsey, and P. C. McIntyre, "Effects of catalyst material and atomic layer deposited TiO2 oxide thickness on the water oxidation performance of metal–insulator–silicon anodes," *Energy & Environmental Science,* vol. 6, no. 8, p. 2487, 2013.
[68] H.-S. Seo, R. Hayakawa, T. Chikyow, and Y. Wakayama, "Multilevel Operation of Resonant Tunneling with Binary Molecules in a Metal–Insulator–Semiconductor Configuration," *The Journal of Physical Chemistry C,* vol. 118, no. 12, pp. 6467-6472, 2014.
[69] K. Sun *et al.*, "Si photoanode protected by a metal modified ITO layer with ultrathin NiO(x) for solar water oxidation," *Phys Chem Chem Phys,* vol. 16, no. 10, pp. 4612-25, 2014.

[70] T. Hisatomi, J. Kubota, and K. Domen, "Recent advances in semiconductors for photocatalytic and photoelectrochemical water splitting," *Chem Soc Rev*, 2014.
[71] S. S. K. Ma, T. Hisatomi, and K. Domen, "Hydrogen Production by Photocatalytic Water Splitting," *Journal of the Japan Petroleum Institute*, vol. 56, no. 5, pp. 280-287, 2013.
[72] F. F. ABDI, "TOWARDS HIGHLY EFFICIENT BIAS-FREE SOLAR WATER SPLITTING," Dissertation, Technische Universiteit Delft, 2013.
[73] M. N. Huda, A. Walsh, Y. Yan, S.-H. Wei, and M. M. Al-Jassim, "Electronic, structural, and magnetic effects of 3d transition metals in hematite," *Journal of Applied Physics*, vol. 107, no. 12, p. 123712, 2010.
[74] F. Le Formal, M. Grätzel, and K. Sivula, "Controlling Photoactivity in Ultrathin Hematite Films for Solar Water-Splitting," *Advanced Functional Materials*, vol. 20, no. 7, pp. 1099-1107, 2010.
[75] C. Jiang, R. Wang, and B. A. Parkinson, "Combinatorial approach to improve photoelectrodes based on BiVO4," *ACS Comb Sci*, vol. 15, no. 12, pp. 639-45, 2013.
[76] L. Fu, H. Yu, C. Zhang, Z. Shao, and B. Yi, "Cobalt Phosphate Group Modified Hematite Nanorod Array as Photoanode for Efficient Solar Water Splitting," *Electrochimica Acta*, 2014.
[77] J. Y. Kim *et al.*, "Single-crystalline, wormlike hematite photoanodes for efficient solar water splitting," *Sci Rep*, vol. 3, p. 2681, 2013.
[78] J. Yang, D. Wang, H. Han, and C. Li, "Roles of Cocatalysts in Photocatalysis and Photoelectrocatalysis," *Accounts of Chemical Research*, vol. 46, no. 8, pp. 1900-1909, 2013.
[79] C. C. McCrory, S. Jung, I. M. Ferrer, S. M. Chatman, J. C. Peters, and T. F. Jaramillo, "Benchmarking hydrogen evolving reaction and oxygen evolving reaction electrocatalysts for solar water splitting devices," *J Am Chem Soc*, vol. 137, no. 13, pp. 4347-57, 2015.
[80] C. C. McCrory, S. Jung, J. C. Peters, and T. F. Jaramillo, "Benchmarking heterogeneous electrocatalysts for the oxygen evolution reaction," *J Am Chem Soc*, vol. 135, no. 45, pp. 16977-87, 2013.
[81] I. J. Godwin and M. E. G. Lyons, "Enhanced oxygen evolution at hydrous nickel oxide electrodes via electrochemical ageing in alkaline solution," *Electrochemistry Communications*, vol. 32, pp. 39-42, 2013.
[82] M. E. G. Lyons, R. L. Doyle, I. Godwin, M. O'Brien, and L. Russell, "Hydrous Nickel Oxide: Redox Switching and the Oxygen Evolution Reaction in Aqueous Alkaline Solution," *Journal of the Electrochemical Society*, vol. 159, no. 12, pp. H932-H944, 2012.
[83] Y. Mao *et al.*, "Amorphous NiO electrocatalyst overcoated ZnO nanorod photoanodes for enhanced photoelectrochemical performance," *New Journal of Chemistry*, vol. 40, no. 1, pp. 107-112, 2016.
[84] Y. Mao, H. Yang, J. Chen, J. Chen, Y. Tong, and X. Wang, "Significant performance enhancement of ZnO photoanodes from Ni(OH)2 electrocatalyst nanosheets overcoating," *Nano Energy*, vol. 6, pp. 10-18, 2014.
[85] M. Gao *et al.*, "Efficient water oxidation using nanostructured alpha-nickel-hydroxide as an electrocatalyst," *J Am Chem Soc*, vol. 136, no. 19, pp. 7077-84, 2014.

[86] A. Singh, S. L. Y. Chang, R. K. Hocking, U. Bach, and L. Spiccia, "Highly active nickel oxide water oxidation catalysts deposited from molecular complexes," *Energy Environ. Sci.*, vol. 6, no. 2, pp. 579-586, 2013.
[87] G. A. Snook, N. W. Duffy, and A. G. Pandolfo, "Evaluation of the effects of oxygen evolution on the capacity and cycle life of nickel hydroxide electrode materials," *Journal of Power Sources*, vol. 168, no. 2, pp. 513-521, 2007.
[88] F. M. Sapountzi, J. M. Gracia, C. J. Weststrate, H. O. A. Fredriksson, and J. W. Niemantsverdriet, "Electrocatalysts for the generation of hydrogen, oxygen and synthesis gas," *Progress in Energy and Combustion Science*, vol. 58, pp. 1-35, 2017.
[89] X. Lu and C. Zhao, "Electrodeposition of hierarchically structured three-dimensional nickel-iron electrodes for efficient oxygen evolution at high current densities," *Nat Commun*, vol. 6, p. 6616, 2015.
[90] D. Xu, Y. Rui, V. T. Mbah, Y. Li, Q. Zhang, and H. Wang, "Binary nickel and iron oxide modified Ti-doped hematite photoanode for enhanced photoelectrochemical water splitting," *International Journal of Hydrogen Energy*, vol. 41, no. 2, pp. 873-881, 2016.
[91] C. Du *et al.*, "Hematite-based water splitting with low turn-on voltages," *Angew Chem Int Ed Engl*, vol. 52, no. 48, pp. 12692-5, 2013.
[92] N. Li *et al.*, "Influence of iron doping on tetravalent nickel content in catalytic oxygen evolving films," *Proceedings of the National Academy of Sciences*, vol. 114, no. 7, pp. 1486-1491, 2017.
[93] B. M. Hunter *et al.*, "Trapping an Iron(VI) Water-Splitting Intermediate in Nonaqueous Media," *Joule*, 2018.
[94] P. Du and R. Eisenberg, "Catalysts made of earth-abundant elements (Co, Ni, Fe) for water splitting: Recent progress and future challenges," *Energy & Environmental Science*, vol. 5, no. 3, p. 6012, 2012.
[95] V. Artero, M. Chavarot-Kerlidou, and M. Fontecave, "Splitting water with cobalt," *Angew Chem Int Ed Engl*, vol. 50, no. 32, pp. 7238-66, Aug 1 2011.
[96] F. Jiao and H. Frei, "Nanostructured cobalt and manganese oxide clusters as efficient water oxidation catalysts," *Energy & Environmental Science*, vol. 3, no. 8, p. 1018, 2010.
[97] A. J. Esswein, M. J. McMurdo, P. N. Ross, A. T. Bell, and T. D. Tilley, "Size-Dependent Activity of Co3O4 Nanoparticle Anodes for Alkaline Water Electrolysis," *The Journal of Physical Chemistry C*, vol. 113, no. 33, pp. 15068-15072, 2009.
[98] J. R. Swierk and T. D. Tilley, "Electrocatalytic Water Oxidation by Single Site and Small Nuclearity Clusters of Cobalt," *Journal of The Electrochemical Society*, vol. 165, no. 4, pp. H3028-H3033, 2017.
[99] K.-L. Yan *et al.*, "Mesoporous Ag-doped Co3O4 nanowire arrays supported on FTO as efficient electrocatalysts for oxygen evolution reaction in acidic media," *Renewable Energy*, 2017.
[100] L. Xi *et al.*, "Co3O4-Decorated Hematite Nanorods As an Effective Photoanode for Solar Water Oxidation," *The Journal of Physical Chemistry C*, vol. 116, no. 26, pp. 13884-13889, 2012.
[101] Y.-C. Liu, J. A. Koza, and J. A. Switzer, "Conversion of electrodeposited Co(OH)2 to CoOOH and Co3O4, and comparison of their catalytic activity for the oxygen evolution reaction," *Electrochimica Acta*, vol. 140, pp. 359-365, 2014.

[102] S. Jiang, Y. Li, X. Zhang, and Y. Li, "Enhancing the photoelectrochemical water splitting activity of rutile nanorods by removal of surface hydroxyl groups," *Catalysis Today*, vol. 259, pp. 360-367, 2016.
[103] C. Liu, F. Wang, Y. Qiu, Q. Liang, N. Mitsuzak, and Z. Chen, "Facile electrodeposition of cobalt hydroxide on anodic TiO 2 nanotubes arrays for enhanced photoelectrochemical application," *Journal of Photochemistry and Photobiology A: Chemistry*, vol. 353, pp. 200-205, 2018.
[104] G. Zhang, S. Zang, and X. Wang, "Layered Co(OH)2 Deposited Polymeric Carbon Nitrides for Photocatalytic Water Oxidation," *ACS Catalysis*, vol. 5, no. 2, pp. 941-947, 2015.
[105] Y. Yu *et al.*, "Enhanced photoelectrochemical efficiency and stability using a conformal TiO2 film on a black silicon photoanode," *Nature Energy*, vol. 2, no. 6, p. 17045, 2017.
[106] V. Ramakrishnan, H. Kim, J. Park, and B. Yang, "Cobalt oxide nanoparticles on TiO2nanorod/FTO as a photoanode with enhanced visible light sensitization," *RSC Adv.*, vol. 6, no. 12, pp. 9789-9795, 2016.
[107] J. Yang *et al.*, "A multifunctional biphasic water splitting catalyst tailored for integration with high-performance semiconductor photoanodes," *Nat Mater*, vol. 16, pp. 335–341, 2017.
[108] Y. Cao, F. Yuan, M. Yao, J. H. Bang, and J.-H. Lee, "A new synthetic route to hollow Co3O4 octahedra for supercapacitor applications," *CrystEngComm*, vol. 16, no. 5, pp. 826-833, 2014.
[109] M. Risch *et al.*, "Water oxidation by amorphous cobalt-based oxides: in situ tracking of redox transitions and mode of catalysis," *Energy & Environmental Science*, vol. 8, no. 2, pp. 661-674, 2015.
[110] K. Barbalace. (1995 - 2018, 07.04). *Periodic Table of Elements.* . Available: https://EnvironmentalChemistry.com/yogi/periodic/
[111] wikepedia. (2007, 07.04). *Abundance of elements in Earth's crust*. Available: https://en.wikipedia.org/wiki/Abundance_of_elements_in_Earth%27s_crust#cite_note-3
[112] statista.de. (2018, 07.04). *Zinkreserven in den wichtigsten Ländern weltweit im Jahr 2017 (in Millionen Tonnen)*. Available: https://de.statista.com/statistik/daten/studie/194101/umfrage/produktion-von-zink-weltweit-nach-laendern/
[113] Ü. Özgür *et al.*, "A comprehensive review of ZnO materials and devices," *Journal of Applied Physics*, vol. 98, no. 4, p. 041301, 2005.
[114] Y. Zhang, M. K. Ram, E. K. Stefanakos, and D. Y. Goswami, "Synthesis, Characterization, and Applications of ZnO Nanowires," *Journal of Nanomaterials*, vol. 2012, pp. 1-22, 2012.
[115] S. Baruah and J. Dutta, "Hydrothermal growth of ZnO nanostructures," *Science and Technology of Advanced Materials*, vol. 10, no. 1, p. 013001, 2009.
[116] P. S. Xu, Y. M. Sun, C. S. Shi, F. Q. Xu, and H. B. Pan, "The electronic structure and spectral properties of ZnO and its defects," *Nuclear Instruments and Methods in Physics Research Section B: Beam Interactions with Materials and Atoms*, vol. 199, pp. 286-290, 2003.
[117] Z. L. Wang and J. Song, "Piezoelectric Nanogenerators Based on Zinc Oxide Nanowire Arrays," *Science*, vol. 312, no. 5771, pp. 242-246, 2006.

[118] Y. Hu and Z. L. Wang, "Recent progress in piezoelectric nanogenerators as a sustainable power source in self-powered systems and active sensors," *Nano Energy,* vol. 14, pp. 3-14, 2015.
[119] F.-R. Fan, Z.-Q. Tian, and Z. Lin Wang, "Flexible triboelectric generator," *Nano Energy,* vol. 1, no. 2, pp. 328-334, 2012.
[120] Y. Wang, Y. Yang, and Z. L. Wang, "Triboelectric nanogenerators as flexible power sources," *npj Flexible Electronics,* vol. 1, no. 1, 2017.
[121] Z. L. Wang, "Triboelectric Nanogenerators as New Energy Technology for Self-Powered Systems and as Active Mechanical and Chemical Sensors," *ACS Nano,* vol. 7, no. 11, pp. 9533-9557, 2013.
[122] A. A. Narasimulu *et al.*, "Significant triboelectric enhancement using interfacial piezoelectric ZnO nanosheet layer," *Nano Energy,* vol. 40, pp. 471-480, 2017.
[123] W. Deng *et al.*, "Enhanced performance of ZnO microballoon arrays for a triboelectric nanogenerator," *Nanotechnology,* vol. 28, no. 13, p. 135401, 2017.
[124] A. B. Djurisic and Y. H. Leung, "Optical properties of ZnO nanostructures," *Small,* vol. 2, no. 8-9, pp. 944-61, 2006.
[125] A. B. Djurišić, A. M. C. Ng, and X. Y. Chen, "ZnO nanostructures for optoelectronics: Material properties and device applications," *Progress in Quantum Electronics,* vol. 34, no. 4, pp. 191-259, 2010.
[126] M. Willander *et al.*, "Luminescence from Zinc Oxide Nanostructures and Polymers and their Hybrid Devices," *Materials,* vol. 3, no. 4, pp. 2643-2667, 2010.
[127] A. Janotti and C. G. Van de Walle, "Fundamentals of zinc oxide as a semiconductor," *Reports on Progress in Physics,* vol. 72, no. 12, p. 126501, 2009.
[128] A. Echresh, C. O. Chey, M. Z. Shoushtari, O. Nur, and M. Willander, "Tuning the emission of ZnO nanorods based light emitting diodes using Ag doping," *Journal of Applied Physics,* vol. 116, no. 19, p. 193104, 2014.
[129] K. Govender, D. S. Boyle, P. O'Brien, D. Binks, D. West, and D. Coleman, "Room-Temperature Lasing Observed from ZnO Nanocolumns Grown by Aqueous Solution Deposition," *Advanced Materials,* vol. 14, no. 17, pp. 1221-1224, 2002.
[130] S. Chu *et al.*, "Electrically pumped waveguide lasing from ZnO nanowires," *Nat Nanotechnol,* vol. 6, no. 8, pp. 506-10, Jul 3 2011.
[131] S. Xu and Z. L. Wang, "One-dimensional ZnO nanostructures: Solution growth and functional properties," *Nano Research,* vol. 4, no. 11, pp. 1013-1098, 2011.
[132] T. Tynell and M. Karppinen, "Atomic layer deposition of ZnO: a review," *Semiconductor Science and Technology,* vol. 29, no. 4, p. 043001, 2014.
[133] A. J. Rettie *et al.*, "Combined charge carrier transport and photoelectrochemical characterization of BiVO4 single crystals: intrinsic behavior of a complex metal oxide," *J Am Chem Soc,* vol. 135, no. 30, pp. 11389-96, 2013.
[134] X. Yang, R. Liu, Y. He, J. Thorne, Z. Zheng, and D. Wang, "Enabling practical electrocatalyst-assisted photoelectron-chemical water splitting with earth abundant materials," *Nano Research,* vol. 8, no. 1, pp. 56-81, 2014.

[135] Z. Chen *et al.*, "Accelerating materials development for photoelectrochemical hydrogen production: Standards for methods, definitions, and reporting protocols," *Journal of Materials Research*, vol. 25, no. 01, pp. 3-16, 2011.
[136] N. Buehler, K. Meier, and J. F. Reber, "Photochemical hydrogen production with cadmium sulfide suspensions," *The Journal of Physical Chemistry*, vol. 88, no. 15, pp. 3261-3268, 1984.
[137] A. Koca and M. Şahin, "Photocatalytic hydrogen production by direct sun light from sulfide/sulfite solution," *International Journal of Hydrogen Energy*, vol. 27, no. 4, pp. 363-367, 2002.
[138] D. Yolaçan and N. Demirci Sankir, "Enhanced photoelectrochemical and photocatalytic properties of 3D-hierarchical ZnO nanostructures," *Journal of Alloys and Compounds*, vol. 726, pp. 474-483, 2017.
[139] S. Guo, X. Zhao, W. Zhang, and W. Wang, "Optimization of electrolyte to significantly improve photoelectrochemical water splitting performance of ZnO nanowire arrays," *Materials Science and Engineering: B*, vol. 227, pp. 129-135, 2018.
[140] C.-F. Liu, Y.-J. Lu, and C.-C. Hu, "Effects of Anions and pH on the Stability of ZnO Nanorods for Photoelectrochemical Water Splitting," *ACS Omega*, vol. 3, no. 3, pp. 3429-3439, 2018.
[141] Q. Mi, A. Zhanaidarova, B. S. Brunschwig, H. B. Gray, and N. S. Lewis, "A quantitative assessment of the competition between water and anion oxidation at WO3 photoanodes in acidic aqueous electrolytes," *Energy & Environmental Science*, vol. 5, no. 2, p. 5694, 2012.
[142] A. Wolcott, W. A. Smith, T. R. Kuykendall, Y. Zhao, and J. Z. Zhang, "Photoelectrochemical Study of Nanostructured ZnO Thin Films for Hydrogen Generation from Water Splitting," *Advanced Functional Materials*, vol. 19, no. 12, pp. 1849-1856, 2009.
[143] E. S. Babu, S.-K. Hong, T. S. Vo, J.-R. Jeong, and H. K. Cho, "Photoelectrochemical water splitting properties of hydrothermally-grown ZnO nanorods with controlled diameters," *Electronic Materials Letters*, vol. 11, no. 1, pp. 65-72, 2015.
[144] K. S. Ranjith, R. Pandian, E. McGlynn, and R. T. Rajendra Kumar, "Alignment, Morphology and Defect Control of Vertically Aligned ZnO Nanorod Array: Competition between “Surfactant” and “Stabilizer” Roles of the Amine Species and Its Photocatalytic Properties," *Crystal Growth & Design*, vol. 14, no. 6, pp. 2873-2879, 2014.
[145] K. Govatsi, A. Seferlis, S. G. Neophytides, and S. N. Yannopoulos, "Influence of the morphology of ZnO nanowires on the photoelectrochemical water splitting efficiency," *International Journal of Hydrogen Energy*, vol. 43, no. 10, pp. 4866-4879, 2018.
[146] Y.-K. Hsu, Y.-G. Lin, and Y.-C. Chen, "Polarity-dependent photoelectrochemical activity in ZnO nanostructures for solar water splitting," *Electrochemistry Communications*, vol. 13, no. 12, pp. 1383-1386, 2011.
[147] A. U. Pawar, C. W. Kim, M. J. Kang, and Y. S. Kang, "Crystal facet engineering of ZnO photoanode for the higher water splitting efficiency with proton transferable nafion film," *Nano Energy*, vol. 20, pp. 156-167, 2016.
[148] Z. Liu, Q. Cai, C. Ma, J. Zhang, and J. Liu, "Photoelectrochemical properties and growth mechanism of varied ZnO nanostructures," *New Journal of Chemistry*, vol. 41, no. 16, pp. 7947-7952, 2017.

[149] W. C. Lee *et al.*, "Marangoni ring-templated vertically aligned ZnO nanotube arrays with enhanced photocatalytic hydrogen production," *Materials Chemistry and Physics*, vol. 149-150, pp. 12-16, 2015.
[150] Y. Qiu, K. Yan, H. Deng, and S. Yang, "Secondary branching and nitrogen doping of ZnO nanotetrapods: building a highly active network for photoelectrochemical water splitting," *Nano Lett*, vol. 12, no. 1, pp. 407-13, 2012.
[151] X. Zhang, Y. Liu, and Z. Kang, "3D branched ZnO nanowire arrays decorated with plasmonic au nanoparticles for high-performance photoelectrochemical water splitting," *ACS Appl Mater Interfaces*, vol. 6, no. 6, pp. 4480-9, 2014.
[152] X. Sun, Q. Li, J. Jiang, and Y. Mao, "Morphology-tunable synthesis of ZnO nanoforest and its photoelectrochemical performance," *Nanoscale*, vol. 6, no. 15, pp. 8769-80, 2014.
[153] N. K. Hassan, M. R. Hashim, and N. K. Allam, "ZnO nano-tetrapod photoanodes for enhanced solar-driven water splitting," *Chemical Physics Letters*, vol. 549, pp. 62-66, 2012.
[154] K.-S. Ahn *et al.*, "ZnO nanocoral structures for photoelectrochemical cells," *Applied Physics Letters*, vol. 93, no. 16, p. 163117, 2008.
[155] K.-S. Ahn *et al.*, "Enhancement of photoelectrochemical response by aligned nanorods in ZnO thin films," *Journal of Power Sources*, vol. 176, no. 1, pp. 387-392, 2008.
[156] S. G. Kumar and K. S. R. K. Rao, "Zinc oxide based photocatalysis: tailoring surface-bulk structure and related interfacial charge carrier dynamics for better environmental applications," *RSC Adv.*, vol. 5, no. 5, pp. 3306-3351, 2015.
[157] A. Janotti and C. G. Van de Walle, "Native point defects in ZnO," *Physical Review B*, vol. 76, no. 16, p. 165202, 2007.
[158] K. Ellmer and A. Bikowski, "Intrinsic and extrinsic doping of ZnO and ZnO alloys," *Journal of Physics D: Applied Physics*, vol. 49, no. 41, p. 413002, 2016.
[159] K. Tang, S.-L. Gu, J.-D. Ye, S.-M. Zhu, R. Zhang, and Y.-D. Zheng, "Recent progress of the native defects and p-type doping of zinc oxide," *Chinese Physics B*, vol. 26, no. 4, p. 047702, 2017.
[160] A. B. Djurišić *et al.*, "Defect emissions in ZnO nanostructures," *Nanotechnology*, vol. 18, no. 9, p. 095702, 2007.
[161] K. Bandopadhyay and J. Mitra, "Zn interstitials and O vacancies responsible for n-type ZnO: what do the emission spectra reveal?," *RSC Adv.*, vol. 5, no. 30, pp. 23540-23547, 2015.
[162] J. Wang, R. Chen, L. Xiang, and S. Komarneni, "Synthesis, properties and applications of ZnO nanomaterials with oxygen vacancies: A review," *Ceramics International*, vol. 44, no. 7, pp. 7357-7377, 2018.
[163] J. Wang *et al.*, "Oxygen vacancy induced band-gap narrowing and enhanced visible light photocatalytic activity of ZnO," *ACS Appl Mater Interfaces*, vol. 4, no. 8, pp. 4024-4030, 2012.
[164] Y. Suhak *et al.*, "Application of ZnO single crystals for light-induced water splitting under UV irradiation," *Materials Chemistry and Physics*, vol. 143, no. 3, pp. 1253-1257, 2014.
[165] N. Liu *et al.*, "Black TiO2 nanotubes: cocatalyst-free open-circuit hydrogen generation," *Nano Lett*, vol. 14, no. 6, pp. 3309-13, Jun 11 2014.

[166] C. Yao *et al.*, "Enhanced photoelectrochemical performance of hydrogenated ZnO hierarchical nanorod arrays," *Journal of Power Sources,* vol. 237, pp. 295-299, 2013.
[167] J. K. Cooper, Y. Ling, C. Longo, Y. Li, and J. Z. Zhang, "Effects of Hydrogen Treatment and Air Annealing on Ultrafast Charge Carrier Dynamics in ZnO Nanowires Under in Situ Photoelectrochemical Conditions," *The Journal of Physical Chemistry C,* vol. 116, no. 33, pp. 17360-17368, 2012.
[168] L. E. Greene *et al.*, "Low-temperature wafer-scale production of ZnO nanowire arrays," *Angew Chem Int Ed Engl,* vol. 42, no. 26, pp. 3031-4, 2003.
[169] K. H. Tam *et al.*, "Defects in ZnO Nanorods Prepared by a Hydrothermal Method," *The Journal of Physical Chemistry B,* vol. 110, no. 42, pp. 20865-20871, 2006.
[170] F. Liu, M. Y. Guo, Y. H. Leung, A. B. Djurišić, A. M. C. Ng, and W. K. Chan, "Effect of starting properties and annealing on photocatalytic activity of ZnO nanoparticles," *Applied Surface Science,* vol. 283, pp. 914-923, 2013.
[171] T. Bora, P. Sathe, K. Laxman, S. Dobretsov, and J. Dutta, "Defect engineered visible light active ZnO nanorods for photocatalytic treatment of water," *Catalysis Today,* vol. 284, pp. 11-18, 2017.
[172] J. Al-Sabahi, T. Bora, M. Al-Abri, and J. Dutta, "Controlled Defects of Zinc Oxide Nanorods for Efficient Visible Light Photocatalytic Degradation of Phenol," *Materials,* vol. 9, no. 4, pp. 238-247, 2016.
[173] F. Kayaci, S. Vempati, I. Donmez, N. Biyikli, and T. Uyar, "Role of zinc interstitials and oxygen vacancies of ZnO in photocatalysis: a bottom-up approach to control defect density," *Nanoscale,* vol. 6, no. 17, pp. 10224-10234, 2014.
[174] F. Kayaci, S. Vempati, C. Ozgit-Akgun, N. Biyikli, and T. Uyar, "Enhanced photocatalytic activity of homoassembled ZnO nanostructures on electrospun polymeric nanofibers: A combination of atomic layer deposition and hydrothermal growth," *Applied Catalysis B: Environmental,* vol. 156-157, pp. 173-183, 2014.
[175] K. S. Ranjith and R. T. Rajendra Kumar, "Surfactant free, simple, morphological and defect engineered ZnO nanocatalyst: Effective study on sunlight driven and reusable photocatalytic properties," *Journal of Photochemistry and Photobiology A: Chemistry,* vol. 329, pp. 35-45, 2016.
[176] X. Zhang *et al.*, "Effect of aspect ratio and surface defects on the photocatalytic activity of ZnO nanorods," *Sci Rep,* vol. 4, p. 4596, 2014.
[177] G. R. Li, T. Hu, G. L. Pan, T. Y. Yan, X. P. Gao, and H. Y. Zhu, "Morphology−Function Relationship of ZnO: Polar Planes, Oxygen Vacancies, and Activity," *The Journal of Physical Chemistry C,* vol. 112, no. 31, pp. 11859-11864, 2008.
[178] K. S. Ranjith and R. T. Rajendra Kumar, "Regeneration of an efficient, solar active hierarchical ZnO flower photocatalyst for repeatable usage: controlled desorption of poisoned species from active catalytic sites," *RSC Advances,* vol. 7, no. 9, pp. 4983-4992, 2017.
[179] J. Wang, P. Liu, X. Fu, Z. Li, W. Han, and X. Wang, "Relationship between Oxygen Defects and the Photocatalytic Property of ZnO Nanocrystals in Nafion Membranes," *Langmuir,* vol. 25, no. 2, pp. 1218-1223, 2009/01/20 2009.

[180] F. Liu, Y. H. Leung, A. B. Djurišić, A. M. C. Ng, and W. K. Chan, "Native Defects in ZnO: Effect on Dye Adsorption and Photocatalytic Degradation," *The Journal of Physical Chemistry C*, vol. 117, no. 23, pp. 12218-12228, 2013.
[181] M. Y. Guo *et al.*, "Effect of Native Defects on Photocatalytic Properties of ZnO," *The Journal of Physical Chemistry C*, vol. 115, no. 22, pp. 11095-11101, 2011.
[182] I. Izumi, W. W. Dunn, K. O. Wilbourn, F.-R. F. Fan, and A. J. Bard, "Heterogeneous photocatalytic oxidation of hydrocarbons on platinized titanium dioxide powders," *The Journal of Physical Chemistry*, vol. 84, no. 24, pp. 3207-3210, 1980.
[183] F. Kayaci, S. Vempati, C. Ozgit-Akgun, I. Donmez, N. Biyikli, and T. Uyar, "Selective isolation of the electron or hole in photocatalysis: ZnO-TiO2 and TiO2-ZnO core-shell structured heterojunction nanofibers via electrospinning and atomic layer deposition," *Nanoscale*, vol. 6, no. 11, pp. 5735-45, 2014.
[184] R. L. Doyle and M. E. G. Lyons, "The Oxygen Evolution Reaction: Mechanistic Concepts and Catalyst Design," pp. 41-104, 2016.
[185] O. Bikondoa, C. L. Pang, R. Ithnin, C. A. Muryn, H. Onishi, and G. Thornton, "Direct visualization of defect-mediated dissociation of water on TiO2(110)," *Nature Materials*, vol. 5, no. 3, pp. 189-192, 2006.
[186] K. Yim *et al.*, "Property database for single-element doping in ZnO obtained by automated first-principles calculations," *Sci Rep*, vol. 7, p. 40907, 2017.
[187] H. Morkoç and Ü. Özgür, *Zinc Oxide - Fundamentals, Materials and Device Technology*. Wiley-VCH Verlag GmbH & Co. KGaA, 2009.
[188] J. G. Reynolds *et al.*, "Shallow acceptor complexes in p-type ZnO," *Applied Physics Letters*, vol. 102, no. 15, p. 152114, 2013.
[189] K.-S. Ahn *et al.*, "Photoelectrochemical Properties of N-Incorporated ZnO Films Deposited by Reactive RF Magnetron Sputtering," *Journal of The Electrochemical Society*, vol. 154, no. 9, p. B956, 2007.
[190] P. P. Patel *et al.*, "Nitrogen and cobalt co-doped zinc oxide nanowires – Viable photoanodes for hydrogen generation via photoelectrochemical water splitting," *Journal of Power Sources*, vol. 299, pp. 11-24, 2015.
[191] X. Yang *et al.*, "Nitrogen-Doped ZnO Nanowire Arrays for Photoelectrochemical Water Splitting," *Nano Letters*, vol. 9, no. 6, pp. 2331-2336, 2009.
[192] I. Rahinov, N. Ditzian, A. Goldman, and S. Cheskis, "NH2 radical formation by ammonia pyrolysis in a temperature range of 800-1000 K," *Applied Physics B: Lasers and Optics*, vol. 77, no. 5, pp. 541-546, 2003.
[193] M. Futsuhara, K. Yoshioka, and O. Takai, "Optical properties of zinc oxynitride thin films," *Thin Solid Films*, vol. 317, no. 1, pp. 322-325, 1998.
[194] V. Sharma, M. Dixit, V. R. Satsangi, S. Dass, S. Pal, and R. Shrivastav, "Photoelectrochemical splitting of water with nanocrystalline Zn1−xMnxO thin films: First-principle DFT computations supporting the systematic experimental endeavor," *International Journal of Hydrogen Energy*, vol. 39, no. 8, pp. 3637-3648, 2014.
[195] M. I. Łukasiewicz *et al.*, "ZnO, ZnMnO and ZnCoO films grown by atomic layer deposition," *Semiconductor Science and Technology*, vol. 27, no. 7, p. 074009, 2012.

[196] S. Basu *et al.*, "Local Structure Investigation of Cobalt and Manganese Doped ZnO Nanocrystals and Its Correlation with Magnetic Properties," *The Journal of Physical Chemistry C*, vol. 118, no. 17, pp. 9154-9164, 2014.
[197] S. V. Bhat and F. L. Deepak, "Tuning the bandgap of ZnO by substitution with Mn2+, Co2+ and Ni2+," *Solid State Communications*, vol. 135, no. 6, pp. 345-347, 2005.
[198] D. Y. Inamdar, A. D. Lad, A. K. Pathak, I. Dubenko, N. Ali, and S. Mahamuni, "Ferromagnetism in ZnO Nanocrystals: Doping and Surface Chemistry," *The Journal of Physical Chemistry C*, vol. 114, no. 3, pp. 1451-1459, 2010.
[199] J. Lu and H. Wang, "Significant infrared lateral photovoltaic effect in Mn-doped ZnO diluted magnetic semiconducting film," *Optics Express*, vol. 20, no. 19, pp. 21552-21557, 2012.
[200] D. A. Schwartz, N. S. Norberg, Q. P. Nguyen, J. M. Parker, and D. R. Gamelin, "Magnetic Quantum Dots: Synthesis, Spectroscopy, and Magnetism of Co2+- and Ni2+-Doped ZnO Nanocrystals," *Journal of the American Chemical Society*, vol. 125, no. 43, pp. 13205-13218, 2003.
[201] W. C. Lee, G. E. Canciani, B. O. S. Alwhshe, and Q. Chen, "Enhanced photoelectrochemical water oxidation by ZnxMyO (M = Ni, Co, K, Na) nanorod arrays," *International Journal of Hydrogen Energy*, vol. 41, no. 1, pp. 123–131, 2015.
[202] Y. Habba, M. Capochichi-Gnambodoe, and Y. Leprince-Wang, "Enhanced Photocatalytic Activity of Iron-Doped ZnO Nanowires for Water Purification," *Applied Sciences*, vol. 7, no. 11, p. 1185, 2017.
[203] A. Hui, J. Ma, J. Liu, Y. Bao, and J. Zhang, "Morphological evolution of Fe doped sea urchin-shaped ZnO nanoparticles with enhanced photocatalytic activity," *Journal of Alloys and Compounds*, vol. 696, pp. 639-647, 2017.
[204] S. B. Ogale, "Dilute doping, defects, and ferromagnetism in metal oxide systems," *Adv Mater*, vol. 22, no. 29, pp. 3125-55, 2010.
[205] C. B. Fitzgerald, "SnO[sub 2] doped with Mn, Fe or Co: Room temperature dilute magnetic semiconductors," *Journal of Applied Physics*, vol. 95, no. 11, p. 7390, 2004.
[206] A. Sharma, M. Varshney, S. Kumar, K.D.Verma, and R. Kumar, "Magnetic Properties of Fe and Ni Doped SnO2 Nanoparticles," *Nanomaterials and Nanotechnology* vol. 1, no. 1, pp. 29-33, 2011.
[207] P. Olsson, C. Domain, and J. F. Guillemoles, "Ferromagnetic Compounds for High Efficiency Photovoltaic Conversion: The Case of AlP:Cr," *Physical Review Letters*, vol. 102, no. 22, p. 227204, 2009.
[208] I. Djerdj, Z. Jaglicic, D. Arcon, and M. Niederberger, "Co-Doped ZnO nanoparticles: Minireview," *Nanoscale*, vol. 2, no. 7, pp. 1096-1104, 2010.
[209] V. Gandhi, R. Ganesan, H. H. Abdulrahman Syedahamed, and M. Thaiyan, "Effect of Cobalt Doping on Structural, Optical, and Magnetic Properties of ZnO Nanoparticles Synthesized by Coprecipitation Method," *The Journal of Physical Chemistry C*, vol. 118, no. 18, pp. 9715-9725, 2014.
[210] M. Arshad, A. Azam, A. S. Ahmed, S. Mollah, and A. H. Naqvi, "Effect of Co substitution on the structural and optical properties of ZnO nanoparticles synthesized by sol–gel route," *Journal of Alloys and Compounds*, vol. 509, no. 33, pp. 8378-8381, 2011.

[211] Y. Caglar, "Sol–gel derived nanostructure undoped and cobalt doped ZnO: Structural, optical and electrical studies," *Journal of Alloys and Compounds*, vol. 560, pp. 181-188, 2013.
[212] A. Klein *et al.*, "Transparent Conducting Oxides for Photovoltaics: Manipulation of Fermi Level, Work Function and Energy Band Alignment," *Materials*, vol. 3, no. 11, pp. 4892-4914, 2010.
[213] I. Y.-Y. Bu, "Optoelectronic properties of sol–gel derived ZnO:Co: Effect of Co concentration," *Superlattices and Microstructures*, vol. 75, pp. 657-666, 2014.
[214] S. Benramache, B. Benhaoua, and H. Bentrah, "Preparation of transparent, conductive ZnO:Co and ZnO:In thin films by ultrasonic spray method," *Journal of Nanostructure in Chemistry*, vol. 3, no. 1, p. 54, 2013.
[215] Y. Lu, Y. Lin, D. Wang, L. Wang, T. Xie, and T. Jiang, "A high performance cobalt-doped ZnO visible light photocatalyst and its photogenerated charge transfer properties," *Nano Research*, vol. 4, no. 11, pp. 1144-1152, 2011.
[216] L. Yanmei *et al.*, "Structure and photoluminescence of arrayed Zn1−xCoxO nanorods grown via hydrothermal method," *Journal of Physics D: Applied Physics*, vol. 40, no. 15, pp. 4592-4596, 2007.
[217] S. Deka and P. A. Joy, "Ferromagnetism induced by hydrogen in polycrystalline nonmagnetic Zn[sub 0.95]Co[sub 0.05]O," *Applied Physics Letters*, vol. 89, no. 3, p. 032508, 2006.
[218] K. J. Kim and Y. R. Park, "Large and abrupt optical band gap variation in In-doped ZnO," *Applied Physics Letters*, vol. 78, no. 4, p. 475, 2001.
[219] S. Benramache, B. Benhaoua, and F. Chabane, "Effect of substrate temperature on the stability of transparent conducting cobalt doped ZnO thin films," *Journal of Semiconductors*, vol. 33, no. 9, p. 093001, 2012.
[220] S. Ramachandran, A. Tiwari, and J. Narayan, "Zn[sub 0.9]Co[sub 0.1]O-based diluted magnetic semiconducting thin films," *Applied Physics Letters*, vol. 84, no. 25, p. 5255, 2004.
[221] Y. Z. Yoo *et al.*, "ZnO–CoO solid solution thin films," *Journal of Applied Physics*, vol. 90, no. 8, p. 4246, 2001.
[222] P. Koidl, "Optical absorption of Co2+ in ZnO," *Physical Review B*, vol. 15, no. 5, pp. 2493-2499, 1977.
[223] R. Elilarassi and G. Chandrasekaran, "Influence of Co-doping on the structural, optical and magnetic properties of ZnO nanoparticles synthesized using auto-combustion method," *Journal of Materials Science: Materials in Electronics*, vol. 24, no. 1, pp. 96-105, 2012.
[224] S. Singh and M. Rao, "Optical and electrical resistivity studies of isovalent and aliovalent 3d transition metal ion doped ZnO," *Physical Review B*, vol. 80, no. 4, p. 045210, 2009.
[225] C. A. Johnson, T. C. Kaspar, S. A. Chambers, G. M. Salley, and D. R. Gamelin, "Sub-band-gap photoconductivity inCo2+-doped ZnO," *Physical Review B*, vol. 81, no. 12, p. 125206, 2010.
[226] J. W. May, J. Ma, E. Badaeva, and X. Li, "Effect of Excited-State Structural Relaxation on Midgap Excitations in Co2+-Doped ZnO Quantum Dots," *The Journal of Physical Chemistry C*, vol. 118, no. 24, pp. 13152-13156, 2014.
[227] C. A. Johnson, A. Cohn, T. Kaspar, S. A. Chambers, G. M. Salley, and D. R. Gamelin, "Visible-light photoconductivity of Zn1−xCoxO and its dependence onCo2+concentration," *Physical Review B*, vol. 84, no. 12, p. 125203, 2011.

[228] W. K. Liu, G. M. Salley, and D. R. Gamelin, "Spectroscopy of Photovoltaic and Photoconductive Nanocrystalline Co2+-Doped ZnO Electrodes," *The Journal of Physical Chemistry B,* vol. 109, no. 30, pp. 14486-14495, 2005.
[229] W. Li, G. Wang, C. Chen, J. Liao, and Z. Li, "Enhanced Visible Light Photocatalytic Activity of ZnO Nanowires Doped with Mn(2+) and Co(2+) Ions," *Nanomaterials (Basel),* vol. 7, no. 1, 2017.
[230] A. Šutka *et al.*, "Co doped ZnO nanowires as visible light photocatalysts," *Solid State Sciences,* vol. 56, pp. 54-62, 2016.
[231] H. Yasuda and Y. Kanemitsu, "Dynamics of nonlinear blue photoluminescence and Auger recombination inSrTiO3," *Physical Review B,* vol. 77, no. 19, 2008.
[232] K. Karmakar, A. Sarkar, K. Mandal, and G. G. Khan, "Stable and Enhanced Visible-Light Water Electrolysis Using C, N, and S Surface Functionalized ZnO Nanorod Photoanodes: Engineering the Absorption and Electronic Structure," *ACS Sustainable Chemistry & Engineering,* vol. 4, no. 10, pp. 5693-5702, 2016.
[233] C. Fàbrega, D. Monllor-Satoca, S. Ampudia, A. Parra, T. Andreu, and J. R. Morante, "Tuning the Fermi Level and the Kinetics of Surface States of TiO2Nanorods by Means of Ammonia Treatments," *The Journal of Physical Chemistry C,* vol. 117, no. 40, pp. 20517-20524, 2013.
[234] D. E. Scaife, "Oxide semiconductors in photoelectrochemical conversion of solar energy," *Solar Energy,* vol. 25, no. 1, pp. 41-54, 1980.
[235] A. L. Rudd and C. B. Breslin, "Photo-induced dissolution of zinc in alkaline solutions," *Electrochimica Acta,* vol. 45, no. 10, pp. 1571-1579, 1/31/ 2000.
[236] M. Law, L. E. Greene, A. Radenovic, T. Kuykendall, J. Liphardt, and P. Yang, "ZnO−Al2O3 and ZnO−TiO2 Core−Shell Nanowire Dye-Sensitized Solar Cells," *The Journal of Physical Chemistry B,* vol. 110, no. 45, pp. 22652-22663, 2006.
[237] R. A. Rakkesh and S. Balakumar, "Facile Synthesis of ZnO/TiO₂ Core–Shell Nanostructures and Their Photocatalytic Activities," *Journal of Nanoscience and Nanotechnology,* vol. 13, no. 1, pp. 370-376, 2013.
[238] Y. Zhao *et al.*, "A Facile Route to the Preparation of Highly Uniform ZnO@TiO2 Core-Shell Nanorod Arrays with Enhanced Photocatalytic Properties," *Journal of Chemistry,* vol. 2017, pp. 1-8, 2017.
[239] W. Feng, L. Lin, H. Li, B. Chi, J. Pu, and J. Li, "Hydrogenated TiO 2 /ZnO heterojunction nanorod arrays with enhanced performance for photoelectrochemical water splitting," *International Journal of Hydrogen Energy,* vol. 42, no. 7, pp. 3938-3946, 2017.
[240] Y. Nosaka and A. Y. Nosaka, "Reconsideration of Intrinsic Band Alignments within Anatase and Rutile TiO2," *J Phys Chem Lett,* vol. 7, no. 3, pp. 431-4, 2016.
[241] D. O. Scanlon *et al.*, "Band alignment of rutile and anatase TiO(2)," *Nat Mater,* vol. 12, no. 9, pp. 798-801, 2013.
[242] M. Pazoki, N. Nafari, and N. Taghavinia, "Ab initio study of electronic effects in the ZnO/TiO2core/shell interface: application in dye sensitized solar cells," *RSC Adv.*, vol. 4, no. 1, pp. 301-307, 2014.
[243] A. N. El-Shazly, A. H. Hegazy, M. M. Rashad, M. F. El-Shahat, and N. K. Allam, "Ultrathin ALD TiO 2 shells for enhanced photoelectrochemical solar

fuel generation," *Journal of Alloys and Compounds,* vol. 739, pp. 178-183, 2018.
[244] S. Hernandez *et al.*, "Optimization of 1D ZnO@TiO2 core-shell nanostructures for enhanced photoelectrochemical water splitting under solar light illumination," *ACS Appl Mater Interfaces,* vol. 6, no. 15, pp. 12153-67, 2014.
[245] S. Hernández *et al.*, "Fast and low-cost synthesis of 1D ZnO–TiO2 core–shell nanoarrays: Characterization and enhanced photo-electrochemical performance for water splitting," *Journal of Alloys and Compounds,* vol. 615, pp. S530-S537, 2014.
[246] S. Hernandez *et al.*, "Comparison of photocatalytic and transport properties of TiO2 and ZnO nanostructures for solar-driven water splitting," *Phys Chem Chem Phys,* vol. 17, no. 12, pp. 7775-86, 2015.
[247] Z. Li, S. Feng, S. Liu, X. Li, L. Wang, and W. Lu, "A three-dimensional interconnected hierarchical FeOOH/TiO(2)/ZnO nanostructural photoanode for enhancing the performance of photoelectrochemical water oxidation," *Nanoscale,* vol. 7, no. 45, pp. 19178-83, 2015.
[248] M. Li *et al.*, "Hierarchical nanowire arrays based on carbon nanotubes and Co3O4 decorated ZnO for enhanced photoelectrochemical water oxidation," *Journal of Materials Chemistry A,* vol. 3, no. 26, pp. 13731-13737, 2015.
[249] N. Koteeswara Reddy, S. Winkler, N. Koch, and N. Pinna, "Electrochemical Water Oxidation of Ultrathin Cobalt Oxide-Based Catalyst Supported onto Aligned ZnO Nanorods," *ACS Appl Mater Interfaces,* vol. 8, no. 5, pp. 3226-32, 2016.
[250] M. Shao, F. Ning, M. Wei, D. G. Evans, and X. Duan, "Hierarchical Nanowire Arrays Based on ZnO Core−Layered Double Hydroxide Shell for Largely Enhanced Photoelectrochemical Water Splitting," *Advanced Functional Materials,* vol. 24, no. 5, pp. 580-586, 2014.
[251] T. Nguyen, M. Boudard, M. J. Carmezim, and M. F. Montemor, "Layered Ni(OH)2-Co(OH)2 films prepared by electrodeposition as charge storage electrodes for hybrid supercapacitors," *Sci Rep,* vol. 7, p. 39980, 2017.

Chapter 2

2 Experimental Methods

2.1 Optical characterization

2.1.1 UV-Vis Spectroscopy (UV-Vis)

In order to gain primary information regarding the optical properties of semiconducting samples, such as the absorption coefficient and bandgap-energy, spectral reflection and transmission data, UV-Vis measurements are particular useful. The measurement principle of a UV-Vis experiment is based on the interaction of light and matter. A light beam of a known but variable wavelength λ is focused on a sample. Upon irradiation multiple sample-beam interactions are possible. These processes are highly dependent on λ but will overall follow the general rule of energy conversion. This means that the energy inherent to the irradiation (e.g. expressed as its intensity I_0) before interacting with the sample can be assumed as unity (i.e. 100 %). Since the energy after the sample-beam interaction must still be unity it is now possible to express an energetic balance in form of the major optical processes possible, namely: reflection (*R*), transmission (*T*), absorption (*A*) and scattering (*S*) of light, equation (2.1) [1]:

$$100 = T + A + R + S \tag{2.1}$$

Scattering can be difficult to measure but may become important when the sample surface is very rough or the particle size becomes very small. However, for thin layers and the majority of the samples presented in this thesis the scattering can be neglected.

A schematic representation of sample-beam interactions (neglecting scattering and multiple reflection events) is shown in Figure 2-1a. If the beam hits the sample, a certain portion of the irradiation will be directly (mirror-like) and diffusely reflected (in response to surface-roughness). The remaining portion of light passing through the sample may be absorbed by the material. Whether the light is absorbed weakly or strongly depends on the materials spectral absorption coefficient α and the thickness of the sample *d*. The Beer-Lambert law (equation (2.2)) links those important material properties and dictates the intensity of the transmitted beam *I*:

$$I(d) = I_0 \cdot e^{-\alpha d} \tag{2.2}$$

If reflection at the front and backside is include one can estimate *I* using equation (2.3)

[2]:

$$I(d) = I_0(1 - R^2) \cdot e^{-\alpha d} \tag{2.3}$$

Finally the transmission, again present in diffuse and direct components, is the ratio of I and $I_0(1\text{-}R^2)$ (equation (2.4)):

$$T = \frac{I(d)}{I_0(1 - R^2)} = e^{-\alpha d} \tag{2.4}$$

In a typical 2-beam UV-Vis spectrometer the intensity of a reference beam – which resembles I_0 – is measured and compared with the intensity of the sample beam that interacts with the sample. For rough samples the diffuse components are the most intense, hence the measurement should be performed using an integrating sphere, which is able to capture the diffuse components. The coating on the inner surface of the sphere (e.g. barium titanate/sulfate) allows for diffuse reflected or transmitted beams to be collected by the detector. By adjusting the sample position the transmission and reflection can then be measured, as shown schematically in Figure 2-1b and c, respectively. In the transmission configuration the directly transmitted beam is included in the measurement as well, since the second part of the sample-beam axis is covered with a white standard (also coated with e.g. barium titanate/sulfate). For the reflection configuration, however, the directly reflected beam may be exiting the sphere again and would thus not be included in the measurement using the setup shown. Since the R_{dir} is relatively low for rough samples (e.g. < 3 % for nanostructures such as the ZnO nanorods in this thesis), this component is less important and may be omitted. For exact measurements, R_{dir} can be measured using a mirror-like setup and equation (2.1) (neglecting scattering) can thus be expressed as (equation (2.5)):

$$100 = \left(T_{diff} + T_{dir}\right) + \left(R_{diff} + R_{dir}\right) + A \tag{2.5}$$

Once the R and T values are determined (note that T is experimentally measured as $T = I/I_0$), equation (2.4) can be rearranged to calculate α (equation (2.6)):

$$\alpha = \frac{-ln\frac{T}{(1 - R^2)}}{d} \tag{2.6}$$

This is crucial for the estimation of the bandgap energy E_G using the Tauc-expression and the related Tauc-plot [3-5]:

$$(\alpha h\nu) = B(h\nu - E_G)^n \tag{2.7}$$

where E_G is the optical band gap energy, hν is the photon energy and B is a constant. The term n describes the forbidden/allowed direct or indirect transitions. Since ZnO exhibits a direct bandgap, n can be taken as 0.5 and the estimation of E_G for ZnO nanorods is possible by extrapolating the linear part of $(\alpha h\nu)^2$ vs. hν onto the x-axis. For energies close to but < E_G the absorption coefficient decays exponentially. The Urbach energy E_U is a measure of this dependence, which is commonly observed near the band gap of a semiconductor. It is usually related to structural disorder or defects energetically localized near the band-edges (band-tail states). The Urbach energy is linked with the absorption coefficient by the following expression, equation (2.8) [6]:

$$\alpha = \alpha_0 e^{\frac{h\nu}{E_U}} \tag{2.8}$$

where α_0 is a constant. The logarithmic function of equation (2.8) identifies a liner dependence of ln(α) from h·ν of the form y = mx + n, where m = $1/E_U$. Thus, the Urbach energy can be estimated from the reciprocal slope of the linear portion in a ln(α) vs. h·ν plot.

The UV-Vis measurements in this thesis were recorded using a Lambda 950 spectrometer from Perkin Elmer with Universal Reflectance Accessories (direct reflection) and a Shimadzu UV-2401PC spectrometer equipped with an integrating sphere (T and R_{diff}). For the transmission measurements an uncoated substrate sample (e.g. glass or FTO coated glass) was taken as a reference and the sample was put into the sample slot with the growth-side facing inside the integrating sphere. Reflection measurements were referenced against the air.

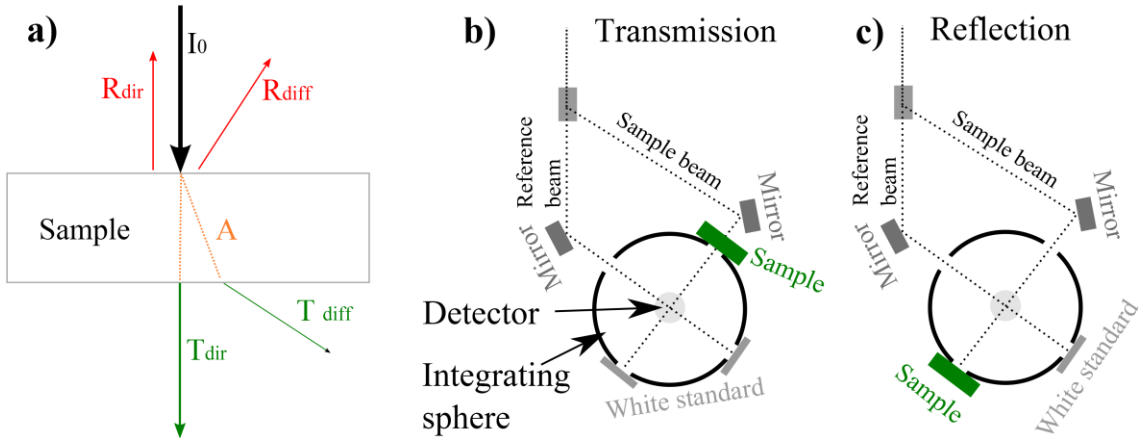

Figure 2-1: a) Schematic representation of sample-beam interactions in a UV-Vis experiment. The measurement setup in transmission and reflection configuration is shown in b) and c), respectively.

2.1.2 **Photo-luminescence spectroscopy (PL)**

Building up on the possible sample-beam interactions described in section 2.1.1, a closely related characterization method investigates some processes that occur in a material upon the absorption of light – photo-luminescence spectroscopy (PL). Considering the case where a sample gets excited with $h\nu \geq E_G$ (bandgap absorption), electrons will be promoted into the conduction band (CB) at a rate of G. The material is now in a non-equilibrated state and will return to equilibrium once the excitation ceases. In order for the material to reach the ground state, the excited charge carriers will recombine at a rate R, with $R \approx G$.

Different recombination processes are possible in a semiconductor and are schematically shown in Figure 2-2 [7]. Firstly, the photo-generated electron can recombine directly from the CB with the photo-generated hole in the valance band (Figure 2-2a). This process – called band-band recombination – emits a photon that will have a wavelength λ of ca. the energy of the bandgap, equation (2.9):

$$\lambda = \frac{h \cdot c}{E_G} \tag{2.9}$$

It is important to note that for ZnO excitonic recombination also exists (not shown). In this case the photo-generated charge carriers are "bound" together forming an electron-hole pair, or exciton. If the exciton binding energy $E_{B,Ex}$ is greater than the thermal energy (e.g. 60 meV vs. 25 meV at room temperature for ZnO, respectively) this recombination mechanism can be present. Otherwise the electron may be thermalized into the CB. Excitonic recombination emits light of E_G - $E_{B,Ex}$.

The second example process shown in Figure 2-2b is the recombination over energetic deep-level defects (trap-states). This process may happen radiatively or non-radiatively. Furthermore it is possible that charge carriers thermalize into defect states (i.e. non-radiatively) if their position is close to the energy band edges (shallow defects). From these defect states a recombination process with a complementary defect state (donor/acceptor recombination) or with the energy bands may occur (see Figure 2-2c). The recombination process will then emit light that exhibits a lower energy compared to E_G. The defect-related recombination processes shown in Figure 2-2b and Figure 2-2c may also be taken as examples of the so-called Shockley-Read-Hall recombination, which is based on theoretical work by these authors on the

recombination of charge carriers in indirect bandgap semiconductors. For such materials, direct recombination is very unlikely because the valence band maximum and conduction band minimum exhibit different k-vectors (crystal momentum). Recombination thus involves another particle/partner, which in the presented cases is an electronic defect in the forbidden gap. Generally, this recombination mechanism transfers at least some of the energy into thermal energy in form of phonons. As a direct bandgap semiconductor, this recombination mechanism is not dominant ZnO - if the crystal is of high quality (low number of defects).

If the electron density in the CB is very high (e.g. high injection case or degenerate doping) Auger recombination may occur. In this three particle process an electron in the CB transfers its energy to a second CB electron, which is then excited into a higher energy level and finally thermalizes to the ground state. This process does not emit light.

Photo-luminescence spectroscopy can detect the radiative recombination processes and since the emitted photons may differ in their wavelengths, this characterization method is particularly helpful when investigating defect-related recombination. In a typical photoluminescence experiment the sample is illuminated with radiation of a monochromatic excitation wavelength λ_{Ex}, as shown schematically in Figure 2-3. Depending of the magnitude of this wavelength the sample will emit radiation of different wavelengths, as a consequence of the interaction of λ_{Ex} with the sample. A spectrum of all emitted wavelengths λ_{Em} is then recorded showing unique features which can be assigned to different processes (e.g. transitions) within the material. Conclusions can then be drawn about impurities and crystallographic quality of the material under test. In contrast to laser sources, the light source shown in Figure 2-3 emits photons of different wavelengths, thus enabling the investigation of the samples response to different λ_{Ex}. In such an excitation PL experiment λ_{Em} is fixed and the λ_{Ex} is changed over the course of the measurement. This approach may be helpful when evaluating the exact recombination mechanism that underpins a certain emission. For the characterization of ZnO samples at room temperature an Agilent Carry Eclipse Fluorescence Spectrophotometer was used. Usually the excitation wavelength was set to 345 nm – which is above the bandgap energy of ZnO – with a slit-width of 2.5 mm.

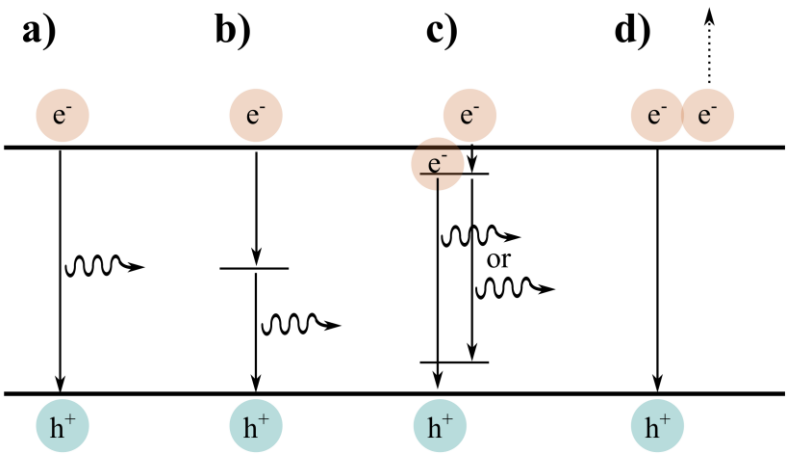

Figure 2-2: Example recombination processes in a semiconductor. a) band-band recombination. b) Recombination over deep-level defects. c) Recombination over shallow defects and donor-acceptor type recombination. d) Auger recombination. Processes in b) and c) are examples for Shockley-Read-Hall Recombination (SRH).

Spectra were acquired in 1 nm steps in a range between 370 nm to 850 nm. The intensity of the impinging and emitting beams could be further adjusted by the slit opening of the individual ports. For each sample set in the following chapters the slit openings where however kept constant. It is also important to note that some measurement artefacts may exist which demand the appropriate use of filters (see Figure A1- 3 and Figure A1- 4 and related comments).

Additionally, a He-Cd laser (λ_{Ex} = 325 nm, 1.6 mW) was used to investigate the PL properties of some samples at lower temperatures (down to 11.5 K) and at varying excitation beam intensities. Cooling of a sample during a PL analysis reduces the non-radiative recombination processes, leading to an enhancement of the PL signal. At very low temperatures the resolution of individual energy levels is increased, since excited charge carriers reside in discrete states. This is particularly helpful when examining

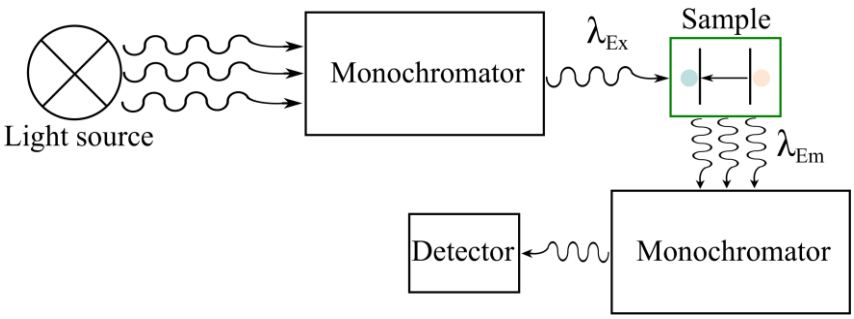

Figure 2-3: Schematic representation of the principle setup of a PL-measurement.

states close to the energy band edges, which would otherwise be thermalized (e.g. an electron in a shallow donor state could be thermalized into the CB at room temperature).

2.1.3 **Raman spectroscopy**

While being mostly neglected in a UV-Vis measurement, scattering events can provide important insight into the characteristic of a material. Especially useful in this regard are scattering phenomena that occur on a molecular level, which form the basis of Raman spectroscopy.

At room-temperature molecules in a solid are always vibrating [8]. A simple way to imagine this, is to think of the bond between individual atoms as a spring that stretches or compresses with a certain frequency [8]. However, from a quantum mechanical point of view the vibrational energy of a molecule is quantized into distinguishable vibrational levels [8]. Since the energy inherent to these vibrational levels is low (ca. 10^{-2} – 10^{-1} eV) the spectroscopic detection of same lies in the infrared range and is expressed in wavenumbers $\bar{\nu}$ (i.e. number of waves that fit into one centimetre), equation (2.10):

$$\bar{\nu} = \frac{1}{\lambda} \tag{2.10}$$

Thus, spectroscopy based on the measurements of vibrational energy is commonly applied in the range of $\bar{\nu}$ = 200 – 4000 cm^{-1} [8].

The molecular vibrations may be excited to a higher level if the frequency of the impinging irradiation matches the vibrational frequency of the molecule. However, if an intense laser with a wavelength e.g. in the visible light region is used, the vibration may be excited into a virtual energy state. Of importance for Raman spectroscopy is now how it will return to a lower energy state, since this may happen over different scattering process. If the vibration returns to its ground level and the scattered irradiation exhibits the same frequency as the impinging irradiation, an elastic scattering process is present (Rayleigh scattering). However, it is also possible that the excited vibrational frequency does not return to its ground level. Thus the scattered photon may either exhibit a lower (Stokes scattering) or higher energy (anti-Stokes scattering) in respect to the impinging photon. These inelastic scattering processes are

called Raman scattering and the change in energy between the impinging and scattered photon is measured as the Raman shift (note that Stokes scattering is dominant due to a higher probability to excite a vibration from a lower, more populated ground state) [8]. Compared to Rayleigh scattering or fluorescence events, Raman scattering is weak.

A micro-Raman system, as used in this thesis, works on the principle that highly monochromatic irradiation from a laser is focused onto a sample and the Raman scattered irradiation is collected using an optical microscope with a high numerical aperture connected to a detector/CCD camera. The use of a microscope allows focusing of the beam on a particular spot on the sample with a beam diameter down to the micrometer level [8]. Using this experimental setup it is thus possible to correlate optical images to the Raman properties.

A big advantage of this characterization method is its ease of use. Micro-Raman measurements require no vacuum, little sample preparation (the surface should be free of contaminations) and typically permits fast spectrum acquisition. Furthermore the laser beam can be scanned over the sample area, producing multiple spectra (mapping) across the sample. Among others, Raman spectroscopy enables the user to determine the material composition and phase, analyze possible strain in the material, investigate the crystal orientation and to examine the influence of defects [8, 9].

For the investigation of ZnO and cobalt-doped ZnO nanorods a Renishaw micro-Raman spectrometer equipped with a 514 nm laser was used. The beam was focused through a Leica 100 x (NA = 0.9) objective and the laser power density on the sample was less than 5 $mW/\mu m^2$ (spot size ca. 1 μm). Raman spectroscopy was mainly used to confirm the phase and crystal structure of the ZnO nanorods and to investigate possible impurities (cobalt doping, oxygen vacancies, carbon contamination).

2.2 Structural characterization

2.2.1 Scanning electron microscopy (SEM) and energy dispersive X-ray spectroscopy (EDS)

While the Rayleigh criterion limits the resolution of optical microscopes to > 10^2 nm at best, electron microscopy allows for imaging and analysis of features in the nanometer and sub-nanometer range [10]. This arises from the fact that electrons, when

accelerated at a high potential, exhibit a very small wavelength [11]. Compared to an optical microscope it is thus possible to resolve such small geometries. In a SEM measurement the sample under test is bombarded with electrons, which are emitted from a cathode and accelerated towards the sample. The electron beam is then scanned over the surface to generate the information on the required area. Different signals can be detected depending on how the electrons (primary electrons) interact with the sample. A number of interactions are possible [11]:

- Change in direction (reflection/scattering) of primary electron without energy loss (elastic scattering) – backscattered electrons (BSE)
- Primary electrons interact with matter and lose energy – so called secondary electron (SE, emitted from the outer shells of the atom) exit the sample exhibiting different direction and less energy than primary electrons (inelastic scattering)
- Primary electrons interact with matter and trigger the emission of material characteristic X-rays
- Primary electrons interact with matter and trigger the emission of material characteristic Auger electrons from the first few atomic layers of the sample

The aforementioned signals (electrons or X-rays) escape from different sample depths/volumes with the order (surface to bulk): Auger electrons (first few monolayers) > secondary electrons (ca. 5 – 50 nm) > backscattered electrons (ca. 50 – 300 nm) > characteristic X-rays (300 nm - up to a few µm) [8]. How deep the actual material activation upon electron beam irradiation is, depends on the density/atomic number of the material and the beam energy (accelerating voltage and beam current).

In order to detect the individual electrons/X-rays, special detectors are needed. Most commonly, a SE detector is used to gain topographic information/images of the sample, since SEs are more surface sensitive than BSEs. For a SE image the brightness is determined by the amount of SEs exiting the material. Similarly, the contrast is generated due to the differences in the number of SEs reaching the detector from various positions on the sample. The texture/roughness of the surface is therefore crucially important for the contrast in a SE image. If a SE exits a surface that is not facing the detector, this position on the sample will be darker compared to a surface that is facing the detector (trajectory effect) [8]. Other surface structures such as kinks

and steps may lead to bright features in a SE image because of an increase of the active surface area when compared to a flat surface (electron number effect) [8].

Additional information about the chemical composition of the sample can be gained from the characteristic X-rays, which are emitted from bulk of the sample. The electron beam-sample interaction may lead to ionization (displacement of a core electron) of an atom and subsequent filling of this vacancy by an electron from a shell farther from the nucleus [11]. The latter process can result in the release of characteristic X-rays, which can be detected using energy dispersive X-ray spectroscopy (EDS). These X-rays are unique to each chemical element since the energy difference between the individual shells varies with the atomic number of the atom [8]. The chemical composition of the sample can thus be analyzed. However, EDS analysis offers a comparably low resolution, when compared to e.g. wavelength dispersive spectrometry (WDS) [8]. This may lead to a partial overlap of X-rays of different elements. Furthermore the quantitative analysis of light elements (e.g. oxygen) remains challenging and may result in a high margin of error [12].

For SEM imaging and EDS analysis in this work a FEI Quanta 650 FEG High Resolution Scanning Electron Microscope equipped with a SE and EDS detector was used. The samples investigated were examined without further modification (e.g. polishing or application of a thin conductive surface-layer). Throughout the work the parameters of SEM images are given in the text/figures. For EDS analysis all spectra were recorded at 20 kV and a beam current setting of 4. The integration time was then adjusted to meet a dead-time of ca. 10 % during the acquisition.

2.2.2 **Transmission electron microscopy (TEM)**

Another electron microscopy technique used for the imaging of samples is based on the transmission of electrons through a specimen and is thus termed transmission electron microscopy (TEM). It is however obvious that, in order for electrons being transmitted through a material, the sample under test must be very thin, otherwise the processes mentioned in section 2.2.1 will be dominant. Hence, the thickness of a TEM sample will usually be considerably less than 1 µm and the sample preparation that comes alongside with this requirement is somewhat challenging in itself [10, 13]. As with other electron microscopies, a beam of electrons is generated from an electron

gun (e.g. a filament of tungsten) and is focused onto the sample using an electro-magnetic lenses [10]. After the sample-beam interactions (e.g. scattering events) the portion of electrons that has been transmitted through the sample can again be focused by electro-magnetic lenses and then directed onto a fluorescent screen or a CCD camera [10]. Importantly, the use of electrons in a TEM enables investigations in the sub-nm or single atom range, if the lens aberrations are low [10].

Some principle TEM contrast formation mechanisms are based on the thickness and density of the sample. If one imagines two samples of identical thickness but different densities, it is easy to postulate that more scattering events will occur in the denser sample as a result of the impinging electron beam. Compared to the sample of lower density, the dense sample will thus appear darker in a bright-field image, since less electrons are transmitted. Similarly a thicker sample will also appear darker [10]. Furthermore the diffraction of electrons at crystal planes as well as the phase shift of scattered electrons can be used to generate contrast in a TEM image [10].

As mentioned earlier, in a TEM measurement the specimen has to be very thin in order to allow the transmission of electrons. In this regard nanorods – such as those presented in this work – offer the advantage that their diameter may be thin enough to meet this criterion. This dramatically reduces the time required for the sample preparation. For layer/wafer like materials, for example, a thin lamella is usually cut out of the sample using the focused ion beam technique, which requires good experimental skills and time. The ZnO nanorods presented in this work, on the other hand, could be scratched off the substrate (e.g. glass or FTO coated glass), dispersed and sonicated in isopropanol and dropped directly onto a lacey carbon grid. After a short drying period, the grid could then be mounted into the holder and investigated. A Jeol JEM-2100 was used to record TEM images of the ZnO nanorods.

2.2.3 **X-ray diffraction (XRD)**

XRD is commonly used for material characterization due to its ability to detect different crystal phases and mixed phases of elements. Among many other applications XRD can also be used to detect substitutional doping in semiconductors, which relies on the fact that the dopant and the lattice element it replaces have different ionic radii. Compared to the ideal crystal, this will manifest itself in a change of the lattice

parameters and thus to a shift in the XRD peak positions. The generation of an XRD signal is explained in the following paragraph.

During an XRD experiment a beam of monochromatic X-rays, generated by accelerating electrons to very high speeds and subsequent bombardment of a metal target, is focused onto a sample [14]. A widely used experimental approach is to rotate the detector and to measure the X-ray intensity being diffracted from the sample at different angles [14]. In the resulting angle-resolved spectra peaks will appear at certain angles, which can be seen as the fingerprint of the material under test.

The underlying principle of XRD measurements is governed by the Bragg`s condition, equation (2.11):

$$n\lambda = 2 \cdot d \cdot \sin(\theta) \tag{2.11}$$

Where λ is the wavelength of the X-ray, θ the angle between the impinging X-ray and the normal to the sample surface, *n* is an integer and *d* is the interplanar spacing.

A schematic illustration of the above mentioned condition can be found in Figure 2-4. Considering that the planes A and B shown are crystal planes of same direction (same Miller indices) separated by the interplanar spacing *d*, the reflected X-rays 1` and 2` will only be in the same phase if the additional distance X-ray 2 has to travel is an integer *n* of the wavelength. If the Bragg condition is fulfilled, the two waves will interfere, leading to a strongly increased signal intensity. Since the wavelength of the X-ray source is constant (e.g. 0.154 nm for a copper source) and *d* is a material property, rotating the detector will result in some angles that obey the Bragg condition and others where the condition is not fulfilled. In turn, a spectrum is generated where interference of the X-rays at certain angles will be visible as peaks. As *d* is unique for every material, a measurement of the intensity as a function of θ (in the measurement the angles are usually given as 2θ) will give an exclusive fingerprint of peaks for different crystal planes, hence, allowing for identification of materials and their crystallographic properties such as the size and shape of the unit cell [14]. The spectra obtained can be compared to a library of standard spectra of materials. These were usually recorded using powders of the material in question. In powder form the crystallites of the material are randomly dispersed and peaks of the individual crystal planes will have a certain intensity ratio in respect to each other. This is different for aligned crystallites, were a single lattice plane can be strongly dominant. From the

XRD spectrum of a sample it is thus possible to get information of the crystal orientation. Additionally, the individual peaks can be analyzed to calculate important parameters like the size of the crystallites (e.g. using the Scherrer equation [15]). Also, the peak positon, when compared to the standard material to be found in libraries like the one published by the Joint Committee on Powder Diffraction Standards (JCPDS), can be used to evaluate the presence of unintentionally/intentionally induced defects. This arises on the background that a change in the bonding configuration or the ionic radius of elements in the material will result in a change of the lattice parameters, which will in turn lead to a peak shift detectable by XRD.

In this work a Panalytical X`Pert MRD diffractometer was used in rocking curve configuration. Operating current and voltage of the generator were set to 45 kV and 40 mA for every measurement. In a typical analysis of plain ZnO samples the spectra were acquired between $2\theta = 20°$ and 70° with a stepsize of 0.2°. The exact experimental configurations are given in the methods section of the individual results chapters (3 to 7).

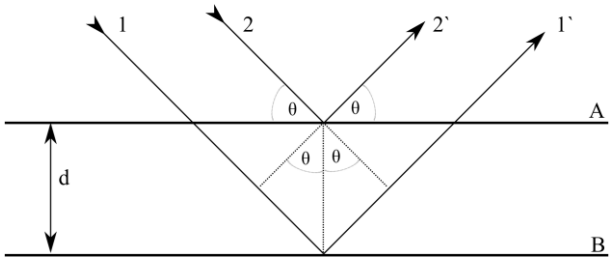

Figure 2-4: Schematic illustration of the Bragg condition.

2.2.4 **X-ray photo-electron spectroscopy (XPS)**

The interaction of X-rays with a sample does not only lead to the diffraction of X-rays but can also lead to scattering events and the emission of photo-electrons [16]. The latter process relies on the photo-electric effect, firstly communicated by Einstein in 1905 for which he received the Nobel Prize in 1921. It is governed by the absorption of an X-ray with the energy $h \cdot \nu$ by a core atom followed by the emission of an electron without energy loss [16]. Based on this principle, the emitted photo-electron leaves the material under test and remains with a kinetic energy E_K – the quantity measured in an XPS experiment [17]. However, if the Fermi energy of the sample equilibrates to the

Fermi energy of the spectrometer, the magnitude of E_K will be a function of the binding energy E_B, equation (2.12) [17]:

$$E_K = h \cdot \nu - E_B - \varphi_{XPS} \tag{2.12}$$

where φ_{XPS} is the work function of the spectrometer. E_B can then be calculated and is element specific. This in turn allows for the identification of the elemental composition of the sample. However, if an atom is part of a chemical compound, consisting of 2 or more different elements, its electrons will be energetically redistributed to a degree [16]. In turn, this leads to shift of the binding energy, which can be observed as "chemical shift" in an XPS experiment [16]. This has proven very useful when examining the chemical phase of a sample, since e.g. metals and their oxides/hydroxides exhibit characteristic binding energy positions and spectra. Additionally, XPS measurements are relatively straightforward in terms of sample preparation and, thanks to the high sensitivity, elements can be detected that are present at > 0.05 %atom [17]. However, in order to reach high sensitivities an ultra-high vacuum is needed [18]. It is also important to be aware of the fact that XPS measurements are only surface sensitive and do not give information about the chemical composition of a sample in the bulk. This arises from the low mean free path or escape depth of a photo-electron for which its energy is conserved [17]. Thus the sampling depth is usually around 10 nm, even if the X-rays penetrate the sample on µm scale. Nevertheless, one can get some idea about the chemical composition of the bulk using depth profiling. The sample is thereby bombarded with e.g. argon ions or clusters that physically remove material from the sample. Subsequent XPS measurements thus allow the user to analyze the distribution of elements in dependence of the depth/distance to surface. It is however important to note that the chemical state of elements/compounds may be affected by the bombardment [19]. Thus the bombardment has to be carried out with care, with due consideration being applied to the removal of surface contamination (e.g. residual carbon compounds).

From an instrumental point of view an XPS spectrum is generated by the following steps. Firstly an anode material (commonly aluminium, Al) is bombarded with high-energy electrons, which leads to the emission of X-rays [18]. Under the aid of Bragg`s law (equation (2.11), the X-rays are then monochromated and focused onto the sample (a quartz crystal is commonly used for this purpose) [18]. The photo-electric effect

then leads to the emission of photo-electrons from the surface of the sample. After focusing the photo-electrons, the kinetic energies of same can be analyzed. For this purpose hemispherical sector analyzers (HSA) are used today, since they offer a high energy resolution [18]. By applying an electrical potential to the two hemispheres of the HSA, it is possible to allow only photo-electrons of a specific kinetic energy to pass through the analyzer and finally hit the detector [18].

The XPS measurements presented in this study were carried out using a Kratos Axis ULTRA spectrometer equipped with a monochromatic Al Kα radiation of energy 1486.6 eV. All experiments were performed at the University of Limerick by Dr. Fathima Laffir. The advantageous carbon C1s peak at 284.8 eV was used as the charge reference in determining the binding energies. The use of argon bombardment for surface carbon removal or material removal is specified in the individual chapters of this work.

2.3 Photo-(electro)chemical characterization

Setup employed in this work

Several photo-electrochemical cells were designed and further developed over the course of the work for the photo electrochemical characterization of the large variety of materials studied. The final version of the setup, including all accessories, is shown in the photograph in Figure 2-5a. The central part of this system is the custom-build PTFE cell, where a sample (i.e. the working electrode, WE) was fixed into the arrangement by compressing it against the base-plate of the PTFE cell (equipped with an additional PTFE gasket). A schematic cut-out view of the compression arrangement of the inside of the cell is shown in Figure 2-5b. In order to generate a tight fit, the compression-plate, sitting below the sample, is screwed onto the base-plate. Depending on the measurement, a filter-optical fibre arrangement could be added to the compression-plate. In this case the compression-plate exhibited an opening at the sample position to allow transmitted light to be collected. The base plate also exhibited a circular opening and its diameter determined the semiconductor-electrolyte contact and illumination area (geometrical). Furthermore the base-plate – which again was screwed to the cell-body equipped with an O-ring – has two inlets to accept tubes connected to a peristaltic pump. This allowed for the circulation of the electrolyte over

the sample surface. However, it was found that the flow of electrolyte over the sample surface was not sufficient to remove bubbles, which formed after prolonged measurements (e.g. chronoamperometry). Nevertheless, the circulation of the electrolyte should be helpful to counteract a possible pH gradient building up in proximity to the sample surface. A major advantage of the detachability of the base-plate was the cleaning of the inner cavity of the cell body, which was necessary when multiple electrolytes were used in the cell. Furthermore it was possible to design base-plates customized to the sample (e.g. smaller contact opening) or the experiment (e.g. no electrolyte circulation for quick measurements).

The cell-body has four threaded openings, which penetrated the inner cavity at an angle. It was therefore possible to insert a reference electrode (RE) and direct its tip close to the sample surface (for the minimization of the ohmic drop). A second inlet of the cell-body was generally occupied by a counter electrode (CE); leaving two more inlets that could accept additional equipment, such as a camera and/or a tube to gently bubble the electrolyte with nitrogen. The entire cell-body, including the four inlets, was designed to be sealable/airtight. Theoretically some inlets could thus be used to analyze the evolving gases. For the illumination of the sample, the cell-body has a circular opening on the top that could be sealed with a quartz window if needed. The setup was intended for measurements where the sample front side was under illumination from the top (e.g. from a solar simulator or a high power LED). However, by using the cell stand shown in Figure 2-5a and detaching the filter-optical fibre arrangement it was also possible to illuminate the sample from the backside using a high power LED. The LEDs (365 nm or 455 nm) were sourced from Roithner Lasertechnik GmbH and then assembled and connected to a homemade driver.

For photo-electrochemical measurements a potentiostat (here a PalmSens 3) was used to control and measure the current or voltage during the experiment. In a potentiostatic measurement the bias potential is applied between the RE and WE, while the current is measured between the CE and WE. A galvanostatic setup, on the other hand, measures the potential difference between WE and RE and the current between the CE and WE is controlled. A coiled platinum wire (surface area > 2 cm^2) and a RedRod electrode (Radiometer Analytical; possibly Ag/AgCl) or saturated calomel electrode (Radiometer Analytical; SCE) were used as CE and RE, respectively.

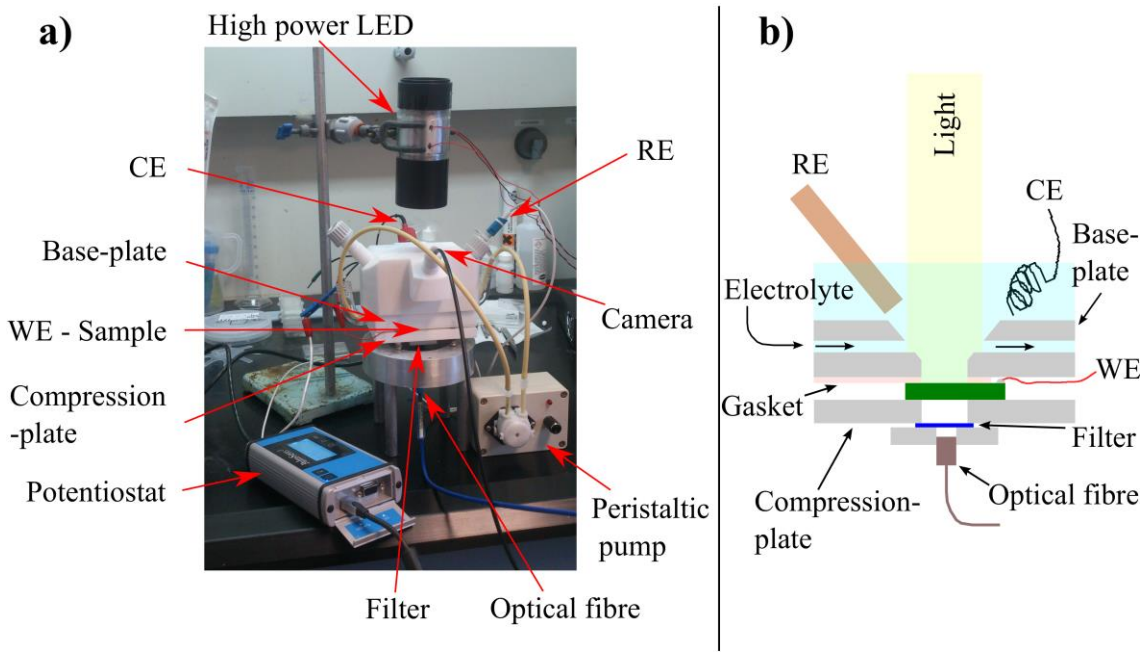

Figure 2-5: a) Photograph of the photo-electrochemical characterization setup. A schematic cut-view of the inside of the photo-electrochemical cell is shown in b).

The reference electrodes used in this work have a standard potential E°_{Ref} of + 199 mV (RedRod – Ag/AgCl) and + 244 mV (SCE) versus SHE. The measured potentials E_{meas} were then corrected to the reversible hydrogen electrode potential (RHE), equation (2.13):

$$E_{vs.\ RHE} = E_{meas} + E^{\circ}_{Ref} + 0.059 \cdot pH \tag{2.13}$$

2.3.1 Linear sweep voltammetry (LSV) and Cyclic voltammetry (CV)

For the investigation of the electrochemical behavior of an electrode in contact with an electrolyte voltammetry techniques, such as LSV and CV, are commonly used. In potentiostatic experiments the applied potential is varied stepwise over time and the corresponding current is recorded. The difference between each applied potential (E_{step}) is usually small and the voltage ramp is scanned relatively fast [1]. For instance, 50 mV/s is a common scan rate in such experiments. With a step size of 5 mV, the current would be sampled at 10 potential steps and the scan speed for each of them would be 0.1 s. In a LSV experiment the potential ramp is fixed between a begin E_{begin} and an end potential E_{end}, whereas in a CV experiment the potential is reversed at the potentials E_{rev1} and E_{rev2}, and E_{begin} can lay somewhere in between. This cycle is often

repeated several times. The type of reactions that occur between the electrode and the electrolyte depends on the magnitude of the applied potential and can be divided into faradaic and non-faradaic processes [20].

If the applied potential is positive/negative enough to oxidize/reduce the electrolyte, charge transfer over the electrode-electrolyte interface occurs (a faradaic process). From a semiconductor physics point of view, the induction of charge transfer processes over the interface due to an applied potential means that the Fermi energy of the semiconductor was sufficiently raised/lowered above/below the reduction/oxidation potential of the electrolyte. In the case of the reduction of the electrolyte, electrons can thus flow from the semiconductor into the electrolyte. Whereas for the oxidation of the electrolyte, electrons from the electrolyte are accepted by the semiconductor.

However, there will be a potential range where no oxidation/reduction of the electrolyte occurs. Nevertheless, processes at the electrode-electrolyte interface, such as adsorption/desorption of species or a structural change of the interface, can still occur (non-faradaic processes) [20]. The external currents that are associated with these processes can still be recorded. This can, for example, be seen in the schematic example of a CV curve given in Figure 2-6. Current flows even before the oxidation potential E_{Ox} is reached. When scanning to higher potentials the current reaches a maximum $I_{p,a}$ at a potential > E_{Ox} (also called the peak potential $E_{p,a}$). Afterwards the current decreases again before the scan direction is reversed at the potential E_{rev1}. The current decrease after $E_{p,a}$ is due to the depletion of the electroactive species at the electrode surface [1]. After reversing the potential, scanning towards more negative potentials leads to the occurrence of a cathodic wave, which – in analogy to the anodic wave – is characterized by E_{Red}, $I_{p,c}$. and $E_{p,c}$. Electrochemically, the cathodic current is the reduction of the oxidized electroactive species residing close to the electrode surface.

If an equilibrium concentration of the reactant and product can be maintained at the electrode surface and no other competing reactions occur the system is said to be reversible (also called Nernstian) [1, 20]. Such systems are characterized by a difference of the peak potentials ΔE_p of around 59 mV/n at 25 °C (n = number of electrons participating in the reaction) and an independency of $I_{p,c}$ and $I_{p,a}$ from the scan rate, with $I_{p,c}/I_{p,a} = 1$ [20]. This, however, represents a somewhat ideal case and

real systems may show deviations from the Nernstian behavior. An example of this would be an increase in the separation of the peak potentials in an irreversible system. In addition, if a system is highly irreversible the absence of a clear anodic/cathodic peak may occur due to the very slow oxidation/reduction [1].

In turn, this behavior can be used to examine the quality of electrodes. When using an electrolyte that is readily oxidized/reduced one may evaluate the ability of the electrode to transfer charges over the interface. For example, in this work, electrodes were tested in the dark for their reaction kinetics using the ferri/ferrocyanide redox couple (10 mM of both, potassium ferricyanide ($K_3Fe(CN)_6$) and potassium ferrocyanide ($K_4Fe(CN)_6$) in 1 M potassium chloride (KCl)). If the transfer kinetics over the interface and within the electrode are appropriate, the resulting cyclic voltammograms would be somewhat similar to the shape presented in Figure 2-6. Poor charge transfer kinetics, on the other hand, would alter the shape of the CV curve as aforementioned (e.g. higher peak-peak splitting, lower peak current and $I_{p,c}/I_{p,a} \neq 1$).

However, the origin of anodic and cathodic peaks does not necessarily need to be due to the oxidation/reduction of the electrolyte but can also result from the redox reactions of the electrode material or defects within same [21, 22]. Cyclic voltammograms are thus often comprised of multiple cathodic/anodic responses. While interpretation of these curves may be difficult, they provide some considerable insight into the participating reactions in a given potential window.

It is for this reason that CV was also applied to test the ZnO-based electrodes described in this thesis. Since the reduction and oxidation of water are the reactions of interest here, aqueous electrolytes were used. To access the entire pH range different electrolyte solutions were prepared (concentrations were usually between 0.1 M and 1 M):

- Acid: hydrochloric acid (HCl)
- Alkaline: sodium hydroxide (NaOH), potassium hydroxide (KOH)
- Neutral: phosphate-buffer (pH 7). Adjustment of the pH by dissolving sodium phosphate monobasic monohydrate (NaH_2PO_4 H_2O) and sodium phosphate dibasic heptahydrate (Na_2HPO_4 $_7H_2O$) in water (18.2 MΩ) until 7.

Furthermore the photo-response of the electrodes was recorded using LSV. In these experiments the potential was scanned from cathodic to anodic and the *I-E*

characteristics of the sample in the dark and under illumination was compared. For the photo-electrochemical results presented in chapters 3 to 7, a solar simulator (LOT, class ACA) was used to illuminate the samples from the top. Standard Test Conditions were applied (100 mW/cm^2, AM 1.5G, 25 °C). The illuminated area was 1 cm^2. However, it is noteworthy that this figure does not represent the actual surface area due to the nanorod geometry of the ZnO electrodes.

The CV and LSV parameters (e.g. step size, scan rate etc.) are given in the individual results chapters.

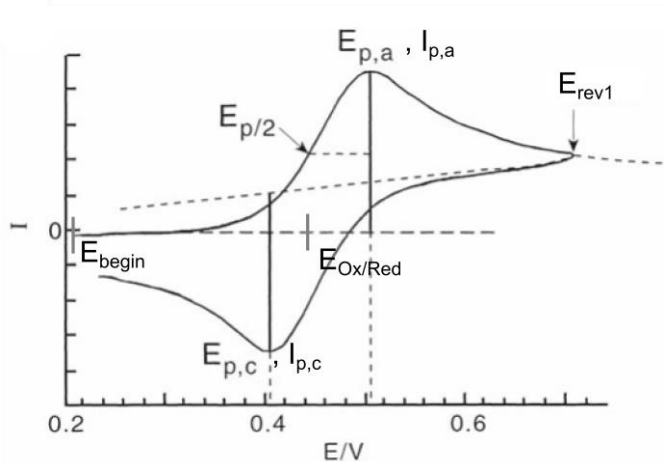

Figure 2-6: Schematic example of a cyclic voltammogram. Important potentials *E* and currents *I* are marked. $E_{p/2}$ represents the half peak potential (i.e. the potential at which the current is $I_p/2$). Adapted from reference [23]. Copyright 2010, Springer.

2.3.2 **Chronoamperometry (CA)**

From the comparison of LSV/CV measurements in the dark and under illumination knowledge can be gained regarding the photo-current onset potential and the magnitude of the photo-current at a given potential (here generally positive). This information is helpful when evaluating the stability of an electrode. As outlined in section 1.4.4, the corrosion of ZnO in aqueous solution is influenced by both applying an electrical bias potential and charge carriers generated upon illumination. Stability experiments – in the form of chronoamperometry (CA) measurements – were thus carried out at a potential where a significant photo-current was observed in the LSV/CV curves.

The basic principle of a CA experiments is to measure the current of the system at certain time intervals t_{int} over a measurement duration of *t*. Depending on the system

in question, it may not be necessary to apply a potential in order to observe a current. However, in this work a fixed positive potential was applied over a time *t*.

Under such conditions a stable photo-anode would retain its initial current over the course of the experiment, whereas a non-stable electrode would generally show a decreasing current over time. This may be due to, for example, surface transformation (e.g. formation of a hydroxide layer) or removal of the electrode material (corrosion). These reactions are in competition with the OER and will lead to performance deterioration over time. However, it is also important to note that in proximity to the electrode surface a concentration gradient of the electroactive species (e.g. OH^- for the OER under alkaline conditions) will build up [20]. Depending on the overall bias (electrical and by irradiation) and the electrolyte concertation, the concentration of the electroactive species can be almost zero. Hence, the recorded current will decrease over time and will finally be limited by the mass transfer of the electroactive species from the bulk of the electrolyte to the surface by diffusion [20]. If the conditions are such that electroactive species is consumed rapidly (i.e. high initial current) one can aid the transport towards the electrode surface by agitating/stirring the electrolyte. Furthermore this may also be helpful to tackle bubble formation on the electrode surface (e.g. O_2 for the OER). Otherwise, the active surface area of the electrode will decrease significantly over time, which in turn results again in a decrease in the recorded current.

The parameters for CA measurements are specified in Chapter 7.

2.3.3 **Electrochemical impedance spectroscopy (EIS)**

When measuring the *I-E* response of a system by applying relatively large potential perturbations – as is for example done in LSV/CV – the electrode will usually be driven under non-equilibrium conditions [20]. By applying a constant potential, an equilibrium of the oxidized and reduced electroactive species may however exist and the electrode can effectively be driven under steady state conditions. This still holds true when a small alternating potential perturbation (E_{AC}) of e.g. 5 – 10 mV is applied to the electrode. In such a small potential range the *I-E* curve of the system is virtually linear and the resulting current response will follow the angular frequency ω ($\omega = 2\pi f$, where *f* is the frequency) of the AC signal [20].

The introduction of the time domain (i.e. frequency) allows for the investigation of reaction pathways and kinetics by analogy with the properties of electrical circuits. This is due to the fact that circuit elements, such as a resistors, capacitors and inductors, respond differently to the sinusoidal AC potential. The current response of a resistor, for example, will follow E_{AC} in the time domain, while a capacitor changes the phase of the current response and its current response will lead the voltage [20]. The total response of a system consisting of multiple components – as is the case for electrochemical cells – will thus mathematically be determined by real (i.e. resistance(s)) and imaginary contributions (e.g. capacitance(s)) [20]. Generally, these contributions can be summarized as the impedance Z(ω), equation (2.14):

$$Z(\omega) = Z_{Re} + jZ_{Im} \tag{2.14}$$

where Z_{Re} and Z_{Im} are the real and imaginary part of the impedance, respectively, and j is the imaginary number ($j = \sqrt{-1}$). For a resistor, not exhibiting an imaginary component, eq. (2.14) shows that Z equals the ohmic resistance (R). In contrast, the impedance of a capacitor (Z_C) or an inductor (Z_L) (described by the capcitance C and inductance L, respectively) does not exhibit a real part and these components show only imaginary components, equations (2.15) and (2.16):

$$Z_C(\omega) = -j\frac{1}{\omega C} = -j\frac{1}{2\pi f C} = -jX_C \tag{2.15}$$

$$Z_L(\omega) = +j\omega L = -j2\pi f L = jX_L \tag{2.16}$$

With X_C and X_L defined as capacitor and inductor reactance, respectively.

As an example, one can imagine the electrical circuit represented in Figure 2-7. All of the individual components will contribute to the total impedance Z_{tot}. Z_{tot} can be described as the sum of R_1 and the impedance of the parallel circuit of R_2 and C_1 (Z_p): $Z_{tot} = Z_{R1} + Z_p$. Z_p is determined by the product of the individual impedances over the sum of the individual impedances.

As noted earlier, the two resistors do not show a frequency dependence. The only individual impedance in the circuit that depends on the frequency is associated with the capacitor C_1. If now, during an EIS measurement, the frequency is changed, the overall Z_{tot} will change in accordance with Z_{C1}. In turn it is possible to determine the values for the individual components from the response of the system to various

frequencies. When the frequency approaches infinity (practically, EIS measurements are carried out up to the MHz range), Z_{C1} approaches zero and thus the total impedance will be dominated by R_1. On the other hand, very low frequencies (practically EIS measurements are carried out down to the mHz range) result in very high X_{C1}. This leads to a convergence of Z_p to R_2. In turn, Z_{tot} will be determined by the sum of R_1 and R_2 – electrically the current will pass through these resistors. The schematic representation of such a circuit in the Nyquist plot of Figure 2-7 illustrates the aforementioned cases. At both extrema (high and low frequencies) the impedance will consist solely of the real part. In an EIS measurement Z_{tot} can now be measured over a range of frequencies in between the extrema and the capacitance of the capacitor C_1 can be determined.

The equivalent circuit shown in Figure 2-7 is also called a simplified Randles cell. It is helpful in associating the various electrical components to the components of the electrochemical reactions. For an electrode in contact with an electrolyte (neglecting diffusion/mass transfer towards the electrode) one may think of R_1, R_2 and C_1 as ohmic resistance of the solution + external components etc., the charge transfer resistance over the electrode into the electrolyte and the double layer capacitance, respectively [20]. While R_1 may sometimes be difficult to influence (e.g. fixed electrolyte concentration), the charge transfer resistance is influenced by the 'quality' of the electrode material. Re-investigating the Nyquist plot in Figure 2-7, one readily observes that the overall charge transfer resistance is correlated to the width of the semicircle. Hence, a low charge transfer resistance and thus good electrode/reaction kinetics will manifest in a narrow semicircle in a Nyquist plot.

However, it is important to note that electrochemical systems may significantly differ from this simplified, somewhat idealized model. A practical example is the use of a semiconductor as an electrode. The band bending at the interface to the electrolyte will lead to emergence of the space charge capacitance and an associated resistance. Every component on the "current path" will thus contribute to the overall impedance. It becomes obvious that, if multiple interfaces and defects exist along this path, the interpretation of the results may not be straightforward. Nevertheless, in the light of the solar water splitting process it is apparent that such more complex systems will only show good device performance if the overall charge transfer resistance (which can be a contribution of many resistances) is low.

Furthermore, it is possible to determine important quantities associated with the semiconductor electrode, such as the charge carrier density and the flat band potential from EIS measurements. This can, for example, be done by fixing the frequency to a medium frequency (e.g. ~ 10^3 Hz) and measuring the impedance at different applied potentials. A medium frequency is chosen because charge transfer processes happen on different timescales. The somewhat sluggish OER, a multiple particle process, will occur more slowly (i.e. at lower frequencies) as compared to the charge transfer within the space charge region. Under the assumption that the capacitance associated with the space charge region is dominant, the consequence is that the potential drop in the Helmholtz layer is small compared to the potential drop over the space charge region, which may be obscured for high charge carrier concentrations [24]. With this in mind one can then, for example, estimate the donor concentration and flat band potential using the Mott–Schottky relation (also see Appendix 1) [24, 25].

Details on the experimental conditions for EIS measurements in this thesis are found in the individual result chapters 3 and 6.

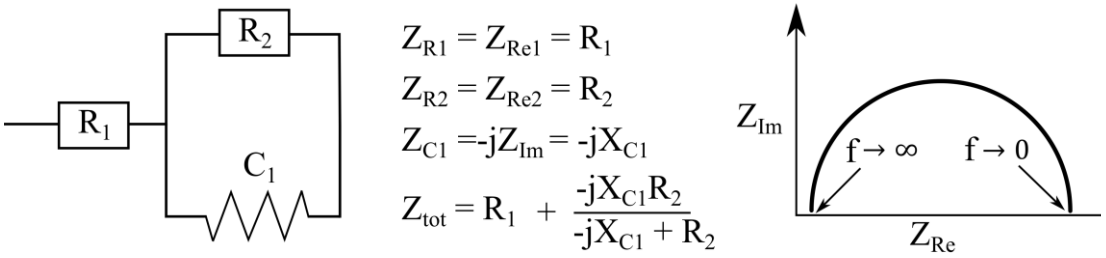

Figure 2-7: Equivalent circuit diagram of a resistor R_1 in series with a parallel circuit consisting of a resistor R_2 and a capacitor C_1 (simplified Randles cell). The impedance of the individual components and schematic representation of the Nyquist plot of the circuit are given in the middle and on the right, respectively.

2.3.4 **Photo-catalytic dye-degradation experiments**

Similar to photo-electrochemical reactions, photo-catalysis utilizes the photo-generation of charge carriers by a semiconductor – often metal oxides like TiO_2 or ZnO – which then undergo reactions with the solution in contact with the material. However, usually photo-catalysis is performed without an external bias. The reaction that should be catalyzed does not necessarily have to be the splitting of water but could, for example, also be the degradation of a pollutant. From a research perspective, dyes are interesting model components in this regard because they offer the possibility to

monitor their degradation by simple spectroscopic methods. Mechanistically it is believed that the photo-catalytic degradation of a dye in an aqueous solution – and therefore the bleaching of the solution – occurs due to the oxidation of the dye by hydroxyl radicals [26-28]. Hydroxyl radical formation can thereby involve both photo-generated electrons in the conduction band and photo-generated holes in the valence band [26-28]. However, side reactions which lead to decolorisation but not necessarily to dye degradation, can also occur, which can somewhat obscure the results [29, 30]. Hence, one has to exercise caution when evaluating the photo-catalytic activity of a material using dyes as model components.

Here, photo-catalytic dye-degradation experiments were performed mainly to get further insight into the material and defect properties of the ZnO nanorod arrays. For this reason the exact mechanism that leads to the dye-degradation was not fully investigated. Nevertheless, minimization of possible intermediate reactions such as the formation of intermediates and sensitization was targeted – see Chapter 4 and Appendix 2 for further detail. By so doing, the photo-catalytic dye-degradation experiments provide an indirect, qualitative insight into the charge carrier life time of the photo-catalyst, because good photo-catalytic performance demands high charge carrier lifetimes [31].

A photograph of the spectroscopic setup used and its principle components for the evaluation of the photo-catalytic properties is shown in Figure 2-8 (left panel). The central piece is a cuvette holder fixed above a magnetic stirrer. On either side of the holder optical fibres can be mounted (including a lens). This axis forms the sample-beam axis, which means that the light generated by the light source (Ocean optics HL-2000) is transmitted through the left fibre and passed through the solution filled cuvette where it is then collected by the right fibre and subsequently by the spectrometer (Ocean optics QE65000). A holder for the high-power LED (equipped with an aspheric lens, LED wavelength either 365 nm or 455 nm but for the photo-catalytic tests presented in this thesis only the 365 nm was used) is located in front of the cuvette and thus resembles the excitation-axis. The intensity of the LED could be adjusted over the bias voltage and was measured using a UV radiometer (UVP – UVX digital radiometer) in the sample plane. During a measurement a hood was used to enclose the cuvette holder (see Figure 2-8 right panel) in order to avoid the collection of background light and to shield the user from stray/reflected light coming from the

high-power LED.

In a typical procedure, the UV-Vis light source and spectrometer were allowed to warm up for ca. 30 min before beginning the measurement. Furthermore, the dye solution was filled into a disposable UV-cuvette and a magnetic stir bar was added. The cuvette was then left in the holder for the warm-up period. Then the spectrometer was set to record a full spectrum (350 – 900 nm) of the dye (every 1 min) and to monitor the absorbance of the dye at its peak absorbance value (every 20 s). The measurement was then started with no sample in the cuvette and in the absence of any excitation. After 9 min the enclosure was lifted and after 10 min a sample was placed into the cuvette with the growth-side facing the high-power LED and the hood was placed back on the holder-arrangement again (note that any artificial changes, e.g. jumps, in the absorbance that may have been caused by lifting/lowering the hood and placing the sample into the cuvette were corrected at the end of each measurement). Subsequently the sample was left in the dark for 90 min, after which the UV irradiation was turned on for 90 min. This on/off cycle was then repeated with 1 h as the time interval. Finally the sample was kept in the dark for one hour followed by a short light on/off cycle (20 min each). The sample was then taken out of the solution and washed in a beaker filled with ethanol and subsequently in H_2O (18.2 MΩ) under constant stirring (30 min each).

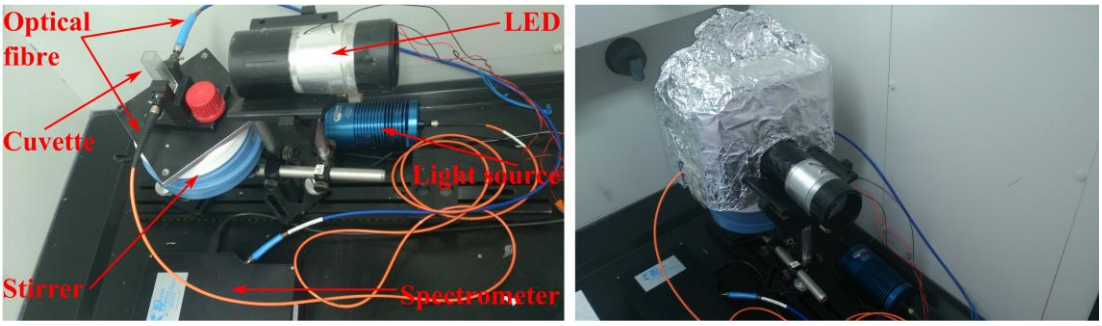

Figure 2-8: Photographs of the setup to measure the photo-catalytic performance of ZnO nanorod arrays. Left) Principle components of the setup. Right) enclosed setup as used during UV-illumination of the sample.

2.4 Growth of ZnO nanorod arrays and sample preparation

The following sections will outline the methods used for the deposition of ZnO-based nanorod arrays. Details regarding the exact precursor concentrations and growth parameters used (e.g. temperatures) are given in the individual results chapters. Hence,

the following sections discuss these methods from a more general point of view.

2.4.1 **ZnO Seed-layer deposition**

The growth of well-aligned nanorods is strongly influenced by the substrate and/or the seed-layer. If the crystal-lattice and orientation of the substrate matches the growth of aligned ZnO nanorods (i.e. growth along the c-axis with (002) plane parallel to the substrate), the arrays can be grown directly on the substrate without the deposition of a ZnO seed-layer. This is exemplified in Figure 2-9, where ZnO nanorods have been grown from solution on a gallium nitride wafer (GaN) without the deposition of a ZnO seed-layer. GaN also exhibits a wurtzite crystal structure and the lattice mismatch between the two materials is very low [32]. This leads to the deposition of well-aligned ZnO nanorods.

If other substrates, such as glass with or without a transparent conductive coating (e.g. fluorine-doped tin oxide, FTO), are used without a ZnO seed-layer coating, subsequent solution-growth will result in the growth of randomly aligned ZnO nanorods with mostly poor substrate coverage. Hence, the aforementioned substrates have been coated with a thin ZnO seed-layer to facilitate that growth and the alignment of ZnO nanorods.

However, prior to the ZnO seed-layer deposition the substrates were cleaned. This has been found to be crucial for a), achieving good seed-layer coverage and homogeneity and b), for achieving good adhesion of the seed-layer to the substrate. For glass substrates (standard microscope glass slides) a cleaning procedure, originally developed for silicon wafers and known as the 'RCA-standard clean1', was adapted [33, 34]. Oxidative breakdown of organic contaminations and heavy metal complexes is achieved in this cleaning procedure by immersing the substrates into a mixture of water (18.2 MΩ), ammonium hydroxide (NH_4OH) and hydrogen peroxide (H_2O_2) in a ratio of 5:1:1, respectively. While the method originally includes heating of the mixture to T = 75-85 °C, in this work the substrates were cleaned at room temperature under sonication conditions for 30 min or longer. Another common method to remove organic contaminations is to clean substrates in different solvents. In the work described in this thesis, this has been done with FTO coated glass substrates by a sequence consisting of sonication for 30 min each in water (18.2 MΩ) with decon 90,

acetone and isopropanol.

The main seed-layer growth method, which was used for the deposition of ZnO seed-layers onto cleaned substrates, is atomic layer deposition (ALD). Theoretically ALD allows for the deposition of highly conformal layers with precise thickness control onto substrates exhibiting rough or smooth surfaces. This level of control arises due to the self-limiting nature of the growth process, which is schematically depicted in Figure 2-10 [35]. In an ALD process a substrate is inserted into the growth chamber, which is subsequently evacuated. Afterwards, growth precursor A is pulsed into the chamber and reacts with the substrate. The following purge step introduces an inert gas (e.g. nitrogen) that removes any unreacted precursor and by-products from the reaction of the precursor and the substrate. Precursor B is then introduced into the chamber and reacts with the reacted precursor A, upon which the desired material is formed. A second purge step is then carried out to remove any unreacted precursor B and reaction by-products. This sequence is then repeated several times to achieve the desired thickness. If the process is operated within the ALD temperature window, the precursor reactions will theoretically lead to the deposition of a maximum of one monolayer in each precursor step, since no gas-phase reactions between the individual precursors elements (i.e. A or B) can occur [35].

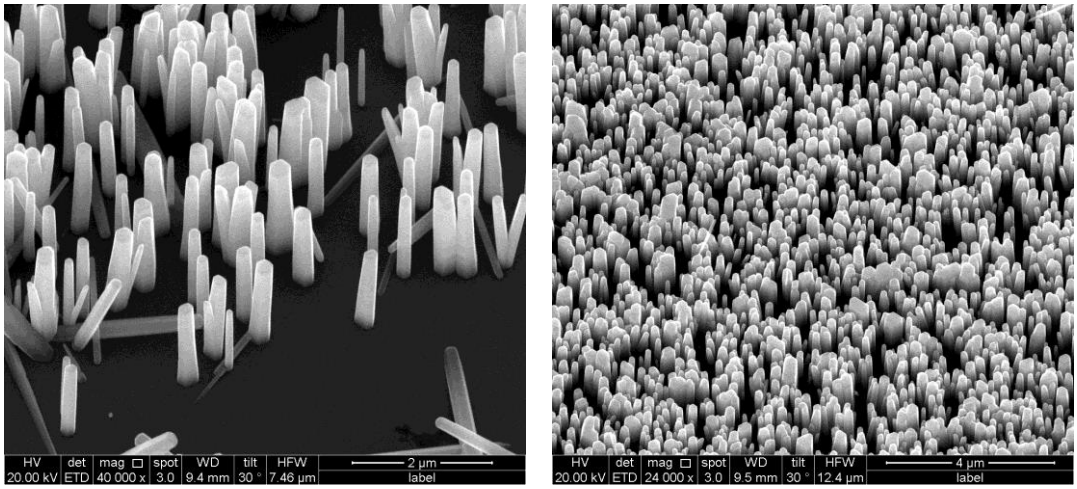

Figure 2-9: Tilt-view SEM micrographs of ZnO nanorods grown on GaN without a ZnO seed-layer. a) Tilt-view image of an area with lower ZnO nanorod coverage. b) Over-view image.

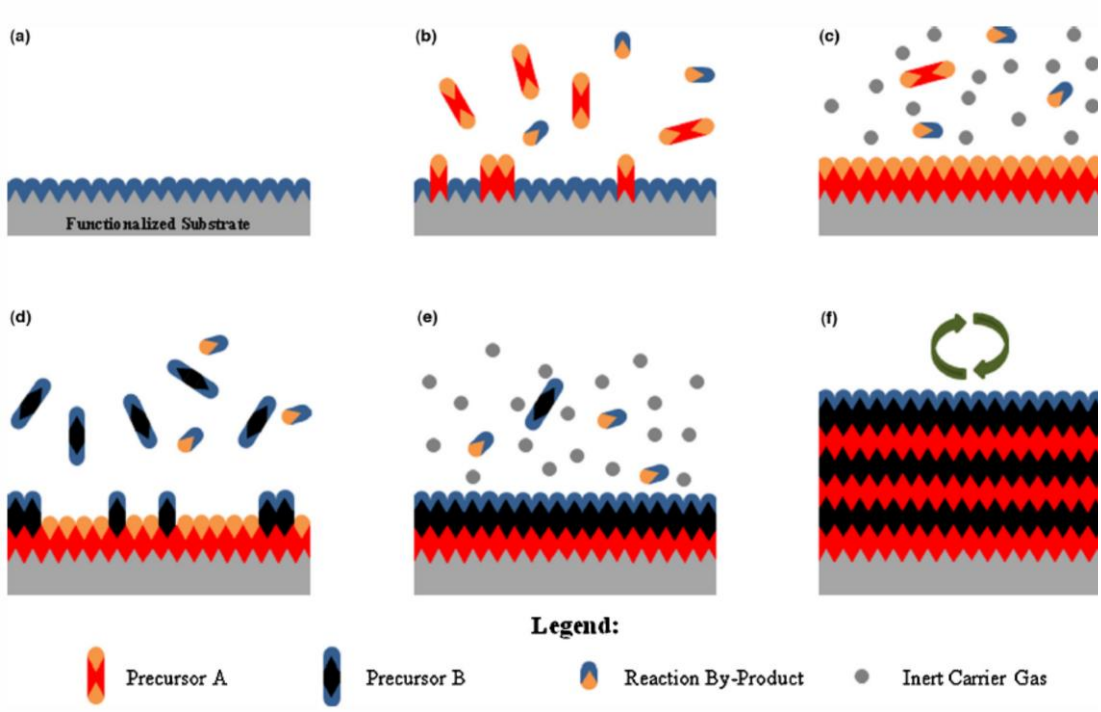

Figure 2-10: Schematic representation of an ALD process. (a) Substrate surface exhibits a natural functionalization or is treated to functionalize the surface. (b) Precursor A is pulsed into the chamber and reacts with the surface. (c) Excess precursor and reaction by-products are purged with inert carrier gas. (d) Precursor B is pulsed and reacts with the surface. (e) Excess precursor and reaction by-products are purged with inert carrier gas. (f) Steps b)–e) are repeated until the desired material thickness is achieved. Reprinted with permission from Ref. [35]. Copyright 2014, Elsevier.

For the ALD of ZnO, diethyl zinc (DEZ) and water are the most commonly used growth precursors [36]. These have also been used in the growth process for the deposition of ZnO seed-layers in this work. The growth parameters represented as the substrate temperature T_{sub}, precursor A pulse duration t_{DEZ}, precursor B pulse duration t_{H2O}, the purge duration t_{purge} and the growth rate are given in Table 2-1. Afterwards the samples were allowed to naturally cool down to room temperature in air. The seed-layers were subsequently subjected to an annealing treatment in air (e.g. 300 °C for 1 h). This was done to improve the crystallinity of the seed-layers and their adhesion to the substrate. Seed-layers can also be easily prepared using wet chemical methods. One way to achieve this is via the decomposition of zinc precursors at elevated temperatures [37, 38] – an approach which has also been adapted for the ZnO seed deposition for some of the layers reported in this work. The method relies on the

Table 2-1: ALD growth parameters for the deposition of ZnO seed-layer.

Growth parameter	Magnitude
T_{sub}	190 °C
t_{DEZ}	0.2 s
t_{H2O}	0.1 s
t_{purge}	10 s
Growth rate	0.175 nm/cycle

formation of nanoparticles of the zinc precursor (e.g. zinc acetate) in solution (e.g. in ethanol). This solution can then be applied to the substrate by e.g. drop-casting or spin-coating. The solvent is then evaporated off and the nanoparticle coated substrates are annealed in air at moderate temperatures [37, 38], leading to the decomposition of the zinc salt to form ZnO crystallites of nanometer size [37]. Details on the growth parameters used for the deposition of such seed-layer are given in Chapter 5 and 7.

2.4.2 **Hydrothermal growth of ZnO**

The term "hydrothermal growth" broadly describes techniques that utilize the growth of crystals from solutions in an enclosed system at temperatures higher than room temperature and at pressures higher than 1 bar [39]. For the synthesis of ZnO nanorods in this work, it is important to note that, in contrast to many other hydrothermal syntheses [39], the applied temperatures and resulting pressures used were very low. Despite the fact that the exact pressure in the used growth vessels was not determined, the pressures used were most likely only slightly above 1 bar, because the growth temperatures used during the nanorod growth were usually below 100 °C. While these criteria would still characterize the growth as "hydrothermal", the methods used could also be described as chemical bath synthesis or chemical bath deposition [40]. Generally, the hydrothermal method enables the dissolution of reactants and complex formation under the aid of the solvent and/or growth modifier, owing to the use of high temperature and pressure [39]. The dissolved reactants and/or complexes then form the growth units that subsequently contribute to the crystal growth. In the case of ZnO, for crystal growth from aqueous solution (without any growth modifier), an alkaline pH is generally chosen because divalent metals do not hydrolyze in acidic solutions

[41]. The hydrolysis of the Zn salt reactant is however needed for the formation of the growth units (here e.g. the tetrahedral hydroxide complexes – pH dependent), which under the influence of temperature (and pressure) dehydrate to form ZnO [41]. However, the dehydration and therefore the growth of ZnO will only occur if the solution reaches supersaturation, whereby the concentration of the alkaline mineralizer and the temperature dictate the solubility of ZnO as well as the growth rate of the ZnO crystals [42]. The growth of ZnO from alkaline solutions is often found to result in the formation of 1D geometries such as rods. This implies preferential growth along one axis, which in turn means a growth directed by one crystal plane – for ZnO the polar (0001) plane ((002) plane when expressed in terms of Miller indices). It was suggested that the formation of ZnO_2^{2-}, which increases with increasing solution pH, is responsible for the attachment to the alternating O^{2-} and Zn^{2+} surface atoms of the polar (002) plane, thus facilitating rapid growth along the c-axis [42].

The solubility of the Zn salts as well as the formation of the ZnO structures upon heating a solution are both influenced by the addition of growth modifiers. In this regard some ligands can act as complexing agents allowing a more controlled release of zinc into the solution when the temperature is increased [40]. Ever since the first controlled deposition of ZnO nanorod arrays onto different substrates reported by Vayssieres et al. [43], hexamethylenetetramine (HMTA, $(CH_2)_6N_4$) has been used extensively as complexing agent. A commonly used synthesis route thus employs an aqueous solution of a zinc precursor (often zinc nitrate hexahydrate) and HMTA [41, 44]. In this growth method, complexing of free Zn^{2+} in the solution is achieved due to the hydrolysis of HMTA to ammonia (forming $[Zn(NH_3)_4]^{2+}$) and formaldehyde. However, HMTA does not only complex the zinc ions but also serves the function of a pH buffer and an OH^- source which have a direct influence on the morphology [40, 41, 45]. In contrast to the aforementioned growth in alkaline solution, the deposition of ZnO using HMTA is often carried out at nearly neutral pH values. The supply of OH^- from the HMTA does nevertheless also lead to the formation of zinc hydroxide in this growth recipe (here $Zn(OH)_2$ is formed) [41, 44]. Initially, the precipitation of $Zn(OH)_2$ governs the growth of ZnO on the substrate [45]. However, with increasing growth time the solution pH increases and the Zn^{2+} concentration decreases, which renders the growth via the $Zn(OH)_2$ thermodynamically unfavourable and facilitates the direct deposition of ZnO [45]. This results in the following summarized growth

mechanism, equations (2.17) - (2.22) [41, 44, 45]:

$$(CH_2)_6N_4 + H_2O \leftrightarrow 4NH_3 + 6HCHO \quad (2.17)$$

$$NH_3 + H_2O \leftrightarrow NH_4^+ + OH^- \quad (2.18)$$

$$Zn^{2+} + 4NH_3 \leftrightarrow [Zn(NH_3)_4]^{2+} \quad (2.19)$$

ZnO growth over hydroxide formation:

$$Zn^{2+} + 2OH^- \leftrightarrow Zn(OH)_2 \quad (2.20)$$

$$Zn(OH)_2 \leftrightarrow ZnO + H_2O \quad (2.21)$$

Or via direct deposition:

$$Zn^{2+} + 2OH^- \leftrightarrow ZnO + H_2O \quad (2.22)$$

Furthermore, solution-based growth techniques, such as the hydrothermal method, can be used to intentionally introduce extrinsic impurities in a bottom-up approach. As mentioned in section 1.4.3, the doping of ZnO represents a facile way of influencing the optical and electric properties of ZnO. During the growth of ZnO structures from solution the incorporation of impurities is often aimed at substituting zinc in the lattice but can also occur due to the occupation of the dopant at an interstitial site, as for example in the case of Li^+ [42]. Generally, the occupation of the Zn site by a dopant is somewhat facilitated, and the crystal structure less distorted, if the ionic radius of the dopant is close to that of Zn^{2+}, which holds true for e.g. Co^{2+}, Ni^{2+} or Li^+ [42, 46]. However, dopants such as Fe^{3+} or Mn^{2+} also offer only a small difference in respect to the ionic radius of Zn^{2+} [47, 48], as opposed to impurities like Na^+ or K^+ [46]. Simply speaking, the introduction of a dopant salt to the growth solution may lead to the availability of dopant growth units in a similar way as described in the general ZnO growth process above. These are then competing with the Zn growth units for the cationic site in the crystal lattice. However, it is also possible that secondary phases are formed, since the growth parameters (precursor concertation, temperature, time etc.) may favour different oxidation states (e.g. Mn_2O_3) or the occurrence of mixed phases (e.g. $ZnCo_2O_4$) [47, 49].

For the (hydrothermal) growth of (cobalt-doped) ZnO nanostructures described in this work the following chemicals were purchased from Sigma Aldrich in reagent grade:

zinc acetate dihydrate (ZnAc), zinc nitrate hexahydrate (ZnN), hexamethylenetetramine (HMTA), cobalt acetate tetrahydrate (CoAc), sodium hydroxide (NaOH), hydrochloric acid (HCl), mono ethanolamine (MEA). Millipore water (18.2 MΩ) was used as the solvent during the synthesis. While the exact growth parameters are given in the experimental sections of the results chapters (3 to 7), it is worth pointing out that the nanorod synthesis was carried out in different vessels (plastic bottles and a simple acid digestion vessel/autoclave). These are shown in Figure 2-11. Note that the autoclave consists of multiple parts: a stainless steel shell with an inner PTFE beaker, a stainless steel/PTFE lid and a stainless steel crew cap with a tightening screw. The oven (either a Binder – Avantgarde Line BD for $T \leq 100$ °C or a MTI – Vacuum oven DZF-6002 for $T \geq 100$ °C) was heated to the desired temperature before the growth was carried out. For the synthesis using an autoclave, the autoclave was also heated prior to introducing in the growth solution. Furthermore some growths were carried out using a water bath as heating source. In these cases plastic bottles were used and these were held in the hot water (not touching the bottom of the water bath) using a clamp mounted to a rod-stand. After the growth, the growth vessels were cleaned by filling them with acid (either HCl or HNO_3; 4 - 24 h) and rinsing them thoroughly with deionized water.

Figure 2-11: Left) growth vessels (autoclave parts and plastic bottle) in a Binder laboratory oven. Right) Close-up photograph of the growth vessels.

2.4.3 **Atomic layer deposition of TiO_2 over-layers**

Some ZnO nanorods were coated with thin titanium dioxide (TiO_2) over-layers (also see Chapter 7). ALD was chosen as a deposition method, primarily because of the advantages it offers in regards to conformity and thickness control (as described in section 2.4.1). Prior to the TiO_2 deposition, the as-grown ZnO nanorod arrays were

thoroughly rinsed in Millipore water (18.2 MΩ), blow dried in a stream of nitrogen and treated in an oxygen plasma (Harrick Plasma – Plasma cleaner PDC-002, 5 min), in order to remove organic contamination. The ZnO nanorod arrays were then loaded into the Cambridge NanoTech Fiji F200LLC ALD system equipped with tetrakis (dimethylamino)titanium (TDMAT) and water as the precursors. For the growth of nominally 2 nm, 5 nm and 10 nm TiO_2 over-layers, the growth parameters listed in Table 2-2 were applied. Afterwards the samples were allowed to cool down naturally to room temperature in air.

Table 2-2: ALD growth parameters for the deposition of TiO_2 over-layers.

Growth parameter	**Magnitude**
T_{sub}	185 °C
T_{TDMAT}	0.3 s
t_{H2O}	0.1 s
t_{purge}	10 s
Growth rate	0.02 nm/cycle

2.4.4 **General sample preparation and rapid thermal annealing (RTA)**

After the ZnO/ZnO:Co nanorod growth the samples were rinsed in Millpore water (18.2 MΩ) and blow dried in nitrogen. Any growth on the backside of the substrates was removed by rubbing with an HCl-soaked (ca. 5 %wt) cotton swab onto the material. Subsequently the samples – which were grown on microscope glass (ca. 2.5 cm x 3 to 7 cm) or FTO coated glass (ca. 1.5 cm x 5 cm) – were processed to meet the sample requirements for the characterization methods. Samples grown on glass slides were thus cut into smaller pieces of usually ca. 2.5 cm x 2.5 cm (e.g. UV-Vis, XRD), ca. 0.8 cm x 2.5 (e.g PL, photo-catalytic performance, Raman) or ca. 1 cm x 1 cm (XPS). For the photo-electrochemical characterization the samples were cut to ca. 1.5 cm x 2.5 cm. Furthermore a small area on the growth-side of the sample was etched back (HCl, ca. 5 %wt) in order to gain access to the electrical contact (FTO). Subsequently a wire was attached to the FTO using RS Pro silver conductive adhesive paint. Some samples were then subjected to a low temperature anneal (1 h at 120 °C + at least 3 h cool down to room-temperature), which improves the durability and conductivity of the contact. If the photo-electrochemical properties were assessed for

an as-grown sample, the paint was allowed to harden at room-temperature for 24 h. Note that this was found to have only a minor effect on the conductivity. Furthermore, some samples were tested for their photo-electrochemical performance before and after an annealing treatment (see Chapter 6 – annealing in air for 3 h at 400 °C + slow cool down in a Thermoscientific – Thermolyne FB1410M-33 furnace; note that the photo-electrochemical measurements were done on different spots). For theses samples the wire was peeled off the sample and the silver conductive adhesive paint was removed by carefully dipping the contact area into acetone, followed by thoroughly rinsing the sample in DI water and blow drying in nitrogen before the annealing treatment.

Additionally, some samples were annealed in air in a laboratory furnace (e.g. see Chapter 6) or under more controlled atmospheres during rapid thermal annealing (RTA). RTA was used extensively in this work (see Chapter 3 and 4) and the processes used are therefore described in more detail in the following section. The profile of the set temperature of a typical RTA process is shown in Figure 2-12. At the beginning of the process the temperature was set to 20 °C (until 130 s). Within this period a vacuum/purge cycle (each 20 s) was implemented to reduce possible contamination, which may result from residues in the RTA chamber. The last step in this first sequence of the example process was a longer vacuum step (50 s). If another atmosphere was used, the gas was introduced into the chamber during this step, with the flowrate adjusted to result in 1 bar of pressure at the end of the 50 s period. After this initial preparation sequence the samples were subjected to a first heating step to 200 °C (rate: 9 °C/s), followed by a stabilization stage at this temperature (15 s). The subsequent temperature ramp was then adjusted to have a comparable heating rate (10 °C/s) in respect to the first heating step (note that from the first stabilization stage the temperature control was switched from the thermocouples to pyrometer). After 20 seconds another stabilization stage was introduced (15 s, 350 °C). The last temperature ramp in the shown example process consists of two parts. At first the temperature was set to reach 420 °C with a rate of 4.7 °C/s followed by a slower ramp up (1.5 C°/s) to the final temperature of 450 °C, which was then held for 10 min (“RTA temperature”). Slower heating rates – especially for the last 30 °C – resulted in a lower temperature overshoot. When cooling down, the profile was also adjusted with different cooling rates. However, the actual cooling was found to be physically limited rather than by

the rates. Thus the length of the entire cooling stage (after the 10 min at 450 °C until the end of process) was adjusted for each process to reach a temperature < 250 °C at the end of the process. This was done to avoid any influence that the automatic introduction of the cooling gas (nitrogen) after the end of the process may have on the samples. Note that during the entire heating and cooling sequence (from 130 s until the end of the process) the respective gas was introduced at a low flowrate or the chamber was held under vacuum.

The main RTA temperatures used in this thesis are 350, 450 and 550 °C. For annealing at 350 °C the heating profile was similar to the process shown in Figure 2-12 but without the last heating ramp (i.e. step ramp with 4.7 °C/s and 1.5 °C/s). If 550 °C was set as the RTA temperature, the 4.7 °C/s heating rate was maintained until 520 °C/s followed by the slower 1.5 °C/s ramp up to 550 °C.

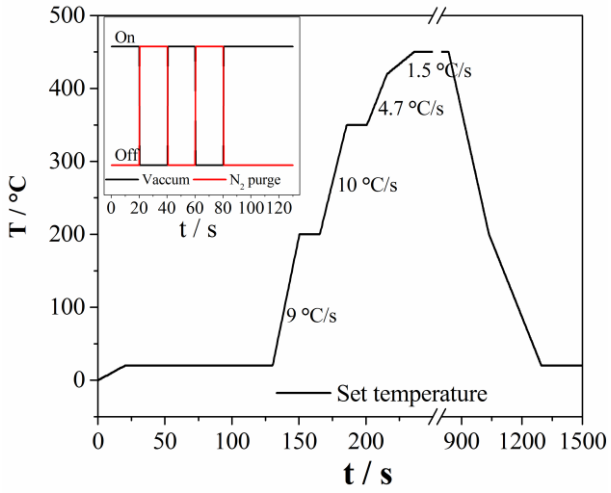

Figure 2-12: Typical temperature profile during a RTA treatment. The temperature rates of each heating step are given in the figure. The inset shows the vacuum/purge cycle of the first 110 s. Note that the introduction of annealing gases (i.e. argon, nitrogen, oxygen, forming gas) was done instead of the last vacuum segment (i.e. t > 80 s).

2.5 References

[1] D. C. Harris, *Quantitative Chemical Analysis*, 2 ed. W. H. Freeman, 1987.
[2] J. I. Pankove, *Optical Processes in Semiconductors*. Dover, 1971.
[3] J. Tauc, "Optical properties and electronic structure of amorphous Ge and Si," *Materials Research Bulletin*, vol. 3, no. 1, pp. 37-46, 1968.
[4] J. Tauc, R. Grigorovici, and A. Vancu, "Optical Properties and Electronic Structure of Amorphous Germanium," *physica status solidi (b)*, vol. 15, no. 2, pp. 627-637, 1966.

[5] S. Kasap and P. Capper, *Springer Handbook of Electronic and Photonic Materials*. Springer, 2007.
[6] S. Zaynobidinov, R. G. Ikramov, and R. M. Jalalov, "Urbach energy and the tails of the density of states in amorphous semiconductors," *Journal of Applied Spectroscopy*, journal article vol. 78, no. 2, pp. 223-227, 2011.
[7] H. Föll. (02.05). *5.1.2 Recombination and Luminescence*. Available: https://www.tf.uni-kiel.de/matwis/amat/semi_en/kap_5/backbone/r5_1_2.html
[8] Y. Leng, *Materials Characterization: Introduction to Microscopic and Spectroscopic Methods*. John Wiley & Sons (Asia) Pte Ltd, 2008.
[9] C. F. Windisch, G. J. Exarhos, C. Yao, and L.-Q. Wang, "Raman study of the influence of hydrogen on defects in ZnO," *Journal of Applied Physics*, vol. 101, no. 12, p. 123711, 2007.
[10] P. J. Goodhew, J. Humphreys, and R. Beanland, *Electron Microscopy and Analysis, Third Edition*. Taylor & Francis, 2000.
[11] B. Fahlman, *Materials Chemistry*. Springer Netherlands, 2007.
[12] A. Materials. (2015, 01.05.). *Using SEM/EDS for the Quantitative Analysis of Light Elements*. Available: https://www.azom.com/article.aspx?ArticleID=11975
[13] P. Goodhew, "General Introduction to Transmission Electron Microscopy (TEM)," in *Aberration-Corrected Analytical Transmission Electron Microscopy*, R. Brydson, Ed.: John Wiley & Sons, 2011.
[14] P. Atkins and L. Jones, *Chemical Principles: The Quest for Insight*, 2nd ed. W. H. Freeman, 2002.
[15] A. L. Patterson, "The Scherrer Formula for X-Ray Particle Size Determination," *Physical Review*, vol. 56, no. 10, pp. 978-982, 11/15/ 1939.
[16] K. Siegbahn, "X-Ray Photoelectron Spectroscopy and Auger Electron Spectroscopy: Introduction," in *Encyclopedia of Analytical Chemistry*: John Wiley & Sons, 2006.
[17] P. van der Heide, "Introduction," in *X-Ray Photoelectron Spectroscopy*: John Wiley & Sons, 2011.
[18] P. van der Heide, "XPS Instrumentation," in *X-Ray Photoelectron Spectroscopy*: John Wiley & Sons, 2011.
[19] T. s. XPS. (2013, 03.05). *Cobalt*. Available: https://xpssimplified.com/elements/cobalt.php#appnotes
[20] A. J. Bard and L. R. Faulkner, *Electrochemical Methods: Fundamentals and Applications*, 2nd ed. John Wiley & Sons, 2000.
[21] J. Yang *et al.*, "A multifunctional biphasic water splitting catalyst tailored for integration with high-performance semiconductor photoanodes," *Nat Mater*, vol. 16, pp. 335–341, 2017.
[22] L. Bertoluzzi, L. Badia-Bou, F. Fabregat-Santiago, S. Gimenez, and J. Bisquert, "Interpretation of Cyclic Voltammetry Measurements of Thin Semiconductor Films for Solar Fuel Applications," *J Phys Chem Lett*, vol. 4, no. 8, pp. 1334-9, 2013.
[23] F. Scholz, *Electroanalytical Methods: Guide to Experiments and Applications*. Springer Berlin Heidelberg, 2010.
[24] K. Rajeshwar, "Fundamentals of Semiconductor Electrochemistry and Photoelectrochemisty," in *Encyclopedia of Electrochemistry, Volume 6,*

Semiconductor Electrodes and Photoelectrochemistry, M. S. Allen J. Bard, Stuart Licht, Ed.: Wiley, 2002, p. 608.

[25] R. Krol, "Principles of Photoelectrochemical Cells," in *Photoelectrochemical Hydrogen Production*(Electronic Materials: Science & Technology: Springer, 2012, pp. 13-67.

[26] A. Mills and C. O'Rourke, "Adsorption and Destruction of Methylene Blue by Semiconductor Photocatalysis," *Green,* vol. 1, no. 1, pp. 105–113, 2011.

[27] F. Kayaci, S. Vempati, C. Ozgit-Akgun, I. Donmez, N. Biyikli, and T. Uyar, "Selective isolation of the electron or hole in photocatalysis: ZnO-TiO2 and TiO2-ZnO core-shell structured heterojunction nanofibers via electrospinning and atomic layer deposition," *Nanoscale,* vol. 6, no. 11, pp. 5735-45, 2014.

[28] I. Izumi, W. W. Dunn, K. O. Wilbourn, F.-R. F. Fan, and A. J. Bard, "Heterogeneous photocatalytic oxidation of hydrocarbons on platinized titanium dioxide powders," *The Journal of Physical Chemistry,* vol. 84, no. 24, pp. 3207-3210, 1980.

[29] A. Mills and J. Wang, "Photobleaching of methylene blue sensitised by TiO2: an ambiguous system?," *Journal of Photochemistry and Photobiology A: Chemistry,* vol. 127, no. 1–3, pp. 123-134, 1999.

[30] S. Bae, S. Kim, S. Lee, and W. Choi, "Dye decolorization test for the activity assessment of visible light photocatalysts: Realities and limitations," *Catalysis Today,* vol. 224, pp. 21-28, 2014.

[31] C.-A.-U. z. Kiel, "Advanced Lab Course - Photocatalysis " 2015.

[32] H. Q. Le *et al.*, "Growth of single crystal ZnO nanorods on GaN using an aqueous solution method," *Applied Physics Letters,* vol. 87, no. 10, p. 101908, 2005.

[33] W. Kern, "The Evolution of Silicon Wafer Cleaning Technology," *Journal of The Electrochemical Society,* vol. 137, no. 6, pp. 1887-1892, 1990.

[34] W. Kern and D. Puotinen, "Cleaning solutions based on hydrogen peroxide for use in silicon semiconductor technology," *RCA Rev.* , vol. 31, pp. 187-206, 1970.

[35] R. W. Johnson, A. Hultqvist, and S. F. Bent, "A brief review of atomic layer deposition: from fundamentals to applications," *Materials Today,* vol. 17, no. 5, pp. 236-246, 2014.

[36] T. Tynell and M. Karppinen, "Atomic layer deposition of ZnO: a review," *Semiconductor Science and Technology,* vol. 29, no. 4, p. 043001, 2014.

[37] L. E. Greene *et al.*, "General Route to Vertical ZnO Nanowire Arrays Using Textured ZnO Seeds," *Nano Letters,* vol. 5, no. 7, pp. 1231-1236, 2005.

[38] L. Cai *et al.*, "V ions implanted ZnO nanorod arrays for photoelectrochemical water splitting under visible light," *International Journal of Hydrogen Energy,* vol. 40, no. 3, pp. 1394-1401, 2015.

[39] K. Byrappa, N. Keerthiraj, and S. M. Byrappa, "Hydrothermal Growth of Crystals—Design and Processing," pp. 535-575, 2015.

[40] K. Govender, D. S. Boyle, P. B. Kenway, and P. O'Brien, "Understanding the factors that govern the deposition and morphology of thin films of ZnO from aqueous solution," *Journal of Materials Chemistry,* vol. 14, no. 16, p. 2575, 2004.

[41] S. Xu and Z. L. Wang, "One-dimensional ZnO nanostructures: Solution growth and functional properties," *Nano Research,* vol. 4, no. 11, pp. 1013-1098, 2011.

[42] L. N. Demianets, D. V. Kostomarov, I. P. Kuz'mina, and S. V. Pushko, "Mechanism of growth of ZnO single crystals from hydrothermal alkali solutions," *Crystallography Reports,* journal article vol. 47, no. 1, pp. S86-S98, 2002.

[43] L. Vayssieres, K. Keis, S.-E. Lindquist, and A. Hagfeldt, "Purpose-Built Anisotropic Metal Oxide Material: 3D Highly Oriented Microrod Array of ZnO," *The Journal of Physical Chemistry B,* vol. 105, no. 17, pp. 3350-3352, 2001.

[44] S. Baruah and J. Dutta, "Hydrothermal growth of ZnO nanostructures," *Science and Technology of Advanced Materials,* vol. 10, no. 1, p. 013001, 2009.

[45] M. N. R. Ashfold, R. P. Doherty, N. G. Ndifor-Angwafor, D. J. Riley, and Y. Sun, "The kinetics of the hydrothermal growth of ZnO nanostructures," *Thin Solid Films,* vol. 515, no. 24, pp. 8679-8683, 2007.

[46] W. C. Lee, G. E. Canciani, B. O. S. Alwhshe, and Q. Chen, "Enhanced photoelectrochemical water oxidation by ZnxMyO (M = Ni, Co, K, Na) nanorod arrays," *International Journal of Hydrogen Energy,* vol. 41, no. 1, pp. 123–131, 2015.

[47] S. Basu *et al.*, "Local Structure Investigation of Cobalt and Manganese Doped ZnO Nanocrystals and Its Correlation with Magnetic Properties," *The Journal of Physical Chemistry C,* vol. 118, no. 17, pp. 9154-9164, 2014.

[48] A. Hui, J. Ma, J. Liu, Y. Bao, and J. Zhang, "Morphological evolution of Fe doped sea urchin-shaped ZnO nanoparticles with enhanced photocatalytic activity," *Journal of Alloys and Compounds,* vol. 696, pp. 639-647, 2017.

[49] S. V. Bhat and F. L. Deepak, "Tuning the bandgap of ZnO by substitution with Mn2+, Co2+ and Ni2+," *Solid State Communications,* vol. 135, no. 6, pp. 345-347, 2005.

Chapter 3

This chapter and accompanying appendix represent an adapted version of the publication:

> J. Kegel, F. Laffir, I. M. Povey, and M. E. Pemble, "Defect-promoted photo-electrochemical performance enhancement of orange-luminescent ZnO nanorod-arrays,"*Physical Chemistry Chemical Physics*, vol. 19, pp. 12255-12268, 2017.

Changes to the publication were only made in regards to formatting requirements.

3 Defect-promoted photo-electrochemical performance enhancement of orange-luminescent ZnO nanorod-arrays

3.1 Abstract

Intentionally defect-rich zinc oxide (ZnO) nanorod-arrays were grown from solution by carefully adjusting the concentration ratio of the growth-precursors used followed by various post-deposition thermal treatments. Post-deposition rapid thermal annealing (RTA) at moderate temperatures (350 °C - 550 °C) and in various atmospheres was applied to vary the defect composition of the grown nanorod-arrays. It is demonstrated that, intense, defect-related orange emission occurs solely upon RTA around 450 °C and is essentially independent of the atmosphere used. Extensive materials characterization was carried out in order to evaluate the origin of the orange-luminescent defects and what influence they have on the ZnO material properties. It is concluded that the oxygen vacancy-zinc interstitial defect complex (V_O-Zn_i) is responsible for the orange luminescence in the prepared materials. A kinetic formation mechanism of the V_O-Zn_i complex dependent on the RTA temperature is proposed and shown to be in accordance with the experimental findings. Furthermore it is shown that this bulk deep-level defect could act as a trap state for photo-generated electrons prolonging the charge carrier lifetime of photo-generated holes and therefore improving the charge carrier separation in the material. As a result the photo-current density under simulated sunlight is found to increase by almost 150 % over as-grown samples. The potential use of this defective material in applications such as solar water splitting is outlined.

3.2 Introduction

In recent years ZnO nanostructures have attracted a great deal of attention.[1] This interest is based on the optical properties of the material such as the large band gap (3.3 eV) and high exciton binding energy of 60 meV. ZnO can be deposited using various techniques.[2] Particularly the hydrothermal growth of various Zinc Oxide (ZnO) micro- and nanostructures has seen enormous research interest since the first successful controlled synthesis on substrates by Vayssieres *et al*.,[3] due to its low-cost, low-temperature and environmentally friendly nature.[4] Hence, nanostructured ZnO grown via such methods are highly promising materials for potential use in gas-

sensing,[5-7] opto-electronics,[2] piezoelectric nanogenerators,[8] photovoltaics and photo-chemical applications such as solar water splitting and photo-catalysis.[9-16]

ZnO exhibits an unintentional, 'natural' n-type character although the precise source of this character is still under debate.[17] Formerly it was believed that oxygen vacancies, V_O, are the source of n-type doping in ZnO but later studies revealed that V_O is a donor-type defect deep in the forbidden gap and thus unlikely to be ionized at room-temperature.[18] On the other hand zinc interstitials form shallow donors which – if close enough to the conduction band minimum (CBM) – can easily be ionized at room-temperature, making these possible sources of n-type doping. The formation energy of Zn_i in n-type ZnO is high (> 6 eV) and therefore it is unlikely for the defect to be present in high concentrations under normal growth conditions.[18] Nevertheless a recent study by Ranjith *et al.* showed that the defect composition of ZnO grown from solution of zinc nitrate hexahydrate ($Zn(NO_3)_2 \cdot 6H_2O$, ZNH) and hexamethyltetramine ($C_6H_{12}N_4$, HMTA) can be changed by changing the ZNH to HMTA ratio.[19] A higher HMTA concentration was found to increase the defect concentration with energetic positions below the (CBM), which the authors attribute to an increased density of Zn_i.

Interestingly both, V_O and Zn_i, were shown to be beneficial for the photo-catalytic decomposition of dyes because they are believed to act as charge carrier traps prolonging the lifetime of either a photo-generated hole or electron.[13, 14, 20-23] This mechanism then improves charge carrier separation and leads to an increased ability to facilitate photo-chemical reactions such as photo-catalytic dye-degradation and solar water splitting.

Another defect observed in ZnO nanostructures grown from aqueous solution gives rise to orange emission centered at around 600 nm.[24-27] This emission is not as commonly reported as the green emission and the origin of this defect emission is still under debate. Interstitial oxygen O_i, doubly ionized oxygen vacancies V_O^{++} and the V_O-Zn_i defect complex are all named as the possible source of orange-luminescent defects in ZnO.[7, 24-35]

In this study we have systematically investigated the influence of the orange-luminescent defect center on the material properties of ZnO nanorod-arrays grown via a solution based method. Rapid thermal annealing at various temperatures and in various atmospheres is used to alternate the defect composition of the as-grown ZnO

nanorods. It is shown that precise temperature control during RTA is necessary to induce these defects whereby the annealing atmosphere has little or no influence on the orange emission. Furthermore it is revealed that ZnO nanorods with a high density of orange-luminescent defects show remarkable photo-electrochemical performance when compared with as-grown and nanorod-arrays annealed at different temperatures. In this regard the defects are believed to act in two ways: bulk donor defects and electron-traps. The latter prolongs the recombination of holes in the valance-band and thus increases the likelihood of photo-chemical reactions. Our experimental study suggests that the V_O-Zn_i defect complex is the source of the orange-luminescent defects in ZnO. A possible temperature-dependent formation mechanism during RTA is presented. The presented results are shown to be in good agreement with earlier theoretical calculations on the V_O-Zn_i defect complex.[36-38]

3.3 Experimental

ZnO nanostructures were synthesized via a solution-based method on ZnO seed layers deposited by atomic layer deposition (ALD). The substrates (microscope glass slides (25 x 75 mm) and fluorine doped tin oxide on glass (FTO)) were sonicated for 1 h in a mixture of Millipore water (H_2O), ammonium hydroxide (NH_4OH) and hydrogen peroxide (H_2O_2) in a ratio of H_2O:NH_4OH:H_2O_2 = 5:1:1 prior to the ALD seed layer growth.

Seed layer preparation by ALD: ALD seed layers were deposited from diethylzinc and water using a Cambridge NanoTech Fiji F200LLC System. A constant substrate temperature of 190 °C was maintained during the growth (400 cycles). After the deposition, the substrates were allowed to cool down naturally in air. The thickness of the prepared ALD seed layers was ca. 70 nm. This comparably thick layer-thickness was chosen to prevent possible impurity migration from the substrate into the hydrothermally grown ZnO nanostructures. After the growth, the ALD seed layers were annealed in air for 1 h at 300 °C.

Solution growth of ZnO nanorod-arrays: ZnO nanorods were grown using a solution of zinc nitrate hexahydrate ($Zn(NO_3)_2{\cdot}6H_2O$, (ZNH)), hexamethylenetetramine ($C_6H_{12}N_4$, (HMTA)) and drops of hydrochloric acid (HCl, 5 %wt) dissolved in Millipore water. All chemicals were purchased from Sigma

Aldrich (reagent grade). As noted previously, in a recent study by Ranjith et al. it was shown that the defect concentration can be successfully alternated by changing the HMTA to ZNH ratio.[19] The authors found that a higher HMTA to ZNH ratio results in a higher intrinsic defect density – especially of Zn_i. We adapted this approach for our study where in a typical procedure 100 ml of solution was prepared by dissolving 0.025 M ZNH and 0.15 M HMTA and 4 drops of 5 %wt HCl in Millipore water. The solution was then constantly stirred for 1 h and transferred into sealable plastic bottle. Substrates were put in almost vertically with the growth side pointing downwards. The sealed bottle was then left in a normal lab oven at 95 °C for 6 h. Afterwards the solution was allowed to cool down naturally and the samples obtained were thoroughly rinsed with Millipore water and blow dried with nitrogen. The backside of the samples was carefully cleaned to remove any possible growth.

Rapid Thermal Annealing (RTA) of ZnO nanorod-arrays: ZnO nanorods were annealed at various temperatures (350 °C, 420 °C/450 °C, 550 °C) and in various atmospheres (Forming gas (forming gas), Nitrogen (N_2), Argon (Ar), Oxygen (O_2) all at 1 bar and Vacuum (VAC)) using a Jipelec 150 RTA system. Gasses were introduced before temperature ramp-up and the samples were annealed for 10 min at the constant temperature.

Characterization: UV-Vis diffuse-spectroscopy was conducted using a Perkin Elmer 950 equipped with an integrated sphere in the range 300 – 800 nm. Photo-luminescence spectra were recorded using a Cary Eclipse spectrophotometer. For emission spectra the ZnO nanorods grown on glass substrates were excited at a wavelength of 345 nm and spectra were recorded from 370 – 850 nm (1 nm resolution) at room temperature. For room temperature excitation spectra samples were excited from 345 – 500 nm and the emission wavelength was fixed at 600 nm. Some samples showing orange emission were subject to low-temperature PL (LT-PL) analysis at 11.5 K. A He-Cd laser (325 nm) was used to excite the samples. A Panalytic X`Pert X-Ray diffractometer (Cu Kα radiation $\lambda = 0.1541874$ nm) was used to record X-ray diffraction (XRD) spectra. First a survey scan ($2\theta = 20 – 70$ °) was run followed by a detailed scan in the range of 30 – 40 ° (interval $\Delta 2\theta = 0.003°$). For calculation of lattice constants and strain the raw peak data was analyzed. XPS measurements were performed at University of Limerick using a Kratos Axis ULTRA spectrometer equipped with a monochromatic Al Kα radiation of energy 1486.6eV. C 1s peak at

284.8eV was used as the charge reference in determining the binding energies. Before XPS characterization the samples were subjected to 300 s of argon sputtering using an Argon Gas cluster source at 10keV and Ar1000+ clusters in order to remove surface contamination. It is important to note that this treatment also leads to the removal of the uppermost ZnO material (ca. 7 nm, based on a removal rate of 1 nm/30s for SiO_2 under the mentioned conditions; assuming surface contamination removal within the first 100 s) and for this reason the XPS measurements are believed to provide some insight into the bulk composition of the samples, rather than just the surface composition. Electrochemical and photo-electrochemical characterization was carried out in a 3-electrode configuration using a PalmSens3 potentiostat. A Saturated Calomel Electrode (+ 244 mV vs. Standard Hydrogen Electrode, SHE) and a Platinum wire were used as the reference and counter electrode, respectively. ZnO nanorods grown on FTO coated glass were used as the working electrode. A wire was attached to the FTO substrate using silver conductive paste. Samples were then incorporated into a home-made PTFE photo-chemical cell leaving 1 cm^2 area exposed to the electrolyte. For Linear Sweep Voltammetry (LSV) the samples were measured in a potential window of -1 V - +1.7 V vs. SCE (potential step = 10 mV, scan speed = 25 mV/s) in 1M phosphate buffer solution of pH = 7. The same electrolyte solution was used for Electrochemical Impedance Spectroscopy (EIS). EIS measurements were done at a fixed frequency of 5 kHz while changing the potential from -0.5 V to 1.6 V vs. RHE. LSV and EIS analysis were carried out in the dark and under simulated sunlight (LSV only; 100 mW/cm^2 @ AM 1.5; LOT solar simulator class ACA). The reported current-densities *j* are in respect to the illuminated area (1 cm^2) and not the real surface area of the nanorod-arrays.

3.4 Results and discussion

Material properties of as-grown samples

Prior to RTA the material properties of as-grown ZnO nanostructures were examined. Figure 3-1 shows the XRD spectrum and a SEM micrograph of a representative sample. In the range of $2\theta = 30° - 38°$ the spectrum has three distinct peaks at 31.7°, 34.4° and 36.2° with the peak centered at 34.4° being the most intense. The three peaks can be assigned to the (100), (002) and (101) planes, respectively. Peak positions agree

well with the JCPDS No 79-2205 reference commonly used for hydrothermally grown ZnO.[4] A slight peak shift towards lower angles can be seen for all peaks.

The very intense (002) peak indicates the growth of well-aligned nanorods along the c-axis which is also supported by the SEM image in Figure 3-1. Average rod length, rod diameter and rod density for the as-grown samples are estimated to be 1.5 µm, 230 nm and $7.8 \cdot 10^8$ cm^{-2}, respectively (ca. 10 cm^2 surface-area on 1 cm^2 substrate). Furthermore the XRD spectrum of Figure 3-1 was taken to estimate the crystallite size d of the as-grown nanorods using the well-known Scherrer equation:

$$d = \frac{k\lambda}{\beta cos(\theta)} \tag{3.1}$$

where k is the shape constant (here k taken as 0.86 (= 0.9 for unknown shape – 0.04 instrument correction) and λ, β and cos(θ) are the X-ray wavelength (λ = 0.1541874 nm), the full width at half maximum (FWHM) and the Bragg angle, respectively. For the as-grown samples the crystallite size was found to be 42 nm. In addition, the lattice constants a and c were calculated using the Miller indices (hkl) for a hexagonal crystal geometry:

$$\left(\frac{1}{d_{hkl}}\right)^2 = \frac{4}{3} + \left(\frac{h^2 + k^2 + hk}{a^2}\right)^2 + \frac{l^2}{c^2} \tag{3.2}$$

The results are summarized in Figure 3-1. It is worth noting that both lattice constants are larger than the ones given by the JCPDS reference. As a rough estimate for the strain ε in the material the difference between the lattice parameters for the as-grown sample and the JCPDS reference can be taken. For strain along a:

$$\varepsilon_a = \frac{a - a_0}{a_0} \cdot 100 \tag{3.3}$$

and along c

$$\varepsilon_c = \frac{c - c_0}{c_0} \cdot 100 \tag{3.4}$$

where a and c are the lattice constants calculated from equation (3.1) and a_0 and c_0 are the lattice constants from the JCPDS reference No 79-2205. From these calculations it can be seen that the material exhibits positive strain after growth in both the ‘a’ and ‘c’ directions. Positive strain is an indicator for tensile strain in the material which can

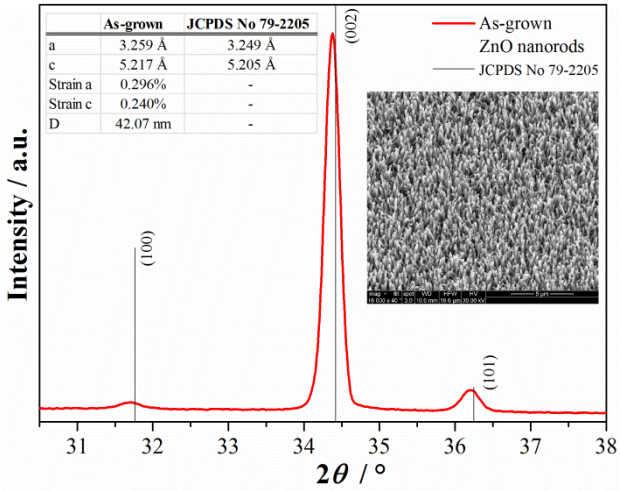

Figure 3-1 XRD spectrum of as-grown ZnO nanorods in the range of 2θ =30 - 38°. Tensile strain can be noticed for as-grown samples compared to the JCPDS reference. Inset: SEM micrograph of as-grown ZnO nanorods (tilt 40°).

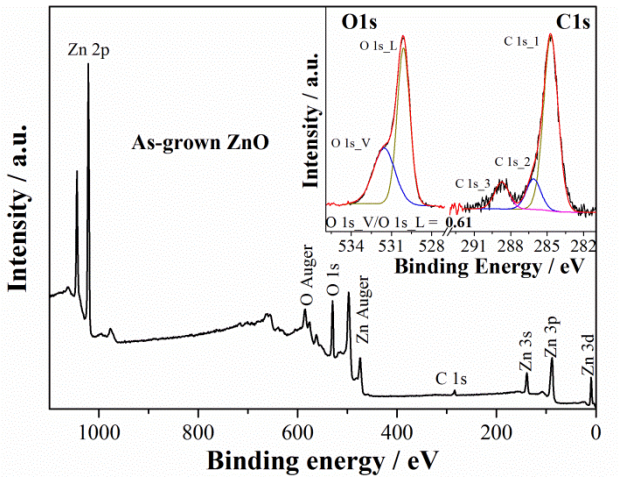

Figure 3-2 XPS survey scan of as-grown ZnO nanorod-arrays. Inset: High resolution scans of the O1s and C1s peak.

be caused by a high number of crystal imperfections and intrinsic defects. The as-grown samples are therefore believed to exhibit a large number defects, which can be related to the high HMTA:ZNH ratio employed.[19]

In order to gain some insight in the chemical configuration of the as-grown material XPS measurements were performed. The XPS survey scan is shown in Figure 3-2 together with the high resolution scans of the O1s and C1s peaks. Zinc, oxygen and carbon were the only elements detected in the sample after sputtering the surface with argon ions for 300 s. The asymmetric O1s peak could be fitted with two peaks centered at 530.2 eV and 531.6 eV (named O1s_L and O1s_V respectively). Additionally a

relatively strong (15.4 at%) C1s signal exhibiting 3 peaks at 284.8 eV, 286.2 eV and 288.8 eV was recorded after argon sputtering (named C1s_1, C1s_2, C1s_3 respectively). The two peaks of the O1s signal are commonly assigned to O^{2-} bound in the wurtzite structure (O1s_L) and oxygen in oxygen deficient regions of the ZnO matrix (e.g. oxygen vacancies; O1s_V).[13, 22, 23] and references within The high resolution O1s scan in Figure 3-2 makes clear that the as-grown nanorod-arrays are highly oxygen deficient, indicated by a high O1s_V/O1s_L ratio of 0.61. It can therefore be expected that the grown films are rich in oxygen vacancies. The high C1s after argon sputtering is somewhat unusual as the generally observed carbon surface contamination is normally readily removed by bombardment with argon ions. Nevertheless these features with their positions at 284.8 eV, 286.2 eV and 288.8 eV were also observed for ZnO nanostructures previously.[39-44] The low binding energy feature C1s_1 can be assigned to "free carbon" whereby the surface contamination is believed to have only a minor contribution in our samples. More so it is likely that a graphitic overlayer forms at the surface of the nanorods similar to the observations of Tu *et al*..[39] The higher binding energy feature C1s_3 is reported to result from carbonate species and/or residues (COOR) from the layer growth process.[39, 40], [41, 42] A peak in the region of 286.2 eV can be an indication of carbon doping in ZnO.[39-42] Here the shift to higher binding energies is often explained by invoking the formation of an O-C-O bond,[39-41] which can mainly result from carbon occupying a zinc site (donor type defect) or carbon binding two oxygen interstitial sites (acceptor type defect).[41, 43, 44] Hence it is reasonable to conclude that the high HMTA concentration in the growth solution leads to unintentional carbon incorporation into the ZnO nanorod-arrays (the C1s_2 peak accounts to ca. 2 at% in the films). With this in mind we note in passing that the growth method presented could therefore be of particular interest for further studies concerning dilute magnetic semiconductors as similar or lower carbon concentrations were reported to lead to room-temperature ferromagnetism.[43, 44]

Further analysis on the as-grown ZnO nanostructures was carried out using RT-PL and UV-Vis diffuse reflectance spectroscopy. The band gap of a semiconductor can be estimated from its absorption coefficient α. The Tauc-expression gives the band gap as a function of α. For a semiconductor with a direct band gap the relation is presented in equation (5):[45]

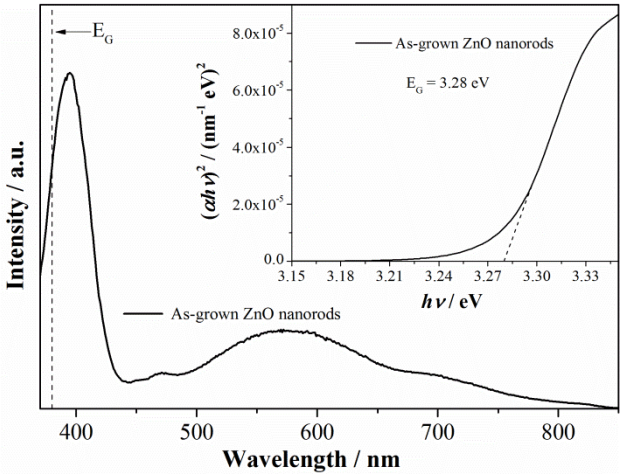

Figure 3-3 RT-PL spectrum of as-grown ZnO nanorods (excitation wavelength = 345 nm). Inset: Tauc-plot of as-grown ZnO nanorods. The band gap energy estimated from UV-Vis is insert in the RT-PL graph as guidance for the eye (E_G = 378 nm).

$$(\alpha hv) = B(hv - E_G)^{0.5} \tag{3.5}$$

Where E_G is the optical band gap energy, hv is the photon energy and B is a constant. Figure 3-3 shows the RT-PL spectra and Tauc-plot of as-grown ZnO nanorods. The Tauc-plot allows the estimation of the band gap energy for the ZnO nanorods by extrapolating the linear part of $(\alpha hv)^2$ on to the x-axis. As can be seen from the inset in Figure 3-3, the optical band gap is found to be 3.28 eV for the as-grown ZnO nanorods, which is in good agreement with literature reports.[2]

The band gap energy E_G is also inserted as guidance for the eye in the RT-PL spectra in Figure 3-3. Two distinct peaks can be seen in these spectra – sharp, intense peak centered at 395 nm (violet) and a broad peak with its center around 575 nm (yellow). Furthermore small features can be recognized in the spectra at 470 nm and 700 nm. These features were found to originate from, or to be influenced by the experimental setup, rather than sample emission.

From Figure 3-3 it is clear that the band-band recombination cannot be the only or main source of the violet emission (395 nm) as the peak center is shifted by 15 nm (0.14 eV) from the estimated band gap energy towards longer wavelengths. This shift is larger than the 60 meV expected from the excitonic binding energy. Hence it is believed that the peak consists of emissions from multiple origins with the main contribution to this peak originating from states close to the band edges (near band edge emission or NBE). Possible point defects located closely underneath the CB edge

are zinc interstitials Zn_i.[27, 46] These defects were found to increase in density with increasing HMTA to ZNH ratio during growth.[19]

The broad yellow emission is a commonly observed feature in the luminescence from ZnO nanostructures grown via solution based methods.[2] Here we have examined this feature by studying an as-grown sample over an extended period of time during which measurements were made at different intervals. The resulting spectra, which focus on the yellow emission, are compiled in Figure 3-4. After the initial PL measurement the sample was subsequently measured 15 times (back-to-back). The prolonged irradiation with UV light (excitation wavelength = 345 nm) led to a decrease of the 575 nm emission with each PL scan (curves (1) and (2) in Figure 3-4). The emission then recovers – but not to its initial intensity – when stored in air at room temperature ((3) and (4) in Figure 3-4). After storing in air for two weeks the sample was annealed in intense UV light (365 nm, 4 mW/cm^2, 2 min) resulting in a dramatic decrease of the yellow emission.

Several conclusions about the origin of the yellow emission can be drawn from Figure 3-4; the emission must result from the surface regions or near surface regions of the rods as it is seen to recover upon storage in air. Also it is likely that the reduction of the observed emission upon irradiation with UV light is due to photo-reduction/oxidation processes occurring between photo-generated charge carriers from the ZnO and adsorbed groups at the surface, thereby reducing the defect emission after UV irradiation. In this respect our results support those reported by other authors which attribute this feature to adsorbents at the surface such as hydroxyl groups (OH^-, $Zn(OH)_2$), hydrogen and water.[24, 25]

Material properties of RTA treated samples

For all samples the photo-luminescence properties were examined before and after the respective RTA treatment. Figure 3-5 summarizes the PL properties of ZnO nanorods annealed at 350 °C, 450 °C and 550 °C in different atmospheres. As-grown samples did not show any major differences in their spectra. For this reason a representative spectrum is given in Figure 3-5 as the as-grown reference. Furthermore the band gap energy E_G for as-grown samples estimated from UV-Vis spectroscopy (see Figure 3-3) is included in the figures.

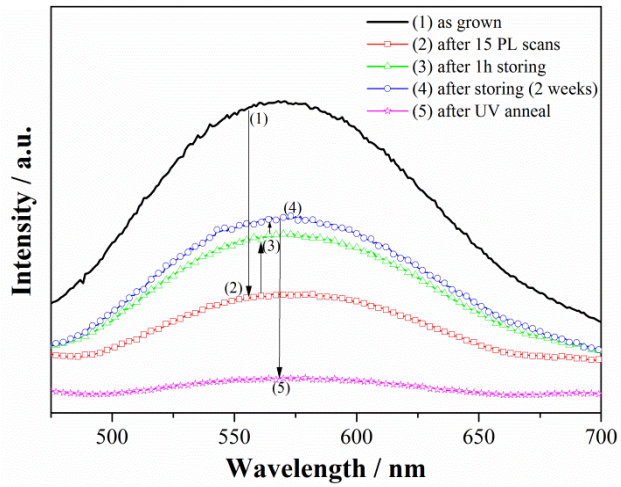

Figure 3-4 RT-PL spectra of as-grown ZnO nanorods after different treatments in order to evaluate the influence on the yellow (575 nm) emission.

At 350 °C all samples show an increased PL emission below 400 nm as well as a shift of the peak maximum in this region towards shorter wavelengths independent of the atmosphere used. The strongest emission can be recognized for the sample annealed in vacuum. Additionally, the samples exhibit a broad visible emission. Compared to the as-grown reference the emission center shifts from 575 nm to 600 nm for the samples annealed in oxygen, argon and forming gas. Furthermore the emission peak for these atmospheres does not include a strong contribution of the 575 nm emission indicating a decrease of same after annealing. For the vacuum annealed sample a peak shift in the visible range was not observed - rather a decrease in the emission centered at 575 nm. As outlined in the previous section the observed reduction centered at 575 nm is due to reaction and possible desorption of surface adsorbents/products. Since the desorption of the adsorbed groups present after growth is temperature dependent, it is believed that all samples exhibit a reduction of hydroxyl-groups and water adsorbed at the surface after annealing at 350 °C.[47] However, desorption of hydrogen – which is found to originate from dissociatively adsorbed water – should be insignificant as the annealing temperature is too low.[47] Desorption of surface absorbents is particularly true for the sample annealed in vacuum. For the other atmospheres the absence of a clear shoulder at 575 nm for the peak centered at 600 nm is an indication of this process.

The peak shift of the emission centered at 395 nm (before RTA) to 385 nm (after RTA at 350 °C) is due to the reduction of defects close to the band edges as well as the

passivation of non-radiative defects. On one hand the chemisorbed hydrogen present on the surface after growth can passivate non-radiative defect centers upon heat treatment leading to an increased radiative recombination.[29, 47] On the other hand a general improvement of the crystal quality is expected as a result of the RTA leading to a reduction of the observed defect states close to the band edges after growth. In turn the radiative band-band recombination emerges as the dominant recombination process visible by the observed peak shift towards shorter wavelengths. This finding is supported by the good agreement between the peak center and the estimated band gap energy from UV-Vis measurements. Furthermore it confirms that the near-UV emission for as-grown samples is dominated by defect states close to the band edges and does only partially originate from the band-band recombination (see Figure 3-3 and related comments).

The different emissions in the visible region (green) – seen for samples annealed at

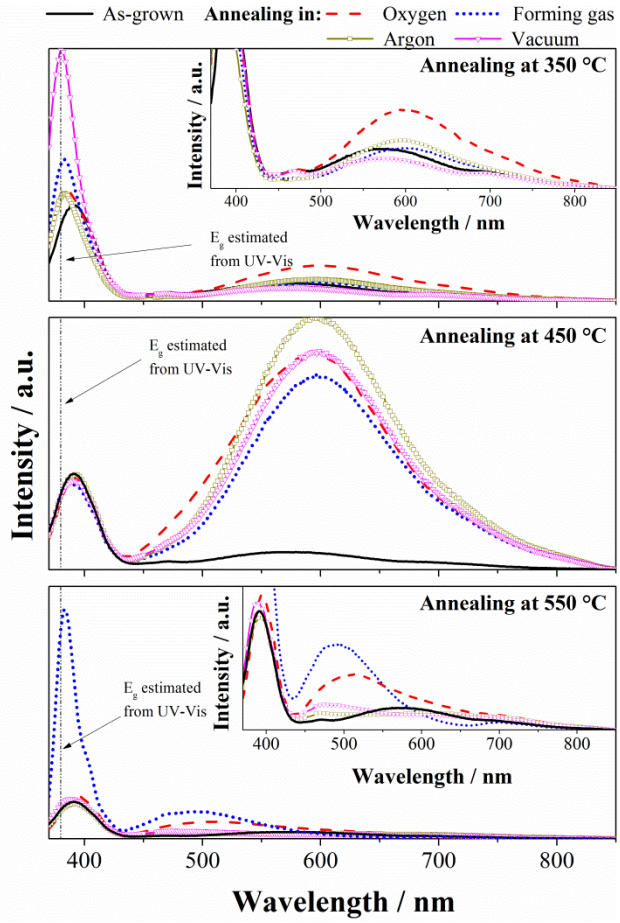

Figure 3-5 RT-PL properties of ZnO nanostructures grown on glass after RTA in different atmospheres at a) 350 °C b) 450 °C and c) 550 °C.

550 °C (lower panel in Figure 3-5) – are fingerprints of defects induced due to the RTA treatment in different atmospheres. The investigation of the origin of these defects was not the objective of the current study and is therefore only discussed briefly by means of the samples annealed in forming gas and oxygen.

The nature of the green emission from ZnO has been debated for decades and different intrinsic defects such as ionized oxygen vacancies (donor type), oxygen anti-sites (acceptor type) or zinc vacancies (acceptor type) and extrinsic defects including copper have all been discussed as possible sources of the emission in question.[18, 26, 29, 48-51] Among the many possibilities zinc vacancies are most generally believed to contribute to the green emission but they do not have to be the only source.[18]

Apart from an increased green emission, annealing in a reducing environment (forming gas) at 550 °C led to sample damage. Partial etching of nanorods at similar temperatures was also observed by other groups where it was concluded that forming gas treatment at these temperatures most likely induces surface defects in the Zn-lattice, probably involving zinc vacancies.[25, 26] Thus, for the sample subjected to a reducing annealing atmosphere, the emission centered at 490 nm (see forming gas curve in lower panel of Figure 3-5) could originate from V_{Zn}. Furthermore it is known that hydrogen can form a shallow donor state just below the CBM.[29] and references within Therefore it might be additionally possible that hydrogen is introduced as a donor defect in the ZnO lattice giving rise to the observed strong emission close to the band gap energy.

Rapid thermal annealing in oxygen shifts the center of the green emission towards longer wavelengths. Thus it is likely that another defect contributes to the observed emission. Oxygen anti-sites and complexes including copper impurities are mentioned in literature reports as a possible origin of emissions centered around 510 nm for samples that were exposed to excess oxygen.[49] [48]

Samples annealed at 450 °C show no substantial change of the UV-emission. Annealing in all atmospheres introduces very strong emission centered around 600 nm (orange). Additionally a shoulder in the green region (500 nm) can be noticed for all samples with the sample annealed in oxygen showing this feature most prominently.

The induction of orange-luminescent defects for all atmospheres is quite remarkable. A dependence on the nature of the RTA atmosphere, as seen for the annealing at

550 °C, could not be observed. Since reducing (forming gas), oxidizing (O_2) as well as inert gases (Ar) have similar effects on the defect composition of the samples it is suggested that the orange-luminescent defects are formed independently of the nature of the atmosphere used.

In addition it is likely that the orange emission centers are created upon heat-treatment from intrinsic defects present in the samples after growth rather than defects additionally induced by RTA as the spectra would show significant differences according to the gases used (see RTA at 550 °C). The strong orange emission indicates that recombination happens foremost over this defect deep in the band gap. Furthermore the unchanged near-UV emission implies that band-band recombination is not a major contributor of recombination in the samples as opposed to the strong emission seen for samples annealed at 350 °C. Desorption of hydrogen at around 400 °C related to a decrease in passivation of non-radiative surface defect might contribute to this observation.[47] The shoulder in the green region possibly results from additional defects induced upon RTA (see discussion for RTA @ 550 °C above).

In order to evaluate whether the orange emission is caused by a defect on the surface of the nanorods a sample with poor rod alignment (which was found to be strongly influenced by the seed layer crystallinity) but strong orange emission was dipped into hydrochloric acid (HCl, pH = 2). As ZnO is unstable in acidic solution the removal of the material starts from the surface and terminates at the core of the rods. After certain time intervals the sample was taken out of the acidic solution, rinsed in MilliQ water, blow-dried in nitrogen and measured for its luminescence properties.

The resulting PL spectra are compiled in Figure 3-6 together with two SEM micrographs showing the sample before and after 20 s exposure to HCl. With increasing etching time the deep level emission as well as the (NBE) decreases. After 180 s the sample is completely etched away with emission being detected from the glass substrate only (note that the influence of the glass substrate is negligible until around 105 s of etching). As can be seen from the SEM micrographs in Figure 3-6 all facets of the nanorods are considerably etched back even after just 20 s exposure to acid. At this stage the initial surface or any possible surface layer can be considered as destroyed leaving the bulk material of the rod behind. The corresponding PL results clearly show that the orange emission does not suddenly vanish within the first seconds

of acid exposure. More so the emission scales with the decrease of the NBE emission thus indicating that the emission must originate from a defect present throughout the entire bulk of the rod.

To further examine the origin of the orange emission observed in samples annealed at 450 °C excitation PL spectra were recorded (emission wavelength 600 nm). The results for all atmospheres and temperatures are summarized in Figure 3-7. All samples annealed at 450 °C show a strong response of the 600 nm emission upon excitation with UV light (345 nm - 390 nm). The strong dependency of the PL intensity from the excitation wavelength points out that the responsible states within the band gap cannot be populated directly by electrons from the valance band. For all atmospheres the observed orange emission involves a transition of an electron from the conduction band minimum or states in the conduction band.

To a small extent shallow donor defects might contribute to the increased intensities between 380 – 390 nm. Since the spectra for samples annealed at 450 °C do not differ significantly in terms of intensity or trend, it is inferred that the same defect is

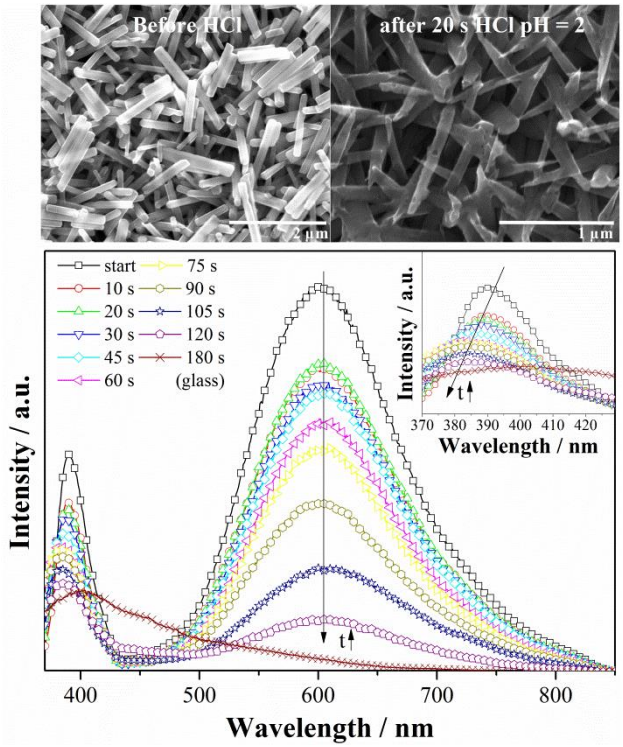

Figure 3-6 Top: RT-PL spectra of ZnO nanorods with strong orange emission before and after exposure to HCl pH2 for 20 s. Bottom) SEM micrographs of the sample before and after 20 s exposure to HCl (pH = 2).

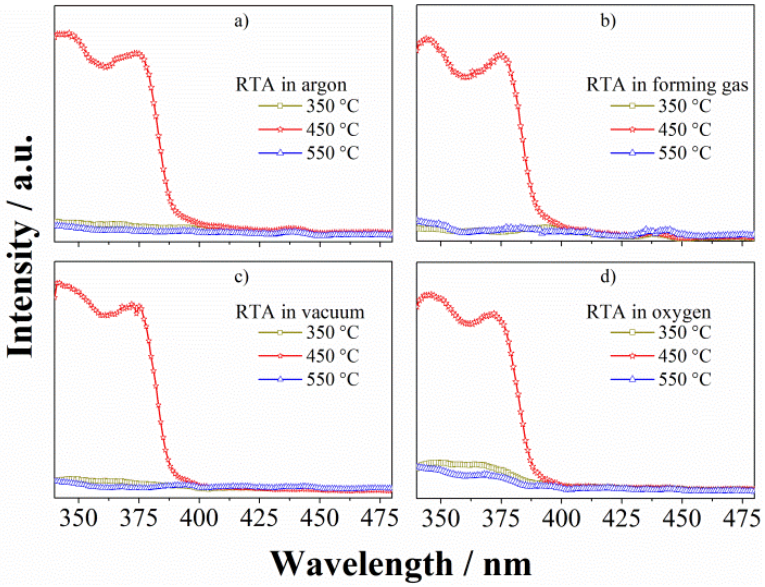

Figure 3-7 Excitation RT-PL spectra of ZnO nanorods annealed in a) argon, b) forming gas, c) vacuum and d) oxygen at 350°C, 450°C and 550°C. The emission wavelength was fixed to 600 nm.

responsible for the orange emission for all atmospheres studied.

Furthermore it was also found that the emission shape does not show any additional radiative processes when exciting the samples with various excitation wavelengths λ_{ex} (see Figure A1- 3 and Figure A1- 4 for a discussion on possible Xe flash lamp artefacts and the emission spectra of a strong orange emitting sample for λ_{ex} = 315 nm - 425 nm). It is generally agreed that the orange emission originates from an electron in the CB being trapped at the defect site but the literature is somewhat contradictory regarding the nature of the defect itself. Some authors report the observation of the orange emission in connection with excess oxygen and thus conclude that oxygen interstitials are the responsible defect.[28, 30-32] The fact that all of the investigated samples in this study show a strong orange emission independent of the annealing atmosphere but related to the temperature during RTA contradicts this hypothesis. If O_i would be the source of the orange emission in our samples one would expect a quenching of the emission after annealing in forming gas or vacuum and clearly the highest emission for samples annealed in oxygen. Furthermore it is unlikely that O_i is introduced in significant quantities at 450 °C as the formation energy is rather high.[18] Other groups relate the orange emission to either doubly ionized oxygen vacancies V_O^{++} or the defect complex V_O-Zn_i.[33-35] [24, 25] It is worth noting that the emissions observed in references [33-35] are slightly shifted compared to the

observed emission center at 600 nm. This could be the result of the different deposition techniques used. In the case of V_O^{++} as the possible emission source, a dependence on the nature of the annealing atmosphere would be expected as well. Here annealing in oxygen should lead to a decrease in PL intensity compared to samples annealed in e.g. vacuum. During annealing in O_2 oxygen vacancies would be filled resulting in a quenched emission. We do not observe such behavior for samples exhibiting orange-luminescent defects (see Figure 3-5).

In order to evaluate if the filling of oxygen vacancies is a time dependent process and thus the associated emission should not be observed after annealing in oxygen for a sufficient period of time, an orange-luminescent sample was additionally annealed in air at 350 °C for 10 h. No significant differences between the emission intensity before and after the long term annealing in air could be observed. Theoretically the disappearance of the orange emission at a RTA temperature of 550 °C is in line with the probability for V_O^{++} to anneal out.[46] However the suggested recombination mechanism in references [33-35], involving a hole being trapped at a singly ionized oxygen vacancy V_O^{+}, is contradicted by theoretical studies that suggest that V_O^{+} is unstable in ZnO.[18, 46]

Compared to our results Bandopadhyay and Mitra recently observed similar PL spectra depending on the excitation wavelength used.[27] They also considered the formation of the V_O-Zn_i complex and found experimental evidence of ionized Zn_i^{++} in the conduction band, which is an essential building block of this complex. However, they assigned the orange emission (605 nm in [27]) to V_O^{++} and did not consider that the complex exhibits a possible energetic position of about 2.1 eV below the CBM and could therefore be a possible source of orange emission itself.[36, 38] [24, 25]

Our experimental observations of the temperature dependency and the atmosphere *independency* of the orange emission is more in favour towards the V_O-Zn_i as a possible source as suggested by other authors as well.[24, 25] With this in mind we postulate that orange-luminescent defects in ZnO nanostructures grown from aqueous solutions are solely induced by a thermal-dependent process. Thus it is likely that the complex is formed by the rearrangement of intrinsic defects present after growth.

Additionally the samples showing orange emission were subject to low-temperature PL analysis at 11.5 K. A He-Cd laser with an excitation wavelength of 325 nm was

used. Figure 3-8 shows the UV/NBE and deep level emission (DLE) of the samples annealed at 450 °C as well as from an as-grown sample. The UV/NBE emission of the as-grown reference is dominated by an indistinguishable feature centered at 3.36 eV. Furthermore a shoulder can be noticed around 3.225 eV. Samples annealed at 450 °C on the other hand show a distinguishable PL response in the UV/NBE region with peaks centered at 3.376 eV, 3.366 eV, 3.314 eV, 3.238 eV and a shoulder around 3.167 eV.

The peaks at 3.376 eV and 3.366 eV are generally attributed to recombination of a free exciton (A-exciton, FX_A) and an exciton bound to a neutral donor (D_0X).[52, 53] In ZnO many neutral donor related emission lines have been reported and for some the chemical nature could be assigned.[53, 54] An exact assignment of the chemical nature of the neutral donor is not possible for our samples as the emission is too broad. Nevertheless in comparison to the as-grown sample the emergence of the D_0X and especially the FX_A emission points towards an improved crystal quality of the annealed samples. Furthermore it is apparent that the emission of the as-grown sample is dominated by defect emission over shallow donors (most likely exciton bound to neutral donor). Thus, the contribution of different shallow donor defects, including

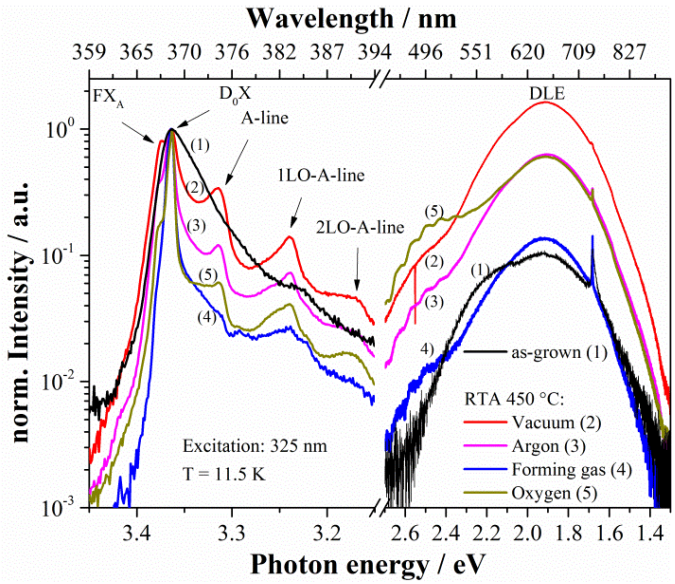

Figure 3-8 Normalized low-temperature PL spectra of samples annealed at 450 °C in different atmospheres with focus on the UV/near band edge emission (NBE) spectra and deep level emission (DLE). Note that the DLE of the sample annealed in forming gas appears so low because of very strong NBE (D_0X) at low temperatures – possibly related to hydrogen acting as possible shallow donor defect.

intrinsic defects, is possible. Also the RTA treatment leads to the disappearance of the shoulder at 3.225 eV which again might be attributed to intrinsic defects in the material.

A curious observation is the pronounced peak at 3.314 eV. This peak is neither caused by an D_0X transition nor is it in the two-electron satellite region.[53] Interestingly the energy difference to the peaks at lower energies (3.238 eV and 3.167 eV) is 72 meV and 147 meV, respectively. This identifies the lower energy features as longitudinal optical (LO) phonon replicas of the peak at 3.314 eV. The observed features (so-called A-line around 3.31 eV) were reported by other groups previously with surface or structural defects, a free to bound transition (conduction band – acceptor), the 1LO-replica of the FX_A line or a bound to free transition (donor – valence band) all being mentioned as possible sources for the emission at 3.31 eV.[55-58]

For our samples the RTA atmosphere has no influence on the appearance of the A-line. However it was found that this emission center is dependent from the temperature as well since as-grown samples do not show these features, samples annealed at 350 °C only weakly but they can be clearly recognized for samples annealed at 450 °C and 550 °C. These findings are consistent with an earlier study showing that thermal treatment leads to the establishment of well-defined A-lines.[55]

No connection between the orange emission and the A-line emission center can be made as the orange emission is not visible for samples annealed at 550 °C but the A-lines are. Nevertheless it is likely that both defect centers are caused by crystal-rearrangement upon heat treatment.

Regarding the deep level emission (DLE) observed at 11.5 K it seems likely that the emission is caused by the contribution of multiple defects over the entire spectrum from green to red. However, the defect centered at ca. 1.9 eV is clearly dominating the spectra. Interestingly the DLE peak is centered to lower energies when compared to the RT PL spectra (see Figure 3-5). The cause of the shift needs further analysis since only a small temperature dependence of the peak position was noticed during cooling of the sample and the excitation with 325 nm from the white light source (system used for RT PL in Figure 3-5) does not change the peak position for the RT-PL experiments.

If the orange luminescence seen for the samples annealed in different atmospheres at 450 °C originates from the same defect – involving oxygen vacancies – its chemical

fingerprint should be observable by XPS. For the samples annealed at 450 °C and 550 °C a XPS analysis was carried out in order to evaluate any possible changes in the chemical configuration. Since the XPS analysis on as-grown samples (see Figure 3-2) revealed a high degree of oxygen deficiency and carbon in the films special focus was put on the examination of the C1s and O1s peaks.

For all the annealed samples the main feature of the C1s peak (C1s_1) was found to be centered at 284.8 eV and therefore not shifted when compared to the as-grown sample in Figure 3-2. Also the positions of the C1s_2 and C1s_3 peaks did not change significantly after RTA (286.1 eV ± 0.1 eV and 288.7 1 eV ± 0.2 eV, respectively).

Concerning a possible correlation of the detected carbon and the orange emission the percentages of the total carbon as well as from the C1s_2 peak (related to unintentional doping – please refer to Figure 3-2 and related comments) were examined. The results for the different annealing atmospheres and temperatures (450 °C and 550 °C) are listed in Table 3-1.

Even after RTA the total carbon concentration in the films ranges between and 7.9 at% and 17.5 at% indicating the presence of a rather robust graphitic shell at the surface of the nanorods. For the samples showing orange luminescence (RTA at 450 °C) the total carbon content (10 at% - 17.5 at%) is comparable to the value measured for as-grown ZnO nanorod-arrays (15.4 at%, Figure 3-2). The same accounts for the C1s_2 peak whereby the orange emitting samples show percentages between 1.6 at% and 2.5 at% compared to 2 at% for the as-grown sample.

In fact no correlation between the high carbon content and the orange luminescence can be established- neither between the total carbon concentration nor the contribution of the C1s_2 signal linked to the unintentional carbon doping. When compared to as-grown samples or nanorod-arrays annealed at other temperatures the samples exhibiting orange emission do not show any trends related to carbon content.

For the samples annealed at 450 °C and 550 °C the binding energies of the two components of the O1s peak – O1s_V and O1s_L – were found to remain virtually unchanged (± 0.1 eV) when compared to the as-grown ZnO nanorods at 531.6 eV and 530.2 eV, respectively. An exception is made for the sample annealed in forming gas at 550 °C. Here both peaks shifted to higher binding energies (530.5 and 532.0 eV). As the Zn 2p is also shifted by + 0.3 eV it is likely that e.g. surface charging is

Table 3-1: XPS high resolution analysis of the C1s peak of annealed ZnO nanorod-arrays with focus on the total carbon content and the C1s_2 feature. For as-grown ZnO: total carbon = 15.4 at%; C1s_2 = 2at%.

C1s – total C	Oxygen	Argon	Forming gas	Vacuum
450 °C	15.0 at%	12.0 at%	10.0 at%	17.5 at%
550 °C	10.5 at%	7.9 at%	12.9 at%	13 at%
C1s_2				
450 °C	2.5 at%	1.7 at%	1.6 at%	2.1 at%
550 °C	1.8 at%	1.3 at%	3.1 at%	1.5 at%

Table 3-2 XPS high resolution analysis of the O1s peak of annealed ZnO nanorod-arrays with focus on the O1s_V/O1s_L ratio. For as-grown ZnO O1s_V/O1s_L = 0.61.

O1s_V/O1s_L	Oxygen	Argon	Forming gas	Vacuum
450 °C	0.46	0.40	0.49	0.57
550 °C	0.49	0.48	0.54	0.60

responsible for the observed shift and no conclusion can be drawn regarding a possible correlation to the green-luminescent defect visible for this sample. The high resolution O1s spectra were carefully analyzed for their O1s_V/O1s_L ratios. Table 3-2 summarizes the ratios for the samples annealed at 450 °C and 550 °C in different atmospheres. All samples exhibit a reduced oxygen vacancy (O1s_V) to lattice oxygen (O1s_L) ratio when compared to the as-grown sample. It is seen that samples annealed in oxygen and argon show the strongest reduction of the vacancy related O1s_V peak which can be attributed to an improved crystal quality (for the sample annealed in argon) and filling of the oxygen vacancies (RTA in O_2 atmosphere).

On the other hand for RTA in vacuum only a small reduction can be seen which is in line with the postulation that the vacuum atmosphere would have effects foremost on the oxygen sub-lattice. It is noteworthy that the O1s_V/O1s_L ratio does not scale with the carbon concentration (e.g. lowest carbon concentration does not lead to lowest O1s_V/O1s_L ratio – compare Table 3-1).

Interestingly all samples annealed at 450 °C show a stronger reduction of the

O1s_V/O1s_L ratio (i.e. less oxygen vacancies) than samples annealed at 550 °C – independent from the atmosphere during RTA. This is somewhat surprising, especially for the samples annealed in oxygen and argon as lower oxygen deficiency would be expected for both atmospheres at 550 °C when compared to 450 °C - for RTA in oxygen due to the increased filling of oxygen vacancies and RTA in argon due to an overall improvement of the crystal quality.

The results from the O1s high resolution XPS scans show that the oxygen vacancy signal is generally reduced upon annealing at 450 °C. When considering the formation of the V_O-Zn_i defect complex it is reasonable to expect a binding energy shift away from the binding energy associated with the single oxygen vacancy. Hence a reduction of the area under O1s_V peak is the consequence – as observed in the reduced O1s_V/O1s_L ratio of the annealed samples. As this finding is particularly true for samples subject to RTA at 450 °C (i.e. lower O1s_V/O1s_L ratio compared to RTA at 550 °C) it is proposed that the reduction of the O1s_V/O1s_L ratio and the appearance of the strong orange emission are directly correlated at the given temperature. This in turn means that the emergence of the orange emission is chemically reflected by "consuming" of oxygen vacancies (binding energy shift in XPS). Furthermore the XPS results confirm that the orange luminescence observed after RTA at 450 °C has a single chemical origin which is found RTA atmosphere independent.

A detailed study on a further set of samples grown on seed layer coated glass and FTO was carried out. Vacuum was used as the annealing atmosphere and the RTA temperature was varied between 350 °C, 450 °C and 550 °C. The ZnO nanorod-arrays grown on seed layer coated glass were used for spectroscopic measurements and samples grown on FTO were subject to photo-electrochemical characterization. The results presented for the as-grown samples given in the figures are representative spectra of all as-grown samples examined.

Figure 3-9 shows the RT-PL spectra of ZnO nanorod-arrays annealed in VAC at different temperatures. For samples annealed at 350 °C and 550 °C an increased emission centered around 380 nm indicates an improved band-band recombination whereas a decreased emission is seen for the sample annealed at 450 °C. The PL emissions within the visible region are in good agreement with the emission obtained

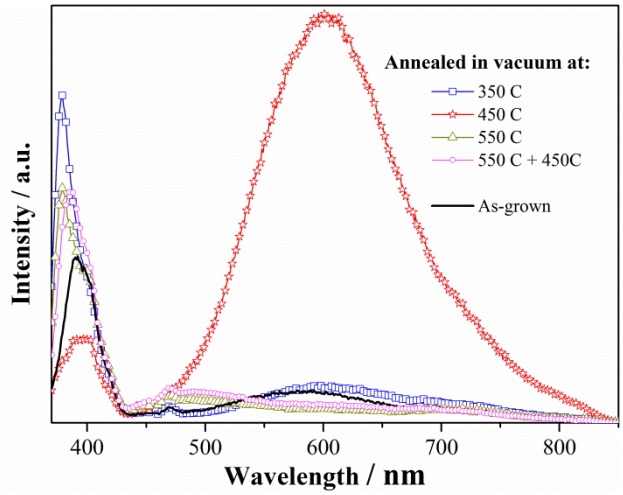

Figure 3-9 RT-PL spectra of ZnO nanostructures annealed in vacuum at different temperatures.

with the ZnO nanostructures examined previously (please refer for Figure 3-5 and related discussion). The orange emission is only present for RTA at 450 °C. As the NBE decreases upon annealing at 450 °C the DLE clearly becomes the dominant recombination channel.

Post RTA treatment at 550 °C the corresponding sample was additionally annealed in vacuum at 450 °C. As can be seen in Figure 3-9, the differences between the PL spectra after RTA at 550 °C and RTA at 550 °C + 450 °C are not major. This is particularly interesting given that no orange emission is observed for this sample. It suggests that the intrinsic defects necessary for the formation of the complex are not accessible anymore after RTA at 550 °C, which is possibly due to the loss of those defects (i.e. they are defects that can be annealed out).

The samples were also studied for their absorption properties and the resulting band gap energies before and after RTA are summarized in Table 3-3. Before RTA all samples exhibit an optical band gap of ca. 3.28 eV. Upon annealing in vacuum the band gap energies change. A small band gap narrowing of ca. 13 meV can be recognized for samples annealed at 350 °C and 450 °C. On the other hand, RTA at550 °C results in a stronger reduction of the band gap (24 meV). During RTA in vacuum at 550 °C additional defects are induced within the band gap as recognized by the PL results (Figure 3-5 and Figure 3-9). It is very likely that the oxygen sub-lattice is influenced by the RTA treatment. Under such circumstances oxygen vacancies would seem to be the likely candidates for the observed phenomena since band gap

Table 3-3 Band gap energy E_G and Urbach energy E_U for ZnO nanostructures before and after RTA in vacuum at different temperatures.

	Before RTA		***After RTA***	
Sample	E_G **/ eV**	E_U **/ meV**	E_G **/ eV**	E_U **/ meV**
350 °C	3.279	45.9	3.265	63.3
450 °C	3.280	43.8	3.267	89.5
550 °C	3.277	46.9	3.253	67.5

'shrinking' with an increasing number of oxygen vacancies has been reported in the literature.[13] In the wavelength region near the band gap the absorption coefficient α of the ZnO nanorods was additionally investigated for the Urbach energy E_U. The Urbach energy is a measure of the exponential dependence of the absorption coefficient on the photon energy ($h\nu < E_G$), which is commonly observed near the band gap of a semiconductor. It is usually related to structural disorder or defects energetically localized near the band-edges (band-tail states). The Urbach energy is linked with the absorption coefficient by the following expression:

$$\alpha = \alpha_0 e^{\frac{h\nu}{E_U}} \tag{3.6}$$

Where α_0 is a constant and $h\nu$ is the photon energy. A plot of ln(α) vs. $h\nu$ should therefore be linear and the Urbach energy can be calculated from the reciprocal slope of the linear portion.

Table 3-3 summarizes the Urbach energy for all samples before and after RTA in vacuum calculated for $h\nu < E_G$. For all samples the Urbach energy increases after RTA. This implies additional energetic states localized near the band-edges. Interestingly the increase in E_U is by far the strongest for the sample annealed at 450 °C. Indeed the excitation PL results (see Figure 3-7) showed that states just below the CBM also contribute to the orange emission. This could be due to a shift of the energy of the Zn_i defects closer to the CBM, as discussed in more detail in the following section. The shift of Zn_i closer to the CB results in an increased density of localized states near the CBM which in turn increases the tail-width evaluated by E_U. As such we suggest that it is reasonable to consider that the increased Urbach energy for the ZnO nanorods annealed 450 °C is directly related to the orange-luminescent defects induced due to

the RTA treatment. For the other annealing temperatures the slightly increased Urbach energies could result from increased structural disorder especially at the rod surface.

From the above discussion it becomes obvious that the orange-luminescent defect center represents a strong recombination channel in the ZnO nanorod-arrays. When comparing the luminescence-efficiency of the samples annealed at different temperatures the orange-luminescent samples clearly out-perform the other samples. Hence, the presence of this defect center successfully inhibits non-radiative recombination which is known to happen on a much faster timescale than radiative recombination processes. For photo-electrochemical applications it could therefore be beneficial to suppress non-radiative recombination and take advantage of the comparably longer lifetime of charge-carriers recombining over the orange-luminescent defect centers.

In order to evaluate whether the orange-luminescent defects could indeed be beneficial for photo-electrochemical applications linear sweep voltammetry (LSV) was carried out on ZnO nanorod-arrays grown on FTO and annealed in vacuum at different temperatures. Here it is noteworthy that the nanorod alignment for arrays grown on FTO was not as good as for samples grown on glass (Figure A1- 1). It is believed that the comparably rough surface of the underlying FTO led to this effect. Furthermore it was found that the appearance of strong orange-luminescence is shifted by about 30 °C towards lower temperatures and that the overall luminescence of the photoelectrodes is less compared to nanorod-arrays grown on glass (see Figure A1- 1). However, when testing different substrates (sapphire, gallium nitride glass, FTO) and seed layers (e.g. prepared after Greene *et al.*[26]) the intensity of the orange emission was found substrate independent. Nevertheless, the FTO/ALD seed layer combination showed the lowest emission among all tested substrate/seed layer combinations.

Figure 3-10 shows the PL-spectra of the prepared photo-electrodes and the corresponding LSV voltammograms. The PL emission for the samples follows the luminescence-trend observed in Figure 3-9 (i.e. strong band-band recombination at 350 °C, orange-luminescence at 420 °C, additional defects around 490 nm and no orange emission at 550 C – please refer to Figure 3-9 and Figure 3-5 for detailed discussion).

Under anodic bias the dark LSV traces are essentially the same with no sample showing a significant earlier dark-current onset potential. As expected for the n-type

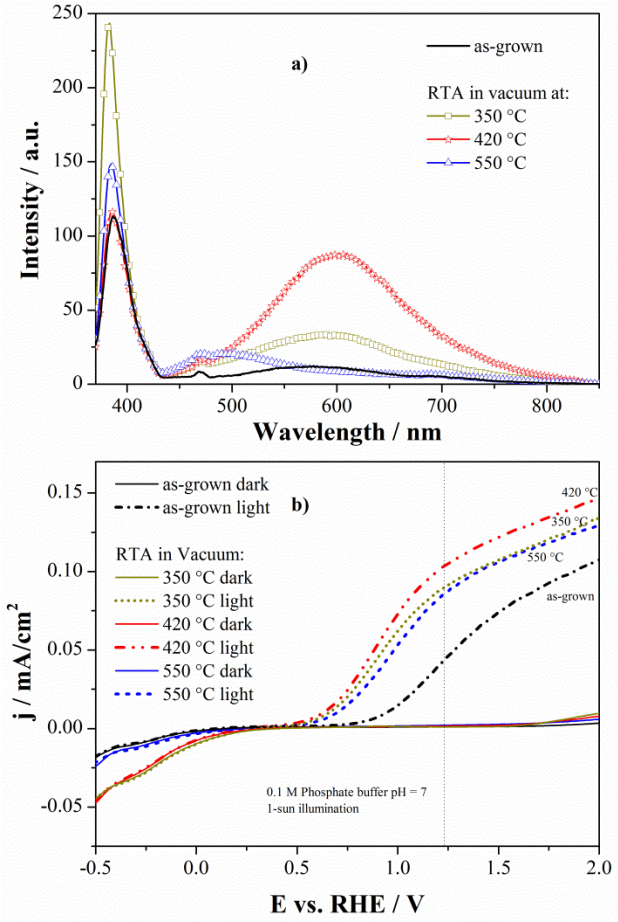

Figure 3-10 a) PL spectra of investigated ZnO nanorod-array photo-electrodes (as-grown and annealed in vacuum at different temperatures). b) Corresponding LSV voltammograms in the dark and under 1-sun illumination.

ZnO nanorod-arrays a current onset can only be detected for potentials higher than 2 V vs. RHE. Under simulated sunlight all samples show a noticeable photo-current. When comparing the annealed samples to the as-grown reference it is noticed that every annealing temperature can improve the photo-current density as well as the photo-current onset potential (ca. 0.25 V cathodic shift for RTA samples). Whereas the samples annealed at 350 °C and 550 °C perform almost identically, the sample exhibiting strong orange emission (420 °C) outperforms all other samples. Photo-current densities at 1.23 V vs. RHE of 43.8 µA/cm^2, 89.8 µA/cm^2, 103.5 µA/cm^2 and 85.9 µA/cm^2 are recognized for the as-grown and annealed at 350 °C, 420 °C and 550 °C samples, respectively. For the sample showing strong orange emission the photo-current density showed an improvement of almost 150 % compared to the as-grown sample and about 20 % over the samples annealed at 350 °C or 550 °C.

The shift of the photo-current onset potential towards more negative potentials implies an improved charge transfer at the semiconductor-electrolyte interface for the annealed samples. From a kinetic point of view this is the result of a higher rate constant of photo-generated holes participating in charge transfer over the interface.[59] Especially charge carrier recombination has big influence on the charge transfer rate constant as it ultimately limits the density of holes available at the surface. Reducing recombination therefore results in an earlier photo-current onset.

Charge carrier recombination also manifests in the slope of the *j-V* curve. Here photo-electrodes exhibiting high recombination of photo-generated charge carriers (including recombination in the bulk, space charge region and on the surface) show a flat incline of the photo-current with applied potential (e.g. as-grown sample in lower panel of Figure 3-10). In turn the opposite is true for samples with low recombination of photo-generated electrons and holes. This is especially the case for the sample exhibiting orange luminescence where the photo-current density rises more steeply compared to the other samples.

Especially at lower applied potentials the photo-current is dominantly influenced by the lifetime of holes recombining over trap states – particularly at the surface of the semiconductor.[60] If recombination over the orange-luminescent defects would happen on a fast timescale (i.e. low hole lifetime) a significant decrease in photocurrent would be the result, given the fact that radiative recombination happens foremost over this channel. As the opposite is observed the recombination of photo-generated electrons and holes must happen comparatively slow.

Assuming that the trapping process and the subsequent recombination with holes in the conduction band happen with a long time constant the lifetime of the photo-generated hole might be increased. Considering charge carrier generation in the bulk of the rod with $x < L_D$ (Debye length), a higher probability of charge carrier diffusion into the space charge region and charge carrier separation would then be the result. This ultimately leads to an increased possibility for oxidation of the electrolyte at the surface, as evidenced by the presented LSV voltammograms.

It is worth noting that a contribution to the photo-current signal from the electrons trapped at the defect sites is also possible. Nevertheless if these charges are collected and detected as photo-current a hole must still be present in the material. Overall these

holes will therefore be able to participate more fully in photo-chemical reactions such as water oxidation.

In addition to charge carrier recombination the charge carrier density as well as the flat band potential have big influence on the obtainable photo-current.[60] As and increased cathodic dark-current can been recognized in the LSV voltammograms for samples annealed at 350 C and 420 C a shift of the flat band potential seems indeed possible. Electrochemical impedance spectroscopy by means of Mott-Schottky analysis was carried out in order to evaluate this possibility (Figure A1- 2). Interestingly it was found that the sample exhibiting orange emission showed non-linear behavior. This may point towards a more complex charge carrier transport over the interface.[61] Given the high density of trap states Fermi-level pinning to surface states seems likely.[60] The photo-electrochemical charge transfer in orange-luminescent ZnO nanorod-arrays will be addressed more fully in a future study.

Origin and formation mechanism of orange-luminescent defects

The experimental results lead to the conclusion that the orange-luminescent defect-center is formed from the rearrangement of intrinsic defects, namely V_O and Zn_i, after growth. It is proposed that these defects form the defect-complex V_O-Zn_i, which was also speculated on by other groups.[24, 25] Theoretical studies showed that the position of the defect in the band gap is around 2.1 eV,[36] which is in good agreement with our PL results.

Additionally the theoretical studies present a valuable insight in the defect formation and related material properties. In references [37, 38] the authors calculated the formation energy to be dependent of the distance between the two point defects. Nevertheless, even at a very low distance (1.1. Å) the formation energy of the V_O-Zn_i complex was calculated to be 3.8 eV [38]. Hence it is unlikely for the complex to be present in high concentrations from a thermodynamic perspective.[37] Kim *et al.* further investigated the possible kinetic formation of the complex by migration of the zinc interstitial into the complex via a kick-out process.[37] In this regard it is important to note that the migration barrier of Zn_i is very low as compared to that for V_O – 0.57 eV and 2.36 eV respectively.[46] Therefore it is assumed that V_O is not mobile even at elevated temperatures. In their theoretical study the authors showed

that if Zn_i is more than 3.6 Å away from V_O it moves with a low migration barrier of 0.5 eV. If the distance between the defects decreases further, Zn_i can migrate towards V_O by the kick-out process. The energy barrier for the kick-out process was calculated to be around 1.3 eV (our results suggest a slightly higher barrier – refer to Appendix 1 for discussion).[37] By overcoming this energy barrier the Zn_i can be kinetically trapped to V_O (binding energy of the complex ca. 0.6 eV).[37] The hybridization of the two point defects results in a shift of the energetic position of levels V_O and Zn_i – V_O shifts deeper into the forbidden gap and Zn_i close or in to the conduction band.[38] Both of these processes have been observed experimentally by Bandopadhyay and Mitra.[27] It is also important to note that the shift of the energy of Zn_i closer to the conduction band leads to the ionization of the defect with two electrons being possibly donated into the CB. Thus this mechanism also provides a plausible explanation as to the origin of the n-type doping in ZnO and shows that it would be dependent on the distance between V_O and Zn_i in the complex.

Considering the experimental results and the theoretical calculations available, the following defect formation process upon RTA is postulated: the as-grown ZnO nanorods exhibit a large number of oxygen deficient defects as evidenced by the XRD and XPS results (Figure 3-1 and Figure 3-2). Additionally adsorbents like hydroxyl-groups, water and hydrogen are present at surface (see Figure 3-4 and related comments). Upon annealing at 350 °C the surface adsorbents desorb – apart from hydrogen which can saturate non-radiative defects at the surface leading to an improved band-band recombination (Figure 3-5).[47]

At 350 °C zinc interstitials are mobile and can move through the nanorod. However, the energy barrier of 1.3 eV for Zn_i to be kinetically trapped to V_O is unlikely to overcome at this temperature. Hence the orange-luminescent V_O-Zn_i complex is not formed to a significant extent.

When the ZnO nanorod-arrays are annealed at 450 °C (420 °C for the presented photo-electrodes) the energy is high enough for zinc interstitials to overcome the barrier of 1.3 eV to enter the complex kinetically via the kick-out process resulting in a strong orange emission centered around 600 nm, independent of the RTA atmosphere (Figure 3-5). The formation of the V_O-Zn_i complex (throughout the entire rod) leads to a shift of the energy of the zinc interstitial defects into the CB or near the CBM. An indication

that this process is occurring may be seen from the increasing Urbach energy (Table 3-3). Hence the donor type defects in the bulk of the rod are ionized leaving a positively charged complex behind. Upon illumination with $\lambda > E_G$ photo-generated electrons in the conduction band can then be trapped by the defect state of the complex in the forbidden gap, leading to the observed orange emission. As indicated by the photo-electrochemical results the trapping of an electron may lead to an increase in charge carrier lifetime of the photo-generated hole, enhancing the photo-electrochemical performance of the ZnO nanorod-arrays. A migration of Zn_i out of the complex is also possible but unlikely as the binding energy of the complex (0.5 - 0.6 eV)[37, 38] + the migration barrier of 1.3 eV would have to be overcome.

This is the case for samples annealed at 550 °C. The energy is high enough for Zn_i to leave the complex. Since it is not trapped any longer by V_O it is likely that the zinc interstitials anneal out at this temperature as evidenced by the cross-annealing at different temperatures in Figure 3-9. Additional defects, depending on the atmosphere used during RTA, are also induced at this temperature. These defects show emissions in the range 450 nm – 550 nm. The origin of those defects is beyond the scope of this present study but at least for the samples annealed in vacuum at 550 °C it is believed that V_O is responsible for the emission centered around 480 nm which is observed by a decreased band gap for these samples, as reported previously by other groups.[13]

3.5 Conclusions

Well aligned, intentionally defect-rich ZnO nanorod-arrays were grown via a low temperature solution-based method. The defect composition of the ZnO structures can be alternated by careful adjustment of the temperature during rapid thermal annealing. It is observed that orange-luminescence occurs when the temperature during RTA was set to ca. 450 °C, independent from the RTA atmosphere. The defects responsible for the orange emission were not found to be present in samples annealed at lower or higher temperatures. XRD, XPS, PL and UV-Vis spectroscopy indicate that the orange luminescent defects are formed from intrinsic defects present in the material after the growth. The experimental evidence leads to the conclusion that the V_O-Zn_i defect complex in the bulk of the nanorods is responsible for the strong orange emission in ZnO grown from aqueous solution. Based on the evidence presented here, combined

with the results of several previous theoretical studies, a possible formation mechanism which would depend critically on the RTA temperature is presented.[36-38] It is suggested that the Zn_i is kinetically trapped to the V_O upon annealing at ca. 450 °C. Lower or higher annealing temperatures are not able to kinetically stabilize the complex.

Importantly, ZnO nanowires with a high density of orange luminescent defects were found to exhibit improved photo-electrochemical performance. An increase in photo-current of almost 150 % at 1.23 eV vs. RHE over as-grown nanorod-arrays was observed and is attributed to an increased charge carrier (hole) lifetime. The V_O-Zn_i defect complex is thereby believed to act as a charge carrier trap enhancing charge carrier lifetime and separation.

It is suggested that the cheap, earth abundant ZnO-based materials described here could form the basis of significantly improved photo-anodes for photo-electrochemical water splitting.

3.6 References

[1] S. Xu and Z. L. Wang, "One-dimensional ZnO nanostructures: Solution growth and functional properties," *Nano Research,* vol. 4, no. 11, pp. 1013-1098, 2011.

[2] A. B. Djurišić, A. M. C. Ng, and X. Y. Chen, "ZnO nanostructures for optoelectronics: Material properties and device applications," *Progress in Quantum Electronics,* vol. 34, no. 4, pp. 191-259, 2010.

[3] L. Vayssieres, "Growth of Arrayed Nanorods and Nanowires of ZnO from Aqueous Solutions," *Advanced Materials,* vol. 15, no. 5, pp. 464-466, 2003.

[4] S. Baruah and J. Dutta, "Hydrothermal growth of ZnO nanostructures," *Science and Technology of Advanced Materials,* vol. 10, no. 1, p. 013001, 2009.

[5] C. M. Chang, M. H. Hon, and I. C. Leu, "Preparation of ZnO nanorod arrays with tailored defect-related characterisitcs and their effect on the ethanol gas sensing performance," *Sensors and Actuators B: Chemical,* vol. 151, no. 1, pp. 15-20, 2010.

[6] G. Kenanakis, D. Vernardou, E. Koudoumas, G. Kiriakidis, and N. Katsarakis, "Ozone sensing properties of ZnO nanostructures grown by the aqueous chemical growth technique," *Sensors and Actuators B: Chemical,* vol. 124, no. 1, pp. 187-191, 2007.

[7] A. B. Djurisic and Y. H. Leung, "Optical properties of ZnO nanostructures," *Small,* vol. 2, no. 8-9, pp. 944-61, 2006.

[8] Z. L. Wang, "Triboelectric Nanogenerators as New Energy Technology for Self-Powered Systems and as Active Mechanical and Chemical Sensors," *ACS Nano,* vol. 7, no. 11, pp. 9533-9557, 2013.

[9] D. Garcia-Alonso, S. Smit, S. Bordihn, and W. M. M. Kessels, "Silicon passivation and tunneling contact formation by atomic layer deposited Al2O3/ZnO stacks," *Semiconductor Science and Technology,* vol. 28, no. 8, p. 082002, 2013.

[10] S. Smit, D. Garcia-Alonso, S. Bordihn, M. S. Hanssen, and W. M. M. Kessels, "Metal-oxide-based hole-selective tunneling contacts for crystalline silicon solar cells," *Solar Energy Materials and Solar Cells,* vol. 120, pp. 376-382, 2014.

[11] M. Liu, C.-Y. Nam, C. T. Black, J. Kamcev, and L. Zhang, "Enhancing Water Splitting Activity and Chemical Stability of Zinc Oxide Nanowire Photoanodes with Ultrathin Titania Shells," *The Journal of Physical Chemistry C,* vol. 117, no. 26, pp. 13396-13402, 2013.

[12] Y. Mao, H. Yang, J. Chen, J. Chen, Y. Tong, and X. Wang, "Significant performance enhancement of ZnO photoanodes from Ni(OH)2 electrocatalyst nanosheets overcoating," *Nano Energy,* vol. 6, pp. 10-18, 2014.

[13] J. Wang *et al.*, "Oxygen vacancy induced band-gap narrowing and enhanced visible light photocatalytic activity of ZnO," *ACS Appl Mater Interfaces,* vol. 4, no. 8, pp. 4024-4030, 2012.

[14] F. Kayaci, S. Vempati, C. Ozgit-Akgun, N. Biyikli, and T. Uyar, "Enhanced photocatalytic activity of homoassembled ZnO nanostructures on electrospun polymeric nanofibers: A combination of atomic layer deposition and hydrothermal growth," *Applied Catalysis B: Environmental,* vol. 156-157, pp. 173-183, 2014.

[15] L. Cai *et al.*, "V ions implanted ZnO nanorod arrays for photoelectrochemical water splitting under visible light," *International Journal of Hydrogen Energy,* vol. 40, no. 3, pp. 1394-1401, 2015.

[16] W. C. Lee, G. E. Canciani, B. O. S. Alwhshe, and Q. Chen, "Enhanced photoelectrochemical water oxidation by ZnxMyO (M = Ni, Co, K, Na) nanorod arrays," *International Journal of Hydrogen Energy,* vol. 41, no. 1, pp. 123–131, 2015.

[17] C. G. Van de Walle, "Defect analysis and engineering in ZnO," *Physica B: Condensed Matter,* vol. 308–310, pp. 899-903, 2001.

[18] A. Janotti and C. G. Van de Walle, "Fundamentals of zinc oxide as a semiconductor," *Reports on Progress in Physics,* vol. 72, no. 12, p. 126501, 2009.

[19] K. S. Ranjith, R. Pandian, E. McGlynn, and R. T. Rajendra Kumar, "Alignment, Morphology and Defect Control of Vertically Aligned ZnO Nanorod Array: Competition between “Surfactant” and “Stabilizer” Roles of the Amine Species and Its Photocatalytic Properties," *Crystal Growth & Design,* vol. 14, no. 6, pp. 2873-2879, 2014.

[20] F. Kayaci, S. Vempati, I. Donmez, N. Biyikli, and T. Uyar, "Role of zinc interstitials and oxygen vacancies of ZnO in photocatalysis: a bottom-up approach to control defect density," *Nanoscale,* vol. 6, no. 17, pp. 10224-10234, 2014.

[21] F. Liu, Y. H. Leung, A. B. Djurišić, A. M. C. Ng, and W. K. Chan, "Native Defects in ZnO: Effect on Dye Adsorption and Photocatalytic Degradation," *The Journal of Physical Chemistry C,* vol. 117, no. 23, pp. 12218-12228, 2013.

[22] J. Al-Sabahi, T. Bora, M. Al-Abri, and J. Dutta, "Controlled Defects of Zinc Oxide Nanorods for Efficient Visible Light Photocatalytic Degradation of Phenol," *Materials,* vol. 9, no. 4, pp. 238-247, 2016.
[23] X. Zhang *et al.*, "Effect of aspect ratio and surface defects on the photocatalytic activity of ZnO nanorods," *Sci Rep,* vol. 4, p. 4596, 2014.
[24] A. B. Djurišić *et al.*, "Defect emissions in ZnO nanostructures," *Nanotechnology,* vol. 18, no. 9, p. 095702, 2007.
[25] K. H. Tam *et al.*, "Defects in ZnO Nanorods Prepared by a Hydrothermal Method," *The Journal of Physical Chemistry B,* vol. 110, no. 42, pp. 20865-20871, 2006.
[26] L. E. Greene *et al.*, "Low-temperature wafer-scale production of ZnO nanowire arrays," *Angew Chem Int Ed Engl,* vol. 42, no. 26, pp. 3031-4, 2003.
[27] K. Bandopadhyay and J. Mitra, "Zn interstitials and O vacancies responsible for n-type ZnO: what do the emission spectra reveal?," *RSC Adv.*, vol. 5, no. 30, pp. 23540-23547, 2015.
[28] C. H. Ahn, Y. Y. Kim, D. C. Kim, S. K. Mohanta, and H. K. Cho, "A comparative analysis of deep level emission in ZnO layers deposited by various methods," *Journal of Applied Physics,* vol. 105, no. 1, p. 013502, 2009.
[29] M. Willander *et al.*, "Luminescence from Zinc Oxide Nanostructures and Polymers and their Hybrid Devices," *Materials,* vol. 3, no. 4, pp. 2643-2667, 2010.
[30] J. Qiu *et al.*, "The growth mechanism and optical properties of ultralong ZnO nanorod arrays with a high aspect ratio by a preheating hydrothermal method," *Nanotechnology,* vol. 20, no. 15, p. 155603, 2009.
[31] Y. Sun, N. George Ndifor-Angwafor, D. Jason Riley, and M. N. R. Ashfold, "Synthesis and photoluminescence of ultra-thin ZnO nanowire/nanotube arrays formed by hydrothermal growth," *Chemical Physics Letters,* vol. 431, no. 4-6, pp. 352-357, 2006.
[32] D. Li *et al.*, "Different origins of visible luminescence in ZnO nanostructures fabricated by the chemical and evaporation methods," *Applied Physics Letters,* vol. 85, no. 9, p. 1601, 2004.
[33] J. D. Ye *et al.*, "Correlation between green luminescence and morphology evolution of ZnO films," *Applied Physics A,* vol. 81, no. 4, pp. 759-762, 2004.
[34] S. Vempati, S. Chirakkara, J. Mitra, P. Dawson, K. Kar Nanda, and S. B. Krupanidhi, "Unusual photoresponse of indium doped ZnO/organic thin film heterojunction," *Applied Physics Letters,* vol. 100, no. 16, p. 162104, 2012.
[35] A. van Dijken, E. A. Meulenkamp, D. Vanmaekelbergh, and A. Meijerink, "The Kinetics of the Radiative and Nonradiative Processes in Nanocrystalline ZnO Particles upon Photoexcitation," *The Journal of Physical Chemistry B,* vol. 104, no. 8, pp. 1715-1723, 2000.
[36] P. S. Xu, Y. M. Sun, C. S. Shi, F. Q. Xu, and H. B. Pan, "The electronic structure and spectral properties of ZnO and its defects," *Nuclear Instruments and Methods in Physics Research Section B: Beam Interactions with Materials and Atoms,* vol. 199, pp. 286-290, 2003.

[37] D.-H. Kim, G.-W. Lee, and Y.-C. Kim, "Interaction of zinc interstitial with oxygen vacancy in zinc oxide: An origin of n-type doping," *Solid State Communications,* vol. 152, no. 18, pp. 1711-1714, 2012.
[38] Y.-S. Kim and C. H. Park, "Rich Variety of Defects in ZnO via an Attractive Interaction between O Vacancies and Zn Interstitials: Origin ofn-Type Doping," *Physical Review Letters,* vol. 102, no. 8, p. 086403, 2009.
[39] N. Tu, K. T. Nguyen, D. Q. Trung, N. T. Tuan, V. N. Do, and P. T. Huy, "Effects of carbon on optical properties of ZnO powder," *Journal of Luminescence,* vol. 174, pp. 6-10, 2016.
[40] X. Liu, H. Du, X. W. Sun, B. Liu, D. Zhao, and H. Sun, "Visible-light photoresponse in a hollow microtube–nanowire structure made of carbon-doped ZnO," *CrystEngComm,* vol. 14, no. 8, pp. 2886–2890, 2012.
[41] S. T. Tan, X. W. Sun, Z. G. Yu, P. Wu, G. Q. Lo, and D. L. Kwong, "p-type conduction in unintentional carbon-doped ZnO thin films," *Applied Physics Letters,* vol. 91, no. 7, p. 072101, 2007.
[42] C. Suk-Ho, L. Daeyoung, P. Joon Won, K. Dong Hak, and L. Minchul, "The Role of Carbon Doping in ZnO," *Journal of the Korean Physical Society,* vol. 57, no. 6, p. 1482, 2010.
[43] S. Akbar, S. K. Hasanain, M. Abbas, S. Ozcan, B. Ali, and S. I. Shah, "Defect induced ferromagnetism in carbon-doped ZnO thin films," *Solid State Communications,* vol. 151, no. 1, pp. 17-20, 2011.
[44] D. K. Mishra *et al.*, "Carbon doped ZnO: Synthesis, characterization and interpretation," *Journal of Magnetism and Magnetic Materials,* vol. 329, pp. 146-152, 2013.
[45] J. Tauc, "Optical properties and electronic structure of amorphous Ge and Si," *Materials Research Bulletin,* vol. 3, no. 1, pp. 37-46, 1968/01/01 1968.
[46] A. Janotti and C. G. Van de Walle, "Native point defects in ZnO," *Physical Review B,* vol. 76, no. 16, p. 165202, 2007.
[47] R. Xie *et al.*, "Enhancement and patterning of ultraviolet emission in ZnO with an electron beam," *Applied Physics Letters,* vol. 88, no. 13, p. 134103, 2006.
[48] K. E. Knutsen *et al.*, "Zinc vacancy and oxygen interstitial in ZnO revealed by sequential annealing and electron irradiation," *Physical Review B,* vol. 86, no. 12, p. 121203(R), 2012.
[49] B. Lin, Z. Fu, and Y. Jia, "Green luminescent center in undoped zinc oxide films deposited on silicon substrates," *Applied Physics Letters,* vol. 79, no. 7, p. 943, 2001.
[50] M. Guo, P. Diao, and S. Cai, "Hydrothermal growth of well-aligned ZnO nanorod arrays: Dependence of morphology and alignment ordering upon preparing conditions," *Journal of Solid State Chemistry,* vol. 178, no. 6, pp. 1864-1873, 2005.
[51] V. Khranovskyy, V. Lazorenko, G. Lashkarev, and R. Yakimova, "Luminescence anisotropy of ZnO microrods," *Journal of Luminescence,* vol. 132, no. 10, pp. 2643-2647, 2012.
[52] A. Teke *et al.*, "Excitonic fine structure and recombination dynamics in single-crystalline ZnO," *Physical Review B,* vol. 70, no. 19, p. 195207, 2004.
[53] B. K. Meyer *et al.*, "Bound exciton and donor–acceptor pair recombinations in ZnO," *physica status solidi (b),* vol. 241, no. 2, pp. 231-260, 2004.

[54] F. Mohammadbeigi, E. S. Kumar, S. Alagha, I. Anderson, and S. P. Watkins, "Carbon related donor bound exciton transitions in ZnO nanowires," *Journal of Applied Physics,* vol. 116, no. 5, p. 053516, 2014.

[55] S. S. Kurbanov, G. N. Panin, and T. W. Kang, "Spatially resolved investigations of the emission around 3.31 eV (A-line) from ZnO nanocrystals," *Applied Physics Letters,* vol. 95, no. 21, p. 211902, 2009.

[56] M. R. Wagner, P. Zimmer, A. Hoffmann, and C. Thomsen, "Resonant Raman scattering at exciton intermediate states in ZnO," *physica status solidi (RRL) – Rapid Research Letters,* vol. 1, no. 5, pp. 169-171, 2007.

[57] M. Schirra *et al.*, "Stacking fault related3.31−eVluminescence at130−meVacceptors in zinc oxide," *Physical Review B,* vol. 77, no. 12, p. 125215, 2008.

[58] K. W. Liu, R. Chen, G. Z. Xing, T. Wu, and H. D. Sun, "Photoluminescence characteristics of high quality ZnO nanowires and its enhancement by polymer covering," *Applied Physics Letters,* vol. 96, no. 2, p. 023111, 2010.

[59] P. Cendula *et al.*, "Calculation of the Energy Band Diagram of a Photoelectrochemical Water Splitting Cell," *The Journal of Physical Chemistry C,* vol. 118, no. 51, pp. 29599-29607, 2014.

[60] Y. K. Gaudy and S. Haussener, "Utilizing modeling, experiments, and statistics for the analysis of water-splitting photoelectrodes," *J. Mater. Chem. A,* vol. 4, no. 8, pp. 3100-3114, 2016.

[61] A. Nakamura, M. Sugiyama, K. Fujii, and Y. Nakano, "Comparison of Semiconductor–Electrolyte and Semiconductor–Metal Schottky Junctions Using AlGaN/GaN Photoelectrochemical Electrode," *Japanese Journal of Applied Physics,* vol. 52, no. 8S, p. 08JN20, 2013.

Chapter 4

This chapter and accompanying appendix represent an adapted version of the publication:

> J. Kegel, V. Z. Zubialevich, M. Schmidt, I. M. Povey, and M. E. Pemble, "Effect of Surface and Defect Chemistry on the Photo-catalytic Properties of Intentionally Defect-rich ZnO Nanorod Arrays," *ACS Applied Materials & Interfaces*, DOI: 10.1021/acsami.8b05130.

Changes to the publication were only made in regards to formatting requirements.

4 Effect of Surface and Defect Chemistry on the Photocatalytic Properties of Intentionally Defect-Rich ZnO Nanorod Arrays

4.1 Abstract

Due to the abundance of intrinsic defects in zinc oxide (ZnO), the material properties are often governed by same. Knowledge of the defect chemistry has proven to be highly important, especially in terms of the photocatalytic degradation of pollutants. Given the fact that defect-free materials or structures exhibiting only one type of defect are extremely difficult to produce, it is necessary to evaluate what influence various defects may have when present together in the material. In this study, intentionally defect-rich ZnO nanorod (NR) arrays are grown using a simple low temperature solution-based growth technique. Upon changing the defect chemistry using rapid thermal annealing (RTA) the material properties are carefully assessed and correlated to the resulting photocatalytic properties. Special focus is put on the investigation of these properties for samples showing strong orange photoluminescence (PL). It is shown that intense orange emitting NR arrays exhibit improved dye-degradation rates under UV light irradiation. Furthermore, strong dye-adsorption has been observed for some samples. This behavior is found to stem from a graphitic surface structure (e.g., shell) formed during RTA in vacuum. Since orange-luminescent samples also exhibit an enhancement of the dye-adsorption a possible interplay and synergy of these two defects is elucidated. Additionally, evidence is presented suggesting that in annealed ZnO NRs structural defects may be responsible for the often observed PL emission at 3.31 eV. However, a clear correlation with the photocatalytic properties could not be established for these defects. Building on the specific findings presented here, this study also presents some more general guidelines which, it is suggested, should be employed when assessing the photocatalytic properties of defect-rich ZnO.

4.2 Introduction

Governed by its low-cost, environmental friendliness, and earth-abundant nature ZnO represents a promising material to be used in various applications such as gas sensing,[1, 2] light emitting diodes,[3-6] and photovoltaics as well as photo(electro)chemical (PEC) applications.[7-15] In these applications, the material

performance is dramatically influenced by intrinsic defects. As-deposited ZnO commonly presents intrinsic defects, whereby the density and nature of the same crucially depends on the deposition technique and deposition environment used.[16-18] Interestingly, several literature reports point out that the existence of intrinsic defects in ZnO does not necessarily lead to poor performing devices and can in fact enhance the device performance, especially for photo(electro)chemical applications.[1, 11, 14, 19-22] In the field of photocatalysis published literature reports suggest that intrinsic defects such as oxygen vacancies V_O and zinc interstitials Zn_i can increase the photocatalytic activity of prepared ZnO nanomaterials toward model pollutant species, usually dyes of various types.[14, 19, 23-25] These studies have identified the defects either as charge-carrier traps which delay the recombination processes of photoexcited charge carriers and/or as surface-sites where the pollutant/dye is degraded via the charge transfer from the pollutant/dye to the defect state. Furthermore, it has recently been shown that strong orange-luminescent ZnO nanorod (NR) arrays – prepared in a similar manner to the samples in this study – can significantly enhance the PEC performance for solar water splitting under simulated solar irradiation.[26] Also in this case an increased charge transfer rate for photogenerated charge carriers (holes) could be observed with the experimental data suggesting that the observed behavior stems from a lower/slower rate of recombination.

Apart from intrinsic defects in the material the activity of ZnO in respect to these PEC reactions can also be influenced by other factors. As summarized by Kumar and Rao, the photocatalytic properties of ZnO can be significantly affected by, e.g. the morphology, crystal facets and their polarity, doping and impurities, and surface modification as well as the deposition of multimaterial structures.[21] Thus, it becomes obvious that the overall photocatalytic activity of a given ZnO structure is influenced by multiple aspects. Therefore, a direct comparison of, for example, different ZnO morphologies with varying defect compositions is not straightforward, since the exact contribution of each individual aspect (i.e., morphology and intrinsic defect) is difficult to determine.

For this reason, in the present study we aim to minimize the number of possible variables by evaluating a range of intentionally defect-rich ZnO NR arrays, all grown using the same growth parameters. In order to investigate the interplay of intrinsic

defects and their possible influence on the photocatalytic properties, we apply postdeposition rapid thermal annealing (RTA) to vary the defect composition and defect density in the films. Initially the study focuses on the observation of strong orange emission from samples annealed around 450 °C. It is important to note that careful material characterization (XRD, PL/excitation-PL, UV-vis, XPS) of similarly deposited ZnO NR arrays has revealed that this defect center is temperature dependent but an annealing atmosphere independent, with the V_O-Zn_i defect-complex being the likely source of the observed orange emission.[26] Building on these earlier results, it is presented that strong dye-adsorption depending on the nature of the dye (here methylene blue (MB) and methyl orange (MO_ are used) can be recognized for some samples annealed at this temperature (450 ℃). By means of Raman spectroscopy, transmission electron microscopy (TEM), low temperature PL (LT-PL), and photocatalytic dye-degradation measurements the extent to which the orange-luminescent defects are responsible for the observed behavior has been evaluated. Additionally the material characterization reveals the presence of a graphitic shell as well as the appearance of structural defects (related to LT-PL emission at 3.31 eV) following certain RTA treatments.

In this way the influence of the interplay of all these defects (orange-luminescent defects, structural defects and graphitic shell) on the observed photocatalytic properties of ZnO NR arrays has been elucidated. Based on the experimental results presented in this study, it is suggested that careful defect-engineering can be used to tailor ZnO toward, and enhance the performance of, specific photo(electro)chemical applications and that a holistic approach involving as many material properties as possible should be employed in order to assess the photocatalytic performance of defect-rich materials.

4.3 Experimental Methods

ZnO seed-layer coated microscope glass slides (25 mm x 75 mm) were used as the growth substrates. Prior to the seed-layer preparation by atomic layer deposition (ALD) the microscope glass slides were sonicated for 1 h in a mixture of Millipore water (H_2O; 18.2 MΩ), ammonium hydroxide (NH_4OH), and hydrogen peroxide (H_2O_2) in a ratio of H_2O:NH_4OH:H_2O_2 = 5:1:1.

Seed-Layer Preparation by ALD

Diethylzinc (Sigma Aldrich) and H_2O were used as the precursors for the ALD of seed-layers using a Cambridge NanoTech Fiji F200LLC System. The growth was carried out over 400 cycles (ca. 70 nm film thickness) at 190 °C substrate temperature followed by natural cooling in air. Subsequently the seed-layer coated substrates were annealed in air for 1 h at 300 °C. A value of 70 nm was deliberately selected as the typical layer thickness since layers of this thickness would most likely prevent possible impurity migration from the substrate into ZnO NRs.

Solution Growth of ZnO NR Arrays

Intentionally defect-rich ZnO NRs were grown using a solution-based method as presented in ref [26]. In short, 100 mL of solution were prepared by dissolving and continuous stirring (1 h) of 0.025 M zinc nitrate hexahydrate ($Zn(NO_3)_2 \cdot 6H_2O$, (ZNH), reagent grade) and 0.15 M hexamethylenetetramine ($C_6H_{12}N_4$, (HMTA), reagent grade) and 4 drops of 5 %wt hydrochloric acid (HCl, reagent grade) in H_2O. As presented by Ranjith *et al.*, a high HMTA to ZNH concentration ratio allows thereby for the deposition of ZnO rich in intrinsic defects – especially Zn_i.[13] Afterward the solution was transferred into a sealable plastic bottle and seed-layer coated substrates were immersed into the solution. The substrates were put in almost vertically, and the growth side was pointing slightly downward. Subsequently the sealed bottle was heated to 95 °C in a standard laboratory oven. After the growth period (6 h), the naturally cooled solution was discarded and the obtained samples were thoroughly rinsed with H_2O and blow dried with nitrogen. In order to avoid possible impairment of later photocatalytic measurements any growth on the backside of the samples was carefully etched back using HCl.

Rapid Thermal Annealing (RTA) of ZnO Nanorod Arrays

The ZnO nanorod arrays were annealed at various temperatures (350, 450, 550 °C) in oxygen (O_2, 1 bar) and/or in vacuum (VAC)) using a Jipelec 150 RTA system. In the case of oxygen as the annealing atmosphere, the RTA chamber was filled with the gas prior to the temperature ramp up. The samples were then annealed for 10 min at the set temperature (ramp rate = 10 °C/s).

Characterization

Samples were subject to LT-PL analysis at 11.5 K using a cw He-Cd laser (λ_{ex} = 325 nm, 1.6 mW) as the excitation source. A Jeol JEM-2100 was used to record TEM images of ZnO NRs. Raman analysis was performed using a Renishaw micro-Raman spectrometer equipped with a 514 nm laser. The beam was focused through a Leica 100 (NA = 0.9) objective. The laser power density on the sample was less than 5 mW/μm^2 (spot size ca. 1 μm).

The photocatalytic properties were tested by placing a ZnO NR array into a UV-cuvette filled with 3 mL of *ca*. 17 μM methylene blue solution (MB) or *ca*. 55 μM methyl orange solution (MO) in H_2O. The absorbance spectrum of the constantly stirred dye solution was then monitored at 664 nm (MB) or 464 nm (MO) every 20 s using an Ocean optics HL-2000-LL lamp and QE65000 spectrophotometer. During a typical analysis, the dye solution was left in the measurement setup for at least 30 min in the dark prior to the insertion of the sample. The last absorbance measurement before the sample was put into the solution was taken to determine the initial dye concentration C_0 (Lambert–Beer law). After the sample was put into the cuvette the dark dye-adsorption was measured for 1.5 h after which the illumination was turned on. This "light on" stage lasted for 1.5 h followed by another off/on cycle (1 h each). Finally an additional "light off" stage was introduced for 20 min. A 365 nm high power UV-LED has been used as light source. The intensity has been adjusted to either 1 mW/cm^2 (low-intensity; l.i.) or 3 mW/cm^2 (high-intensity; h.i.). Since multiple photocatalytic measurements have been performed on each sample, the results presented have been labeled in accordance to the number of measurements the sample had been subjected to (e.g., (1) for the first, (2) for the second photocatalytic measurement, etc.). Between the photocatalytic measurements the samples were washed in ethanol and Millipore water (30 min each).

It is important to note that the real surface area of the samples could not be determined. Hence, sample comparisons on the basis of the absolute changes of the dye concentration are not meaningful. The reader should therefore evaluate each dye-degradation diagram presented as an individual measurement sequence. Since all the measurements in one dye-degradation plot are taken on the same sample (if not mentioned otherwise), knowledge of the exact surface area is not necessary. This

approach allows us to draw conclusions regarding the general trends among the samples (e.g., dark dye-adsorption, changes in the photocatalytic activity upon annealing, etc.). Furthermore, absolute comparisons of the dye-degradation performance between measurements on the same sample are possible. Because of the latter, dye-degradation rates for each measurement have been calculated from the first light on stage. In order to avoid confusion (i.e., unwanted sample comparison), these rates are listed in Table A2- 1 and Table A2- 2.

Furthermore, it is important to make the reader aware of the shortcomings that dye discoloration-tests may represent when evaluating the photocatalytic performance of materials. A major drawback – especially when investigating visible light active materials – is that dyes may also absorb visible light. This can induce e.g. self-decomposition or dye-sensitization of the photocatalyst leading to a discoloration of the solution that may then be misinterpreted to stem from the photocatalyst.[27-29] Similarly, in the case of MB, discoloration may also occur due to the reduction of MB to the leuco methylene blue form (LMB). Since LMB is only an intermediate and can be readily form MB again when oxygen is present in the solution (pH dependent) the dye is not fully degraded, and discoloration rates may be again misleading.[27] Also the charge of the dye is crucial, as attractive forces between the photocatalyst and dye can lead to higher degradation rates. The pH of the dye solution may even intensify this effect.[27, 29] In the present study the aforementioned effects were minimized by choosing 365 nm as the illumination wavelength (no/little absorption of the MB and MO but full absorption of ZnO, see Figure A2- 1), performing the tests in nearly neutral solution (less “artificial” dye-adsorption) and light on/off cycling. The latter allows examining a possible recolorization which can be an indication of a not fully degraded dye (e.g., LMB formation for MB decomposition). Finally it is important to point out that while it is certainly true that the dye testing can be influenced by many factors, for the purpose of the present study, comparative measurements were carried out only. These were done on a series of materials that are all essentially the same in terms of structure, bulk composition, and morphology. Our materials differ only in the number and nature of the defects present.

4.4 Results and discussion

Prior to the RTA treatment various samples were evaluated for the reproducibility of

the described deposition method. Furthermore the material characterization depicted in Figure A2- 2 was carried out to ensure that no major differences between the samples exist. As visible from the PL, XRD and SEM measurements in Figure A2- 2, the synthesis procedure leads to comparable NR array growth - structurally as well as optically in terms of their overall defect emission shape.

In an earlier study it was demonstrated that RTA at temperatures of *ca*. 450 °C leads to strong, defect-related orange emission, from samples prepared using the growth method outlined in this paper. These defects occurred regardless of the annealing atmosphere used (argon, oxygen, forming gas, nitrogen, vacuum) and represented the dominating recombination channel in these structures.[26]

Fueled by these earlier results photocatalytic measurements on a set of samples, annealed at 450 °C in contrasting RTA conditions – vacuum and oxygen, have been carried out. The defect-related orange emission was readily observed for both of the annealed samples (Figure 4-1a). While the as-grown sample shows deep-level defect (DLD) emission 1 order of magnitude smaller than the near-band-edge (NBE) emission, the DLD/NBE intensity ratio drastically increased for both samples subjected to RTA at 450 °C. The DLD-related peak for these samples was centered around 1.9 eV (orange) with two smaller shoulders being noticeable in the range 2.6–2.1 eV. The DLD emission spectrum was fitted with three Gaussian peaks indicating that the orange emission at 1.9 eV was responsible for more than 90 % of the total intensity (see Figure A2- 3).

Additionally the RTA treated samples exhibited clear features in the NBE emission with peaks at ca. 3.375, 3.363, 3.313, 3.240, and 3.170 eV. For the as-grown sample only a broad peak at ca. 3.363 eV and a sub-bandgap emission centered around 3.225 eV could be noticed.

Figure 4-1a already includes the assignment of the observed NBE peaks stemming from a detailed discussion in a later section of this paper. For the moment it is only important to note the following: RTA at 450 °C leads to the emergence of strong defect-related orange emission with intensity on the same order of magnitude as the NBE – regardless of the annealing atmosphere used. Furthermore, contrasting RTA

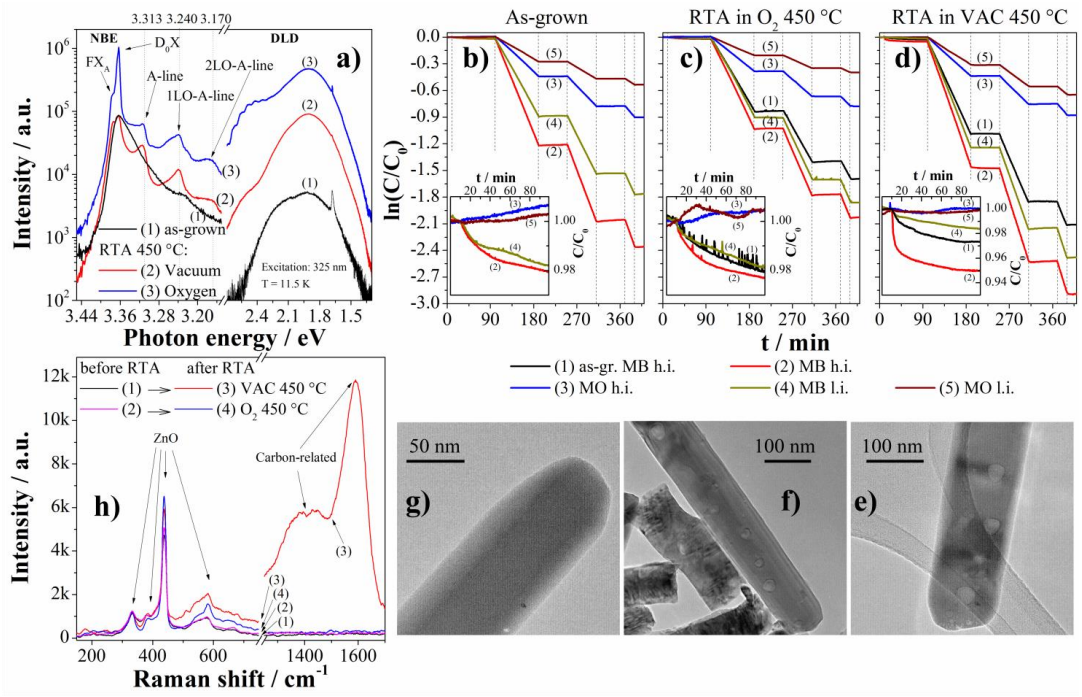

Figure 4-1: Materials characterization for as-grown and RTA treated (450 °C; in vacuum or oxygen) ZnO NR arrays. (a) LT-PL spectra of as-grown + RTA treated ZnO NR arrays. (b - d) Dark dye-adsorption and photocatalytic dye-degradation curves in methylene blue (MB) and methyl orange (MO) for as-grown + RTA treated samples. (insets) Change of the dye concentration in the first dark stage magnified. Dye-degradation was carried out under illumination from a UV-LED (365 nm) with high intensity (3 mW/cm^2; h.i.) or low intensity (1 mW/cm^2; l.i.). Corresponding TEM micrographs of annealed ZnO NR arrays: (e) VAC 450 °C, f) O_2 450 °C, and (g) as-grown ZnO nanorod. (h) Raman spectra of ZnO nanorod arrays before and after RTA in O_2 or VAC at 450 °C revealing the presence of a graphitic structure in the case of vacuum as annealing atmosphere (e.g. shell/layer or clusters).

conditions do not influence the appearance of characteristic peaks in the NBE emission. These peaks and their positions are essentially the same for the samples annealed in oxygen or vacuum.

With the knowledge of the changes in defect chemistry that results from the RTA – especially in regards to the strong orange DLD emission – the samples have been analyzed for their photocatalytic properties. First an as-grown sample has been analyzed. Its photocatalytic properties are shown in Figure 4-1b. When the sample is put into the solution (after initial stage without sample – dye solution only), the concentration is observed to decrease when MB is the dye used. On the other hand, virtually no change in the dye concentration can be noticed when MO is used as the

dye. However, MB is known to be easily adsorbed to various surfaces. Thus, it is possible that the dye is also attracted by the substrate. Therefore, the adsorption of MB cannot conclusively being attributed to the ZnO nanorod arrays alone. It is noteworthy that the dark adsorption is very similar for the two measurements performed on the sample, indicating the acceptable level of reproducibility of the measurement.

After turning on the UV-LED, both dyes are degraded by the ZnO nanorod arrays, as evidenced by a decreasing C/C_0 ratio. The difference in the magnitude of degradation between the two dye solutions used is related to the higher concentration of MO compared to MB. When comparing the photocatalytic dye-degradation of the sample under high (curves 2 and 3 in Figure 4-1b) and low intensity (curves 4 and 5 in Figure 4-1b), it can be seen that for MB (cationic) as well as for MO (anionic) a higher illumination intensity leads to faster dye-degradation.

Under the assumption that a higher illumination intensity leads to a higher photogenerated charge carrier density, the measurements suggest that the increased photocatalytic activity is due to an increased charge carrier transfer at the dye solution/ZnO interface. The exact mechanism of dye-degradation is not the topic of this study but studies on both systems ZnO/MO and ZnO/MB conclude that photogenerated holes in the valence band and photogenerated electrons in the conduction band (and trapped at defect sides) contribute to the dye-degradation.[21, 30-33] However, for MB an assessment of the formation of dye intermediates is to a certain extent possible by evaluating the dark stage after the first illumination stage. If the bleaching of the dye solution is caused due to the formation of the LMB over the reduction of MB by electrons from the conduction band from ZnO, a recovery of the C/C_0 ratio should be observed during this stage. In a dark, well aerated system (in this study constant stirring), LMB would thereby rapidly react with oxygen to form MB thus leading to the recovery.[27, 34] The fact that a strong recovery of the MB concentration is not observed indicates that this degradation mechanism is not dominant for the samples. However, it is important to note that the reoxidation to MB may be considerably slower in the case of LMB bonded to OH^- groups (e.g., bound to the nanorod surface).[35] On a longer time scale, the binding of LMB to the nanorod surface could in turn lead to photocatalyst poisoning, as also observed for other intermediates of the ZnO-MB system.[36]

The dye-degradation curves for the samples subjected to RTA in O_2 and vacuum at 450 °C are shown in Figure 4-1c and d, respectively. In order to evaluate the influence of RTA on the photocatalytic performance the samples were also studied prior to the heat treatment. These curves (black traces 1 in Figure 4-1c and d) show a similar behavior among all stages of the experiment when compared to the as-grown sample in Figure 4-1b.

After RTA both samples show an improved photocatalytic dye-degradation of MB and MO. For the orange-luminescent samples a higher number of charge carriers have thus to be present at the surface in order to facilitate the catalytic reactions. Since the defect-related recombination in these samples is dominant, this must in turn mean that recombination itself involves slow-trapping of a photogenerated electron to increase the lifetime of the photogenerated hole or that the defect states are active toward dye-degradation themselves.

When comparing these two samples, it is however noticed that the sample annealed in vacuum shows a strong dark adsorption of MB. The first dark stage is magnified for these samples in Figure 4-1c and d. For the first measurement after RTA (trace 2 – red; MB) a strong decrease of the dye concentration is visible for the sample annealed in vacuum. Interestingly no dark absorption could be observed for the measurements in MO solution. Since the dark adsorption is so different for dyes with different polarity it seems appropriate to reason that the surface of the nanorod arrays annealed in vacuum at 450 °C must exhibit some sort of charge – in this case negative.

From the results presented so far it is concluded that the observed dye-adsorption is not directly related to any of the observed PL features. It is not related either to the strong orange emission nor to the defect centers responsible for the features in the NBE ("A-lines") because if it were, then the sample annealed in oxygen would show a similar dark dye-adsorption.

Furthermore, it is noteworthy that after RTA both annealed samples degrade MB faster under low intensity illumination (1 mW/cm^2, curves 4 in Figure 4-1c and d) than compared to measurements under high intensity illumination but before RTA (3 mW/cm^2, curves 1 in Figure 4-1c and d). Thus, it may be possible that due to the relatively low MB concentration of *ca*. 17 µM the dye-degradation at higher illumination intensities might be somewhat mass transport limited.

In order to get a better understanding of what governs the observed photocatalytic properties TEM (Figure 4-1e – g) and Raman analysis (Figure 4-1h) have been carried out on these samples. Focusing on the TEM image of an as-grown NR first (Figure 4-1g) no obvious structural defects can be observed. This situation changes upon RTA. Here structural defects can be seen for both vacuum and O_2 as the annealing atmospheres (Figure 4-1e and Figure 4-1f, respectively). The defects are visible throughout the entire length of the rods and also the density of the defects seems to be independent of the annealing atmosphere used. A closer evaluation and correlation of the structural defects to the PL properties is carried out in a later section. However, for the moment it is important to note the appearance of the structural defects in both annealed sample does in turn indicate that these defects can also not be responsible for the strong dye-adsorption in the dark of the vacuum annealed sample.

The Raman measurements shown in Figure 4-1h were initially taken to (a) confirm the deposition of hexagonal NRs and (b) to look for possible manifestations of defects in the spectra. In short, the modes seen in the range 150 – 750 cm^{-1} can indeed be all attributed to wurtzite ZnO while no meaningful information may be gathered regarding the nature of any intrinsic point defects.[37-40] However, it is noteworthy that the intensity of the dominant E_2(H) mode (ca. 439 cm^{-1}) is increased after both RTA treatments. Generally, an increase in the peak intensity is associated with an improvement of the crystal quality.[20] When comparing the A_1(LO) mode (broad feature around 580 cm^{-1}) for both annealed samples, it can be additionally noticed that the sample annealed in vacuum exhibits and increased intensity. Since this mode is commonly associated with oxygen deficiency it may be reasonable to expect a slight increase in the concentration of oxygen vacancies upon RTA in vacuum.[20, 41, 42] Also the intensity of the collected spectra does not differ strongly for the respective samples. However, a surprising observation was made while scanning to longer Raman shifts (right part in Figure 4-1h). While all other samples showed no response for Raman shifts > 750 cm^{-1} the sample which has been annealed in vacuum at 450 °C exhibits a strong Raman signal in the range 1250 – 1700 cm^{-1}.

These signals cannot be assigned to ZnO but are in fact carbon-related modes that have been observed by other authors.[43-46] The peak centered around 1590 cm^{-1} originates from the G-band (graphitic or graphene-like) and the shoulder between ca. 1300 - 1500 cm^{-1} is the manifestation of the D-band (disordered/defective carbon).[43, 46]

From previous XPS measurements on samples prepared in a similar fashion to the samples in this study, it is known that such films are rich in carbon.[26] However, the concentration of carbon in the films (carbon residues as well as unintentional doping) has been found to be comparable for all samples grown and independent of the annealing atmosphere used. An example XPS spectrum (after prolonged argon bombardment for surface contamination removal) of a NR array annealed in vacuum at 450 °C is shown in Figure A2- 4. The high carbon concentration in the films is believed to originate from the high HMTA concentration in the growth solution. As reported previously, the high amount of HMTA is needed for the synthesis of intentionally defect rich NR arrays.[26]

Given the higher intensity of the G-band in the Raman measurements, RTA in vacuum at 450 °C must therefore lead to the formation of Raman active graphitic but defect-rich structures (e.g., layer or clusters) in or around the ZnO nanorods. From this first set of samples multiple questions regarding the influence of defects on the photocatalytic properties of the ZnO nanorod arrays persist:

- Is the improved photocatalytic performance unique to orange-luminescent ZnO NRs, or is the improvement only due the annealing treatment itself?
- May oxygen vacancies be responsible for the improved dye-degradation as they have been shown to aid photocatalytic processes?[23, 47]
- Are the structural defects unique to orange-luminescent ZnO NRs, and do they affect the photocatalytic properties?
- What causes the strong dark dye-adsorption for RTA in vacuum, and is the observed graphitic structure somehow linked to it?

In order to evaluate these questions another set of samples was annealed in vacuum but at multiple temperatures. These samples were then measured with respect to their physical and photocatalytic properties. The samples were then recharacterized following a second RTA treatment in oxygen at 380 °C. Furthermore, a lower illumination intensity (1 mW/cm^2) was chosen for the photocatalytic experiments since the measurements with varying intensities and MB as dye in Figure 4-1 indicated a possible mass transport limitation for the reaction performed using higher illumination intensities.

Before turning to the photocatalytic properties, we shall however examine first what

the nature of the observed structural defects and orange emission may be. The LT-PL spectra of the second set of samples are shown in Figure 4-2a-d. These spectra are again divided between NBE- and DLD-related bands.

Starting with the DLD emission of the samples annealed in vacuum only (Figure 4-2b-d), it can be seen that the emission changes significantly depending on the RTA temperature. While the intensity of the DLD band is comparably low for the samples annealed at 350 and 550 °C, very strong orange emission can be seen at 450 °C. Upon RTA at 550 °C additional defects are introduced centered around 2.5 eV. Given that vacuum was used as the annealing atmosphere it appears likely that these defects stem from the oxygen sublattice (e.g., oxygen vacancies). Additionally it is important to note that annealing at temperatures > 400 °C results in the desorption of hydrogen.[48] Hydrogen, however, can passivate deep-level defects and a possible desorption may thus lead to the emergence/increase of PL emissions in the visible region (especially green) and a decrease of the NBE.[49-51] For further discussion on the DLD emission of comparable samples the reader is referred to ref. [26].

In light of the appearance of strong orange emission upon RTA at 450 °C, it is however important to point out that this defect-emission is observed independent of the RTA atmosphere used (e.g., forming gas, argon, oxygen, vacuum). PL spectra of samples annealed in argon and forming gas are thus presented in Figure A2- 5 and Figure A2-5, respectively. Furthermore, the sample presented in Figure A2- 5 was investigated for the possible diffusion of oxygen vacancies toward the nanorod surface upon annealing treatments, as recently suggested by Bora et al.[52] For the presented samples this effect could however not be as clearly observed as in the mentioned literature report. Importantly the analysis revealed that long-term annealing prior and after the RTA treatment does neither affect the appearance of the orange emission nor does any of the annealing treatments have significant influence on the structural properties of the NRs (e.g., the surface remains comparable after RTA).

Cross-annealing in oxygen leads to a slight increase of the orange emission for the sample which had been previously subject to RTA in vacuum at 350 °C. No change of the emission shape is recognized for the sample which already showed strong orange emission. This is an important finding as it illustrates that the orange emission cannot

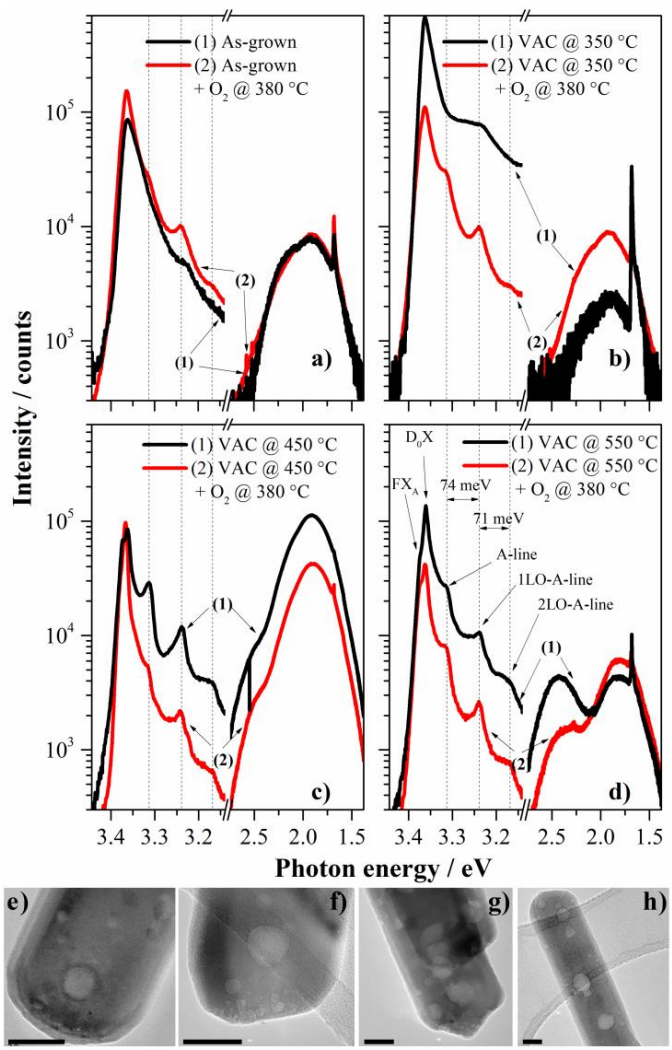

Figure 4-2: (a-d) LT-PL spectra of ZnO NR arrays before and after RTA in O_2 at 380 °C. Samples shown in b-d were subject to RTA in vacuum at 350 °C, 450 °C, or 550 °C, respectively. Please note that the spectra contain an artifact at ca. 1.68 eV originating from the second harmonic of the NBE peak at ca. 3.363 eV. (e-g) TEM images of the samples annealed in vacuum at 350 °C, 450 °C, or 550 °C, respectively. (h) TEM image of a NR which had been RTA treated in VAC at 450 °C and subsequently in O_2 at 380 °C. The scale bar in the images represents 50 nm.

be eliminated due to annealing in contrasting conditions (oxidizing and reducing). It further underlines a possible kinetic formation of this defect center as a function of the RTA temperature. For the sample which was first annealed in vacuum at 550 °C the intensity of the emission at ca. 2.5 eV is reduced upon cross-annealing. This may point toward a possible filling of oxygen vacancies at the NR surface due to annealing in oxygen. When focusing on the NBE, peaks at ca. 3.375, 3.363, 3.313, 3.240, and 3.170 eV are again visible for all annealed samples. The peaks seem to become more

pronounced with increasing RTA temperature. This is especially true when comparing the different spectra of samples annealed in vacuum at 350 and 450 °C (Figure 4-2b and c, respectively). However, a further temperature increase (550 °C in Figure 4-2d) does not lead to an additional increase in the NBE features.

The peaks centered around 3.375 and 3.363 eV can be assigned to free excitonic recombination (A-exciton, FX_A) and transitions of excitons bound to neutral donors D_0X, respectively.[53, 54] The presence of an undefined NBE peak, as is the case for the as-grown sample, implies that the NRs are highly defect-rich after the deposition. Especially the FX_A, which gets more pronounced with higher annealing temperatures, indicates an overall improvement of the crystallinity upon RTA. However, the RTA also leads to the emergence of the peaks at ca. 3.313, 3.240, and 3.170 eV, which are not located in the two electron satellite region.[54] These peaks show a separation of 74 meV and 71 meV (see Figure 4-2d) which is close to the optical phonon energy in ZnO (72 meV). It is therefore reasonable to assign the peaks at 3.240 and 3.170 eV as first and second longitudinal optical (LO) phonon replica of the peak at 3.313 eV, which is termed as the "A-line". The A-line luminescence features are often observed in ZnO, but their origin is still controversial.[55-59] Based on the optical phonon energy it becomes obvious that the A-line cannot be the phonon replica of the FX_A since the energy difference is too little (62 meV). The appearance of the A-lines is annealing atmosphere independent (see also Figure 4-1a) and also cross-annealing in oxygen at 380 °C does not show any influence on these features. Furthermore, it is important to note that the A-line emission is also not related to the observed DLD emission – especially with respect to the orange emission which was found to be annealing atmosphere independent but temperature dependent.

Interestingly the A-line emission coincides with the appearance of structural defects throughout the nanorods. As can be seen from the TEM images of the samples annealed in vacuum at 350, 450, and 550 °C (Figure 4-2e-g), respectively) these structural defects are present on/in all of the annealed samples. Furthermore, the TEM analysis revealed the presence of these defects throughout the entire rod (bulk and surface) and along the full length, indicating that their appearance is growth-stage independent. Also the structural defects are not influenced by subsequent RTA in oxygen (see example TEM image of a nanorod from a sample annealed in VAC 450 °C + O_2 380 °C in Figure 4-2h).

Some structural defects are shown in more detail in Figure 4-3. The crystal lattice can clearly be seen for both an as-grown as well as an annealed sample (Figure 4-3a and b, respectively). For the as-grown NR-tip no obvious inclusions or impurities are recognized. This is in contrast to the NR depicted in Figure 4-3b, which exhibits structural defects. A lighter contrast, as seen for all of these defects, results from an increased transmission trough the rods. This in turn may identify the defects as areas with less material. A hypothesis which is further supported by the fact that the crystal structure inside and around the rod is unchanged (Figure 4-3b). The "real" position of the electronic defect is therefore believed to reside at the edges of the lighter area – visible by a darker outline where the crystal lattice appears to be damaged.

A dark outline and the related lattice damage are also clearly visible for the defect shown in Figure 4-3c – especially in the upper part of the defect. However, this defect was specifically investigated for its stability upon prolonged electron-beam irradiation (200 kV). After 2 min its shape changed significantly (Figure 4-3d). Sample beam interactions are not unusual in TEM, however the rearrangement of the crystal in the bombarded area is the signature of local energy differences in the samples. No "healing" of the defect could be observed.

Figure 4-3e and f show visual differences of a structural defect depending on the TEM focus. While the investigated rod tip was in focus in Figure 4-3e the image in Figure 4-3f shows the same detail slightly out of focus. In the focused image the structural defect is almost not visible. However, when slightly out of focus defects can be clearly observed. This is an important finding since it provides evidence that the defects are indeed locally determined and that one defect does not propagate throughout the entire rod.

Additional PL analysis, on samples annealed at 450 °C, was carried out in order to further investigate the nature of the A-line as well as the orange emission in the samples. First, it is noted that during temperature dependent PL measurements the peak center of the A-line shifted to lower energies with increasing temperature (red-shift, see Figure A2- 6). The energy shift (in the range between 11.5 and 120 K) is ca. 12.6 meV compared to 17.7 and 21.3 meV for the D_0X and FX_A transitions, respectively. If the A-line emission observed here was caused due to a free-to-bound

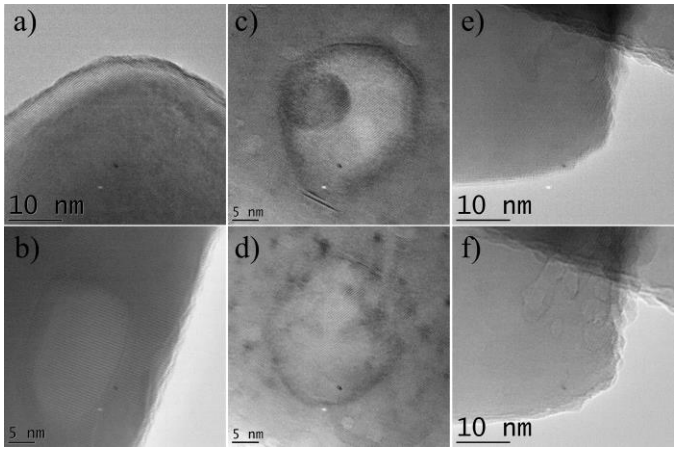

Figure 4-3: Detailed TEM images of ZnO NRs. (a) Tip of an as-grown ZnO NR. (b) Detail of a structural defect of an annealed sample. (c) Detail of a structural defect at the beginning of prolonged electron beam radiation (200 kV). (d) The same detail as in c but after 2 min of radiation. (e) Tip of an annealed nanorod when in focus. (f) The same detail as in e but slightly out of focus, resolving structural defects.

(FB) transition – as suggested by various authors[56, 58, 60-63] – the slope of the peak position shift as a function of temperature should be similar to the FX_A transition (after thermally correcting the A-line peak values).[56] However, for the samples examined in this study, the slope after the correction is still different (Figure A2- 6 and related comments). In turn this may be taken as a first indication that the A-line transition in these samples is of a different nature.

From the temperature-variable PL measurements an activation energy E_A of 7.9 meV was estimated, which could be attributed to the dominant orange emission in the DLD range. However, compared to the NBE peaks this emission center (ca. 1.9 eV) shows a blue-shift with increasing temperature (Figure A2- 7). Interestingly a significant shift is only visible for temperatures > 100 K. If a shallow donor is assumed to be involved in the transition it might be reasonable to expect thermalized electrons in the conduction band from these states at a specific temperature. As the recombination would then happen from the conduction band minimum (CBM) a blue-shift of the emission would occur, which could be partly compensated by the thermal shrinking of the bandgap.[57, 63] It is thus possible that the orange emission is dominated by the recombination between discrete defect states at lower temperatures but resembles a transition of an electron from the CBM into deep defect state with increasing temperature.

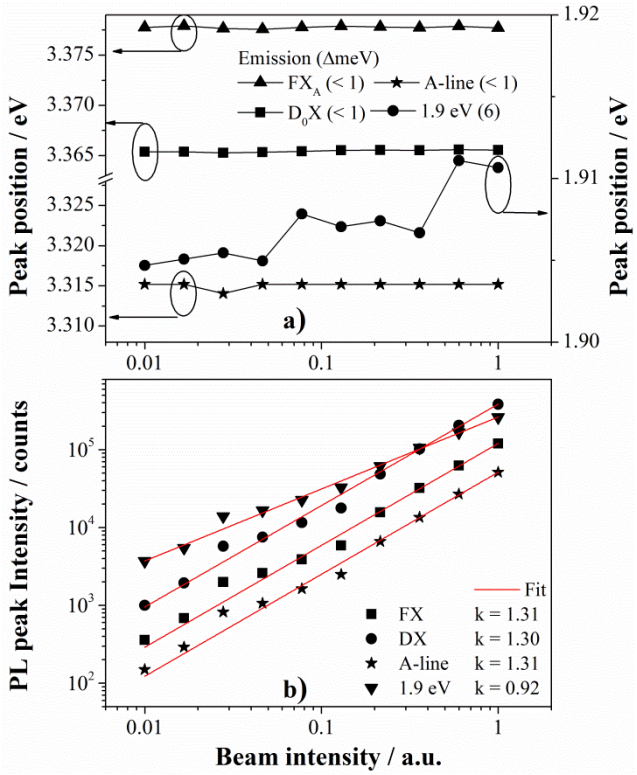

Figure 4-4: Peak position (a) and peak intensity (b) vs laser-beam intensity for the NBE emissions and the orange emission (centered at 1.9 eV) recorded from LT-PL measurements at 11.5 K. The lines in a are used as guides for the eyes.

Second, PL measurements with varying laser intensity were recorded and the peak position of the PL emission (Figure 4-4a) and intensity (Figure 4-4b) were examined as a function of the beam intensity. In regards to the A-line emission of the NBE, it was found that the peak position does not change significantly with varying beam intensity. In fact it can be seen that the change (< 1 meV) is similar to the FX_A and D_0X transitions. On the other hand a blue-shift of the peak position (6 meV) with increasing beam intensity has been observed for the defect center at 1.9 eV. Similarly the peak intensity can be investigated in relation to the intensity of the laser beam. Since the beam intensity was only varied by 2 orders of magnitude, the power dependence of the luminescence can be described as $I \propto L^k$ (where I is the PL intensity, L is the beam intensity, and k is a coefficient) and can thus be computed as $I = aL^k$,[64, 65] where a is a further coefficient. Free- and bound-excitonic transitions exhibit a coefficient k > 1. On the other hand, free-bound (FB) and donor-acceptor (DA) recombination processes progress with k < 1. [64, 65] The coefficient k has been determined to be 1.31, 1.30, 1.31, and 0.92 for the FX_A, D_0X, A-line and 1.9 eV

transition, respectively.

The absence of a peak shift and an intensity change with k > 1 for the A-line emission as a function of the beam intensity rules out the possibility of a FB or DA transition as possible origin. Furthermore the intensity change is strikingly similar to the excitonic transitions (FX_A and D_0X). Since the appearance of the A-line emission and the structural defects are coincidental, it is thus postulated that the A-line emission in this study is related to the structural defects (bound-exciton at structural defects). That structural defects may be involved in this emission has been also proposed by others.[55, 58, 66] However, the temperature and beam intensity dependent PL results in this study are more in favor of a bound-excitonic nature, similar to the finding of Kurbanov et al. which found speck-like defects upon annealing of ZnO nanocrystals.[55]

Following the explanations above it also becomes obvious that the 1.9 eV defect emission must be of different origin – either of DA or FB nature. The observed blue-shift with increasing beam intensity may be taken as a fingerprint of a DA transition at low temperature. Since more donor-acceptor pairs are photoexcited the distance between the defects decreases, which in turn leads to a blue-shift with increasing beam intensity.[57, 67]

Finally, the evidence presented here further supports the hypothesis that the orange emission of these samples may originate from the kinetic formation of the V_O-Zn_i defect complex.[26, 49, 68] Theoretical calculations of the defect-complex have shown that the formation via a kick-out process leads to the shift of the Zn_i closer to/into the CBM while the V_O shifts closer to the valence band.[69, 70] Together with the evidence from the temperature-dependent PL measurements it is postulated that at low temperatures photoluminescent transitions between these discrete defect states also contribute to the recorded signal. At room-temperature the recombination process is believed to happen mainly from the conduction band to the V_O state. Future research regarding the orange-luminescent defect center is nevertheless needed. In particular electron paramagnetic resonance (EPR) measurements could prove highly valuable for the examination of the recombination mechanism but also for the evaluation of the photocatalytic reactions and the involvement of intermediates.[71]

Based on the knowledge gained regarding the nature of the orange emission and the

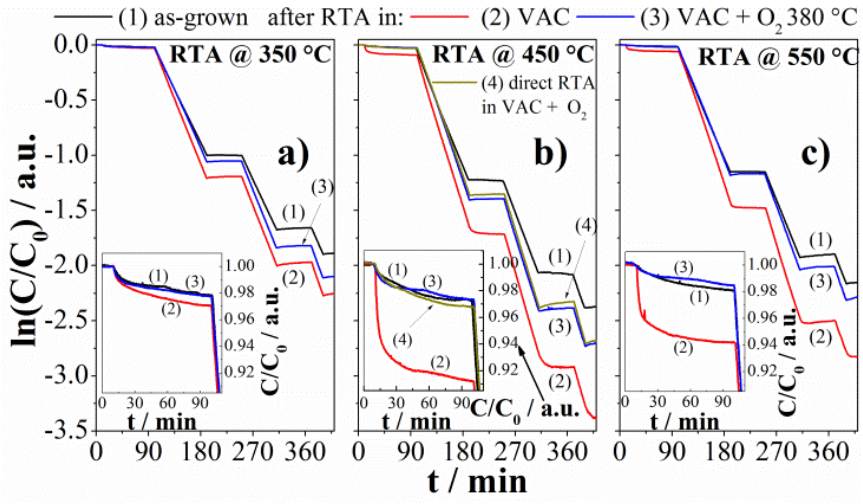

Figure 4-5: (a-c) Dark dye-adsorption and photocatalytic dye-degradation curves in MB for samples before and after RTA in VAC at different temperatures + after cross-annealing in O_2 at 380 °C. Illumination intensity: 1 mW/cm^2. (insets) Magnification of the change of MB concentration in the dark. Panel b also includes a sample which was only measured after receiving both RTA in VAC 450 °C + O_2 at 380 °C (trace 4). Only samples measured after RTA in VAC 450 and 550 °C show strong dye adsorption.

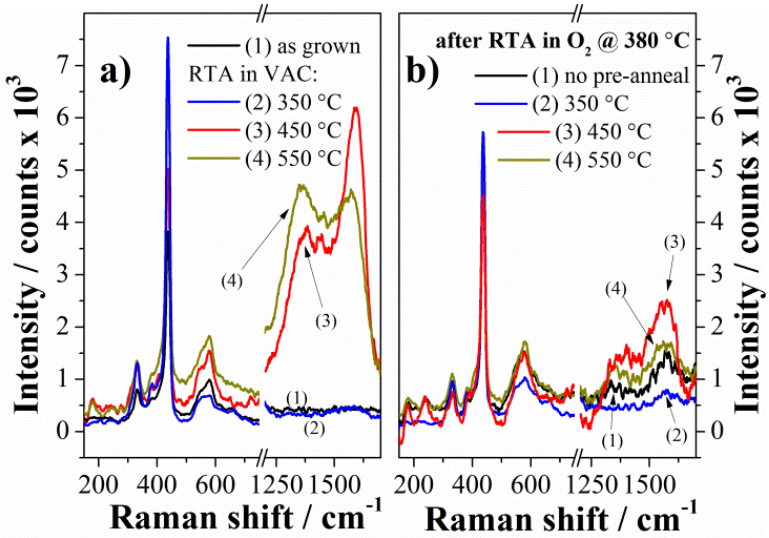

Figure 4-6: Raman spectra of samples annealed in vacuum at different temperatures before (a) and after (b) cross-annealing in O_2 at 380 °C. After cross-annealing in O_2 at 380 °C, the intensity of carbon related modes (e.g., graphitic shell) decreases dramatically.

structural defects an assessment of the photocatalytic properties of the defect-rich NR arrays cross-annealed in oxygen was carried out. The dye-degradation spectra together with the Raman spectra of the samples before and after annealing in oxygen are shown

in Figure 4-5 and Figure 4-6, respectively. Investigating the behavior of the samples in the dark first, no strong dark dye-adsorption could be observed for the sample annealed at 350 °C (Figure 4-5a). However, strong dye-adsorption in the dark was again present for the strong orange emitting sample (450 °C in Figure 4-5b, also compare to Figure 4-1d) but was also seen for the sample annealed in vacuum at 550 °C (Figure 4-5c). Interestingly cross-annealing in oxygen destroys the strong dark dye-adsorption for these samples. The same holds true for a sample that had been not tested for its photocatalytic performance prior to RTA in vacuum at 450 °C + O_2 at 380 °C (trace 4 in Figure 4-5b).

To evaluate these effects, annealed samples were measured for their Raman responses after each RTA step. As can be seen from Figure 4-6a, only annealing conditions that lead to strong dark dye-adsorption (450 and 550 °C) also result in the appearance of intense carbon-related modes in the Raman. However, these modes are dramatically decreased upon the cross-annealing step in O_2 at 380 °C (Figure 4-6b).

As elucidated in the first part of section 4.4, the carbon-related modes cannot be attributed to any of the observed PL emissions (including the observed structural defects). More so these features are found to be annealing atmosphere and temperature dependent. Thus, it is postulated that annealing in vacuum at elevated temperatures (> 400 °C) leads to diffusion of carbon from the bulk of the rods toward the surface, forming a graphitic structure (e.g., overlayer/shell). An additional RTA step in O_2 then results in "burning off" of these structures. In turn it becomes clear that the strong dark dye-adsorption of MB is directly correlated to the graphitic structure which must exhibit a negative charge.

Importantly a charged surface could lead to a better degradation of pollutants due to an increased attraction of same toward the nanorod surface. Hence, when evaluating the influence of a particular deep-level defect on the photocatalytic performance one has to pay extra attention to a possible interplay and synergy between the defect and possible surface effects. When both contribute to the photocatalytic performance a direct correlation to the effect of the deep-level defect may not be established. In the present study this problem has been tackled by cross-annealing the samples in oxygen. Furthermore, it is noteworthy that the dye-adsorption effect is diminished after several subsequent measurements.

Regarding the photocatalytic dye-degradation all samples show an improvement (i.e., increased degradation rate) after the respective RTA in vacuum (2 traces in Figure 4-5). However, it should be noticed that that sample annealed at 450 °C (strong orange emission) shows a larger improvement compared to samples annealed at 350 or 550 °C.

As mentioned above, it may be possible that an interplay between the strong dye-adsorption and the orange-luminescent defects leads to the enhanced degradation characteristics. An indication for this may be seen in the reduction of the degradation rate upon cross-annealing in oxygen. Based on the performance after cross-annealing, the apparent quantum efficiency (number of degraded dye molecules/number of incident photons) was estimated to be ca. 36.7 % (first light-on stage). Although the degradation rate decreases after cross annealing, the orange luminescent sample still shows an overall improvement of the photocatalytic performance when compared to the as-grown measurement – a behavior which was also observed when MO was used as a dye (see Figure A2- 8). This is not as clearly seen for the samples which were subject to RTA in vacuum at 350 or 550 °C prior to the cross-annealing step. In addition to the removal of carbon the cross-annealing in oxygen could therefore also play a crucial role in terms of the defect chemistry. It is reasonable to expect a certain filling of oxygen vacancies upon this treatment (see also decreased DLD emission at ca. 2.5 eV after cross-annealing in oxygen for the sample subjected to RTA in vacuum at 550 °C - Figure 4-2d), which in turn could lead to a reduced dye-degradation since oxygen vacancies have been reported to aid same.[23, 47] However, under the assumption that higher temperatures during the RTA in vacuum lead to a higher number of oxygen vacancies, it can be expected that the orange-luminescent defects (V_O-Zn_i defect complex) are indeed a major contributor to the enhanced photocatalytic performance for the sample annealed in vacuum at 450 °C. These results are in line with previous experimental evidence that suggest that the orange-luminescent defect centers act as slow electron traps which prolong the hole lifetime and therefore increase the possibility to run photochemical reactions.

4.5 Conclusions

A simple, low-temperature solution-based growth method was used to grow

intentionally defect-rich ZnO NR arrays. While keeping variables such as growth conditions/technique and morphology unchanged a careful analysis of the material properties and resulting photocatalytic performance of rapid thermally annealed ZnO nanorod arrays was carried out. The presence of various defects could be confirmed with structural defects, strong orange emission and a graphitic structure (e.g shell) dominating the material properties. Inherent to all annealed samples (T_{RTA} 350 - 550 °C) is the appearance of structural defects, which were attributed to the PL emission at ca. 3.31 eV. No direct influence on the photocatalytic performance could be established for these defects. Rapid thermal annealing at 450 °C in vacuum gave rise to strong orange defect emission. Building on an earlier study, further evidence has been provided that the orange emission in the samples is caused by the V_O-Zn_i defect-complex. Interestingly, these samples showed strong dye-adsorption and an improvement of the photocatalytic dye-degradation. The experimental studies suggest that a graphitic structure (e.g., shell) is responsible for the dark adsorption. In turn this may enforce the dye-degradation by orange-luminescent samples due to the attraction of MB toward the sample surface as a result of the graphitic structure.

Finally some more general conclusions regarding the assessment of photocatalytic properties of defect-rich materials can be drawn from the specific findings of this study. First, a comparison between different morphologies and/or growth methods is troublesome unless the defect chemistry is similar. Second, the significance of other possible contributions (e.g., surface-functionality and polarity, nature of the dye, other defects) needs to be evaluated prior to assessing the influence of a specific defect. Whenever possible, appropriate postdeposition treatments (e.g., cross-annealing and plasma- and surface treatment) should be used to help minimize these contributions. Finally, an interplay of intrinsic defects – which can mask the real contribution of a specific defect –must be expected when various defect centers are present in the material.

4.6 References

[1] C. M. Chang, M. H. Hon, and I. C. Leu, "Preparation of ZnO nanorod arrays with tailored defect-related characterisitcs and their effect on the ethanol gas sensing performance," *Sensors and Actuators B: Chemical*, vol. 151, no. 1, pp. 15-20, 2010.

[2] Y. Zhang, M. K. Ram, E. K. Stefanakos, and D. Y. Goswami, "Synthesis, Characterization, and Applications of ZnO Nanowires," *Journal of Nanomaterials,* vol. 2012, pp. 1-22, 2012.
[3] A. Echresh, C. O. Chey, M. Z. Shoushtari, O. Nur, and M. Willander, "Tuning the emission of ZnO nanorods based light emitting diodes using Ag doping," *Journal of Applied Physics,* vol. 116, no. 19, p. 193104, 2014.
[4] S. W. Lee, H. D. Cho, G. Panin, and T. Won Kang, "Vertical ZnO nanorod/Si contact light-emitting diode," *Applied Physics Letters,* vol. 98, no. 9, p. 093110, 2011.
[5] S.-H. Hwang, T.-H. Chung, and B.-T. Lee, "Study on the interfacial layer in ZnO/GaN heterostructure light-emitting diode," *Materials Science and Engineering: B,* vol. 157, no. 1-3, pp. 32-35, 2009.
[6] R. Könenkamp, R. C. Word, and M. Godinez, "Ultraviolet Electroluminescence from ZnO/Polymer Heterojunction Light-Emitting Diodes," *Nano Letters,* vol. 5, no. 10, pp. 2005-2008, 2005.
[7] D. Garcia-Alonso, S. Smit, S. Bordihn, and W. M. M. Kessels, "Silicon passivation and tunneling contact formation by atomic layer deposited Al2O3/ZnO stacks," *Semiconductor Science and Technology,* vol. 28, no. 8, p. 082002, 2013.
[8] S. Smit, D. Garcia-Alonso, S. Bordihn, M. S. Hanssen, and W. M. M. Kessels, "Metal-oxide-based hole-selective tunneling contacts for crystalline silicon solar cells," *Solar Energy Materials and Solar Cells,* vol. 120, pp. 376-382, 2014.
[9] S. Xu and Z. L. Wang, "One-dimensional ZnO nanostructures: Solution growth and functional properties," *Nano Research,* vol. 4, no. 11, pp. 1013-1098, 2011.
[10] F. Liu, M. Y. Guo, Y. H. Leung, A. B. Djurišić, A. M. C. Ng, and W. K. Chan, "Effect of starting properties and annealing on photocatalytic activity of ZnO nanoparticles," *Applied Surface Science,* vol. 283, pp. 914-923, 2013.
[11] F. Liu, Y. H. Leung, A. B. Djurišić, A. M. C. Ng, and W. K. Chan, "Native Defects in ZnO: Effect on Dye Adsorption and Photocatalytic Degradation," *The Journal of Physical Chemistry C,* vol. 117, no. 23, pp. 12218-12228, 2013.
[12] M. Liu, C.-Y. Nam, C. T. Black, J. Kamcev, and L. Zhang, "Enhancing Water Splitting Activity and Chemical Stability of Zinc Oxide Nanowire Photoanodes with Ultrathin Titania Shells," *The Journal of Physical Chemistry C,* vol. 117, no. 26, pp. 13396-13402, 2013.
[13] K. S. Ranjith, R. Pandian, E. McGlynn, and R. T. Rajendra Kumar, "Alignment, Morphology and Defect Control of Vertically Aligned ZnO Nanorod Array: Competition between “Surfactant” and “Stabilizer” Roles of the Amine Species and Its Photocatalytic Properties," *Crystal Growth & Design,* vol. 14, no. 6, pp. 2873-2879, 2014.
[14] F. Kayaci, S. Vempati, I. Donmez, N. Biyikli, and T. Uyar, "Role of zinc interstitials and oxygen vacancies of ZnO in photocatalysis: a bottom-up approach to control defect density," *Nanoscale,* vol. 6, no. 17, pp. 10224-10234, 2014.
[15] L. Cai *et al.*, "V ions implanted ZnO nanorod arrays for photoelectrochemical water splitting under visible light," *International Journal of Hydrogen Energy,* vol. 40, no. 3, pp. 1394-1401, 2015.

[16] A. Janotti and C. G. Van de Walle, "Fundamentals of zinc oxide as a semiconductor," *Reports on Progress in Physics,* vol. 72, no. 12, p. 126501, 2009.
[17] A. B. Djurišić, A. M. C. Ng, and X. Y. Chen, "ZnO nanostructures for optoelectronics: Material properties and device applications," *Progress in Quantum Electronics,* vol. 34, no. 4, pp. 191-259, 2010.
[18] G. P. Papari *et al.*, "Morphological, Structural, and Charge Transfer Properties of F-Doped ZnO: A Spectroscopic Investigation," *The Journal of Physical Chemistry C,* vol. 121, no. 29, pp. 16012-16020, 2017.
[19] J. Al-Sabahi, T. Bora, M. Al-Abri, and J. Dutta, "Controlled Defects of Zinc Oxide Nanorods for Efficient Visible Light Photocatalytic Degradation of Phenol," *Materials,* vol. 9, no. 4, pp. 238-247, 2016.
[20] J. Wang *et al.*, "Oxygen vacancy induced band-gap narrowing and enhanced visible light photocatalytic activity of ZnO," *ACS Appl Mater Interfaces,* vol. 4, no. 8, pp. 4024-4030, 2012.
[21] S. G. Kumar and K. S. R. K. Rao, "Zinc oxide based photocatalysis: tailoring surface-bulk structure and related interfacial charge carrier dynamics for better environmental applications," *RSC Adv.,* vol. 5, no. 5, pp. 3306-3351, 2015.
[22] X. Zhang *et al.*, "Effect of aspect ratio and surface defects on the photocatalytic activity of ZnO nanorods," *Sci Rep,* vol. 4, p. 4596, 2014.
[23] J. Wang, P. Liu, X. Fu, Z. Li, W. Han, and X. Wang, "Relationship between Oxygen Defects and the Photocatalytic Property of ZnO Nanocrystals in Nafion Membranes," *Langmuir,* vol. 25, no. 2, pp. 1218-1223, 2009.
[24] S. S. Warule, N. S. Chaudhari, B. B. Kale, and M. A. More, "Novel sonochemical assisted hydrothermal approach towards the controllable synthesis of ZnO nanorods, nanocups and nanoneedles and their photocatalytic study," *CrystEngComm,* vol. 11, no. 12, pp. 2776-2783, 2009.
[25] S. Baruah, S. S. Sinha, B. Ghosh, S. K. Pal, A. K. Raychaudhuri, and J. Dutta, "Photoreactivity of ZnO nanoparticles in visible light: Effect of surface states on electron transfer reaction," *Journal of Applied Physics,* vol. 105, no. 7, p. 074308, 2009.
[26] J. Kegel, F. Laffir, I. M. Povey, and M. E. Pemble, "Defect-promoted photo-electrochemical performance enhancement of orange-luminescent ZnO nanorod-arrays," *Phys Chem Chem Phys,* vol. 19, no. 19, pp. 12255--12268, 2017.
[27] A. Mills and C. O'Rourke, "Adsorption and Destruction of Methylene Blue by Semiconductor Photocatalysis," *Green,* vol. 1, no. 1, pp. 105–113, 2011.
[28] X. Yan, T. Ohno, K. Nishijima, R. Abe, and B. Ohtani, "Is methylene blue an appropriate substrate for a photocatalytic activity test? A study with visible-light responsive titania," *Chemical Physics Letters,* vol. 429, no. 4-6, pp. 606-610, 2006.
[29] S. Bae, S. Kim, S. Lee, and W. Choi, "Dye decolorization test for the activity assessment of visible light photocatalysts: Realities and limitations," *Catalysis Today,* vol. 224, pp. 21-28, 2014.
[30] T. Chen, Y. Zheng, J. M. Lin, and G. Chen, "Study on the photocatalytic degradation of methyl orange in water using Ag/ZnO as catalyst by liquid chromatography electrospray ionization ion-trap mass spectrometry," *J Am Soc Mass Spectrom,* vol. 19, no. 7, pp. 997-1003, 2008.

[31] M. Y. Guo *et al.*, "Effect of Native Defects on Photocatalytic Properties of ZnO," *The Journal of Physical Chemistry C,* vol. 115, no. 22, pp. 11095-11101, 2011.
[32] J. Kaur, S. Bansal, and S. Singhal, "Photocatalytic degradation of methyl orange using ZnO nanopowders synthesized via thermal decomposition of oxalate precursor method," *Physica B: Condensed Matter,* vol. 416, pp. 33-38, 2013.
[33] Y. Wang, R. Shi, J. Lin, and Y. Zhu, "Enhancement of photocurrent and photocatalytic activity of ZnO hybridized with graphite-like C3N4," *Energy & Environmental Science,* vol. 4, no. 8, pp. 2922–2929, 2011.
[34] A. Mills and J. Wang, "Photobleaching of methylene blue sensitised by TiO2: an ambiguous system?," *Journal of Photochemistry and Photobiology A: Chemistry,* vol. 127, no. 1–3, pp. 123-134, 1999.
[35] M. Imran, A. B. Yousaf, X. Zhou, K. Liang, Y. F. Jiang, and A. W. Xu, "Oxygen-Deficient TiO2-x/Methylene Blue Colloids: Highly Efficient Photoreversible Intelligent Ink," *Langmuir,* vol. 32, no. 35, pp. 8980-8987, 2016.
[36] K. S. Ranjith and R. T. Rajendra Kumar, "Regeneration of an efficient, solar active hierarchical ZnO flower photocatalyst for repeatable usage: controlled desorption of poisoned species from active catalytic sites," *RSC Advances,* vol. 7, no. 9, pp. 4983-4992, 2017.
[37] S. Baruah and J. Dutta, "Hydrothermal growth of ZnO nanostructures," *Science and Technology of Advanced Materials,* vol. 10, no. 1, p. 013001, 2009.
[38] S. Kuriakose, B. Satpati, and S. Mohapatra, "Enhanced photocatalytic activity of Co doped ZnO nanodisks and nanorods prepared by a facile wet chemical method," *Phys Chem Chem Phys,* vol. 16, no. 25, pp. 12741-12749, 2014.
[39] D. K. Mishra *et al.*, "Carbon doped ZnO: Synthesis, characterization and interpretation," *Journal of Magnetism and Magnetic Materials,* vol. 329, pp. 146-152, 2013.
[40] D. Vernardou *et al.*, "The effect of growth time on the morphology of ZnO structures deposited on Si (100) by the aqueous chemical growth technique," *Journal of Crystal Growth,* vol. 308, no. 1, pp. 105-109, 2007.
[41] C. F. Windisch, G. J. Exarhos, C. Yao, and L.-Q. Wang, "Raman study of the influence of hydrogen on defects in ZnO," *Journal of Applied Physics,* vol. 101, no. 12, p. 123711, 2007.
[42] X. He, H. Yang, Z. Chen, and S. S. Y. Liao, "Effect of Co-doping content on hydrothermal derived ZnO array films," *Physica B: Condensed Matter,* vol. 407, no. 15, pp. 2895-2899, 2012.
[43] N. Tu, K. T. Nguyen, D. Q. Trung, N. T. Tuan, V. N. Do, and P. T. Huy, "Effects of carbon on optical properties of ZnO powder," *Journal of Luminescence,* vol. 174, pp. 6-10, 2016.
[44] X. Liu, H. Du, X. W. Sun, B. Liu, D. Zhao, and H. Sun, "Visible-light photoresponse in a hollow microtube–nanowire structure made of carbon-doped ZnO," *CrystEngComm,* vol. 14, no. 8, pp. 2886–2890, 2012.
[45] J. Khanderi, R. C. Hoffmann, A. Gurlo, and J. J. Schneider, "Synthesis and sensoric response of ZnO decorated carbon nanotubes," *Journal of Materials Chemistry,* vol. 19, no. 28, pp. 5039–5046, 2009.

[46] G. Katumba, B. W. Mwakikunga, and T. R. Mothibinyane, "FTIR and Raman Spectroscopy of Carbon Nanoparticles in SiO2, ZnO and NiO Matrices," *Nanoscale Research Letters,* vol. 3, no. 11, pp. 421-426, 2008.

[47] F. Kayaci, S. Vempati, C. Ozgit-Akgun, N. Biyikli, and T. Uyar, "Enhanced photocatalytic activity of homoassembled ZnO nanostructures on electrospun polymeric nanofibers: A combination of atomic layer deposition and hydrothermal growth," *Applied Catalysis B: Environmental,* vol. 156-157, pp. 173-183, 2014.

[48] R. Xie *et al.*, "Enhancement and patterning of ultraviolet emission in ZnO with an electron beam," *Applied Physics Letters,* vol. 88, no. 13, p. 134103, 2006.

[49] A. B. Djurišić *et al.*, "Defect emissions in ZnO nanostructures," *Nanotechnology,* vol. 18, no. 9, p. 095702, 2007.

[50] T. Sekiguchi, N. Ohashi, and Y. Terada, "Effect of Hydrogenation on ZnO Luminescence," *Japanese Journal of Applied Physics,* vol. 36, no. 3A, pp. L289-L291, 1997.

[51] N. Ohashi, T. Ishigaki, N. Okada, T. Sekiguchi, I. Sakaguchi, and H. Haneda, "Effect of hydrogen doping on ultraviolet emission spectra of various types of ZnO," *Applied Physics Letters,* vol. 80, no. 16, pp. 2869-2871, 2002.

[52] T. Bora, P. Sathe, K. Laxman, S. Dobretsov, and J. Dutta, "Defect engineered visible light active ZnO nanorods for photocatalytic treatment of water," *Catalysis Today,* vol. 284, pp. 11-18, 2017.

[53] A. Teke *et al.*, "Excitonic fine structure and recombination dynamics in single-crystalline ZnO," *Physical Review B,* vol. 70, no. 19, p. 195207, 2004.

[54] B. K. Meyer *et al.*, "Bound exciton and donor–acceptor pair recombinations in ZnO," *physica status solidi (b),* vol. 241, no. 2, pp. 231-260, 2004.

[55] S. S. Kurbanov, G. N. Panin, and T. W. Kang, "Spatially resolved investigations of the emission around 3.31 eV (A-line) from ZnO nanocrystals," *Applied Physics Letters,* vol. 95, no. 21, p. 211902, 2009.

[56] K. W. Liu, R. Chen, G. Z. Xing, T. Wu, and H. D. Sun, "Photoluminescence characteristics of high quality ZnO nanowires and its enhancement by polymer covering," *Applied Physics Letters,* vol. 96, no. 2, p. 023111, 2010.

[57] Z. Yang and J. L. Liu, "Donor-acceptor-pair photoluminescence in Ga-doped ZnO thin films grown by plasma-assisted molecular beam epitaxy," *Journal of Vacuum Science & Technology B, Nanotechnology and Microelectronics: Materials, Processing, Measurement, and Phenomena,* vol. 28, no. 3, pp. C3D6-C3D9, 2010.

[58] M. Schirra *et al.*, "Stacking fault related3.31−eVluminescence at130−meVacceptors in zinc oxide," *Physical Review B,* vol. 77, no. 12, p. 125215, 2008.

[59] M. R. Wagner, P. Zimmer, A. Hoffmann, and C. Thomsen, "Resonant Raman scattering at exciton intermediate states in ZnO," *physica status solidi (RRL) – Rapid Research Letters,* vol. 1, no. 5, pp. 169-171, 2007.

[60] B. P. Zhang, N. T. Binh, Y. Segawa, K. Wakatsuki, and N. Usami, "Optical properties of ZnO rods formed by metalorganic chemical vapor deposition," *Applied Physics Letters,* vol. 83, no. 8, pp. 1635-1637, 2003.

[61] Q. X. Zhao, M. Willander, R. E. Morjan, Q. H. Hu, and E. E. B. Campbell, "Optical recombination of ZnO nanowires grown on sapphire and Si substrates," *Applied Physics Letters,* vol. 83, no. 1, pp. 165-167, 2003.

[62] Q. Wang, Y. Yan, Y. Zeng, Y. Lu, L. Chen, and Y. Jiang, "Free-Standing Undoped ZnO Microtubes with Rich and Stable Shallow Acceptors," *Sci Rep*, vol. 6, p. 27341, 2016.
[63] H. He, Q. Yang, C. Liu, L. Sun, and Z. Ye, "Size-Dependent Surface Effects on the Photoluminescence in ZnO Nanorods," *The Journal of Physical Chemistry C*, vol. 115, no. 1, pp. 58-64, 2011.
[64] T. Schmidt, K. Lischka, and W. Zulehner, "Excitation-power dependence of the near-band-edge photoluminescence of semiconductors," *Physical Review B*, vol. 45, no. 16, pp. 8989-8994, 1992.
[65] A.-S. Gadallah and M. M. El-Nahass, "Structural, Optical Constants and Photoluminescence of ZnO Thin Films Grown by Sol-Gel Spin Coating," *Advances in Condensed Matter Physics*, vol. 2013, pp. 1-11, 2013.
[66] J. L. Morrison *et al.*, "Optical properties of ZnO and MgZnO nanocrystals below and at the phase separation range," *Journal of Applied Physics*, vol. 104, no. 12, p. 123519, 2008.
[67] K. Tamura *et al.*, "Donor–acceptor pair luminescence in nitrogen-doped ZnO films grown on lattice-matched ScAlMgO4 (0001) substrates," *Solid State Communications*, vol. 127, no. 4, pp. 265-269, 2003.
[68] K. H. Tam *et al.*, "Defects in ZnO Nanorods Prepared by a Hydrothermal Method," *The Journal of Physical Chemistry B*, vol. 110, no. 42, pp. 20865-20871, 2006.
[69] D.-H. Kim, G.-W. Lee, and Y.-C. Kim, "Interaction of zinc interstitial with oxygen vacancy in zinc oxide: An origin of n-type doping," *Solid State Communications*, vol. 152, no. 18, pp. 1711-1714, 2012.
[70] Y.-S. Kim and C. H. Park, "Rich Variety of Defects in ZnO via an Attractive Interaction between O Vacancies and Zn Interstitials: Origin of n-Type Doping," *Physical Review Letters*, vol. 102, no. 8, p. 086403, 2009.
[71] G. Vitiello *et al.*, "5,6-Dihydroxyindole-2-carboxylic Acid–TiO2 Charge Transfer Complexes in the Radical Polymerization of Melanogenic Precursor(s)," *The Journal of Physical Chemistry C*, vol. 120, no. 11, pp. 6262-6268, 2016.

Chapter 5

This chapter and accompanying appendix represent an adapted version of the publication:

> J. Kegel, J. Halpin, F. Laffir, I. M. Povey, and M. E. Pemble, "Rapid low-temperature solution growth of ZnO:Co nanorod arrays with controllable visible light absorption," *CrystEngComm*, vol. 19, pp. 1938-1946, 2017.

Changes to the publication were only made in regards to formatting requirements.

5 Rapid low-temperature solution growth of ZnO:Co nanorod arrays with controllable visible light absorption

5.1 Abstract

Cobalt doped zinc oxide (ZnO:Co) nanorod arrays with strong visible light absorption were successfully grown via a solution-based method. The deposition technique presented allows the rapid (1 h) growth of well aligned nanorods directly onto seed-layer coated substrates at low temperatures (ca. 85 °C), which when compared to previously reported growth methods represents a significant advance in terms of routes to the production of visible-light absorbing ZnO-based materials. Changing the cobalt concentration in the growth solution allows for the controlled growth of ZnO:Co nanorods with variable visible light absorption. The emergence of strong additional, cobalt 3d related visible light absorption features and band gap narrowing with increasing concentration of cobalt (until 20 % cobalt/zinc concentration in growth solution) is demonstrated. A cobalt concentration of up to 2.2 atom % (at 30 % cobalt/zinc concentration in growth solution) can be achieved and careful analysis of the crystal growth process and material properties of the nanorod arrays shows that Co^{2+} successfully replaces Zn^{2+} in the lattice.

5.2 Introduction

Potential routes to the fabrication of ZnO doped with small amounts (a few atomic percent) of Co^{2+} ions have attracted a great deal of attention in recent years – since ZnO:Co has emerged as a promising material to be used as diluted magnetic semiconductor (DMS).[1, 2] Furthermore ZnO:Co could be an interesting candidate for photo-chemical applications due to visible light photoconductivity and possible ferromagnetic properties improving charge carrier separation.[3-5] For this latter application the materials ability to absorb visible light is paramount

At the present time, literature reports on the influence of Co doping on the optical properties of ZnO:Co are somewhat incoherent and difficult to compare due to the various deposition techniques and doping concentrations used. Some groups reported a blue shift of the band gap with increasing Co-concentration.[6, 7] Mostly the Burstein-Moss effect is given as an explanation for the broadening of the band gap with increasing doping concentration.[6, 8] On the other hand, a red shift with

increasing Co concentration was observed by other groups.[4, 9, 10] This latter finding is strengthened by photo-luminescence (PL) measurements which show a shift of the radiative recombination near the band edge towards higher wavelengths.[11, 12] Strong semiconductor-metal (sp-d) inter-actions are given as a reason for the observed red shift.[9, 13] A combination and competition of both the Burstein-Moss effect[1] and sp-d interactions, in dependence on the doping concentration appears plausible.

In addition, some optical measurements give evidence of additional transitions in the visible region of the spectrum but again, literature reports vary in this regard. Whereas many researchers report that they do not detect any additional features in UV-Visible spectroscopy (UV-Vis) or PL measurements,[7, 12, 14-16] other groups do seem to observe additional features.[4, 9-11, 13, 17, 18] Generally these features (and their distinct shapes) are attributed to the split of Co 3d states in the tetrahedral crystal field symmetry (wurtzite structure) of ZnO,[19] leading to sharp transitions around 550 nm, 610 nm and 650 nm.[19-21]

Interestingly the sensitization of the Co d-d features with other charge transfer mechanisms (i.e. metal to ligand conduction band charge transfer ($ML_{CB}CT$) and the ligand valence band to metal charge transfer ($L_{VB}MCT$)) can lead to visible light photoconductivity.[5, 22-24] Also it was shown by different groups that ZnO:Co can be successfully used for photo-chemical applications such as visible light photo-catalysis and photo-electrochemical water oxidation.[4, 25-27]

Most reports that identify additional absorption in the visible range used higher temperatures deposition methods (> 200 °C) to prepare the ZnO:Co materials. Thus it may be suggested that in order for the material to exhibit visible absorption caused by Co d-d transitions, higher deposition temperatures/methods are required. Furthermore the majority of the studies referred to above prepared suspended nanostructures and did not deposit ZnO:Co directly onto substrates, apart from the work described in references[17, 18] which employed thin film deposition techniques at temperatures > 500 °C. Reports on low temperature growth (< 120 °C) of ZnO:Co which exhibits additional d-d absorption features are scarce.[20, 28-30] Growth directly onto substrates (i.e. not the growth of suspended particles/nanorods) is thereby only

[1] For an explanation of the Burstein-Moss effect please refer to section 1.4.3 and Ref. [212] of Chapter1.

reported in ref. [27] and [27, 30], for experiments involving very low levels of cobalt doping (i.e. little additional d-d absorption). A low-temperature solution-based growth of ZnO:Co directly on to substrates that produces nanorod arrays exhibiting strong additional absorption in the visible range would therefore represent a new and novel route to the fabrication of ZnO:Co structures with potential optoelectronic and photochemical applications.

In this letter we report on a low-temperature (85 °C), solution-based method for the deposition of ZnO:Co directly onto seed-layer coated substrates. The growth from strong basic solution happens rapidly, resulting in the formation of ZnO:Co nanorods of 3 µm length within 1 h of deposition. Evaluation of the crystal growth process points out that Ethanolamine plays a crucial role for both the deposition of undoped and cobalt doped ZnO nanorods. Careful analysis of the cobalt-doped samples confirm the successful substitution of Zn^{2+} by Co^{2+} with no additional impurity phases (e.g. Co_xO_y, $Co(OH)_2$, or metallic Co-clusters) being detected by XRD, XPS and Raman spectroscopy. Up to a certain concentration of cobalt in the growth solution (20 %) the samples show a red shift of the band gap and the increase of Co d-d related absorption features in the visible range. A detailed explanation of possible mechanisms leading to the observed optical properties is given. Due to the strong visible light absorption the developed solution-based growth method opens up a new route to fabricate ZnO:Co nanorod arrays at low-temperatures, which will further advance the use of the material especially for solar energy related applications.

5.3 Experimental

Chemicals for ZnO nanorod and seed layer deposition: zinc acetate dihydrate (ZnAc, reagent grade), 4M sodium hydroxide solution (NaOH), ethanolamine (EA), cobalt(II) acetate tetrahydrate (CoAc, reagent grade). All chemicals were purchased from Sigma Aldrich. Millipore water (H_2O) was used as the solvent for nanorod growth. Methanol was used as the solvent for seed layer deposition.

Substrate cleaning at room temperature: Microscope glass slides were used as substrates. Prior to the seed layer deposition the glass slides were cleaned ultrasonically in mixture of Millipore water, ammonium hydroxide (NH_4OH) and Hydrogen peroxide (H_2O_2) in ratio of 5:1:1 for 30 min. Afterwards the substrates were

rinsed with Millipore water and dried in nitrogen.

Seed layer deposition at room temperature: The solution for seed layer deposition was prepared following the recipe of Cai et al.[31] A methanolic NaOH solution (0.03 M) was added to a pre-heated (60 °C) solution of ZnAc in methanol (0.1 M) and stirred for one hour. The solution was then dropped onto the substrate and spun at 2500 rpm for 30 seconds. The substrate was then immediately transferred to a pre-heated hotplate (100 °C) for 10 min. Afterwards the substrate was transferred to a lab furnace for annealing in air at 350 °C for 30 min. The procedure outlined above was then repeated two more times.

ZnO and ZnO:Co nanorod growth: First 1.1 g ZnAc were dissolved in 20 ml H_2O under constant stirring at room temperature until a clear solution was obtained. Afterwards 7.5 ml of 4M NaOH solution were added yielding a milky solution at first which then clears up again under constant stirring. After the solution was clear for 2 min 5 ml MEA were added to the solution under constant stirring for 30 min. Finally the volume of the solution was increased to 50 ml by adding Millipore H_2O. Subsequently the final solution was transferred to a sealable plastic bottle.

Seed layer coated substrates where then placed in the plastic bottle at a slight angle, seed layer facing down. Consequently the sealed plastic bottles were put into a pre-heated (85 °C) water bath for one hour. After the growth the samples were thoroughly rinsed in Millipore water and blow-dried in nitrogen.

For the growth of cobalt doped ZnO nanostructures CoAc was added to solution before adding the NaOH. The cobalt precursor was added according to the desired concentration-ratio of ZnAC/CoAc. Stated percentages of cobalt are therefore the concentration of CoAc with respect to the ZnAc concentration in the growth solution (actual cobalt concentrations are mentioned specifically).

Characterization: Scanning Electron Microscopy was carried out using a FEI Quanta 650 FEG High Resolution Scanning Electron Microscope. XPS measurements were performed at University of Limerick using a Kratos AXIS 165 spectrometer equipped with a mono Al Kα X-ray gun. Survey and high resolution scans were recorded with a 1 eV and 0.05 eV resolution, respectively. XRD spectra were taken using a Panalytical X`Pert MRD X-Ray diffractometer (Cu Kα radiation $\lambda = 0.1541874$ nm) in rocking curve configuration. The resolution of the scans was 0.02°. A Renishaw micro-Raman

spectrometer equipped with a 514 nm laser was used for Raman analysis. Diffuse reflectance and transmittance measurements in the range of 300 – 800 nm were done using a Perkin Elmer 950 UV-Vis spectrometer equipped with an integrating sphere.

5.4 Results and discussion

The growth characteristics of ZnO and ZnO:Co were investigated by SEM in order to get some insight into the various stages of the nanorod growth. Figure 5-1 shows SEM micrographs of the ZnO seed layer (Figure 5-1a), undoped ZnO nanorods (Figure 5-1b) and ZnO:Co growth (30 % Co/Zn concentration) at various time intervals (Figure 5-1c-h).

Figure 5-1a depicts layer growth induced via spin-coating. Three sub-layers can be recognized in this image. This structure is the result of the three consecutive spin-coating runs. Each sub-layer consists of ca. 20 nm small ZnO particles forming a conformal layer. Scratches as shown in Figure 5-1a were found to be somewhat rare, which we interpret as being indicative of good overall substrate coverage by the seed layer. Subsequent growth of undoped ZnO results in the formation of well aligned nanorod arrays with an overall length of about 3 µm (Figure 5-1 b). Furthermore the rods exhibit pointed tips, which can be attributed to the alkalinity of the growth solution resulting in a Zn^{2+} concentration gradient along the rod during the growth.[32] The average rod diameter was estimated to be 70 nm.

The various growth stages of ZnO:Co at different times (Figure 5-1c-g) give some insight into the growth process. After 10 min the ZnO seed layer is over-coated with an inhomogeneous additional layer. XRD analysis showed only ZnO peaks for this sample (see Figure A3- 1 for growth time dependent XRD spectra). Since no XRD data could be recorded for the ZnO seed layer the XRD patterns seen for this sample must result from the growing surface-layer. ZnO nanowire growth starts after the formation of this surface-layer. As can be seen from Figure 5-1d the growing nanorods are covered by a thin, flaky layer. At this growth stage the rods start to grow at either the interface between the seed layer and the surface ZnO-layer present after 10 min, or directly from the top of the surface-layer and additional layer growth then happens simultaneously. The former appears more likely, given the flaky nature of the layer in places where there seems to be no ZnO nanorod growth. XRD analysis carried out on

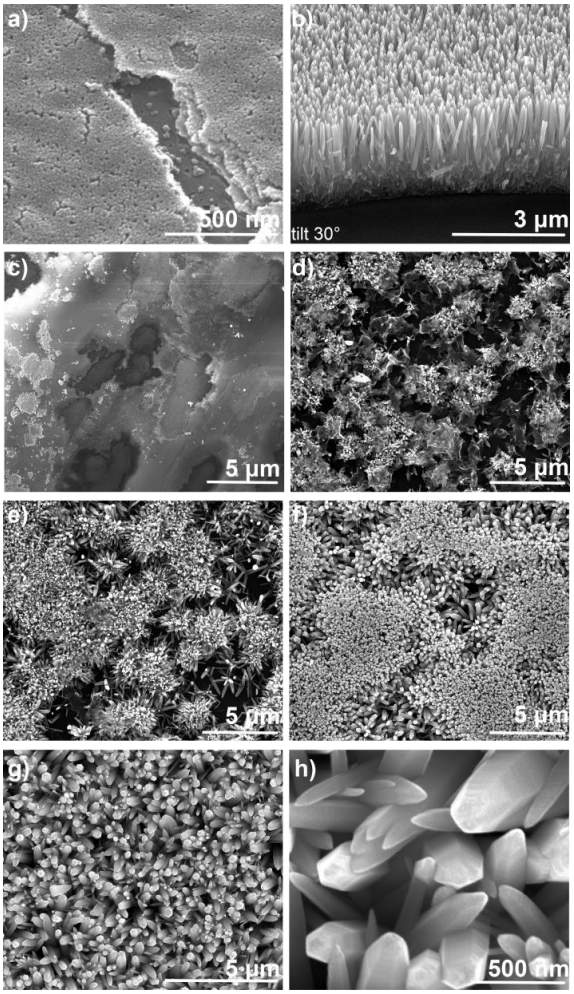

Figure 5-1: SEM micrographs of a) ZnO seed layer deposited via spin-coating b) ZnO nanorods after 1 h growth time c)-g) ZnO:Co (30 % Co) after 10 min, 20 min, 30 min, 40 min and 1h, respectively. h) Top-view of the pointed tips of ZnO:Co (30 % Co) nanorods after 1 h growth time.

this sample showed only peaks attributed to ZnO. After 30 minutes only some slight residues of the initial surface-layer are observed to be present on the surface and the ZnO nanorods grow more densely on the surface resulting in an almost complete layer after 40 min of growth. The "growing-together" of the ZnO nanorods is not visible anymore after one hour of growth (Figure 5-1g). Nevertheless it is important to point out that the inhomogeneous growth during the initial stages probably results in the formation of what appears as an inhomogeneous layer in the lower part of the cross-section shown in Figure 5-1b.

The growth of undoped ZnO nanorods or nano-needles from strong alkaline solution is a commonly observed process.[33] and references within At high pH values, the growth of ZnO from solution occurs foremost via the formation and decomposition of $Zn(OH)_4^{2-}$

complexes.[32-36] A zinc source (zinc metal or ZnO) as a seed layer substrate is thereby crucial for the successful nucleation in the process[34] and as such the rapid deposition of ZnO nanorod from alkaline solutions has been reported elsewhere.[37, 38]

In our process the addition of 7.5 ml 4M NaOH to 20 ml zinc acetate solution leads firstly to the formation of a precipitate which then readily dissolves under constant stirring to form a clear solution. However, after about 10 minutes of constant stirring a second, white precipitate forms, which does not dissolve after further stirring. XRD analysis of the second precipitate (not shown) identifies the white powder as $Zn(OH)_2$ (Wülfingite, JCPDS Card No. 38-0385). At this high pH (> 13) and at a Zn/OH- ratio of 1/6 it would be expected that the stable, soluble species $[Zn(OH)_4]^{2-}$ is the major zinc source in the solution.[33, 39, 40] Nevertheless, a side reaction whereby the $Zn(OH)_4^{2-}$ decomposes into $Zn(OH)_2\downarrow$ and 2 OH^- is also possible.[34] Furthermore McBride *et al*. showed that for a comparable zinc nitrate/NaOH system a considerable concentration of Zn^{2+} can still be found 5 min after the NaOH is added to the zinc nitrate solution.[41] Similar to what we have observed, in their study $Zn(OH)_2$ was also detected as a second precipitate after 10 – 15 minutes. Thus it is quite likely that in the ZnAc/NaOH system some remaining unreacted Zn^{2+} ions may also be present shortly after the NaOH is added. The Zn^{2+} ions bind to the ethanolamine (EA) to form a stable complex. It is therefore proposed that in the 'final' growth solution both, Zn^{2+}/EA complexes and $[Zn(OH)_4]^{2-}$, are present.

Upon heating the solution ZnO growth and precipitation occurs, incorporating $Zn(OH)_4^{2-}$ as growth units:

$$Zn^{2+} + 4OH^- \rightarrow [Zn(OH)_4]^{2-} \quad (5.1)$$

$$[Zn(OH)_4]^{2-} \rightarrow ZnO\downarrow + 2OH^- + H_2O \quad (5.2)$$

As the growth along the c-axis is energetically favourable (lowest surface energy for (002) plane), rod-type growth is preferred in the system.[26] The $[Zn(OH)_4]^{2-}$ growth units adsorb to the (002) plane and facilitate the ZnO growth following equation (5.2).[26, 42] Heating the solution leads to a high concentration of $[Zn(OH)_4]^{2-}$ growth units in solution due the release of Zn^{2+} out of the Zn^{2+}/EA complexes and subsequent growth unit formation after equation (5.1). This then results in rapid nanorod growth

due to strong adsorption of the $Zn(OH)_4^{2-}$ on the surface of ZnO nuclei formed during the initial growth stage and the following decomposition of the complex to form ZnO.[35] It is noteworthy that in the method presented water could be replaced by e.g. an organic solvent as the hydroxyl groups necessary to form the growth units after equation (5.1) are delivered by the basic medium, in this case sodium hydroxide.

It is also noteworthy that no growth on the substrates could be optically observed for experiments using solutions that did not contain either EA or hexamethylentetramine (HMTA) instead of EA. The precise effects of EA on the nature of the growth processes is currently under investigation and will be addressed in a future study.

Also, for the synthesis of cobalt-doped ZnO we have found that the EA plays a crucial role. If no EA is added to the ZnAc/CoAc + NaOH solution the pink hexaaqua cobalt (II) ion is deprotonated and the forming cobalt hydroxide precipitates out leaving a clear solution:

$$[Co(H_2O)_6]^{2+} + 2OH^- \rightarrow Co(H_2O)_4(OH)_2\,(s) + 2\,H_2O \qquad (5.3)$$

If EA is added quickly to the solution a dark green/black stable solution forms. As in the case of Zn^{2+} the EA forms a stable complex (no precipitation) with Co^{2+}. Moreover the dark green/black solution can also be obtained from solution where cobalt hydroxide is fully precipitated before adding the EA. It is therefore suggested that this observation indicates possible competition of OH^- and ethanolamine for the cobalt source. Additionally, it is also possible that at higher pH values the hydroxyl group enters the Co-EA complex.[43]

Heating of the solution leads to the partly release of cobalt ions into solution visible by a slight discoloration of the solution. The doping of the ZnO crystals then occurs due to the competition between the available zinc and cobalt sources in the solution whereby Co^{2+} can directly occupy the Zn^{2+} site in the hexagonal crystal lattice. As evidenced by the unique optical properties of the material, the Co^{2+} ions are most likely tetrahedrally coordinated in the wurtzite crystal structure (see Figure 5-5 and Figure 5-6 and related comments). It has been suggested that doping of the crystal occurs over octahedrally coordinated Co^{2+} ions in solution which then bind to ZnO crystallites with a tetrahedral coordination as Co^{2+} monomers or Co^{2+} containing acetate clusters.[12, 44] Further reaction of these groups with OH^- results in substitutionally doped Co^{2+} ions in the ZnO host lattice.[12, 44] Additionally the presence of Co^{2+} in the growth

solution changes the aspect ratio of the rods when compared to pure ZnO. A decreasing reaction rate with increasing Co^{2+} concentration leads to rod-growth with lower aspect ratios as frequently observed for ZnO:Co.[12, 30, 42, 44] In particular, the higher solubility products for cobalt-related groups as well as an added reaction barrier due to the conversion of Co^{2+} ions from octahedral to tetrahedral geometries contribute to the lower reaction rate.[42, 44] However, a higher cobalt concentration in the growth solution increases the doping concentration as the probability of the chemical doping process is increased. The maximum achievable doping concentration (solubility limit) is thereby dependent on the crystallite size and the growth temperature. For a grain size of 100 – 1000 nm the solubility limit varies from about 4 atom% (< 200 °C) to 15 atom% (ca. 800 °C).[45]

For further structural analysis and investigations into the possible formation of impurity phases, such as Co_xO_y, $Co(OH)_2$ or metallic Co-clusters, the sample with the highest cobalt concentration (30 % Co/Zn concentration in growth solution) was further analyzed by XRD. Figure 5-2 shows the XRD spectra of a nominally undoped reference sample and the 30 % Co sample. For both samples the (002) peak, centred at 34.4°, is the most intense, confirming the good alignment of the nanorods showing predominant growth in the c-axis direction for undoped and Co-doped ZnO nanorods. The inset in Figure 5-2 shows the other peaks detected by XRD. These weak features can all be assigned to the wurtzite structure of the ZnO nanorods and only a small shift from the JCPDS reference card No. 79-2205 – commonly used for hydrothermally grown ZnO[32] – can be noticed.

For the cobalt-doped sample no additional features could be observed over the entire spectra, indicating the absence of significant quantities of possible mixed phases (*e.g.* $ZnCo_2O_4$ [46, 47] or cobalt oxides as for example Co_3O_4 [48]). Following the XRD results XPS and Raman analysis was carried out for further verification of the chemical state of cobalt in the 30 % ZnO:Co sample. The XPS survey scan, as well as the high-resolution Co 2p scan, is shown in Figure 5-3.

For the sample with 30 % Co in the growth solution the survey scan mainly shows peaks assigned to zinc, oxygen, cobalt and carbon. A weak signal originating from the Co 2p peak could be detected in the region 805 – 775 eV which was then recorded at higher resolutions in order to observe its shape more clearly (inset in Figure 5-3). This

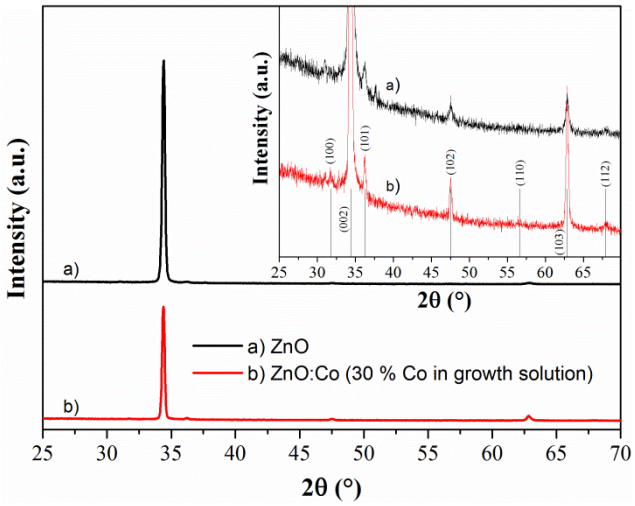

Figure 5-2: XRD spectra of undoped ZnO and ZnO:Co with 30 % Co/Zn concentration in the growth solution. Inset: Focus on XRD peaks other than ZnO (002) with no difference being recognized for the cobalt doped sample compared to ZnO. The peak positions of the crystal planes were taken from JCPDS Ref. No: 79-2205.

magnified spectrum was fitted using 4 peaks with binding energies for the Co $2p_{3/2}$ and Co $2p_{1/2}$ being obtained at 779.4 eV and 795.2 eV with the presence of satellite states at around 784 eV and 801 eV, respectively. The resulting energy split between the Co $2p_{3/2}$ and Co $2p_{1/2}$ was measured to be 15.8 eV, which is close to 15.5 eV, the value which is reported as being the binding energy difference for Co^{2+} surrounded by oxygen.[49-53] No low binding energy feature – around 778 eV, which might be

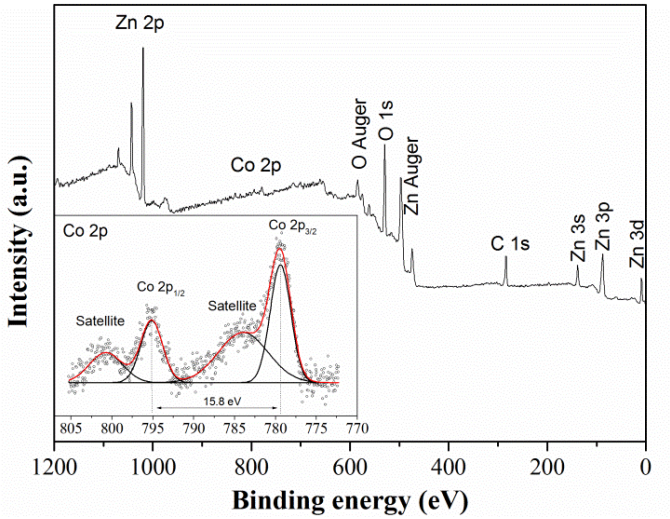

Figure 5-3: XPS survey and Co 2p high-resolution (inset) scans of ZnO:Co nanorods (30 % Co/Zn concentration in growth solution). Cobalt is found to be present in the Co^{2+} state.

expected in the presence of metallic Co-clusters,[54] could be observed in these spectra. The high binding energy difference also confirms that within the levels of sensitivity of the experiment no $ZnCo_2O_4$ was formed during the growth, as the binding energy difference reported for this mixed phase is significantly lower.[46]

Based on the high-resolution XPS scan the cobalt concentration at the surface was estimated to be around 3 at%. However the surface scan also reveals the presence of high amounts of carbon and oxygen attributable to surface contamination, amounting to ca. 32 at% and 42 at% respectively, such that the Zn levels at the surface are artificially low (23 at%). After depth profiling carbon and oxygen levels fall as expected for the removal of surface contamination and the Zn and O levels determined from the survey scans approach the expected levels (43.7 at% and 50.9 at% respectively; carbon 3.2 %) while the Co levels appear to stabilize at ca. 2.2 at%. It is noteworthy that the cobalt concentration in our films is substantially higher than has been achieved via deposition from comparable methods.[30]

Raman spectra, comparing the 30 % ZnO:Co sample with the ZnO reference, are shown in Figure 5-4. In the range of 150 cm^{-1} to 850 cm^{-1} 5 peaks are visible. The peaks at 333 cm^{-1}, 382 cm^{-1}, 439 cm^{-1}, and 580 cm^{-1} are all associated with the wurtzite ZnO crystal structure and can be assigned to the E_{2H}-E_{2L} second order mode, A_1(TO) mode, E_2(H) mode and A_1(LO) mode respectively, in agreement with previous

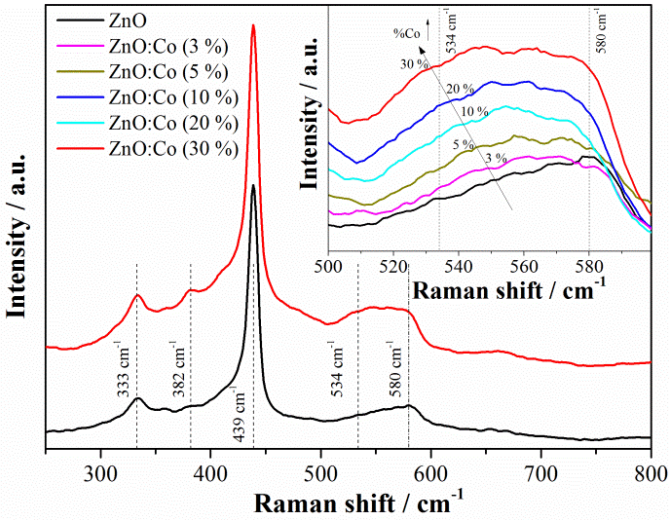

Figure 5-4: Raman spectra of ZnO and ZnO:Co (30 % Co in growth solution). For the cobalt doped sample the emergence of a local vibrational mode related to cobalt bound to donor defects [11, 51] around 534 cm^{-1} can be recognized.

studies.[11, 26, 30, 42, 51, 55] A Lorentzian fit of the E_2(H) mode revealed that the FWHM of the peak broadens for the doped ZnO:Co as compared to undoped reference. This peak broadening is due to the distortion of the host lattice by the incorporation of cobalt.[55] Additionally, the intensity of the A_1(LO) mode is commonly related to the presence of oxygen deficiency within the film, *e.g.* intrinsic defects such as zinc interstitials and oxygen vacancies in the material.[42, 56, 57] In this case the increased intensity of this mode for the cobalt-doped sample as compared to the undoped sample suggests that the Co-doped sample contains a higher density of defects and lattice disorder- an observation which is also in line with the broadening of the E_2(H) mode peak.

For a closer examination of the signal around 534 cm^{-1} the inset in Figure 5-4 shows the Raman spectra of all samples investigated in the range 500 cm^{-1} to 600 cm^{-1}. Here it can be noted that the spectra show a peak broadening scaling with the cobalt concentration in the growth solution, where the undoped reference sample exhibits a response mainly from the A_1(LO) mode the cobalt-doped samples show an increased signal around 540 cm^{-1}. As this signal scales with the cobalt concentration it can be concluded that cobalt doping leads to the appearance of an additional or more intense peak around 534 cm^{-1}. The origin of this mode is still under debate. It has been assigned as an "anomalous" mode in ZnO ([57] and references within) or, in the case of cobalt doping, as a local vibrational mode related to cobalt bound to donor defects.[11, 51] It has been reported that the hybridization of the Co 3d states with shallow donors can lead to the appearance of a spin-split impurity band resulting in room temperature ferromagnetism.[58] Furthermore the appearance of the spin-split impurity band can also be the reason for the observed band gap-shrinking as the spin-split impurity interacts with conduction band.[58-60] This effect is further explained in a following section. Thus the emergence of the mode centred at around 530 cm^{-1} is a further proof of the successful Co^{2+} doping in our nanorod structures. Also the Raman measurements showed no evidence of additional phases in the films.

The optical properties of ZnO:Co were examined using diffuse-reflectance spectroscopy. Absorption spectra of samples with Co concentration of 3 – 30 % in the growth solution are presented together with the spectrum recorded from the undoped ZnO reference in Figure 5-5. All cobalt-doped samples show a shift of the absorption

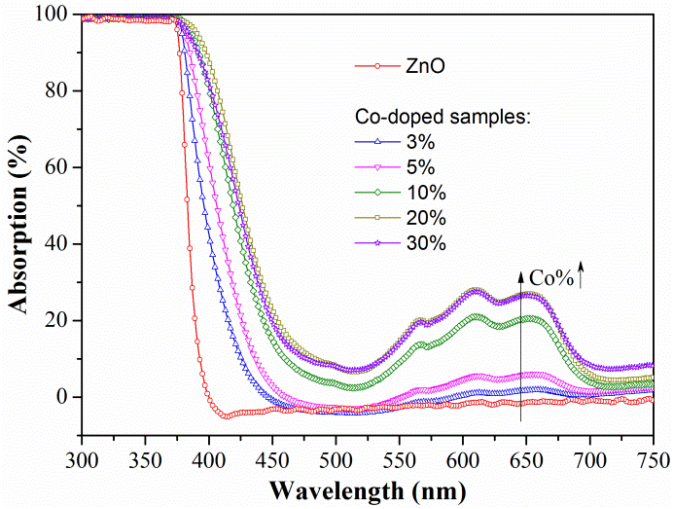

Figure 5-5: Absorption spectra for ZnO:Co with Co-concentration of 3 - 30 % in the growth solution. Increasing Co concentration results in an earlier absorption onset and additional Co 3d related absorption features in the visible range.

onset towards longer wavelengths as well as the emergence of additional absorption features in the range between 500 nm and 700 nm. Both the shift of the absorption onset and the intensity of the additional absorption in the visible region are seen to increase with increasing cobalt concentration. However, this increase is observed to reach a plateau at higher cobalt concentrations (20 % and 30 % Co/Zn concentration in growth solution). Based on the collected UV-Vis transmission *T* and reflection *R* spectra the absorption coefficient α(hν) and band gap energy E_G were calculated/estimated using following formula:[61, 62]

$$\alpha(h\nu) = \frac{1}{d}\ln\left(\frac{\left(1-R(\lambda)\right)^2}{T(\lambda)}\right) \tag{5.4}$$

$$\alpha(h\nu) = B\left(\frac{(h\nu - E_G)^{\frac{1}{2}}}{h\nu}\right) \tag{5.5}$$

Whereby hν, *d* and *B* are the photon energy, the film thickness (taken as 3 µm) and a constant, respectively. The band gap energy was estimated from the extrapolation of the straight section in a plot of $(\alpha h\nu)^2$ vs. h*ν*. Furthermore the Urbach energy E_U was

determined from the straight section in a plot of ln(α) vs. hν (for h$\nu < E_G$).[2]

Figure 5-6 shows the plots for the estimation of E_G and E_U and summarizes the estimated values for the ZnO reference and cobalt doped samples. The results show that the band gap decreases with increasing cobalt concentration in the growth solution until 20 % Co/Zn concentration. At higher cobalt concentrations (30 % Co/Zn concentration in growth solution) the band gap increases again. This effect has been observed previously.[16, 63] The shrinking of the band gap for ZnO:Co with low Co-doping concentrations is commonly assigned to a strong semiconductor metal interaction (sp- d interactions; lifting the valence band and/or lowering the CB).[9, 10, 13, 27, 28] From DMS studies it has been suggested that the hybridization of shallow intrinsic donor defect levels and cobalt impurity ion levels can lead to the formation of a spin-split impurity band at the Fermi-level just below the CBM, even at low doping-concentrations.[58, 59] Strong interactions between Zn 4s orbitals and the Co 3d states can therefore be expected and might explain the observed band gap narrowing observed for our samples grown using low cobalt concentrations in the growth solution. Nevertheless, if the donor density reaches a certain threshold, the spin-split impurity band model breaks[59] and the CB becomes populated as well, leading to a shift of the Fermi level into the CB. Whereby the cobalt impurity perhaps acts as an active shallow donor – depending on the concentration in the films – due to possible

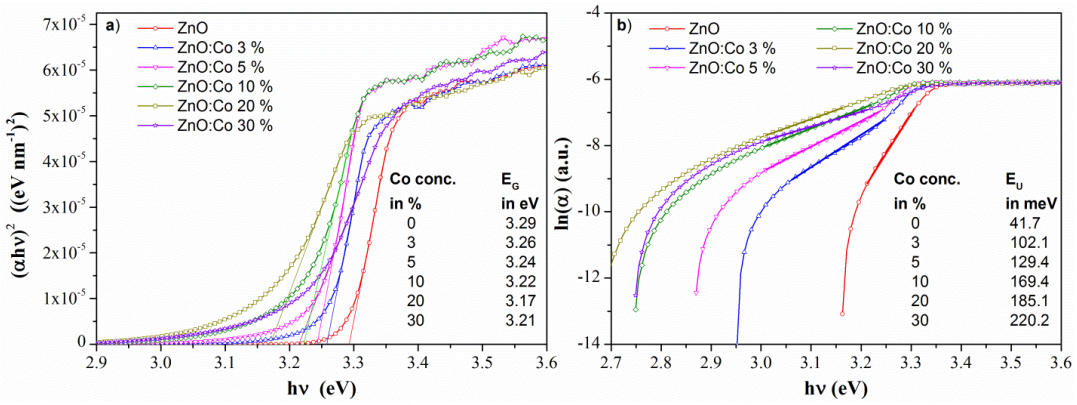

Figure 5-6: a) Tauc-plots of ZnO and ZnO:Co nanowire arrays with different Co-concentration in the growth solution. The estimated band gap energies E_G are given for each sample. b) Estimation of the Urbach Energy E_U for ZnO and ZnO:Co samples

[2] See section 2.1.1 for details on the estimation of E_U.

charge transfer from the Zn 4s↑ state to the Co 3d↓ state.[51] Thus, it is possible that at higher cobalt doping concentrations the direct optical transition of the ZnO host lattice does not occur between the VB and the CB minimum but instead between the VB and the next higher unoccupied conduction state (Burstein–Moss effect). This can explain the observed increase in the band gap energy for the sample grown with 30 % Co/Zn concentration in growth solution in our study, which is in line with the Raman results suggesting an increased lattice disorder and higher defect density together with the emergence of the spin-split impurity band related mode.

The particular electronic structure of ZnO:Co will influence the absorption properties in many ways. It was found that charge transfer (CT) from both the metal to the ligand conduction band ($ML_{CB}CT$ – as defined in[5, 22, 44]) and the ligand valence band tothe metal ($L_{VB}MCT$ – as defined in[5, 22, 44]), are possible. In this way photo-excitation of the CT processes is possible with light smaller than the band gap.[22-24, 44] Whereby it is believed that the $L_{VB}MCT$ occurs at energies just below the band gap energy, and is attributed to the reduction of Co^{2+} to Co^{+} by an excited valance electron.[22, 24] The $ML_{CB}CT$ is represented by a broader absorption peak in the spectra ($h\nu > 2$ eV) where the broader nature of the feature arises due to the different energetic locations of the d-d cobalt states within the band gap.[22]

Johnson *et al*. claim that the observed band gap shrinking is in fact a misinterpretation of the $L_{VB}MCT$.[23] They observed the appearance of a stepwise trend of α with photon energy hν for photon energies > 3 eV at higher cobalt concentrations (11 at%). Following the explanations proposed above it is reasonable to attribute the first part of the stepwise profile observed in their data at lower energies to the $L_{VB}MCT$ process (reduction of Co^{2+} to Co^{+}) and the second part of the stepwise profile observed at high energies to the excitation of an electron into an empty state in the conduction band. However, the absence of these features in our data (see Figure 5-6) strengthens the argument that the observed shrinking of the band gap for our films is due to the semiconductor-metal interaction at low doping concentrations (up to 20 % Co/Zn concentration in growth solution).

For higher doping concentrations the $L_{VB}MCT$ and Burstein-Moss effect become more dominant. As described above, the $L_{VB}MCT$ results from Co^{2+} states below/around the conduction band minimum. The induction of Co^{2+} into the ZnO lattice, contributing to

the L_{VB}MCT with an accompanying increase in structural disorder, should therefore be visualized by an increase in the Urbach energy E_U scaling with the increase of cobalt in the material. This is indeed what we observe. In our samples E_U increases with increasing cobalt concentration in the growth solution – even for 30 % Co/Zn concentration in growth solution where a band gap broadening could be observed.

Thus, it is quite possible that different mechanisms are competing in terms of the observed absorption properties depending of the actual doping concentration. At low concentration the semiconductor-metal interaction is dominant resulting in a band gap narrowing and increasing Urbach energies. At higher concentrations, in our case for samples grown at 30 % Co/Zn concentration in growth solution, population of the CB occurs due to an increased donor density which pushes the direct band-band transition towards longer wavelengths. Evidence for this latter process comes in the form of the increasing band gap energy and equally increasing Urbach energy for the sample with the highest Co concentration. On the basis of these findings we propose that for higher cobalt concentrations (*e.g.* > 5 % actual doping concentration) the L_{VB}MCT and Burstein-Moss effect will inherently result in a blue shift of the band gap, similar to the findings of Johnson *et al*.[23]

In addition, the incorporation of Co^{2+} into the ZnO lattice results in the emergence of additional absorption features in the wavelength range of 500 nm to 700 nm (see Figure 5-5). Generally these features (and their distinct shapes) are explained by the splitting of 3d states under the influence of the tetrahedral crystal field of ZnO. Sharp transitions recognized around 550 nm, 610 nm and 650 nm therefore originate from d-d metal transitions,[19] as has been frequently reported by other groups.[9, 20-22, 28] Hence, an increase in the intensity of these features is further evidence of successful substitution of Zn^{2+} by Co^{2+} in the tetrahedral crystal field symmetry (wurzite structure) of ZnO. However, no further increase of the absorption in the range of 500 nm to 700 nm can be observed for the sample prepared with 30 % Co/Zn concentration in growth solution. This most likely points towards a possible solubility limit of Co^{2+} in the ZnO lattice at this specific growth temperature (85 °C).[30] On the other hand published data in literature reports shows that at higher Co concentrations the absorption intensity of the d-d absorption features start to level and the L_{VB}MCT and ML_{CB}CT absorption features ($h\nu$ > 650 nm)[24] start to increase with increasing cobalt concentration.[20, 63] As an increased influence of the L_{VB}MCT has been

identified (band tailing, Figure 5-5 and Figure 5-6) for the sample with 30 % Co/Zn concentration in the growth solution it is possible that the $L_{VB}MCT$ is suppressing a further increase of the cobalt d-d related absorption features.

5.5 Conclusions

A simple low-temperature solution based method for the deposition of ZnO:Co onto seed layer coated substrates (here glass) has been presented. Using this technique, 3 µm long ZnO:Co nanowires can be grown within 1 hour. Careful analysis of the crystal growth process reveals that the rods grow after the deposition of a surface ZnO layer within the first stage of the process. The interplay between the high OH^-/Zn ratio and complexing of the transition metals by ethanolamine are identified to be key for the successful growth of ZnO:Co nanorod arrays by the presented method. The structures investigated exhibit cobalt concentrations of up to 2.2 %atom. No impurity phases could be detected via XRD, XPS and Raman spectroscopy. We therefore propose that our method leads to the successful doping of ZnO with Co^{2+}, whereby the Co^{2+} ions occupy Zn^{2+} sites. We observe a shrinking of the band gap for samples prepared from solutions with a Co/Zn concentration ratio of 3 – 20 % in the growth solution. However, increasing this ratio further to 30 % leads to broadening of the band gap. Semiconductor-metal interactions, structural disorder and increased donor concentration as well as charge transfer processes between the host and the dopant as possible mechanisms explaining the observed changes of the absorption properties are discussed in the light of increasing Co content. Additionally, we observe the emergence of strong additional absorption features in the visible light spectrum due to cobalt-related d-d transitions. To the best of our knowledge, these features have not been previously observed as strongly for ZnO:Co grown by a low temperature technique directly onto seed layer coated substrates. The method presented could therefore be of great interest for the simple preparation of low-cost materials for solar energy applications, as it is known from literature reports that the particular absorption properties of ZnO:Co can lead to improvement in photoconductivity as well as photo-catalysis and photo-electrochemical water splitting using visible light.[4, 5, 22-27]

5.6 References

[1] I. Djerdj, Z. Jaglicic, D. Arcon, and M. Niederberger, "Co-Doped ZnO nanoparticles: Minireview," *Nanoscale,* 10.1039/C0NR00148A vol. 2, no. 7, pp. 1096-1104, 2010.

[2] S. B. Ogale, "Dilute doping, defects, and ferromagnetism in metal oxide systems," *Adv Mater,* vol. 22, no. 29, pp. 3125-55, 2010.

[3] P. Olsson, C. Domain, and J. F. Guillemoles, "Ferromagnetic Compounds for High Efficiency Photovoltaic Conversion: The Case of AlP:Cr," *Physical Review Letters,* vol. 102, no. 22, p. 227204, 2009.

[4] Y. Lu, Y. Lin, D. Wang, L. Wang, T. Xie, and T. Jiang, "A high performance cobalt-doped ZnO visible light photocatalyst and its photogenerated charge transfer properties," *Nano Research,* vol. 4, no. 11, pp. 1144-1152, 2011.

[5] J. W. May, J. Ma, E. Badaeva, and X. Li, "Effect of Excited-State Structural Relaxation on Midgap Excitations in Co2+-Doped ZnO Quantum Dots," *The Journal of Physical Chemistry C,* vol. 118, no. 24, pp. 13152-13156, 2014.

[6] M. Arshad, A. Azam, A. S. Ahmed, S. Mollah, and A. H. Naqvi, "Effect of Co substitution on the structural and optical properties of ZnO nanoparticles synthesized by sol–gel route," *Journal of Alloys and Compounds,* vol. 509, no. 33, pp. 8378-8381, 2011.

[7] Y. Caglar, "Sol–gel derived nanostructure undoped and cobalt doped ZnO: Structural, optical and electrical studies," *Journal of Alloys and Compounds,* vol. 560, pp. 181-188, 2013.

[8] A. Klein *et al.,* "Transparent Conducting Oxides for Photovoltaics: Manipulation of Fermi Level, Work Function and Energy Band Alignment," *Materials,* vol. 3, no. 11, pp. 4892-4914, 2010.

[9] D. Y. Inamdar, A. D. Lad, A. K. Pathak, I. Dubenko, N. Ali, and S. Mahamuni, "Ferromagnetism in ZnO Nanocrystals: Doping and Surface Chemistry," *The Journal of Physical Chemistry C,* vol. 114, no. 3, pp. 1451-1459, 2010.

[10] S. Basu *et al.,* "Local Structure Investigation of Cobalt and Manganese Doped ZnO Nanocrystals and Its Correlation with Magnetic Properties," *The Journal of Physical Chemistry C,* vol. 118, no. 17, pp. 9154-9164, 2014.

[11] V. Gandhi, R. Ganesan, H. H. Abdulrahman Syedahamed, and M. Thaiyan, "Effect of Cobalt Doping on Structural, Optical, and Magnetic Properties of ZnO Nanoparticles Synthesized by Coprecipitation Method," *The Journal of Physical Chemistry C,* vol. 118, no. 18, pp. 9715-9725, 2014.

[12] L. Yanmei *et al.,* "Structure and photoluminescence of arrayed Zn1−xCoxO nanorods grown via hydrothermal method," *Journal of Physics D: Applied Physics,* vol. 40, no. 15, pp. 4592-4596, 2007.

[13] S. Deka and P. A. Joy, "Ferromagnetism induced by hydrogen in polycrystalline nonmagnetic Zn[sub 0.95]Co[sub 0.05]O," *Applied Physics Letters,* vol. 89, no. 3, p. 032508, 2006.

[14] S. Benramache, B. Benhaoua, and H. Bentrah, "Preparation of transparent, conductive ZnO:Co and ZnO:In thin films by ultrasonic spray method," *Journal of Nanostructure in Chemistry,* vol. 3, no. 1, p. 54, 2013.

[15] S. Benramache, B. Benhaoua, and F. Chabane, "Effect of substrate temperature on the stability of transparent conducting cobalt doped ZnO thin films," *Journal of Semiconductors,* vol. 33, no. 9, p. 093001, 2012.

[16] I. Y.-Y. Bu, "Optoelectronic properties of sol–gel derived ZnO:Co: Effect of Co concentration," *Superlattices and Microstructures,* vol. 75, pp. 657-666, 2014.
[17] S. Ramachandran, A. Tiwari, and J. Narayan, "Zn[sub 0.9]Co[sub 0.1]O-based diluted magnetic semiconducting thin films," *Applied Physics Letters,* vol. 84, no. 25, p. 5255, 2004.
[18] Y. Z. Yoo *et al.*, "ZnO–CoO solid solution thin films," *Journal of Applied Physics,* vol. 90, no. 8, p. 4246, 2001.
[19] P. Koidl, "Optical absorption of Co2+ in ZnO," *Physical Review B,* vol. 15, no. 5, pp. 2493-2499, 1977.
[20] R. Elilarassi and G. Chandrasekaran, "Influence of Co-doping on the structural, optical and magnetic properties of ZnO nanoparticles synthesized using auto-combustion method," *Journal of Materials Science: Materials in Electronics,* vol. 24, no. 1, pp. 96-105, 2012.
[21] S. Singh and M. Rao, "Optical and electrical resistivity studies of isovalent and aliovalent 3d transition metal ion doped ZnO," *Physical Review B,* vol. 80, no. 4, p. 045210, 2009.
[22] W. K. Liu, G. M. Salley, and D. R. Gamelin, "Spectroscopy of Photovoltaic and Photoconductive Nanocrystalline Co2+-Doped ZnO Electrodes," *The Journal of Physical Chemistry B,* vol. 109, no. 30, pp. 14486-14495, 2005/08/01 2005.
[23] C. A. Johnson, A. Cohn, T. Kaspar, S. A. Chambers, G. M. Salley, and D. R. Gamelin, "Visible-light photoconductivity of Zn1−xCoxO and its dependence onCo2+concentration," *Physical Review B,* vol. 84, no. 12, p. 125203, 2011.
[24] C. A. Johnson, T. C. Kaspar, S. A. Chambers, G. M. Salley, and D. R. Gamelin, "Sub-band-gap photoconductivity inCo2+-doped ZnO," *Physical Review B,* vol. 81, no. 12, p. 125206, 2010.
[25] W. C. Lee, G. E. Canciani, B. O. S. Alwhshe, and Q. Chen, "Enhanced photoelectrochemical water oxidation by ZnxMyO (M = Ni, Co, K, Na) nanorod arrays," *International Journal of Hydrogen Energy,* vol. 41, no. 1, pp. 123–131, 2015.
[26] S. Kuriakose, B. Satpati, and S. Mohapatra, "Enhanced photocatalytic activity of Co doped ZnO nanodisks and nanorods prepared by a facile wet chemical method," *Phys Chem Chem Phys,* vol. 16, no. 25, pp. 12741-12749, 2014.
[27] P. P. Patel *et al.*, "Nitrogen and cobalt co-doped zinc oxide nanowires – Viable photoanodes for hydrogen generation via photoelectrochemical water splitting," *Journal of Power Sources,* vol. 299, pp. 11-24, 2015.
[28] M. Tortosa, M. Mollar, B. Marí, and F. Lloret, "Optical and magnetic properties of ZnCoO thin films synthesized by electrodeposition," *Journal of Applied Physics,* vol. 104, no. 3, p. 033901, 2008.
[29] P. M. Aneesh, C. T. Cherian, M. K. Jayaraj, and T. Endo, "Co2+ doped ZnO nanoflowers grown by hydrothermal method," *Journal of the Ceramic Society of Japan,* vol. 118, no. 1377, pp. 333-336, 2010.
[30] C.-W. Liu *et al.*, "Enhancement in the structure quality of ZnO nanorods by diluted Co dopants: Analyses via optical second harmonic generation," *Journal of Applied Physics,* vol. 117, no. 8, p. 084315, 2015.
[31] L. Cai *et al.*, "V ions implanted ZnO nanorod arrays for photoelectrochemical water splitting under visible light," *International Journal of Hydrogen Energy,* vol. 40, no. 3, pp. 1394-1401, 2015.

[32] S. Baruah and J. Dutta, "Hydrothermal growth of ZnO nanostructures," *Science and Technology of Advanced Materials,* vol. 10, no. 1, p. 013001, 2009.
[33] S. Xu and Z. L. Wang, "One-dimensional ZnO nanostructures: Solution growth and functional properties," *Nano Research,* vol. 4, no. 11, pp. 1013-1098, 2011.
[34] X. Wu, H. Bai, C. Li, G. Lu, and G. Shi, "Controlled one-step fabrication of highly oriented ZnO nanoneedle/nanorods arrays at near room temperature," *Chem Commun (Camb),* no. 15, pp. 1655-7, 2006.
[35] X. Wang, Q. Zhang, Q. Wan, G. Dai, C. Zhou, and B. Zou, "Controllable ZnO Architectures by Ethanolamine-Assisted Hydrothermal Reaction for Enhanced Photocatalytic Activity," *The Journal of Physical Chemistry C,* vol. 115, no. 6, pp. 2769-2775, 2011.
[36] Q. Li *et al.*, "Room-temperature nonequilibrium growth of controllable ZnO nanorod arrays," *Nanoscale Res Lett,* vol. 6, p. 477, 2011.
[37] M. Kokotov, A. Biller, and G. Hodes, "Reproducible Chemical Bath Deposition of ZnO by a One-Step Method: The Importance of "Contaminants" in Nucleation," *Chemistry of Materials,* vol. 20, no. 14, pp. 4542-4544, 2008.
[38] M. Kokotov and G. Hodes, "Reliable chemical bath deposition of ZnO films with controllable morphology from ethanolamine-based solutions using KMnO4 substrate activation," *Journal of Materials Chemistry,* vol. 19, no. 23, p. 3847, 2009.
[39] K. Govender, D. S. Boyle, P. B. Kenway, and P. O'Brien, "Understanding the factors that govern the deposition and morphology of thin films of ZnO from aqueous solution," *Journal of Materials Chemistry,* vol. 14, no. 16, p. 2575, 2004.
[40] R. A. Reichle, K. G. McCurdy, and L. G. Hepler, "Zinc Hydroxide: Solubility Product and Hydroxy-complex Stability Constants from 12.5–75 °C," *Canadian Journal of Chemistry,* vol. 53, no. 24, pp. 3841-3845, 1975.
[41] R. A. McBride, J. M. Kelly, and D. E. McCormack, "Growth of well-defined ZnO microparticles by hydroxide ion hydrolysis of zinc salts," *Journal of Materials Chemistry,* vol. 13, no. 5, pp. 1196-1201, 2003.
[42] X. He, H. Yang, Z. Chen, and S. S. Y. Liao, "Effect of Co-doping content on hydrothermal derived ZnO array films," *Physica B: Condensed Matter,* vol. 407, no. 15, pp. 2895-2899, 2012.
[43] R. S. Subrahmanya, "Polarographic behaviour of metals in ethanolamines," *Proceedings - Mathematical Sciences,* journal article vol. 45, no. 3, pp. 195-203, 1957.
[44] D. A. Schwartz, N. S. Norberg, Q. P. Nguyen, J. M. Parker, and D. R. Gamelin, "Magnetic Quantum Dots: Synthesis, Spectroscopy, and Magnetism of Co2+- and Ni2+-Doped ZnO Nanocrystals," *Journal of the American Chemical Society,* vol. 125, no. 43, pp. 13205-13218, 2003.
[45] B. B. Straumal, A. A. Mazilkin, S. G. Protasova, A. A. Myatiev, P. B. Straumal, and B. Baretzky, "Increase of Co solubility with decreasing grain size in ZnO," *Acta Materialia,* vol. 56, no. 20, pp. 6246-6256, 2008.
[46] S. Wang, Z. Ding, and X. Wang, "A stable ZnCo2O4 cocatalyst for photocatalytic CO2 reduction," *Chemical Communications,* 10.1039/C4CC07225A vol. 51, no. 8, pp. 1517-1519, 2015.

[47] H. Chen *et al.*, "Mesoporous ZnCo2O4 microspheres composed of ultrathin nanosheets cross-linked with metallic NiSix nanowires on Ni foam as anodes for lithium ion batteries," *Nano Energy*, vol. 10, pp. 245-258, 2014.
[48] S. K. Meher and G. R. Rao, "Effect of Microwave on the Nanowire Morphology, Optical, Magnetic, and Pseudocapacitance Behavior of Co3O4," *The Journal of Physical Chemistry C*, vol. 115, no. 51, pp. 25543-25556, 2011.
[49] M. Naeem *et al.*, "Effect of reducing atmosphere on the magnetism of Zn 1− x Co x O (0≤ x ≤0.10) nanoparticles," *Nanotechnology*, vol. 17, no. 10, p. 2675, 2006.
[50] C. C. Wang *et al.*, "The Intrinsic Room-Temperature Ferromagnetism in ZnO:Co Thin Films Deposited by PLD," *Advances in Condensed Matter Physics*, vol. 2012, pp. 1-5, 2012.
[51] X. F. Wang *et al.*, "Signature of Intrinsic High-Temperature Ferromagnetism in Cobalt-Doped Zinc Oxide Nanocrystals," *Advanced Materials*, vol. 18, no. 18, pp. 2476-2480, 2006.
[52] H.-J. Lee, S.-Y. Jeong, C. R. Cho, and C. H. Park, "Study of diluted magnetic semiconductor: Co-doped ZnO," *Applied Physics Letters*, vol. 81, no. 21, p. 4020, 2002.
[53] G. Li *et al.*, "Structure and properties of Co-doped ZnO films prepared by thermal oxidization under a high magnetic field," *Nanoscale Res Lett*, vol. 10, p. 112, 2015.
[54] M. C. Biesinger, B. P. Payne, A. P. Grosvenor, L. W. M. Lau, A. R. Gerson, and R. S. C. Smart, "Resolving surface chemical states in XPS analysis of first row transition metals, oxides and hydroxides: Cr, Mn, Fe, Co and Ni," *Applied Surface Science*, vol. 257, no. 7, pp. 2717-2730, 2011.
[55] A. Popa *et al.*, "Co doped ZnO semiconductor materials: structural, morphological and magnetic properties," *Open Physics*, vol. 9, no. 6, pp. 1446-1451, 2011.
[56] J. Wang *et al.*, "Oxygen vacancy induced band-gap narrowing and enhanced visible light photocatalytic activity of ZnO," *ACS Appl Mater Interfaces*, vol. 4, no. 8, pp. 4024-4030, 2012.
[57] C. F. Windisch, G. J. Exarhos, C. Yao, and L.-Q. Wang, "Raman study of the influence of hydrogen on defects in ZnO," *Journal of Applied Physics*, vol. 101, no. 12, p. 123711, 2007.
[58] M. Venkatesan, C. B. Fitzgerald, J. G. Lunney, and J. M. Coey, "Anisotropic ferromagnetism in substituted zinc oxide," *Phys Rev Lett*, vol. 93, no. 17, p. 177206, 2004.
[59] J. M. Coey, M. Venkatesan, and C. B. Fitzgerald, "Donor impurity band exchange in dilute ferromagnetic oxides," *Nat Mater*, vol. 4, no. 2, pp. 173-9, 2005.
[60] K. J. Kim and Y. R. Park, "Spectroscopic ellipsometry study of optical transitions in Zn[sub 1−x]Co[sub x]O alloys," *Applied Physics Letters*, vol. 81, no. 8, p. 1420, 2002.
[61] J. I. Pankove, *Optical Processes in Semiconductors*. Dover, 1971.
[62] S. Kasap and P. Capper, *Springer Handbook of Electronic and Photonic Materials*. Springer, 2007.

[63] S. V. Bhat and F. L. Deepak, "Tuning the bandgap of ZnO by substitution with Mn2+, Co2+ and Ni2+," *Solid State Communications*, vol. 135, no. 6, pp. 345-347, 2005.

Chapter 6

6 One-pot synthesis of $Co(OH)_2$ and/or Co_3O_4 decorated cobalt-doped ZnO nanorod-arrays and their potential as (photo-)anode materials

6.1 Abstract

The generation and storage of clean energy presents one of the most urgent current research topics in materials science. Metal oxides like zinc oxide (ZnO) are particularly promising materials to be used in core technologies such as batteries, photovoltaics or solar fuel production and solar water splitting. In order to be economically viable, the deposition of the electrode materials used in the aforementioned applications should be as cost effective as possible, while maintaining good device characteristics. Here, a simple low-temperature solution-based deposition method is reported that allows the growth of high surface area, cobalt-doped ZnO nanorod-arrays decorated with cobaltic over-coatings. Control over the visible light absorption and the nature of the cobaltic over-coating (e.g. $Co(OH)_2$ and/or Co_3O_4) can be achieved by changing the growth parameters during the one-pot synthesis. Based on a thorough materials characterization, the study focuses on the evaluation of the underlying growth principles and resulting material properties. In this regard the (solar driven) oxidation of water is taken as an example reaction in order to gain further insight into the functionality of the structures. A growth mechanism is proposed that will allow the optimization of the resulting structures for individual applications, but which could also prove valuable for other metal-oxide/hydroxide material combinations.

6.2 Introduction

In recent years, cobalt-doped zinc oxide (ZnO:Co) has attracted broad attention from the research community due to its interesting material properties such as visible light absorption and possible room-temperature ferromagnetism.[1-6] Hence, research regarding this material is, for example, driven by its application as a dilute magnetic semiconductor, as an electrode material for batteries or photo-electrochemical cells and as a photocatalyst.[2, 7-13] For the latter applications, the charge carrier transport over the semiconductor-electrolyte interface is of the highest importance. Improved transfer kinetics – especially in regards to the oxidation of water – are generally

achieved using additional catalyst coatings. Cobalt hydroxide ($Co(OH)_2$) and cobalt oxide (Co_3O_4) are interesting candidates for the catalyst layer due to their relatively earth-abundant nature and their potential to offer the relatively low over-potentials that are required to drive reactions such as water oxidation.[14-18] Additionally, Co_3O_4 has gained interest due the possibility of it being able to catalyze water splitting in neutral or even acidic conditions.[19-21]

A simple, cheap, reproducible route to the synthesis of both the catalyst layer and the bulk electrode material is therefore desirable. While some research has been conducted on structures of ZnO/ZnO:Co decorated with $Co(OH)_2$ or Co_3O_4 for various applications,[22-24] a one-pot synthesis of such structures has only very recently been reported for the ZnO/$Co(OH)_2$ system.[23] However, a method that permits the controlled incorporation of cobalt into the ZnO host lattice as well as facilitating the growth of the surface catalyst phase ($Co(OH)_2$, Co_3O_4) has, to the best of our knowledge, not been reported thus far.

In this report a one-pot, two-step hydrothermal method is presented that addresses this issue directly. The crucial role of monoethanolamine (MEA), used during the low-temperature synthesis, is evaluated and a possible growth mechanism and its dependence on the growth conditions is discussed. It is demonstrated that the visible light absorption (related to the substitutional cobalt doping) can be increased by increasing the MEA concentration. Similarly it is demonstrated that $Co(OH)_2$ or Co_3O_4 containing structures, depending on the MEA concentration used, can be grown during a second growth stage in order to decorate the already deposited ZnO:Co NR arrays. On the basis of electrochemical measurements in alkaline solution the potential use of the ZnO:Co-$Co(OH)_2$/Co_3O_4 structures as electrode materials for energy-related applications is outlined.

6.3 Experimental

$Co(OH)_2$/Co_3O_4-decorated ZnO/ZnO:Co NR arrays were grown hydrothermally on substrates coated with ZnO seed layers deposited by atomic layer deposition (ALD). Microscope glass slides and fluorine doped tin oxide coated glass (FTO, 10 Ω/sq) were used as substrates. Glass slides were cleaned by sonication in a mixture of Millipore water (H_2O), ammonium hydroxide (NH_4OH) and hydrogen peroxide (H_2O_2) in a ratio

of H_2O:NH_4OH:H_2O_2 = 5 : 1 : 1 for 1 h, prior to the ALD seed layer growth. FTO substrates were cleaned by subsequent sonication in diluted decon 90, acetone and isopropyl alcohol (IPA) for 30 min each. The substrates were rinsed with Millipore water and blow dried in a stream of nitrogen after the cleaning procedure.

Seed layer preparation by ALD

Using a Cambridge NanoTech Fiji F200LLC System, seed layers were deposited from diethylzinc and water as precursor materials. 150 growth cycles were carried out to yield a nominal layer thickness of ca. 30 nm. The substrate temperature was held constant at 190 °C throughout the growth. After naturally cooling in air the seed layer coated substrates were annealed (air) for 1h at 350 °C.

Synthesis of undecorated and $Co(OH)_2$/Co_3O_4-decorated ZnO/ZnO:Co NRAs

For the synthesis of undoped and substitutionally-doped ZnO:Co NR arrays a previously reported growth method has been adapted.[25] 0.55 g zinc acetate (ZnAc, reagent grade, Sigma Aldrich) and 0.207 g cobalt acetate (reagent grade, Sigma Aldrich) were dissolved in 20 ml of water (H_2O, 18.2 MΩ) under constant stirring for 20 min. Afterwards, 7.5 ml of 4M sodium hydroxide (NaOH) were added and the solution was stirred for 1.5 min, after which the required amount of monoethanolamine was added (MEA, reagent grade, Sigma Aldrich – see Table 6-1 for concentrations used). After stirring for 7h the black solution was transferred to a pre-heated Teflon lined autoclave (200 ml or 100 ml) and the seed layer-coated substrates were immersed into the solution almost vertically (growth side facing down). Subsequently the autoclave was closed and left in a standard laboratory oven at 90 °C for usually 16 h (first growth stage, 1GS).

The growth of $Co(OH)_2$/Co_3O_4-decorated ZnO:Co NR arrays was carried out as outlined above but after the first growth stage the autoclave was placed into another pre-heated laboratory oven (150 °C). The growth duration of this second growth stage (2GS) was varied between 45 min, 1.5 h and 4.5 h.

The samples prepared from this one-pot (two-step) method are listed in Table 6-1. As a parameter for their characterization the ratio of the MEA concentration (c_{MEA}) to the metal concentration ($c_M = c_{Zn}+c_{Co}$) is introduced as $R_{MEA/M} = c_{MEA}/(c_{Zn}+c_{Co})$. The (un-)decorated ZnO:Co samples are labeled according to $R_{MEA/M}$ and whether the growth included only the first growth stage (prefix ‘1’) or both growth stages (prefix ‘2’).

Undoped ZnO NR arrays were grown in order to compare their (photo-)electrochemical performance to that of the (un)decorated ZnO:Co samples. The growth was carried out following the procedure outlined for the 1GS without the addition of CoAc to the growth solution. The over-coating with $Co(OH)_2/Co_3O_4$ was performed by putting the ZnO NR arrays into a pre-reacted (after 1GS) growth solution with subsequent heating to 150 °C (see 2GS).

Characterization

Scanning Electron Microscopy (SEM) and energy dispersive X-ray spectroscopy (EDS) was carried out using a FEI Quanta 650 FEG High Resolution Scanning Electron Microscope. Absorption spectra were calculated from diffuse reflectance and transmission spectra recorded using a Shimadzu UV-2401PC UV-Vis spectrometer equipped with an integrating sphere. A Panalytic X'Pert X-ray diffractometer (Cu Kα radiation λ = 0.1541874 nm) was used to record X-ray diffraction (XRD) spectra. A Kratos Axis ULTRA spectrometer equipped with a monochromatic Al Kα radiation of energy 1486.6 eV was used for the XPS measurements (performed at University of Limerick). The advantageous carbon C1s peak at 284.8 eV was used as the charge

Table 6-1: Samples of the growth studies of Chapter 6 prepared using the one-pot (two-step) method. The samples are labelled in accordance to their $R_{MEA/M}$ (= $c_{MEA}/(c_{Zn}+c_{Co})$) and whether the growth included a second growth stage (2GS – heating to 150 °C) or if the first growth stage was applied only (1GS).

Sample	V_{MEA}/C_{MEA} [ml/mol]	$R_{MEA/M}$	1GS	2GS
1-3	0.6/0.2	3	90 °C, 16h	-
1-6	1.2/0.4	6	90 °C, 16h	-
1-9	1.8/0.6	9	90 °C, 16h	-
2-3-0.75h	0.6/0.2	3	90 °C, 16h	To 150 °C, 45 min
2-3-1.5h	0.6/0.2	3	90 °C, 16h	To 150 °C, 1.5 h
2-3-4.5h	0.6/0.2	3	90 °C, 16h	To 150 °C, 4.5 h
2-9-0.75h	1.8/0.6	9	90 °C, 16h	To 150 °C, 45 min
2-9-1.5h	1.8/0.6	9	90 °C, 16h	To 150 °C, 1.5 h
2-9-4.5h	1.8/0.6	9	90 °C, 16h	To 150 °C, 4.5 h

reference in determining the binding energies. The spectra presented were all taken on samples which were not subjected to carbon removal by Argon bombardment, since this treatment may result in an oxidation state change due to Ar^+-sample interactions. Indeed it was found that for samples exhibiting an $Co(OH)_2$ or Co_3O_4 over-coating prolonged Ar^+-bombardment (10 keV and Ar1000+ clusters) resulted in the formation of metallic cobalt. A 3-electrode configuration was used for the electrochemical characterization. An Ag/AgCl electrode (+199 mV vs. Standard Hydrogen Electrode, SHE) and a coiled platinum wire were used as the reference and counter electrode, respectively. Working electrodes were prepared by removing some of the undecorated or $Co(OH)_2/Co_3O_4$-decorated ZnO/ZnO:Co NR arrays using hydrochloric acid and attaching a wire to the FTO substrate using silver conductive paste. The working electrodes were then incorporated into a home-made PTFE cell (1 cm^2 electrolyte exposure area). Water oxidation experiments were carried out in 1 M KOH. These experiments were performed as cyclic voltammetry (CV) and electrochemical impedance spectroscopy (EIS) scans. CV scans were recorded at a scan rate of 50 mV/s and a step size of 5 mV in a potential window of -1 V – 0.9 V vs. Ag/AgCl. The same scan parameters were used for the photo-electrochemical measurement using linear sweep voltammetry (LSV). EIS measurements were carried out at an applied potential E_{appl} = 0.675 V vs. Ag/AgCl. The AC perturbation was set to 10 mV and the frequency range was 50 kHz – 0.5 kHz. Furthermore CV scans were recorded in ferro/ferricyanide (aqueous solution of 10 mM potassium ferricyanide and 10 mM potassium ferrocyanide trihydrate in 1 M potassium chloride) immediately after the CV and EIS experiments in 1 M KOH (after thorough rinsing of the cell with H_2O) on the same measurement spot. These CV scans were recorded at a scan rate of 50 mV/s and a step size of 5 mV in a potential window of -0.2 V – 0.7 V vs. Ag/AgCl.

6.4 Results and discussion

In previous studies ZnO:Co nanorods with strong visible light absorption have been grown from strong alkaline solutions at temperatures as low as 85 °C.[25, 26] While the growth temperature and the concentration of the cobalt precursor salt were found to be important for the cobalt incorporation into the NRs, the role of MEA during the synthesis has not yet been elucidated in detail.[25, 26]

Therefore, the effect of the MEA concentration on the ZnO:Co NR-array growth was

evaluated first. This included a set of samples which was grown using different $R_{MEA/M}$ (3, 6 or 9) while keeping the other growth parameters constant. By means of SEM, EDS, XRD and UV-Vis measurements these samples were then analyzed in order to investigate possible changes of the material properties. The resulting SEM images, XRD and UV-Vis spectra are shown in Figure 6-1, Figure 6-2 and Figure 6-3, respectively.

The top-view images in Figure 6-1 reveal an increasing rod-thickness and a higher degree of irregularity (i.e. non hexagonal rods) scaling with the MEA concentration. The rods also grew longer for sample solutions with higher $R_{MEA/M}$ (6.9 µm, 8.6 µm, 9.7 µm for $R_{MEA/M}$ = 3, 6, 9, respectively). On a macroscopic scale the growth from higher MEA concentrations therefore leads to a film of densely packed, highly oriented NRs with a higher overall sample volume per cm^2. Furthermore the overall cobalt concentrations in the films seem not to be significantly affected by the MEA concentration used during the synthesis. Here EDS measurements – distinguished by a higher statistical significance due to a deeper excitation depth when compared to XPS measurements – revealed a comparable cobalt concentration of 0.45 $\%_{at}$ +-0.02 for all samples.

The aforementioned structural differences also directly influence the XRD patterns

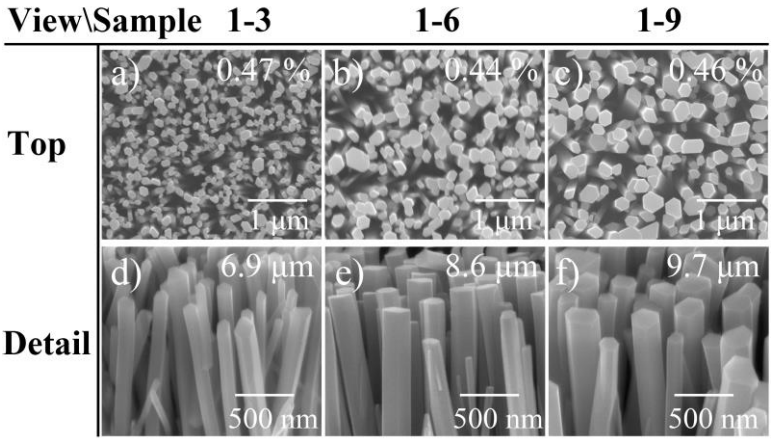

Figure 6-1 Top-view and detail-view (tilted) SEM micrographs of ZnO:Co NR arrays grown from $R_{MEA/M}$ = 3, 6 or 9 (a) + d), b) + e), c) + f), respectively). Samples were grown at 90 °C for 16 h – no 2GS. The average Co concentration determined by EDS measurements is given in the top-view images. The average height of the NR arrays is given in the detail-view images.

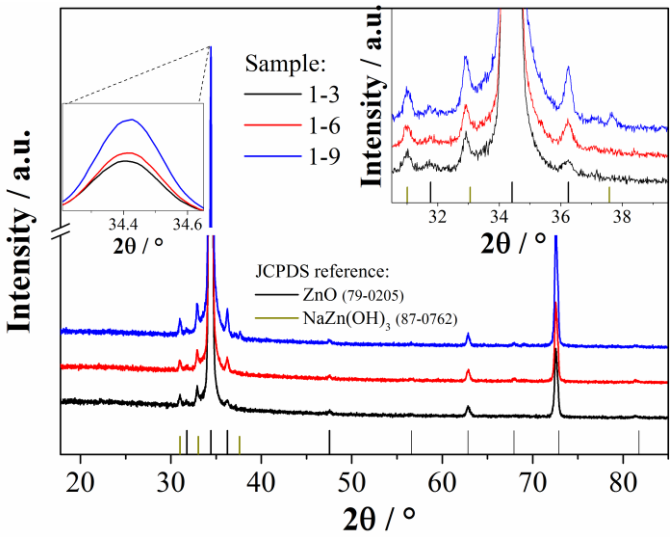

Figure 6-2. XRD spectra of ZnO:Co NR arrays grown at 90 °C for 16 h from solutions of $R_{MEA/M}$ = 3, 6 or 9 (colour online). The insets magnify the range 2θ = 30 - 40° and intensity of the (002) peak.

obtained as shown in Figure 6-2. Here samples grown using higher MEA concentrations show an increased (002) response at 2θ = 34.4° and the intensity of this peak was found to scale with the $R_{MEA/M}$ (inset in Figure 6-2). This can be attributed to the strong c-axis growth of the rods ([002] parallel to the substrate) paired with an increased overall sample volume. Further XRD peaks are visible throughout the examined range of 2θ = 18 - 90°. Most of these can be attributed to ZnO of which the peak positions of the JCPDS reference card (No. 79-0205) are included in the figure. However, the peaks at 2θ ca. 31°, 32.9° and 37.7° cannot be indexed as ZnO. In an earlier publication these peaks were tentatively assigned to $NaZn(OH)_3$ (JCPDS reference card no. 87-0762).[26] Additional growth and XRD experiments of undoped ZnO samples (see Figure A4- 1) were carried out in order to investigate this hypothesis. Importantly these experiments, including growths without MEA and from a zinc nitrate precursor (i.e. no carbon source), revealed that these peaks remain present as long as the growth is carried out at high pH. It is therefore indeed likely that the observed peaks are somehow related to sodium, with $NaZn(OH)_3$ as the probable origin.

It is also important to note that no cobalt-related secondary phases have been observed in the XRD spectra. While this does not exclude the possibility of growth of ultra-small cobalt-containing materials on the rod-surface (see discussion regarding the electrochemical characterization), XPS measurements point towards the successful

incorporation of Co^{2+} into the host lattice (i.e. Co-O bonding, see Figure 6-6 and related comments).

The absorption spectra of the ZnO:Co NR array samples are shown together with the spectrum from an undoped reference sample in Figure 6-3. It is readily observed that the doped samples differ qualitatively from an undoped ZnO reference sample. Additional absorption peaks in the range 550 nm – 700 nm as well as a shift of the near-UV absorption towards longer wavelengths are visible for these samples. These characteristic features can be attributed to the replacement of Zn^{2+} by Co^{2+} in the tetrahedral crystal field symmetry of the ZnO lattice and have been discussed in greater detail elsewhere.[8, 25-32] For the purpose of this study it is important to realize that the intensity of these features (i.e. the visible light absorption) gradually increases with the MEA concentration. Since the cobalt concentrations determined by EDS do not differ significantly, the increasing sample volume scaling with the MEA volume is believed to be the main contributor in this respect.

Following the initial growth experiments, another set of samples was synthesized. These samples were grown with an additional second growth stage (2GS) following the first growth stage (refer to section 6.3 for details). In order to evaluate two strongly differing MEA concentrations, $R_{MEA/M}$ was chosen as 3 or 9 for these samples.

The SEM images (Figure 6-4) show details of the rod tips of the second set of samples (for top view images see Figure A4- 2). Similar to the NR arrays of the first set of samples, the synthesis using a higher MEA concentration resulted in the growth of

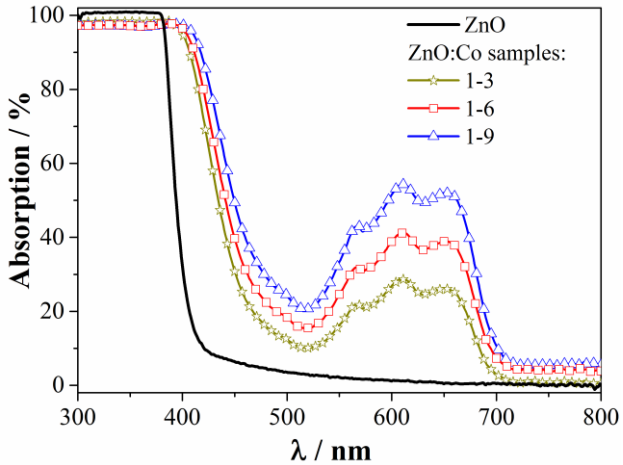

Figure 6-3. UV-Vis absorption spectra of of ZnO:Co NR arrays grown at 90 °C for 16 h from solutions of $R_{MEA/M}$ = 3, 6 or 9.

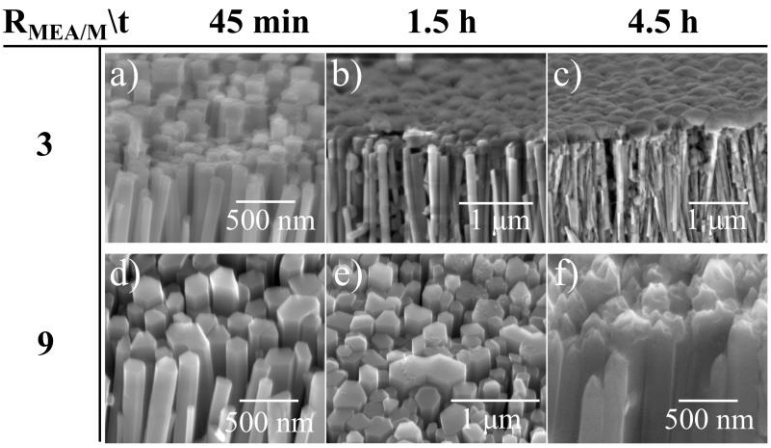

Figure 6-4. Tilt-view detail SEM images of samples subjected to a second growth stage (2GS, for t = 45 min, 1.5 h or 4.5 h) grown from $R_{MEA/M}$ = 3 (a), b), c)) and $R_{MEA/M}$ = 9 (d), e), f)).

longer and thicker NRs. Importantly, the 2GS leads to the decoration of the nanorods with an additional material, as is best seen for the samples where the 2GS was 4.5 h duration (Figure 6-4c and Figure 6-4f). The structure of these materials appears to be dependent on the MEA concentration used. Rapid deposition was noticed for samples grown from 0.6 ml MEA ($R_{MEA/M}$ = 3). Even 45 min of deposition leads to a thin layer covering the rod tips. After 1.5 h a comparatively thick layer is already observed (ca. 8.7 $\%_{at}$ Co from EDS measurements). In contrast, the SEM analysis revealed almost no deposition (at 45 min) and only little coverage (at 1.5 h – ca. 0.67 $\%_{at}$ Co from EDS measurements) for a MEA volume of 1.8 ml ($R_{MEA/M}$ = 9; Figure 6-4d and Figure 6-4e, respectively). When the 2GS was carried out for a longer duration (4.5 h) a substantial coverage – predominantly on the rod tips – is visible for both MEA volumes. Nevertheless, the overall thickness of the additional coating is higher for the sample grown from $R_{MEA/M}$ = 3.

Examining the XRD spectra of the 4.5 h samples in Figure 6-5 reveals that most of the recorded responses can be attributed to ZnO and (most likely) $NaZn(OH)_3$ (compare Figure 6-2 and Figure A4- 1). However, additional peaks appear in the spectra – especially in the range between 2θ = 30 – 40° (see inset). For the sample grown from $R_{MEA/M}$ = 3 (sample 2-3-4.5h) these peaks are visible at 18.9°, 36.8°, 38.45° and 59.2°. These can all be attributed to the Co_3O_4 reference card JCPDS 43-1003. On the other hand, for the sample grown using a higher MEA concentration (sample 2-9-4.5h) the lower overall coating thickness leads to a lower signal intensity associated with the additional XRD peaks. For this sample additional peaks are recognized at 32.5° and

37.9°. These can be attributed to the (100) and (101) plane of β-$Co(OH)_2$, respectively (JCPDS 30-0443).

In order to confirm the XRD results, XPS analysis was carried out. The increased surface sensitivity of XPS measurements (probe depth ca. 10 nm) allowed investigating the samples grown for 1.5 h during the 2GS. These samples (2-3-1.5h and 2-9-1.5h) were compared to an uncoated sample (1-9). The Co/Zn ratios quantified from the XPS measurements were found to increase from 0.04 over 0.1 to 2.0 for the uncoated sample (1-9), sample 2-9-1.5h and sample 2-3-1.5h, respectively. This is

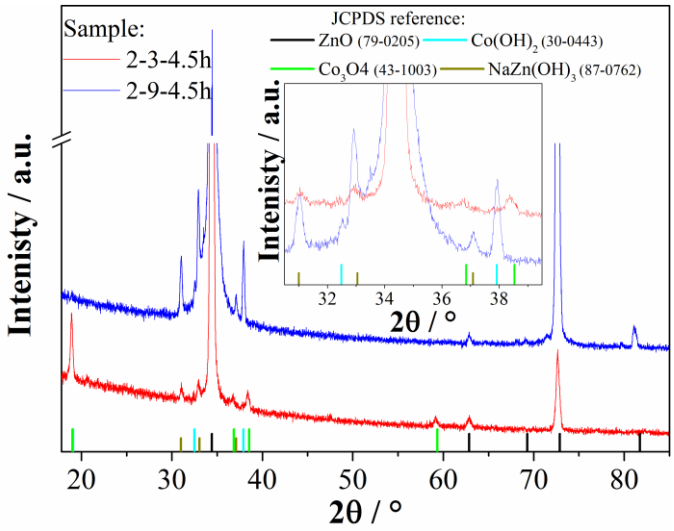

Figure 6-5. XRD spectra of decorated ZnO:Co NR arrays grown from $R_{MEA/M}$ = 3 or 9. The duration during the second growth stage was 4.5 h. The inset magnifies the range 2θ = 30 - 40°.

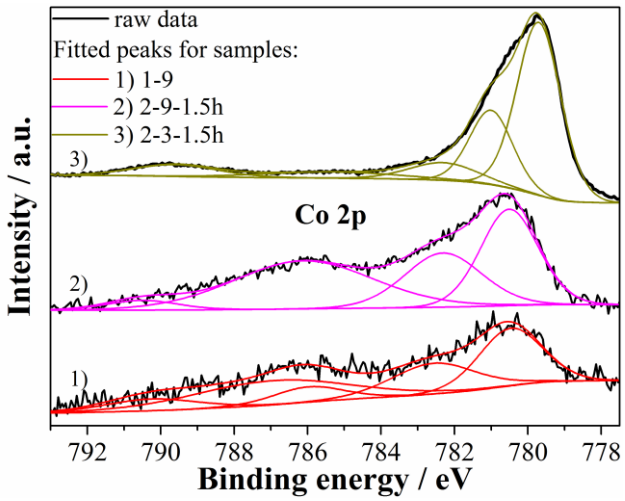

Figure 6-6. XPS spectra of nominally uncoated ZnO:Co NRs (trace 1, $R_{MEA/M}$ = 9) and decorated ZnO:Co NRs ($R_{MEA/M}$ = 9 or 3 for trace 2 and 3, respectively). The decorated samples were subjected to a second growth stage for 1.5 h.

Table 6-2. Binding energy positions of the fitted peaks of Figure 6-6 ($Co2p_{3/2}$ feature only; given in eV). [1]peak positions as suggested in Ref. [33].

Sample	Peak1	Peak 2	Peak 3	Peak 4	Peak 5
1)	780.5	782.6	786.0	787.0	790.2
2)	780.5	782.3	786.1	790.5	
3)	779.7	781.0	782.3	785.3	789.6
[1]CoO	780.0	782.1	785.5	786.5	
[1]$Co(OH)_2$	780.4	782.2	786.0	790.4	
[1]Co_3O_4	779.6	780.9	782.2	785.2	789.5

consistent with the SEM images of the cobalt containing over-layer structures formed in the 2nd growth stage (Figure 6-4e and b, for top-view SEM images see Figure A4-2). The Co 2p spectra of these samples are shown in Figure 6-6. Qualitatively, the uncoated ZnO:Co NRs (sample 1-9, $R_{MEA/M} = 9$) and the sample grown using the same growth parameters but with a 2GS (sample 2-9-1.5h; traces 1 and 2 in Figure 6-6, respectively) identify Co^{+2} with its intense satellite peaks at approximately 786 eV as the dominant cobalt compound. However, the spectrum corresponding to the sample grown from a low MEA concentration (sample 2-3-1.5h, trace 3 in Fig 6) is indicative of a significant Co^{+3} component, noting that this species gives rise to only very weak satellite features. XPS analysis of the Co 2p peak is not straightforward due to strong overlap of the different oxides/hydroxides and $2p_{3/2}$ multiplet/satellite structures with that of $2p_{1/2}$, but also because of the difficulty in finding pure cobalt reference compounds. However, Biesinger et al. presented some general advice on fitting Co 2p XPS spectra.[33] The Co $2p_{3/2}$ features were thus fitted with 4-5 peaks, incorporating similar fitting parameters and the resulting peak positions are compared in Table 6-2. A similar approach was recently followed by Yang et al. who were able to distinguish between $Co(OH)_2$ and Co_3O_4 in their samples.[17]

The peak positions of the fitted spectra support the qualitative assessment of the spectra, especially in regards to the shift of the main Co $2p_{3/2}$ peak (e.g. 779.7 eV vs. 780.5 eV for the two samples subject to a 2GS). The fitted Co $2p_{3/2}$ peak positions of the sample prepared with $R_{MEA/M} = 3$ + 2GS (sample 3) are close to the listed reference peaks for Co_3O_4. In turn this confirms that these NRs are decorated with a mixed

valance component (2^+ and 3^+ oxidation state), possibly of Co_3O_4 nature.

Fitting of Co $2p_{3/2}$ spectrum from the sample grown from $R_{MEA/M}$ = 9 + 2GS (sample 2) showed component peaks that are closer to the reference peak positions for $Co(OH)_2$. This confirms Co^{2+} as the dominant oxidation state and, together with the XRD results, points towards the hydroxide phase as being dominant.

Due the low overall cobalt content in the uncoated sample 1 (ca. 0.9 %at. +-0.1 for all samples of the first set), fitting of the spectrum is rather ambitious due to the low signal to noise ratio. When compared to sample 2 a significant additional peak around 787 eV is visible, which agrees with one of the characteristic reference peaks for CoO. A clear assignment of the dominant phase is not possible but it is postulated that the surface may be composed of a mixture of CoO and $Co(OH)_2$. Furthermore, in view of the problem posed by the lack of pure CoO as reference,[33] the spectrum was compared with that of McIntyre,[34] which is also cross referenced in Beisenger et al. It can be seen that the ratio of the principal peak at ~781 eV to the satellite peak ~786 eV of sample 1 resembles the reported Co 2p of reference CoO.[34] Thus, supporting the UV-Vis and XRD measurements, that indicate a replacement of Zn^{2+} by Co^{2+} in the ZnO crystal lattice (i.e. Co-O bond formation).

It is important to note, that the material characterization described here clearly demonstrates the ability to grow ZnO:Co NR arrays with an over-coating containing mainly Co^{2+} or Co^{2+}/Co^{3+} (possibly of $Co(OH)_2$ and Co_3O_4 nature, respectively), using the reported one-pot growth method. Furthermore, using a medium MEA volume for the synthesis (e.g. here 1.2 ml in 50 ml solution) could potentially lead to the deposition of $Co(OH)_2/Co_3O_4$ mixed phases, which have shown great potential as electrocatalyst materials.[17]

Following the experimental results from the two sets of samples, a possible growth mechanism is proposed. Since the growth of ZnO nanorods from highly alkaline solution is well-researched, the proposed growth reactions for the first growth stage are presented together with the initial growth solution composition and further growth influences in Appendix 4. However, in respect to the role of MEA some aspects are worth mentioning here. Firstly, MEA acts as complexing agent for zinc and cobalt when preparing the growth solution ($[Zn(MEA)_m]^{2+}$, $[Co(MEA)_m]^{2+}$ /$[Co(MEA)(OH)_x]^{2-x}$). Secondly, since higher MEA concentrations in the growth

solution were found to increase the ZnO growth, MEA is believed to exhibit a growth-directing function similar to the results of other groups.[35-37]. Additionally, MEA is crucial for the doping of the rods during the first growth stage. When the growth is terminated after the first stage it can be observed that the solution is still dark/black, thus most of the cobalt must still be complexed. In turn this also confirms a temperature dependent disassociation of the metal-MEA complexes, similar to earlier works on the stability of metal-complexes.[38, 39] While zinc is already significantly released at low temperatures (e.g. 70 °C) cobalt is held in its complex also at higher temperatures. It is therefore expected that the zinc and cobalt complexes ($[Zn(MEA)_m]^{2+}$, $([Co(MEA)_m]^{2+}/[Co(MEA)(OH)_x]^{2-x}$) exhibit different temperature stabilities.

However, when heating the solution to 90 °C during the first growth stage, lower amounts of cobalt are nevertheless released and available for the doping of the rods. It is important to note that for the substitution of zinc in the crystal lattice cobalt must be in its 2+ oxidation state. As presented in the description of the starting solution (see Appendix 4), the complexing with amines and the high alkalinity however favour the 3+ state as the most stable. Thus it is necessary to reduce cobalt from 3+ to 2+ for the doping to occur. Here MEA plays another crucial role. After dissolving in water and heating MEA can be decomposed to form organic compounds (e.g. aldehydes, formate) and ammonia, where dissolved oxygen is directly involved in the degradation of MEA.[40] Importantly, ammonia is a reducing agent due to its free lone-pair of electrons. This in turn allows the presence of some Co^{2+} in the solution, whereby $[Co(OH)_4]^{2-}$ is likely the major component at 90 °C.[41] While it might be expected that the reductive nature of the solution is increased with increasing MEA concentration, a higher Co^{2+} concentration in the NRs could not be conclusively observed for samples grown from a higher MEA volume. This may be the result of a Co^{2+} dilution limit in ZnO depending on the growth temperature.[42]

Doping of the nanorods occurs due to the competition of the available zinc and cobalt sources, where Co^{2+} can directly occupy the Zn^{2+} site in the crystal lattice. The doping process is reported to involve octahedrally coordinated cobalt species (e.g. $[Co(OH)_4]^{2-}$; note the omission of water molecules), which bind to the ZnO nucleus.[43, 44] For the substitution to occur these species must then be transformed into the tetrahedral ZnO geometry. The successful incorporation of Co^{2+} can therefore be directly observed from the d-d visible light transition since these are fingerprints of

cobalt in the tetrahedral crystal field of ZnO.[8, 28, 31] However, the transformation from an octahedral to a tetrahedral environment adds an additional reaction barrier which may lead to the growth of thicker rods, as has been observed by others.[43, 45, 46]

It is important to point out that the incorporation of Co^{2+} into ZnO requires the presence of a ZnO nucleus.[43] When all the zinc is consumed and precipitated no further ZnO nucleus formation occurs and therefore the binding of the octahedrally coordinated cobalt species may be somewhat hindered. In turn the overall growth of the structures slows down dramatically. Of even higher importance in this respect is the fact that the growth solution is not yet supersaturated with cobalt (i.e. the majority of Co is still complexed with MEA). This is believed to be the main reason as to why no significant $Co(OH)_2$ and/or Co_3O_4 growth occurs on the experimental timescale employed here.

During the second growth stage the temperature is increased. While all the zinc has already reacted and precipitated, higher temperatures lead to an increased release of cobalt (Co^{3+}) into the growth solution. The higher the temperature and heating rate, the higher the rate of release of cobalt. Hence supersaturation of the solution occurs, making the agglomeration and growth of $Co(OH)_2$ and/or Co_3O_4 possible. Additionally, the decomposition of MEA is accelerated. This leads to higher NH_3 concentrations in the solution and therefore a higher probability that this may reduce Co^{3+} to Co^{2+} and subesquent reaction to $[Co(OH)_4]^{2-}$. It is acknowledged that the reduction to Co^{2+} can also happen due to the formation of hexaamminecobalt(III) and its rapid decomposition into hexaamminecobalt(II) at this elevated temperature, as suggested by Wang et al. and Li et al..[47, 48] These authors further report on the hydrolysis of hexaamminecobalt(II) to $Co(OH)_2$.[47, 48] However, in the present study the influence of a high OH^- concentration most likely leads to the formation of larger amounts of $[Co(OH)_4]^{2-}$ in the growth solution first (6.1):

$$[Co(NH_3)_6]^{2+} + 4OH^- \leftrightarrow [Co(OH)_4]^{2-} + 6NH_3 \qquad (6.1)$$

Equation (6.1) demands high NH_3 concentrations to be present in order for large amounts of $[Co(OH)_4]^{2-}$ to be formed. The concentration of Co^{2+} (in form of $[Co(OH)_4]^{2-}$ as growth units) may thus be determined by the MEA concentration in the growth solution, either by direct reduction of Co^{3+} or complex formation after equation (6.1). Importantly, both cobalt-complexes in equation (6.1) are charged and

could therefore adsorb more easily to the polar (002) plane, which in turn may explain why for all samples subjected to a second growth stage, the coverage of the rod tips was the strongest. Thus, it seems likely that the initial growth of the cobaltic decoration occurs due to the adsorption of growth species (e.g. $[Co(OH)_4]^{2-}$) onto the basal plane and subsequent reactions in dependence of the MEA concentration, as described below.

In the case of a high MEA concentration (here e.g. $R_{MEA/M}$ = 9), and therefore an increased reduction of Co^{3+} to Co^{2+}, the high concentration of $[Co(OH)_4]^{2-}$ leads to the $Co(OH)_2$ formation becoming dominant (6.2):

$$[Co(OH)_4]^{2-} \leftrightarrow Co(OH)_2 + 2OH^- \quad (6.2)$$

However, if a low MEA concentration is chosen (here e.g. $R_{MEA/M}$ = 3), it is reasonable to expect a somewhat lower/slower reduction to Co^{2+}. In turn, this leaves a significant amount of Co^{3+} in the solution, which would favour the formation of Co_3O_4 as a mixed-valance oxide. Co_3O_4 may be formed under hydrothermal conditions according to (6.3):[49, 50]

$$[Co(OH)_4]^{2-} + 2CoOOH \leftrightarrow Co_3O_4 + 2OH^- + 2H_2O \quad (6.3)$$

As equation (6.3) shows, besides $[Co(OH)_4]^{2-}$ the trivalaent cobalt oxy-hydroxide is needed as growth precursor for Co_3O_4. Hence, the formation of CoOOH, which may form under the influence of dissolved oxygen, would be in direct competition to the formation of large amounts of $[Co(OH)_4]^{2-}$. Indirect evidence for this competition comes from the fact that the air volume in the autoclave has a major influence on the cobalt phase, whereby larger air volumes – and therefore a higher concentration of dissolved oxygen – are shown to result in an increased Co_3O_4 formation.[49, 51] In the synthesis presented here, a lower air volume in the autoclave should thus lead to an increase in the $[Co(OH)_4]^{2-}$ concentration and hence less CoOOH. Significant $Co(OH)_2$ growth after (6.2) would be the consequence. This is indeed what is observed in the SEM images in Figure A4- 2, where two samples were grown from the same growth solution but in different autoclaves (100 ml and 200 ml). Due to the lower air volume (50 ml as compared to 150 ml) significant co-deposition of $Co(OH)_2$ and Co_3O_4 occurs even when a low MEA concentration is used ($R_{MEA/M}$ = 3).

Following the growth experiments, the electrochemical properties of the ZnO:Co and Co_3O_4/$Co(OH)_2$ decorated structures, in the form of cyclic voltammetry (CV) and

electrochemical impedance spectroscopy (EIS) in 1M KOH, were investigated and the results are presented in Figure 6-7 and Figure 6-8, respectively. A duration of 1.5 h for the 2GS was chosen for the decorated samples. Undoped ZnO with or without Co_3O_4/$Co(OH)_2$ decoration reference samples are included in the figures and the MEA concentration is employed as a figure of merit for comparison in the following discussion.

Firstly, attention is drawn to the as-grown samples. The samples with no 2GS (black curves in Figure 6-7 and Figure 6-8) exhibit only a very moderate water oxidation performance. In contrast, most samples that were subject to a 2GS – either directly for ZnO:Co structures (blue traces) or additional over-coating for ZnO structures (dark yellow traces) – show improved oxidation currents by comparison. Here the ZnO/ZnO:Co - Co_3O_4 structures perform best, as compared to the $Co(OH)_2$ decorated samples. In particular the ZnO/ZnO:Co - Co_3O_4 samples exhibit an earlier current

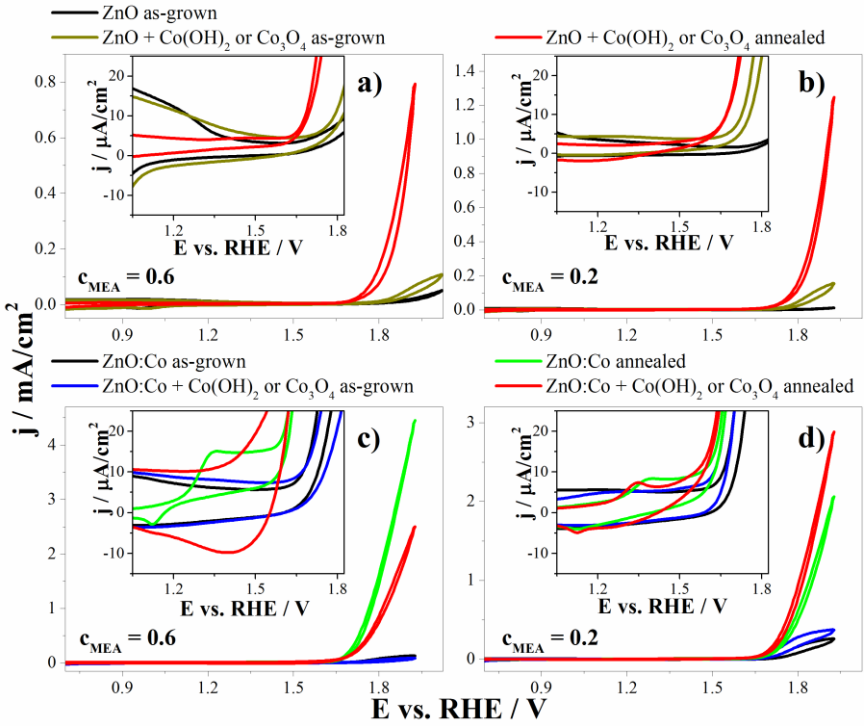

Figure 6-7. Voltammograms in the dark of a) and b) undoped ZnO NR arrays without/with $Co(OH)_2$ or Co_3O_4 over-growth, respectively; c) and d) cobalt doped ZnO:Co NR arrays without/with $Co(OH)_2$ or Co_3O_4 over-growth, respectively. The insets show the pre-OER range higher magnified. Annealing was carried out at 400 °C for 3h – please note that $Co(OH)_2$ was thus converted to Co_3O_4. Electrolyte: 1M KOH; scan rate = 50 mV/s.

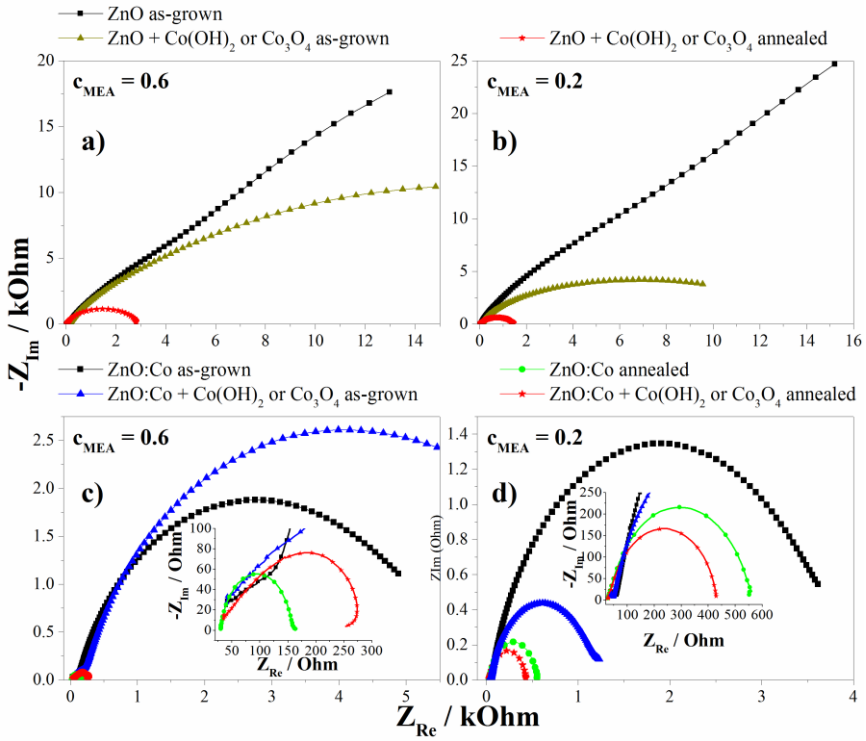

Figure 6-8. Nyquist plots of a) and b) undoped ZnO NR arrays without/with $Co(OH)_2$ or Co_3O_4 over-growth, respectively; c) and d) cobalt doped ZnO:Co NR arrays without/with $Co(OH)_2$ or Co_3O_4 over-growth, respectively. Annealing was carried out at 400 °C for 3h – please note that $Co(OH)_2$ was thus converted to Co_3O_4. The insets magnify the Nyquist plots of the annealed nominally non-decorated and Co_3O_4 decorated ZnO:Co NR arrays. Electrolyte: 1M KOH; E_{appl} = 1.7 V vs. RHE; E_{AC} = 10 mV; f = 50k – 0.5 Hz.

onset (see insets) and resulting reduced overpotentials. This in turn might be taken as an indication of the catalytic function of the Co_3O_4, which was reported to exhibit slightly lower OER overpotentials as compared to $Co(OH)_2$ and CoOOH.[52, 53] However, the exact reason for the slightly better oxygen evolution reaction (OER) kinetics for the as-grown Co_3O_4 decorated samples is not yet clear and requires further study. Further reduction of the OER over-potentials could potentially be achieved by using smaller Co_3O_4 structures, as reported by Esswein et al..[15] Nevertheless, the resistivity of the samples is still high, as indicated by the slow rise of the oxidation current. The EIS experiments further confirm these observations (see black traces in Figure 6-8). When, for example, focusing on panel d) of Figure 6-8 the reduction of the overall charge transfer resistance – visible by the width of the semicircle – can be readily observed when comparing the Co_3O_4 decorated (blue trace) to the undecorated (black trace) samples. Another important finding from the EIS measurements is that,

undoped ZnO NR arrays exhibit a higher charge transfer resistance when compared to ZnO:Co NR arrays – independent of the MEA volume used.

Additional CV experiments in ferro/ferrycianide (Figure A4- 3) revealed a poor capacity of the electrodes to reduce/oxidize the Fe^{2+}/Fe^{3+} redox-couple for all as-grown samples. This may be indicative of poor electrode quality for the as-grown ZnO/ZnO:Co NRs, which in turn would hinder the charge transfer. Furthermore, these experiments showed that the charge transfer within the structures can be greatly improved by an annealing treatment (see Figure A4- 3).

The OER kinetics are also strongly influenced by the annealing treatment. Here it is important to note that $Co(OH)_2$ is transformed to Co_3O_4 by the annealing treatment used in this study. For all annealed samples a cathodic shift of the onset potential as well as lower resistivity and significantly increased anodic current density can be recognized from the CV curves in Figure 6-7. Benefitting from lower onset potentials, the overpotentials at 0.8 mA/cm^2 are also improved for the samples. Comparing the annealed decorated samples only (red curves in Figure 6-7), the overpotentials were found as 0.7 V, 0.66 V, 0.56 V and 0.55 V for panel Figure 6-7a to d, respectively. The overall charge transfer resistance is greatly reduced upon annealing, with values lower than 500 Ω at 1.7 V vs. RHE for the Co_3O_4 decorated ZnO:Co structures, as symbolized by the EIS spectra of these samples. The lowest overall charge transfer resistance of ca. 150 Ω was recognized for the nominally un-decorated ZnO:Co NR sample grown from c_{MEA} = 0.6 (see inset of Figure 6-8c). Despite an apparent improvement of the water oxidation performance, the annealed anode materials still perform worse when compared to other water oxidation anodes,[17, 52, 54, 55] but show similar OER characteristics to ZnO/CoO (readily oxidized to Co_3O_4) anodes prepared using chemical bath deposition (ZnO) followed by electrochemical deposition (CoO).[56] Further optimization of the structures is thus needed.

Some general trends from the CV and EIS measurements can be recognized. Firstly, the undoped ZnO NR arrays – independent of the $Co(OH)_2/Co_3O_4$ decoration – exhibit a more anodic onset of the OER current and considerably higher over-potentials at 1 mA/cm^2. A good way to appreciate the later OER onset is to focus on the annealed decorated samples in the insets of Figure 6-7 (red curves). While the current onset for the annealed decorated ZnO NR arrays is observed at around 1.68 V vs. RHE, this

value shifts cathodically by more than 60 mV for the annealed decorated ZnO:Co NR arrays. This must somehow be related to the ZnO:Co NRs themselves and might point towards a shift of the energy band positions or the Fermi energy with respect to the water redox potential. Additionally, the annealed decorated ZnO:Co NR arrays show a stronger cathodic shift (insets of Figure 6-7c and d, red curves) as compared to the annealed undecorated ZnO:Co NR arrays (green curves in the insets of Figure 6-7c and d). Overall the annealed decorated ZnO:Co sample grown from c_{MEA} = 0.6 shows the earliest onset at around 1.58 V vs. RHE. However, this sample suffered from a higher internal resistance as suggested by the Bode plots in Figure A4- 4.

Secondly, the insets of Figure 6-7 reveal that in particular the annealed ZnO:Co NR arrays (nominally non-decorated and decorated) show additional oxidation and reduction features just before the OER onset. These features are significantly stronger for the annealed ZnO:Co NR arrays (decorated or nominally un-decorated) as compared to the annealed decorated ZnO NR arrays. It has been reported that redox features in this potential range can be attributed to the conversion between the different cobalt oxidation states ($Co^{2+} \leftrightarrow Co^{3+}$, $Co^{3+} \leftrightarrow Co^{4+}$).[16, 17, 49] However, increasing the scan rate during the CV experiments is reported to result in the merging of the various oxidation features into a single, broader feature.[49] The catalytic function for Co-based materials is reported to stem from the oxidation of cobalt to Co^{3+} and Co^{4+}.[16, 17] For both, $Co(OH)_2$ and Co_3O_4, it can thus be expected that, when applying an anodic potential and/or under solar irradiation, CoOOH (i.e. Co^{3+}) is formed at the catalyst surface with a further transformation to CoO_2 (i.e. Co^{4+}).[49] Water oxidation may then occur due to the formation of the O-O bond at two or more catalytically active Co^{4+} sites. [16, 17, 57] In turn, Co^{4+} is reduced but can be readily oxidized again under the mentioned conditions.[57] Importantly, for the samples presented here, good OER kinetics have only been observed for samples that exhibited these features. This is in line with earlier reports that find that the surface redox behaviour of Co^{2+} and Co^{3+} correlate with the catalytic activity.

Somewhat surprisingly in this regard is that both annealed nominally undecorated ZnO:Co NR arrays show the cobalt redox features as well. Especially for the annealed undecorated ZnO:Co NR sample grown c_{MEA} = 0.6 M, which exhibits these features relatively strongly. This apparent anomaly is discussed below.

While the material characterization by SEM, XPS and XRD did not conclusively reveal the presence of a cobalt containing over-coating, the presented CV measurements clearly indicate the oxidation state transition of cobalt. The observed redox features may have different origins for these samples. Firstly, it could be that the observed redox features may be the result of the oxidation/reduction of Co^{2+} in the bulk and surface of the rods (possibly participating in the OER). Or they might stem from the prolonged deposition time during the first growth stage (1GS = 16 h) which may lead to the formation of ultrathin cobaltic over-coatings.

In order to check for the latter explanation additional samples were grown with varying deposition times for the 1GS (10 h and 24 h, $R_{MEA/M}$ = 9, no 2GS). If the latter explanation is valid, longer deposition times should lead to an increased deposition of cobaltic over-coatings on the rod-surface, while shorter growth duration may result in the opposite. The cyclic voltammograms and EIS spectra of these samples (after annealing at 400 °C in air for 3 h) are presented in the appendix as Figure A4- 5. These measurements suggest that the improved OER kinetics are not the result of a significant additional cobaltic over-coatings for the growth durations investigated here, since the performance of the samples has been found to be very similar. Thus, it is more plausible that the observed redox features are related to the cobalt doping of the rods. The undecorated ZnO:Co NR sample grown from 1.8 ml MEA showing these features more clearly may thus benefit from an improved crystal quality.

Additionally, the sample grown for 24 h was measured for its photo-electrochemical response under simulated solar irradiation (100 mW/cm^2, AM 1.5G). The recorded LSV curves were recorded in the following sequence: (1) under chopped solar irradiation, (2) in the dark, (3) under constant solar irradiation with a 400 nm longpass filter and (4) re-measured in the dark are presented in Figure 6-9.

Excitation of the sample with simulated solar irradiation leads to the emergence of a photo-current with an onset potential of ca. 0.5 V vs. RHE. Importantly, the visible light activity (measurements with the 400 nm longpass filter) of the undecorated ZnO:Co NR array is significantly higher when compared to an undoped reference sample, which is included as black traces in Figure 6-9. For the undecorated ZnO:Co

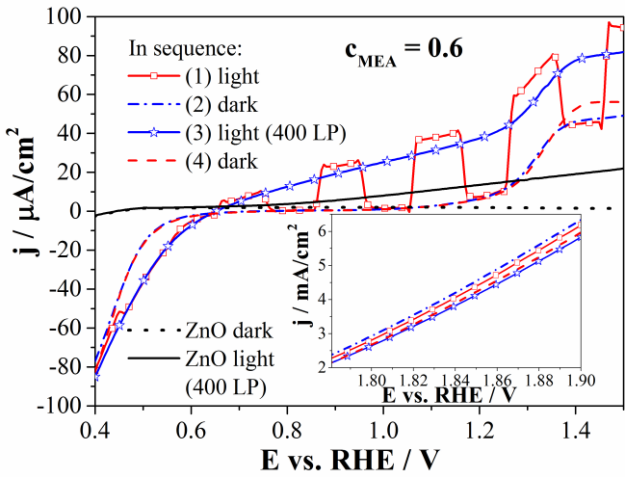

Figure 6-9. LSV curves of a nominally undecorated ZnO:Co and ZnO NR arrays in the dark and under simulated solar irradiation (with and without a 400 nm longpass filter (400 LP)). The samples were annealed at 400 °C for 3h. Electrolyte: 1M KOH; scan rate = 50 mV/s. The inset shows the current at higher potentials for the undecorated ZnO:Co NR array. Please note that the max current obtained is slightly higher compared to the CVs presented in Figure A4- 5, due to the transport of the cell to the solar simulator (i.e. agitation of the electrolyte = desorption of oxygen, re-establishment of the electrolyte`s pH at the NR surface.)

NR array attenuation with a 400 nm longpass filter leads to a photo-current decrease of only about 15 %, when compared to the measurement without the filter. Thus, the majority of the photo-current in these samples is due to visible light absorption. This important finding confirms that ZnO:Co can be utilized as photo-active material for solar applications. However, realistically, it is important to realize that the generated photo-current is low and considerably higher photo-currents have been achieved under 1-sun illuminations by others – even with undoped ZnO.[7, 12, 26, 58-61] Here, the slow rise of the photo-current with increasing potential points towards high recombination losses within the NRs.

Further evidence to support this hypothesis can be recognized when one examines the high potential end of the LSV curves (inset of Figure 6-9). While the current in this range was found to drop with increasing scan number (non-stirred solution resulting in adsorption of oxygen, lower pH at electrode surface; e.g. compare the two dark scans) the light scans, performed *before* the dark scans, showed an even *smaller* current. Upon solar irradiation additional charge carriers are generated. Together with a high applied potential this leads to a high carrier density in the rods. If the photo-excited electrons and holes are not separated and transported fast enough, the high

charge carrier density leads to a high rate of recombination - possibly due to Auger recombination, which demands high carrier densities. Such recombination may be a contributing factor for the observations presented here. This is because the separation between the dark and light scans was found to increase with the applied potential and therefore increasing charge carrier density (see inset of Figure 6-9).

The potential of these materials as photo-anodes is currently being evaluated together with an investigation of the cobaltic over-coatings as possible photo-corrosion inhibiting barrier layers for the underlying ZnO:Co NR arrays. In regards to the latter aspect it is noteworthy that no structural changes were observed for undecorated ZnO:Co nanorods before and after the photo-electrochemical characterization in the SEM analysis of Figure A4- 6.

6.5 Conclusions

A simple low-temperature, one-pot hydrothermal method has been presented, that allows for the deposition of $Co(OH)_2$ and/or Co_3O_4 decorated cobalt-doped ZnO (ZnO:Co) nanorod-arrays. Using the growth method presented, the nanorod volume – and therefore the visible light absorption – can be changed by changing the monoethanolamine (MEA) concentration used in the growth solution. Furthermore the MEA concentration was found to influence the deposition of $Co(OH)_2$ and/or Co_3O_4 over-coatings during a second growth stage. With this in mind, the crucial role of MEA as complexing-, growth-directing- and reducing agent has been discussed and, based on experimental results, a possible growth mechanism has been proposed. The samples were also investigated for their functionality, taking the oxidation of water as an example reaction. CV and EIS measurements in alkaline solution showed improved water oxidation kinetics for the ZnO:Co and $Co(OH)_2/Co_3O_4$-decorated ZnO:Co nanorod-arrays. Over-potentials for water oxidation as low as 0.55 V at 1 mA/cm^{-2} were achieved and the cobalt-doped ZnO nanorod-arrays also showed visible light activated photo-currents. However, future research must now aim at optimizing the structures in order to reduce the over-potential and increase the visible light activity. Controlling the $Co(OH)_2/Co_3O_4$ catalyst loading and the deposition of a more uniform $Co(OH)_2/Co_3O_4$ over-coating may present one way of achieving these aims. Additionally, further (photo-)electrochemical experiments are required for the detailed evaluation of the catalytic performance of the structures and to properly evaluate the

use of the presented method for the deposition of photo-anodes for solar water splitting.

6.6 References

[1] I. Djerdj, Z. Jaglicic, D. Arcon, and M. Niederberger, "Co-Doped ZnO nanoparticles: Minireview," *Nanoscale,* vol. 2, no. 7, pp. 1096-1104, 2010.

[2] S. B. Ogale, "Dilute doping, defects, and ferromagnetism in metal oxide systems," *Adv Mater,* vol. 22, no. 29, pp. 3125-55, 2010.

[3] S. Basu *et al.*, "Local Structure Investigation of Cobalt and Manganese Doped ZnO Nanocrystals and Its Correlation with Magnetic Properties," *The Journal of Physical Chemistry C,* vol. 118, no. 17, pp. 9154-9164, 2014.

[4] D. Y. Inamdar, A. D. Lad, A. K. Pathak, I. Dubenko, N. Ali, and S. Mahamuni, "Ferromagnetism in ZnO Nanocrystals: Doping and Surface Chemistry," *The Journal of Physical Chemistry C,* vol. 114, no. 3, pp. 1451-1459, 2010.

[5] V. Gandhi, R. Ganesan, H. H. Abdulrahman Syedahamed, and M. Thaiyan, "Effect of Cobalt Doping on Structural, Optical, and Magnetic Properties of ZnO Nanoparticles Synthesized by Coprecipitation Method," *The Journal of Physical Chemistry C,* vol. 118, no. 18, pp. 9715-9725, 2014.

[6] R. K. Singhal, N. Jakhar, A. Samariya, S. N. Dolia, and S. Kumar, "Effect of Co and O defects on ferromagnetism in Co-doped ZnO: An X-ray absorption spectroscopic investigation," *Physica B: Condensed Matter,* vol. 530, pp. 1-6, 2018.

[7] P. P. Patel *et al.*, "Nitrogen and cobalt co-doped zinc oxide nanowires – Viable photoanodes for hydrogen generation via photoelectrochemical water splitting," *Journal of Power Sources,* vol. 299, pp. 11-24, 2015.

[8] C. A. Johnson, A. Cohn, T. Kaspar, S. A. Chambers, G. M. Salley, and D. R. Gamelin, "Visible-light photoconductivity of Zn1−xCoxO and its dependence onCo2+concentration," *Physical Review B,* vol. 84, no. 12, p. 125203, 2011.

[9] S. Kuriakose, B. Satpati, and S. Mohapatra, "Enhanced photocatalytic activity of Co doped ZnO nanodisks and nanorods prepared by a facile wet chemical method," *Phys Chem Chem Phys,* vol. 16, no. 25, pp. 12741-12749, 2014.

[10] W. Zang, P. Li, Y. Fu, L. Xing, and X. Xue, "Hydrothermal synthesis of Co–ZnO nanowire array and its application as piezo-driven self-powered humidity sensor with high sensitivity and repeatability," *RSC Adv.,* vol. 5, no. 102, pp. 84343-84349, 2015.

[11] H.-J. Lee, S.-Y. Jeong, C. R. Cho, and C. H. Park, "Study of diluted magnetic semiconductor: Co-doped ZnO," *Applied Physics Letters,* vol. 81, no. 21, p. 4020, 2002.

[12] W. C. Lee, G. E. Canciani, B. O. S. Alwhshe, and Q. Chen, "Enhanced photoelectrochemical water oxidation by ZnxMyO (M = Ni, Co, K, Na) nanorod arrays," *International Journal of Hydrogen Energy,* vol. 41, no. 1, pp. 123–131, 2015.

[13] F. Mueller, D. Geiger, U. Kaiser, S. Passerini, and D. Bresser, "Elucidating the Impact of Cobalt Doping on the Lithium Storage Mechanism in Conversion/Alloying-Type Zinc Oxide Anodes," *ChemElectroChem,* vol. 3, no. 9, pp. 1311-1319, 2016.

[14] V. Ramakrishnan, H. Kim, J. Park, and B. Yang, "Cobalt oxide nanoparticles on TiO2nanorod/FTO as a photoanode with enhanced visible light sensitization," *RSC Adv.*, vol. 6, no. 12, pp. 9789-9795, 2016.
[15] A. J. Esswein, M. J. McMurdo, P. N. Ross, A. T. Bell, and T. D. Tilley, "Size-Dependent Activity of Co3O4 Nanoparticle Anodes for Alkaline Water Electrolysis," *The Journal of Physical Chemistry C,* vol. 113, no. 33, pp. 15068-15072, 2009.
[16] J. R. Swierk and T. D. Tilley, "Electrocatalytic Water Oxidation by Single Site and Small Nuclearity Clusters of Cobalt," *Journal of The Electrochemical Society,* vol. 165, no. 4, pp. H3028-H3033, 2017.
[17] J. Yang *et al.*, "A multifunctional biphasic water splitting catalyst tailored for integration with high-performance semiconductor photoanodes," *Nat Mater,* vol. 16, pp. 335–341, 2017.
[18] L. Xi *et al.*, "Co3O4-Decorated Hematite Nanorods As an Effective Photoanode for Solar Water Oxidation," *The Journal of Physical Chemistry C,* vol. 116, no. 26, pp. 13884-13889, 2012.
[19] V. Artero, M. Chavarot-Kerlidou, and M. Fontecave, "Splitting water with cobalt," *Angew Chem Int Ed Engl,* vol. 50, no. 32, pp. 7238-66, 2011.
[20] F. Jiao and H. Frei, "Nanostructured cobalt and manganese oxide clusters as efficient water oxidation catalysts," *Energy & Environmental Science,* vol. 3, no. 8, p. 1018, 2010.
[21] K.-L. Yan *et al.*, "Mesoporous Ag-doped Co3O4 nanowire arrays supported on FTO as efficient electrocatalysts for oxygen evolution reaction in acidic media," *Renewable Energy,* 2017.
[22] D. Cai *et al.*, "High-performance supercapacitor electrode based on the unique ZnO@Co(3)O4(4) core/shell heterostructures on nickel foam," *ACS Appl Mater Interfaces,* vol. 6, no. 18, pp. 15905-12, 2014.
[23] Y. Bai, W. Liu, C. Yu, T. Wang, J. Feng, and S. Xiong, "One-Pot Solvothermal Synthesis of ZnO@α-Co(OH)2 Core–Shell Hierarchical Microspheres with Superior Lithium Storage Properties," *The Journal of Physical Chemistry C,* vol. 120, no. 5, pp. 2984-2992, 2016.
[24] L. Zhang, X. Jing, J. Liu, J. Wang, and Y. Sun, "Facile synthesis of mesoporous ZnO/Co 3 O 4 microspheres with enhanced gas-sensing for ethanol," *Sensors and Actuators B: Chemical,* vol. 221, pp. 1492-1498, 2015.
[25] J. Kegel, J. Halpin, F. Laffir, I. M. Povey, and M. E. Pemble, "Rapid low-temperature solution growth of ZnO:Co nanorod arrays with controllable visible light absorption," *CrystEngComm,* vol. 19, no. 14, pp. 1938-1946, 2017.
[26] J. Kegel, I. M. Povey, and M. E. Pemble, "ZnO Nanorod-Arrays as Photo-(Electro)Chemical Materials: Strategies Designed to Overcome the Material's Natural Limitations," *Journal of The Electrochemical Society,* vol. 165, no. 4, pp. H3034-H3044, 2017.
[27] C. A. Johnson, T. C. Kaspar, S. A. Chambers, G. M. Salley, and D. R. Gamelin, "Sub-band-gap photoconductivity inCo2+-doped ZnO," *Physical Review B,* vol. 81, no. 12, p. 125206, 2010.
[28] P. Koidl, "Optical absorption of Co2+ in ZnO," *Physical Review B,* vol. 15, no. 5, pp. 2493-2499, 1977.

[29] J. W. May, J. Ma, E. Badaeva, and X. Li, "Effect of Excited-State Structural Relaxation on Midgap Excitations in Co2+-Doped ZnO Quantum Dots," *The Journal of Physical Chemistry C*, vol. 118, no. 24, pp. 13152-13156, 2014.
[30] R. Elilarassi and G. Chandrasekaran, "Influence of Co-doping on the structural, optical and magnetic properties of ZnO nanoparticles synthesized using auto-combustion method," *Journal of Materials Science: Materials in Electronics*, vol. 24, no. 1, pp. 96-105, 2012.
[31] W. K. Liu, G. M. Salley, and D. R. Gamelin, "Spectroscopy of Photovoltaic and Photoconductive Nanocrystalline Co2+-Doped ZnO Electrodes," *The Journal of Physical Chemistry B*, vol. 109, no. 30, pp. 14486-14495, 2005.
[32] M. Tortosa, M. Mollar, B. Marí, and F. Lloret, "Optical and magnetic properties of ZnCoO thin films synthesized by electrodeposition," *Journal of Applied Physics*, vol. 104, no. 3, p. 033901, 2008.
[33] M. C. Biesinger, B. P. Payne, A. P. Grosvenor, L. W. M. Lau, A. R. Gerson, and R. S. C. Smart, "Resolving surface chemical states in XPS analysis of first row transition metals, oxides and hydroxides: Cr, Mn, Fe, Co and Ni," *Applied Surface Science*, vol. 257, no. 7, pp. 2717-2730, 2011.
[34] N. S. McIntyre and M. G. Cook, "X-ray photoelectron studies on some oxides and hydroxides of cobalt, nickel, and copper," *Analytical Chemistry*, vol. 47, no. 13, pp. 2208-2213, 1975.
[35] Y. Zhang, T. Bian, J. Gu, X. Zheng, and Z. Li, "Controllable ZnO architectures with the assistance of ethanolamine and their application for removing divalent heavy metals (Cu, Pb, Ni) from water," *New Journal of Chemistry*, vol. 42, no. 5, pp. 3356-3362, 2018.
[36] F. Boudjouan *et al.*, "Effects of stabilizer ratio on photoluminescence properties of sol-gel ZnO nano-structured thin films," *Journal of Luminescence*, vol. 158, pp. 32-37, 2015.
[37] P. Hosseini Vajargah, H. Abdizadeh, R. Ebrahimifard, and M. R. Golobostanfard, "Sol–gel derived ZnO thin films: Effect of amino-additives," *Applied Surface Science*, vol. 285, pp. 732-743, 2013.
[38] H. Irving and R. J. P. Williams, "Order of Stabilily of Metal Complexes," *Nature*, vol. 162, pp. 746-747, 1948.
[39] R. S. Subrahmanya, "Polarographic behaviour of metals in ethanolamines," *Proceedings of the Indian Academy of Sciences*, journal article vol. 46, no. 6, pp. 443-453, 1957.
[40] S. Chi and G. T. Rochelle, "Oxidative Degradation of Monoethanolamine," *Industrial & Engineering Chemistry Research*, vol. 41, no. 17, pp. 4178-4186, 2002.
[41] J. Chivot, L. Mendoza, C. Mansour, T. Pauporté, and M. Cassir, "New insight in the behaviour of Co–H2O system at 25–150°C, based on revised Pourbaix diagrams," *Corrosion Science*, vol. 50, no. 1, pp. 62-69, 2008.
[42] B. B. Straumal, A. A. Mazilkin, S. G. Protasova, A. A. Myatiev, P. B. Straumal, and B. Baretzky, "Increase of Co solubility with decreasing grain size in ZnO," *Acta Materialia*, vol. 56, no. 20, pp. 6246-6256, 2008.
[43] D. A. Schwartz, N. S. Norberg, Q. P. Nguyen, J. M. Parker, and D. R. Gamelin, "Magnetic Quantum Dots: Synthesis, Spectroscopy, and Magnetism of Co2+- and Ni2+-Doped ZnO Nanocrystals," *Journal of the American Chemical Society*, vol. 125, no. 43, pp. 13205-13218, 2003.

[44] L. Yanmei *et al.*, "Structure and photoluminescence of arrayed Zn1−xCoxO nanorods grown via hydrothermal method," *Journal of Physics D: Applied Physics,* vol. 40, no. 15, pp. 4592-4596, 2007.
[45] C.-W. Liu *et al.*, "Enhancement in the structure quality of ZnO nanorods by diluted Co dopants: Analyses via optical second harmonic generation," *Journal of Applied Physics,* vol. 117, no. 8, p. 084315, 2015.
[46] X. He, H. Yang, Z. Chen, and S. S. Y. Liao, "Effect of Co-doping content on hydrothermal derived ZnO array films," *Physica B: Condensed Matter,* vol. 407, no. 15, pp. 2895-2899, 2012.
[47] B. Wang, X.-Y. Lu, and Y. Tang, "Synthesis of snowflake-shaped Co3O4 with a high aspect ratio as a high capacity anode material for lithium ion batteries," *Journal of Materials Chemistry A,* vol. 3, no. 18, pp. 9689-9699, 2015.
[48] Y. Li and Y. Wu, "Critical Role of Screw Dislocation in the Growth of Co(OH)2Nanowires as Intermediates for Co3O4Nanowire Growth," *Chemistry of Materials,* vol. 22, no. 19, pp. 5537-5542, 2010.
[49] Y. Cao, F. Yuan, M. Yao, J. H. Bang, and J.-H. Lee, "A new synthetic route to hollow Co3O4 octahedra for supercapacitor applications," *CrystEngComm,* vol. 16, no. 5, pp. 826-833, 2014.
[50] G. Furlanetto and L. Formaro, "Precipitation of Spherical Co3O4 Particles," *Journal of Colloid and Interface Science,* vol. 170, no. 1, pp. 169-175, 1995.
[51] Y. Dong, K. He, L. Yin, and A. Zhang, "A facile route to controlled synthesis of Co3O4 nanoparticles and their environmental catalytic properties," *Nanotechnology,* vol. 18, no. 43, p. 435602, 2007.
[52] Y. Jiang, X. Li, T. Wang, and C. Wang, "Enhanced electrocatalytic oxygen evolution of alpha-Co(OH)2 nanosheets on carbon nanotube/polyimide films," *Nanoscale,* vol. 8, no. 18, pp. 9667-75, 2016.
[53] Y.-C. Liu, J. A. Koza, and J. A. Switzer, "Conversion of electrodeposited Co(OH)2 to CoOOH and Co3O4, and comparison of their catalytic activity for the oxygen evolution reaction," *Electrochimica Acta,* vol. 140, pp. 359-365, 2014.
[54] C. C. McCrory, S. Jung, I. M. Ferrer, S. M. Chatman, J. C. Peters, and T. F. Jaramillo, "Benchmarking hydrogen evolving reaction and oxygen evolving reaction electrocatalysts for solar water splitting devices," *J Am Chem Soc,* vol. 137, no. 13, pp. 4347-57, 2015.
[55] C. C. McCrory, S. Jung, J. C. Peters, and T. F. Jaramillo, "Benchmarking heterogeneous electrocatalysts for the oxygen evolution reaction," *J Am Chem Soc,* vol. 135, no. 45, pp. 16977-87, 2013.
[56] N. Koteeswara Reddy, S. Winkler, N. Koch, and N. Pinna, "Electrochemical Water Oxidation of Ultrathin Cobalt Oxide-Based Catalyst Supported onto Aligned ZnO Nanorods," *ACS Appl Mater Interfaces,* vol. 8, no. 5, pp. 3226-32, 2016.
[57] M. Risch *et al.*, "Water oxidation by amorphous cobalt-based oxides: in situ tracking of redox transitions and mode of catalysis," *Energy & Environmental Science,* vol. 8, no. 2, pp. 661-674, 2015.
[58] J. Kegel, F. Laffir, I. M. Povey, and M. E. Pemble, "Defect-promoted photo-electrochemical performance enhancement of orange-luminescent ZnO nanorod-arrays," *Phys Chem Chem Phys,* vol. 19, no. 19, pp. 12255--12268, 2017.

[59] Y. Qiu, K. Yan, H. Deng, and S. Yang, "Secondary branching and nitrogen doping of ZnO nanotetrapods: building a highly active network for photoelectrochemical water splitting," *Nano Lett,* vol. 12, no. 1, pp. 407-13, 2012.

[60] K. Govatsi, A. Seferlis, S. G. Neophytides, and S. N. Yannopoulos, "Influence of the morphology of ZnO nanowires on the photoelectrochemical water splitting efficiency," *International Journal of Hydrogen Energy,* vol. 43, no. 10, pp. 4866-4879, 2018.

[61] B.-S. Wang *et al.*, "An overlapping ZnO nanowire photoanode for photoelectrochemical water splitting," *Catalysis Today,* 2018.

Chapter 7

This chapter represent an adapted version of the publication:

> J. Kegel, I. M. Povey, and M. E. Pemble, "ZnO Nanorod-Arrays as Photo-(Electro)Chemical Materials: Strategies Designed to Overcome the Material's Natural Limitations" *Journal of The Electrochemical Society,* vol. 165, pp. H3034-H3044, 2018.

Changes to the publication were only made in regards to formatting requirements. Major parts of this chapter represent the work presented as an invited talk titled "Tailoring Zinc Oxide Nanorod-Arrays for Photo-(electro)Chemical Applications", given at the 231st ECS Meeting, New Orleans, 2017.

7 ZnO nanorod-arrays as photo-(electro)chemical materials: strategies designed to overcome the material's natural limitations

7.1 Abstract

The urgent need for clean and storable energy drives many currently topical areas of materials research. Among the many materials under investigation zinc oxide is one of the most studied in relation to its use in photo-(electro)chemical applications. This study aims to give an overview of some of the main challenges associated with the use of zinc oxide for these applications: the high density of intrinsic defects which can lead to fast recombination, low visible light absorption and the occurrence of photo-corrosion. Employing simple low-temperature solution based methods; it is shown how defect-engineering can be used to increase the photo-electrochemical performance and how doping can strongly increase the visible light absorption of zinc oxide nanorod-arrays. Furthermore the deposition of ultra-thin titanium dioxide layers using atomic layer deposition is investigated as possible route for the protection of zinc oxide against photo-corrosion.

7.2 Introduction

As one of the most studied metal-oxides Zinc Oxide (ZnO) has already found its way into many industrial applications. Nevertheless enormous research interest is still focused on this earth-abundant, environmentally-friendly material as it offers interesting material properties such as a high exciton binding energy, a direct band gap and comparably high charge carrier mobility.[1] Furthermore the ability to grow ZnO nanostructures using a wide range of deposition techniques offers new perspectives for the material to be used in opto-electronics.[2] Low-temperature solution based methods are of particular interest as possible routes to the low-cost growth of high surface-area nanostructures for the integration of ZnO into novel energy production and storage devices.[3]

The steadily growing research areas of solar water splitting and photo-catalysis are prominent examples of areas where interest in ZnO-based materials and devices may be found.[4-11] For these applications the nature of the semiconductor/electrolyte interface plays a crucial role. It is of the highest importance to carefully engineer the

materials properties in order ensure effective charge carrier transport across the interface. In turn it must be the goal of materials research to tailor the ZnO toward these target applications, where possible addressing the key issues of:

Low visible-light absorption. **–** Since ZnO exhibits a large band gap (ca. 3.3 eV) only a small fraction of sunlight is absorbed thus dramatically hindering the use of ZnO for photo-(electro)chemical applications. A common strategy to change the electronic structure of a semiconductor is the introduction of dopants into the host material. In the case of ZnO the material has been doped with various elements whereby many studies focus on doping with transition metals (TMs) such as nickel, magnesium, iron or cobalt.[7, 12-17] Historically, research focused on transition metal doping has been fueled by the possible creation of ferromagnetism in these materials – especially in the case of cobalt doping.[12, 15, 18-21] On the other hand, incorporation of transition metals can also lead to visible light absorption. This is particularly valid for co-doping with cobalt where the presence of the Co^{2+} in the tetrahedral field of the ZnO host lattice leads to sharp d-d transitions [22] as well as charge transfer (CT) between the metal and the ligand conduction band ($ML_{CB}CT$, equation (7.1)) and between the ligand valance band and the metal ($L_{VB}MCT$, equation (7.2)) upon photo-excitation hν:[23, 24]

$$ML_{CB}CT: Co^{2+} + h\nu \rightarrow Co^{3+} + e^{-}_{CB} \quad (7.1)$$

$$L_{VB}MCT: Co^{2+} + h\nu \rightarrow Co^{1+} + h^{+}_{VB} \quad (7.2)$$

The particular electronic structure of ZnO:Co also gives rise to visible light photo-conductivity. It has been shown that the interplay between the d-d transitions and the aforementioned CTs (both closely related to the cobalt concentrations in the films) plays a crucial role for sub-band gap photoconductivity, which is of high interest for solar energy related research.[23-25] For the synthesis of these materials, solution based methods are particularly attractive, since they are relatively cheap to employ and operate at low temperatures. However, while different low temperature deposition methods are reported [18, 26-29] the direct, low temperature growth of ZnO:Co onto substrates is found to result in comparably low cobalt related d–d visible light absorption.[28, 30] A main focus here is therefore the development of simple methods

for the growth of ZnO:Co with controllable cobalt concentration and therefore visible light activity.

***Fast charge carrier recombination over intrinsic defects.* –** Intrinsic defects are frequently observed in ZnO grown from various techniques. Depending on their position within the forbidden gap they are characterized as either shallow (possibly ionized) or deep level defects. Generally defects are centers of charge carrier recombination which ultimately limits the efficiency of a photo-electrode. Recombination processes can either occur under radiative conditions (e.g. via the emission of visible light) or non-radiative conditions involving for example thermal relaxation. Radiative recombination processes – which occur on a slower timescale than non-radiative recombination – can be identified using photo-luminescence measurements. For ZnO various light-emitting defect centers (intrinsic but also extrinsic) can be detected using this technique.[2, 31, 32] The assignment of the photo-luminescence to a specific defect is not always straight forward as the frequently observed, rather broad visible emission for ZnO can have multiple origins contributing to the signal [32]. Furthermore the nature and density of luminescent defects is strongly dependent of the growth technique. Orange emission for example is often observed for ZnO structures grown from solution. The origin of this emission is not yet fully understood and several different explanations have been debated in the literature [33-38]. Since the defect-chemistry will strongly influence the later device performance, careful defect-engineering is necessary to accelerate the use of ZnO as photo-active material.

***Photo-corrosion.* –** As ZnO nanostructures are prone to photo-corrosion it is necessary to develop strategies to protect the material against its self-destruction. Since the photo-corrosion process is dependent on the chemical oxidation potential of the material in respect to the oxidation potential of the electrolyte (e.g. water) a possible route is to adjust the pH value of the electrolyte assuming that the oxidation potential of the material does not change with the same slope as the pH value.[39] Although it has been found that the oxidation potential of ZnO does not shift with the pH of the electrolyte [39] photo-corrosion even occurs in highly alkaline media leading to the

decomposition of the material following equation (7.3):[40]

$$ZnO + 2h^+ + nH_2O \rightarrow Zn(OH)_n{}^{(2-n)+} + 1/2O_2 + nH^+ \quad (7.3)$$

where n depends on the pH value of the electrolyte. The corrosion process itself is thereby believed to include the rapid formation of oxygen molecules under the influence of surface-trapped holes resulting in the expulsion of Zn^{2+}.[41]

Another strategy for the inhibition of photo-corrosion of ZnO is therefore to avoid a direct interface of the material and the electrolyte by employing chemical barrier layers. The barrier itself must again have a suitable oxidation potential in respect to the electrolyte. On the other hand it is also necessary that the layer allows the transport of charge carriers from the underlying material (i.e. suitable energy band alignment with respect to ZnO).[39] A promising example incorporating this strategy is the work on protected Metal-Insulator-Semiconductor structures, which showed stable photo-currents for days or even months.[42-44]

In this study the aforementioned challenges, which hinder the use of ZnO for several photo-electrochemical applications, are addressed. Firstly a route to high visible light absorption by means of the synthesis of cobalt-doped ZnO is reported. Using this method it is possible to control the degree of visible light absorption which is key for the achievement of visible light photo-conductivity in ZnO:Co materials.

Secondly an alternative view on intrinsic defects, which are commonly seen as performance limiting centers of recombination, is presented. Interestingly, intrinsic defects (e.g. oxygen vacancies and zinc interstitials) have been found to aid photo-catalytic reactions.[9, 45-47] To take advantage of this curious behavior it is described how intentionally induced defect centers, which give rise to strong orange photo-luminescence, can influence and possibly enhance the photo-electrochemical performance of ZnO.

Finally ZnO-TiO_2 core-shell structures were deposited using atomic layer deposition (ALD) – a growth technique known for its good layer uniformity and thickness control. Due to the exceptional chemical stability and theoretically suitable band edge position titanium dioxide (TiO_2) may be a suitable chemical barrier layer material for ZnO. These structures were investigated as possible route for the protection of ZnO against photo-corrosion.

7.3 Experimental

***Seed layer preparation.* –** The substrates (glass and fluorine-doped tin oxide (FTO) coated glass slides) used in this study were cleaned prior to the seed-layer deposition. Glass substrates were sonicated in a mixture of Millipore water, ammonium hydroxide (NH_4OH) and hydrogen peroxide (H_2O_2) in a ratio of 5:1:1 for 30 min. FTO substrates were sonicated in a solution of decon90 and Millipore water then in acetone and lastly in isopropyl alcohol (IPA) for 30 min each. After the cleaning procedure the substrates were rinsed with Millipore water and blow dried in a stream of nitrogen.

For the preparation of cobalt-doped ZnO nanorod-arrays a Cambridge NanoTech Fiji F200LLC atomic layer deposition (ALD) system was used for the deposition of ZnO seed layers from diethylzinc and water. These films (400 cycles – ca. 70 nm) were grown at a substrate temperature of 190°C and allowed to cool naturally in air. The ALD seed layers were subsequently annealed in air at 300°C for 1 h in a laboratory furnace. It is noteworthy that ALD represents a versatile tool to achieve various nanorod-morphologies simple by adjusting the layer thickness.[48] Also the growth of ZnO nanorod-arrays with higher inter-rod spacing can be achieved using this technique.[49]

The seed layers for one set of orange-luminescent ZnO nanorod-arrays were grown as outlined above. Furthermore, another set of samples was grown on spin-coated seeds (ca. 30 nm thick) whereby the seeding solution was prepared after Greene et al.[50] The different seed-layer deposition methods were employed to investigate whether or not the seed-layer may have an influence on the occurrence of the observed strong orange-luminescence.

For the deposition of ZnO-TiO_2 core-shell structures a wet-chemical seeding method was employed following the procedure outlined in Ref. [6].

***Solution-based synthesis of ZnO and ZnO:Co nanorod-arrays.* –** Different chemical routes to the solution-based deposition of ZnO and ZnO:Co nanorod-arrays were used for the three approaches presented here in order to tailor ZnO for photo-(electro)chemical applications. The syntheses outlined were carried out using the following chemicals: zinc acetate dihydrate (ZnAc, reagent grade), zinc nitrate hexahydrate (ZNH, reagent grade), hexamethylenetetramine (HMTA, reagent grade),

hydrochloric acid (HCl, 5%wt), 4M sodium hydroxide solution (NaOH), ethanolamine (EA, reagent grade), cobalt(II) acetate tetrahydrate (CoAc, reagent grade), and Millipore water (H_2O).

Synthesis of cobalt-doped ZnO nanorod-arrays. **–** The growth solution was prepared by adapting a recently reported solution based method.[51] 1.1 g ZnAc and the required amount of CoAc were dissolved in ca. 25 ml H_2O under constant stirring for 30 min at room temperature (0.125 g, 0.250 g, 0.374 g for 10%, 20% and 30% Co concentration in respect to Zn concentration in the growth solution, respectively. The term "Co/Zn concentration ratio" is used throughout this article to describe this ratio). Subsequently 7.5 ml of 4M NaOH solution were quickly added and the solution was allowed to stir for an additional 45 sec after which 5 ml EA was added to the solution. After increasing the volume to 50 ml by adding H_2O the growth solution was then left under constant stirring for two hours. The final solution was then transferred to a pre-heated Teflon-lined autoclave. Under a slight angle (ca. 15° of the vertical), the substrates were then immersed into the solution with the seed layer facing down. After closing, the autoclave was put back into a laboratory furnace (115°C). The growth was carried out for 2 h with subsequent natural cooling. Finally the samples were thoroughly rinsed in H_2O and blow-dried in nitrogen.

Synthesis of ZnO-TiO_2 core-shell structures. **–** The solution-based deposition of the ZnO nanorod-arrays was carried out as outlined in the previous section but in this case samples were grown in a closed plastic bottle at 85°C for 1 h and without the addition of CoAc. The as-grown ZnO-nanorods were then over-coated with ALD TiO_2 using a Cambridge NanoTech Fiji F200LLC system with tetrakis (dimethylamino)titanium (TDMAT) and water as the precursors. First TDMAT was pulsed into the growth chamber (0.3 s) followed by a nitrogen purge (10 s), a H_2O pulse (0.1 s) and another nitrogen purge (10 s). This procedure was repeated until a nominal TiO_2 thickness of 2 nm, 5 nm or 10 nm was reached (growth rate ca. 0.5 Å/cycle). During the deposition the TDMAT precursor and substrate temperature were held at 90°C and 180°C, respectively.

Synthesis of ZnO nanorod-arrays for defect-engineered photo-electrodes. **–** Intentionally defect-rich ZnO nanorod-arrays were grown following the solution-based method outlined in Ref. [38]. In short, 0.025 M ZNH, 0.15 M HMTA and 4 drops of 5%wt. HCl were dissolved in H_2O to yield 100 ml of growth solution which was then constantly stirred for 1 h and transferred into a sealable plastic bottle. Substrates were put in almost vertically with the growth side pointing downwards. The sealed bottle was subsequently put into a standard laboratory oven (95°C, 6 h). After natural cooling of the solution, the samples were thoroughly rinsed with H_2O and blow dried with nitrogen.

The as-grown ZnO nanorod-arrays were subjected to post-deposition rapid thermal annealing (RTA) at various temperatures (350°C- 550°C) and in various atmospheres (introduced before temperature ramp-up; forming gas (5% H_2 in N_2), Oxygen (O_2) all at 1 bar) using a Jipelec 150 RTA system. The set temperature during RTA was held constant for 10 min.

It is important to note that the different approaches to the solution-based growth of ZnO nanorod-arrays presented above are necessary to achieve the functionality desired in each section. For example, effective cobalt-doping (e.g. intense d-d cobalt-related absorption in the visible range) could not be achieved when the cobalt precursor was simply added to the growth solution used to grow defect-rich ZnO nanorod-arrays (third recipe noted above). On the other hand, the occurrence of strong orange-luminescence post RTA-treatment is only achieved when the nanorod-arrays are grown using this particular recipe. With this in mind, the reader is advised that each sub- results and discussion section is dealt with independently. This is to avoid direct comparison between results of individual sections which may be misleading due to the different synthesis routes used and their possible effect on the material properties.

Materials characterization. **–** For structural characterization scanning electron microscopy (SEM) and energy dispersive x-ray spectroscopy (EDS) was carried out using a FEI Quanta 650 FEG High Resolution Scanning Electron Microscope equipped with an EDS detector. A Panalytical X`Pert MRD X-Ray diffractometer (Cu Kα radiation $\lambda = 0.1541874$ nm, scan resolution 0.02°) in rocking curve configuration was used for X-ray diffraction measurements (XRD). Diffuse reflectance and

transmittance spectra in the range of 300 – 800 nm were recorded by means of a Perkin Elmer 950 UV-Vis spectrometer equipped with an integrating sphere. For the evaluation of the chemical stability the transmission of ZnO-TiO_2 core-shell structures under acid exposure (HCl, pH = 2, 15 ml) was constantly measured using an Ocean Optics UV-Vis spectrometer and light source (QE 65000 and HL-2000, respectively). For the recording of transmission electron micrographs (TEM) a Jeol JEM-2100 was used. The photo-electrodes prepared were characterized in a home-made electrochemical cell in 3-electrode configuration (reference electrode = saturated calomel electrode SCE, counter electrode = coiled platinum wire). Potential control during cyclic voltammetry (CV), linear sweep voltammetry (LSV) as well as chronoamperometric measurements was achieved using a PalmSens 3 potentiostat. For all photo-electrochemical measurements a solar-simulator (AM 1.5 G, 100 mW/cm^2) was used as a light source. The electrolyte contact area (0.1 M phosphate buffer solution pH = 7) for all investigated photo-electrodes was 1 cm^2. It is important to note that all given current-densities *j* were not corrected using the actual surface area of the samples but are in respect to the (constant) area of illumination employed (1 cm^2).

7.4 Results and Discussion

Cobalt doping for enhanced visible light absorption. **–** Figure 7-1 shows SEM micrographs of undoped ZnO (Figure 7-1a) as well as cobalt doped ZnO:Co with various cobalt concentrations in the growth solution (Figure 7-1b-d). Without the addition of cobalt to the growth solution well aligned and thin nanorods are grown. Upon addition of cobalt to the growth solution the rod-diameter increases, resulting in thicker rods (10% Co/Zn concentration ratio in the growth solution) and almost layer like growth with thick crystallites for higher cobalt concentrations (20% and 30% Co/Zn concentration ratio in the growth solution). The growth of ZnO nanorods with lower aspect ratios from solutions with higher Co^{2+} concentration has been observed by other groups as well and has been attributed to a decreasing reaction rate [28, 52-54]. In particular the higher solubility products for cobalt-containing species as well as an added reaction barrier due to the conversion of Co^{2+} ions from octahedral to tetrahedral geometries results in a the lower reaction rate [53, 54].

Following the SEM analysis EDS spectra were taken on 3 random spots on each

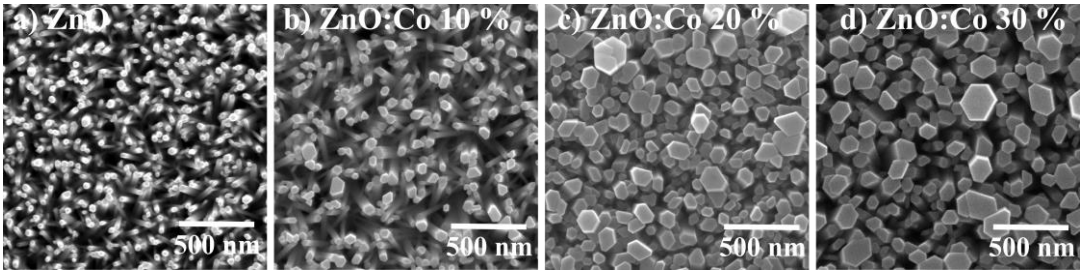

Figure 7-1: Topview SEM micrographs of undoped (a) and cobalt doped (b-d) ZnO nanorods grown on glass. Percentages given represent the Co/Zn concentration ratio.

Table 7-1: Average elemental concentrations calculated from three random spots on the respective sample. As the detection of oxygen using this method may be subject to some considerable error the table only symbolizes the trend of the elemental concentrations in dependence of the cobalt/zinc concentration ratio in the growth solution.

Element	**ZnO**	**ZnO:Co 10 %**	**ZnO:Co 20 %**	**ZnO:Co 30 %**
O	48.71%	48.81%	53.26%	53.68%
Co	-	0.66%	0.98%	1.33%
Zn	51.29%	50.52%	45.76%	44.99%

sample (same microscope configurations used for all measurements) in order to calculate an average elemental concentration for each sample. However the exact determination of the oxygen content is difficult using this technique since the detected signals may have larger margins of error. The elemental concentrations given in Table 7-1 are therefore only helpful to represent the general trend of the concentrations with varying cobalt concentration in the growth solution.

As a general trend, it can be seen that by increasing the cobalt/zinc ratio the ZnO nanorod-arrays get richer in oxygen. This process does not seem to scale linearly with the Co/Zn concentration ratio and might be influenced by the distinct growth differences between samples with a lower (undoped and 10% Co/Zn concentration ratio in growth solution; nanorod geometry) and higher Co/Zn ratios (20% and 30% Co/Zn concentration ratio in growth solution; densely packed nanorods – almost layer-like). The cobalt concentration of the samples on the other hand does scale with the Co/Zn concentration ratio of the growth solution. The EDS measurements therefore confirm that a higher concentration of cobalt in the growth solution also leads

to higher cobalt concentrations in the films and thus possibly also to a higher number of Co^{2+} replacing Zn^{2+} in the ZnO lattice.

The structural properties of the nanorod-arrays were analyzed by XRD and the results are compiled in Figure 7-2a. XRD spectra were taken from 2θ = 15 - 70°. As only the ZnO (103) peak (at 2θ = 62.87°) was detected in the range for 2θ > 40° Figure 7-2a focuses on the range 2θ = 15 - 40°. Between 2θ = 30 - 40° multiple peaks are visible with peak centers being recorded at ca. 31.0°, 31.84°, 32.92°, 34.39° and 36.22°.

The peaks at 31.84°, 34.39° and 36.22° are in good agreement with the JCPDS reference card No. 79-2205 – commonly used for the characterization of hydrothermally-grown ZnO [55] – and can be assigned to the ZnO (100), (002) and (101), respectively. Interestingly all samples show additional XRD peaks at 31.0° and 32.92°. As these peaks are found independent of the cobalt concentration in the growth solution (i.e. also the undoped reference samples exhibits these peaks) it is reasonable to expect them to originate from an additional zinc species. Due to the high sodium concentration in the growth solution it is possible that some sort of sodium zincate or sodium zinc hydroxide is formed. For this reason Figure 7-2a shows the reported peaks of the JCPDS reference card No. 76-0656 for $Na(Zn(OH)_3)$, which are close to the observed peaks. However, based on only two XRD peaks a final conclusion about the exact species responsible for the additional peaks at 31.0° and 32.92° cannot be drawn.

The XRD spectra were also evaluated looking for possible Co containing secondary phases. As many of these cobalt species (e.g. $Co(OH)_2$, Co_2O_3, CoO and Co_3O_4) would show an XRD response in the range between 2θ = 30 - 40° and strong signals between 15 - 20° Figure 7-2a also evaluates the recorded spectra between 2θ = 15 - 20°. No cobalt related peaks could be detected regardless of the Co concentration in the growth solution.

If cobalt is incorporated in the host lattice one would expect a peak shift in respect to the undoped samples as the doping would result in an increased stress in the material. A shift of the (002) peak to larger angles is indeed what has been observed (inset in Figure 7-2a) when compared to the undoped sample. As the ionic radius of Co^{2+} (56 pm) is slightly lower than that of Zn^{2+} (60 pm) doping of the nanorods leads to a decrease in the lattice constants and therefore a peak shift toward larger angles.[4] For the prepared cobalt doped samples the peak shift thereby increases with increasing

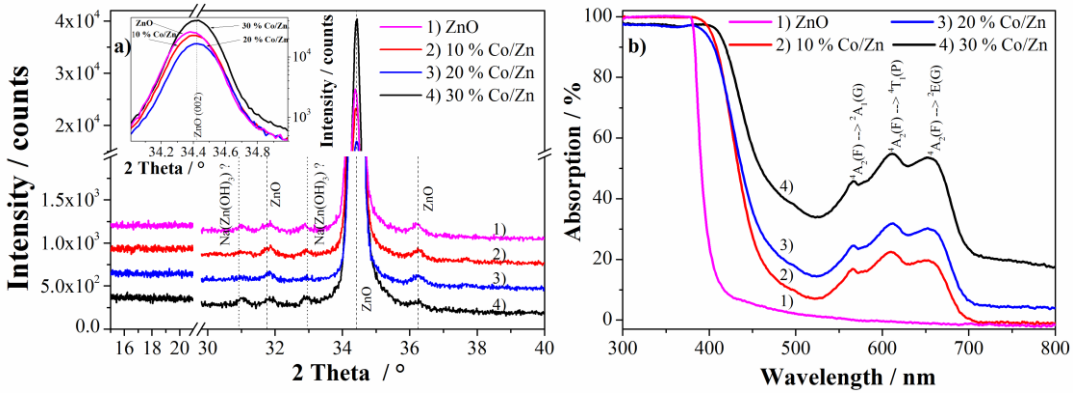

Figure 7-2: a) XRD spectra of undoped and cobalt doped ZnO nanorod-arrays. For better visibility the spectra were offset by 300 counts to each other. Inset: Magnification of the (002) peak revealing a peak shift scaling with the cobalt concentration in the growth solution. b) Absorption spectra of undoped and cobalt doped ZnO nanorod-arrays. The visible light absorption increases with increasing cobalt concentration in the growth solution.

cobalt concentration – an indication of successful doping of the ZnO nanorod-arrays.

UV-Vis spectroscopy measurements were subsequently carried out on the same set of samples. The absorption spectra of the samples are shown in Figure 7-2b. All cobalt doped samples exhibit a red-shifted absorption edge when compared to the undoped ZnO nanorod-arrays. Additionally strong visible light absorption scaling with the cobalt concentration in the growth solution can be seen for the doped samples. For the sample with a Co/Zn concentration ratio of 30% in the growth solution the absorption in the visible is increased up to $50\%_{abs}$ over the undoped reference sample. Clear features at ca. 566 nm, 610 nm and 655 nm are noticeable in the absorption spectra of the cobalt doped samples. Earlier studies identify these features as the $^4A_2(F) \rightarrow {}^2A_1(G)$, $^4A_2(F) \rightarrow {}^4T_1(P)$ and $^4A_2(F) \rightarrow {}^2E(G)$ cobalt d-d transitions in the tetrahedral environment of the ZnO lattice [22] indicating the presence of Co^{2+} in a high spin state [15] thus confirming the successful doping of ZnO with cobalt.

It is noteworthy that the method presented here therefore represents an easy route to alternate visible light absorption just by changing the concentrations of the growth precursors in the solution. The control of both visible light absorption and cobalt concentration in the films is an essential factor to consider for the deposition of functional materials such as diluted magnetic semiconductors or materials for photo-(electro)chemical applications. Photo-electrochemical studies of the materials described here are currently underway in our laboratories and will be reported in a

separate publication.

Defect-engineered photo-electrodes with enhanced photo-electrochemical performance. **–** First as-grown ZnO nanorod-arrays grown using the same solution based nanorod growth-technique but using different seed-layer deposition methods were compared with one another to evaluate any differences in their structural, optical end photo-electrochemical properties. Figure 7-3 shows SEM micrographs, transmission spectra as well as linear sweep voltammetry (LSV) curves of these structures (in the dark and under illumination).

When comparing the alignment and thickness of the nanorods in the SEM micrographs (Figure 7-3a) it can be seen that nanorods grown on spin-coated seed-layers, using the seeding solution given in Ref. [50], are generally better aligned and thinner. This optical impression of the presence of 'better alignment' was confirmed by XRD measurements (not shown) as the peak associated with the (002) plane of hexagonal ZnO grown on the spin-coated seed layers was far more intense than that for the nanorod-arrays grown on seed-layers deposited by ALD. The reason for the enhanced alignment of the rods on spin-coated seed-layers lies in the preferred (002) orientation of the seed-layer crystallites.[50] The deposited ALD seed-layers do not exhibit a preferred orientation and thus lead to less aligned nanorod-arrays.

Furthermore a direct correlation between the structural and optical properties of the as-grown nanorod-arrays could also be established (transmission spectra in Figure 7-3). Here it is noticed that nanorods grown on the spin-coated seed layers show an increased transmission over the visible range of the spectrum. The increase in transmission is caused by a reduction of the reflectance of the samples due to the better alignment and possibly thinner rod-diameter. Higher levels of transmission in the visible range are especially important for applications such as dye sensitized solar cells or photo-electrochemical cells using multiple absorber materials (e.g. a wide-bandgap semiconductor on top of a narrow bandgap material). Figure 7-3b shows the LSV curves of as-grown ZnO nanorods grown on different seed layers. Both samples show comparable dark currents with only a small current being detected in the reductive part of the curve. No significant oxidative current can be noticed for the samples. However, under illumination with simulated sunlight (AM 1.5 G, 100 mW/cm^2)

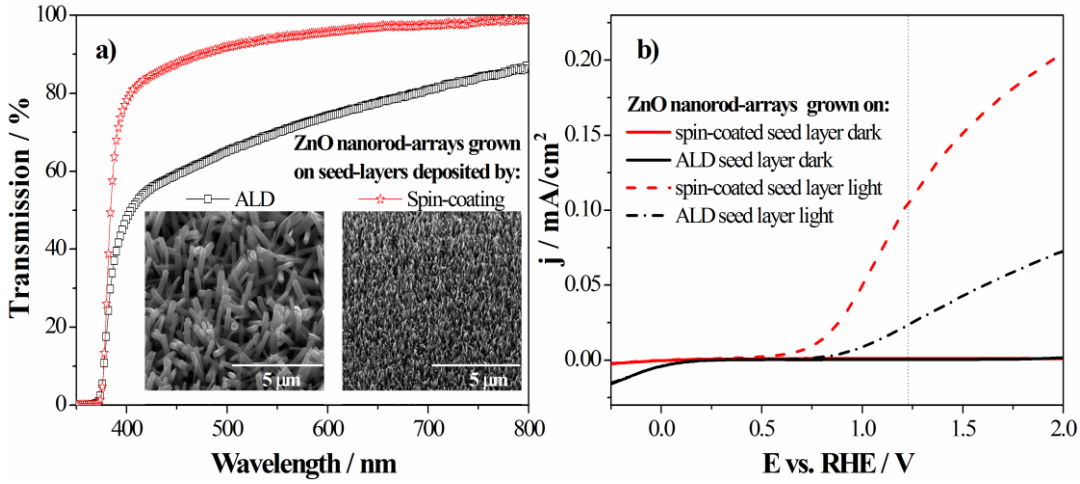

Figure 7-3: Comparison of as-grown ZnO nanorod-arrays grown on different seed-layers. a) Transmission spectra and SEM micrographs. b) Linear sweep voltammograms of the as-prepared photo-electrodes (illumination: 100 mW/cm^2, AM 1.5 G). Note that the transmission spectra were taken from co-deposited ZnO nanorod-arrays grown on glass.

both electrodes show a considerable oxidative photo-current. Here the onset potential of the photo-current is shifted toward more negative potentials for the sample grown on the spin-coated seed layer (ca. 0.5 V compared to 0.75 V for nanorod-arrays grown on the ALD seed layer). Also the magnitude of the photo-current is essentially higher for the sample grown on spin-coated seed layers. At 1.23 eV vs. RHE this photo-electrode generates ca. 0.1 mA/cm^2 compared to 0.023 mA/cm^2 observed for ZnO nanorods grown on seed layers deposited by ALD.

As the current densities given in the figure are in respect to the illuminated area it seems appropriate to attribute the better performance of the ZnO nanorod-arrays grown on the spin-coated seed layers to the bigger surface area due to the thinner diameter of the rods. However, it can also be seen that the slope with which the photo-current rises is steeper than for the nanorods grown on ALD seeds and no saturation is reached at higher positive potentials. For this reason these features cannot solely be related to the surface area of the samples. It is proposed that they are actually indicative of a lower rate of recombination (steeper rise of photo- current) as well as a greater number of photo-generated holes participating in chemical reactions with the electrolyte (saturation of photo-current). For the nanorod-arrays grown on spin-coated seed layers the lower recombination rate could result from the thinner rod diameter as it easier for bulk charge carriers to reach the interface where they can be separated. Additionally it

is reasonable to expect a higher saturation current from these samples as the reflection is lower compared to the nanorod-arrays grown on seed layers deposited by ALD.

Subsequently rapid thermal annealing was used to alter the defect composition of the as-grown ZnO nanorod-arrays. Samples grown on ALD seed layers were annealed in forming gas (5% H_2 in N_2; 350°C, 430°C, 550°C) and the nanorod-arrays grown on spin-coated seed layers were exposed to oxygen during RTA (350°C, 450°C, 550°C). Additionally, ZnO nanorod-arrays grown on different substrates and seed layers were subjected to RTA in oxygen at 450°C to evaluate the influence that different substrates or seed layers might have on the defect composition.

Figure 7-4 compiles the PL spectra of the annealed samples as well as the LSVs recorded from the photo-electrodes. Focusing on the photo-luminescence results first (Figure 7-4a and b), all samples investigated show a more or less sharp response in the near UV region and a broad emission in the visible range. For the as-grown samples in Figure 7-4a and b the center of the near UV peak is located at 390 nm and the visible emission is centered at around 575 nm (yellow). The broad feature in the visible is frequently observed for samples grown from solution and the origin of this emission has mainly been attributed to surface adsorbents from the growth solution.[33, 34, 38] As the band-band recombination of ZnO would be expected to be closer to 380 nm the peak in the near UV is likely caused by contributions of multiple recombination processes (i.e. band-band and recombination over shallow defects). A shift of the near UV peak toward 380 nm can be seen for samples annealed at 350°C, indicating increased direct recombination between the energy bands due to improved crystallinity of the rods and passivation of non-radiative defects. The latter is especially valid when forming gas is used as the annealing atmosphere since hydrogen is known to passivate non-radiative defects – especially those at the surface.[33, 34] Furthermore the yellow emission is decreased due to desorption of surface adsorbents at elevated temperatures.[56]

When the annealing temperature is increased (430°C for forming gas) and (450°C for O_2) the near UV peak decreases again but strong orange emission (centered around 600 nm) is noticed for both samples making recombination induced by this defect center the dominant recombination channel. The appearance of the orange-emission is seen to be highly temperature dependent but atmosphere independent (i.e. reductive as

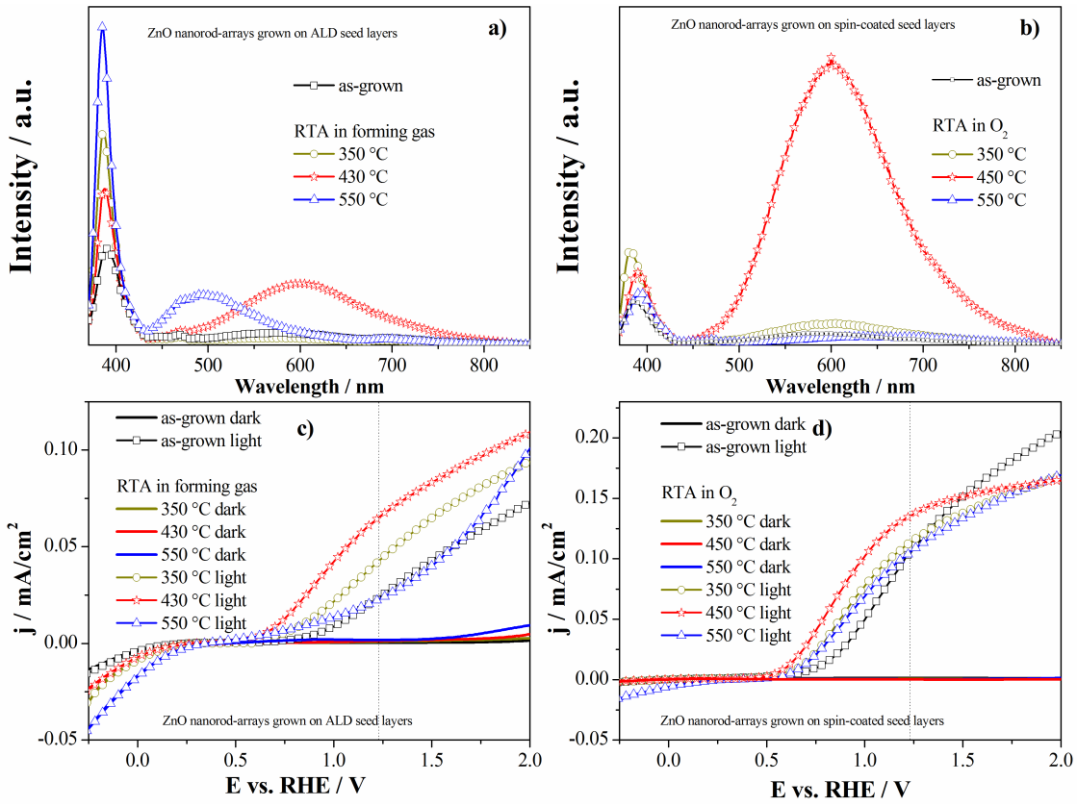

Figure 7-4: Photo-luminescence spectra and corresponding linear sweep voltammograms of RTA treated ZnO photo-electrodes; a) and c) for samples grown on ALD deposited seed-layers (RTA in forming gas). b) and d) for samples grown on spin-coated seed-layers (RTA in O_2). Illumination: 100 mW/cm^2, AM 1.5G. Electrolyte: 0.1 M phosphate buffer solution (pH = 7).

well as oxidative atmospheres lead to orange-emission). Furthermore it has recently been shown that strong-orange emission occurs for various annealing atmospheres at ca. 450°C while keeping the seed-layer deposition the same.[38] It is noteworthy that samples prepared on ALD deposited seed layers showed generally less orange emission when compared to nanorod-arrays grown on spin-coated seed layers. When co-annealing nanorod-arrays prepared on different seed layers and different substrates (glass, gallium nitride, FTO, sapphire) it was found that the substrate does not influence the orange emission. However, for the combination FTO + ALD seed layer the orange emission was found to be the lowest among all samples. Furthermore, this substrate-seed layer combination also showed the worst alignment and coverage, which may point toward an influence of the structural properties on the photo-luminescence. It is however important to point out that orange-emission for nanorod-arrays annealed at temperatures of ca. 450°C occurs regardless of the seed-layer used. This in turn rules out that the seed-layer is responsible for the observed PL

characteristics.

For a detailed discussion on the observed orange emission and its nature the reader is referred to recent literature.[38] In that paper evidences have been presented that the oxygen vacancy-zinc interstitial defect complex V_O-Zn_i might be responsible for the observed orange emission. Due to advances in computational studies of ZnO over the past decades, it is now widely accepted that the deep-level oxygen vacancy is thermodynamically stable in its neutral V_O and doubly ionized state V_O^{++} with V_O being more abundant due to the lower formation energy.[2, 32] The singly ionized oxygen vacancy V_O^{+} is thermodynamically unstable but can be created e.g. by light illumination.[57, 58] A zinc interstitial defect on the other hand resides shallow close to the conduction band and can thus be ionized at room temperature (Zn_i^{++} is the stable state).[36, 59] The formation of the V_O-Zn_i defect-complex may seem counter-intuitive at first given the donor-like nature of both intrinsic defects. However, it has been demonstrated that the defect-complex might exist upon kinetic formation via a kick-out process.[60] Kim et al. found the quantum mechanical hybridization between the electronic orbitals of the deep- and shallow-donor states (V_O, and Zn_i, respectively) responsible for the strong attraction between the individual defects.[61] A related, interesting aspect is that highly oxygen deficient materials were calculated to have a higher concentration of zinc interstitials when an interaction of these two defects is allowed. This would lead to the creation of more ionized zinc interstitials and in turn enhanced n-type character.[61] Furthermore it is worth noting that the number of possible charge transition states is increased the closer the two point defects are together. This can lead to changes in the opto-electronic properties (e.g. intrinsic n-type doping and photo-luminescence) as compared to the single point defect case.[60, 61] In the opinion of the authors it would therefore be interesting to investigate whether it is possible for the V_O-Zn_i complex to stabilize an oxygen vacancy in its singly ionized state which, due to its spin dependent recombination processes,[62] could help to identify the exact recombination mechanism for the observed orange emission.

Interestingly the orange emission disappears when the ZnO nanorod-arrays are annealed at higher temperatures (550°C) – again, irrespective of the annealing atmosphere. However, these higher annealing temperatures lead to the introduction of additional defects, which is especially visible for the sample annealed in forming gas. Here a strong emission centered around 490 nm is detected which might be the result

of some destructive, decomposition processes at the surface of the nanorods.[2] Indeed strong material damage for samples annealed at 600°C was observed optically.

When correlating the observed PL properties to the photo-electrochemical performance of those samples (LSV voltammograms in Figure 7-4c and d) it can be seen that annealing of the samples leads to a cathodic shift of the photo-current onset potential when compared to the as-grown reference samples. Interestingly the samples exhibiting strong orange-luminescence show the biggest shift as well as a steeper rise of the photo-current leading to significantly improved photo-current densities at 1.23 V vs. RHE (dotted line in the figures). These *j-V* characteristics are especially important for real working devices as a main goal of solar water splitting is to achieve the highest possible photo-current under the lowest possible applied bias potential.

The cathodic shift of the photo-current onset potential is the result of an improved hole transfer rate of the electrodes.[63] Both the charge carrier concentration (here donor type) as well as charge carrier recombination have big influence on the photo-current onset potential as well as the photo-current density in general.[64] Assuming that the Fermi energy is not "pinned" to the surface, a high charge carrier density increases the band bending at the semiconductor-electrolyte interface and thus also the driving force for holes to oxidize the electrolyte.

Charge carrier recombination on the other hand affects the photo-current i_{ph} directly and its effects are also visible in the slope of the j-V curve of a photo-electrode. An immediate and steep increase of the photo-current is an indication of a lower or slower rate of recombination in the bulk, the space charge region as well as the surface of a photo-electrode. This is indeed what is observed for samples with strong orange luminescence. Considering the possible slow trapping of a photo-generated electron by the orange-luminescent defect, the recombination with a photo-generated hole in the valence band might be delayed. This would in turn result in an increased probability for the hole to diffuse to the space charge region (generation in the bulk) or toward the surface (generation in the space charge region). Furthermore trapped electrons might contribute to the enhanced photo-current density as well.

Nonetheless, for the sample annealed in O_2 at 450°C (very strong orange emission) the photo-current seems to plateau at a lower value when a higher positive bias potential is applied (Figure 7-4d). To what extent the orange-luminescent defects are responsible

for the current saturation has to be established in further investigations. However, when assuming that the V_O-Zn_i defect complex is responsible for the observed orange emission it is possible that plateau of the photocurrent is the result of an increased charge carrier concentration, which has been shown to reduce the saturation current.[64]

***ZnO-TiO₂ core-shell structures with improved photo-electrochemical stability.* –** In order to evaluate the chemical stability and the photo-corrosion behavior of the TiO_2 over-coated ZnO nanorod-arrays, different layer thicknesses of the TiO_2 barrier layer were deposited. The as-deposited core-shell structures were characterized in order to get some insight in the optical and structural material properties. Figure 7-5 summarizes the material properties of the as-grown TiO_2-ZnO core-shell nanorod-arrays.

Upon over-coating the ZnO nanorods with thicker TiO_2 layers (5 nm and 10 nm) an optical color change (samples appear brownish) can be noticed. These impressions have been verified by UV-Vis spectroscopy in Figure 7-5a. A thin TiO_2 layer (2 nm) does not show a significant difference in the absorption spectra when compared to the ZnO reference sample. However, for thicker layers – especially for the sample with 10 nm TiO_2 over-coating – a significant increase in visible light absorption can be noticed. The brownish color and the higher visible light absorption point toward possible carbon contamination of these samples. As the samples where pre-cleaned in oxygen plasma prior to the ALD deposition it appears likely that the contamination is a direct result of the ALD deposition (e.g. residue of the titanium precursor).

To prove whether the high visible-light absorption is caused by a change of the underlying ZnO a Tauc analysis[65] of the absorption data has been carried out (Figure 7-5b). This analysis allows the estimation of the band gap energy E_G. For the uncoated ZnO reference the so-determined E_G is 3.265 eV. The TiO_2 coated samples show band gap energies of 3.268 eV and 3.270 eV for 2 nm and 5 nm/10 nm layer thickness, respectively.

For the ZnO-TiO_2 core-shell structures no definitive dependence of the band gap energy on TiO_2 layer thickness is apparent. Indeed the estimated band gap energies of

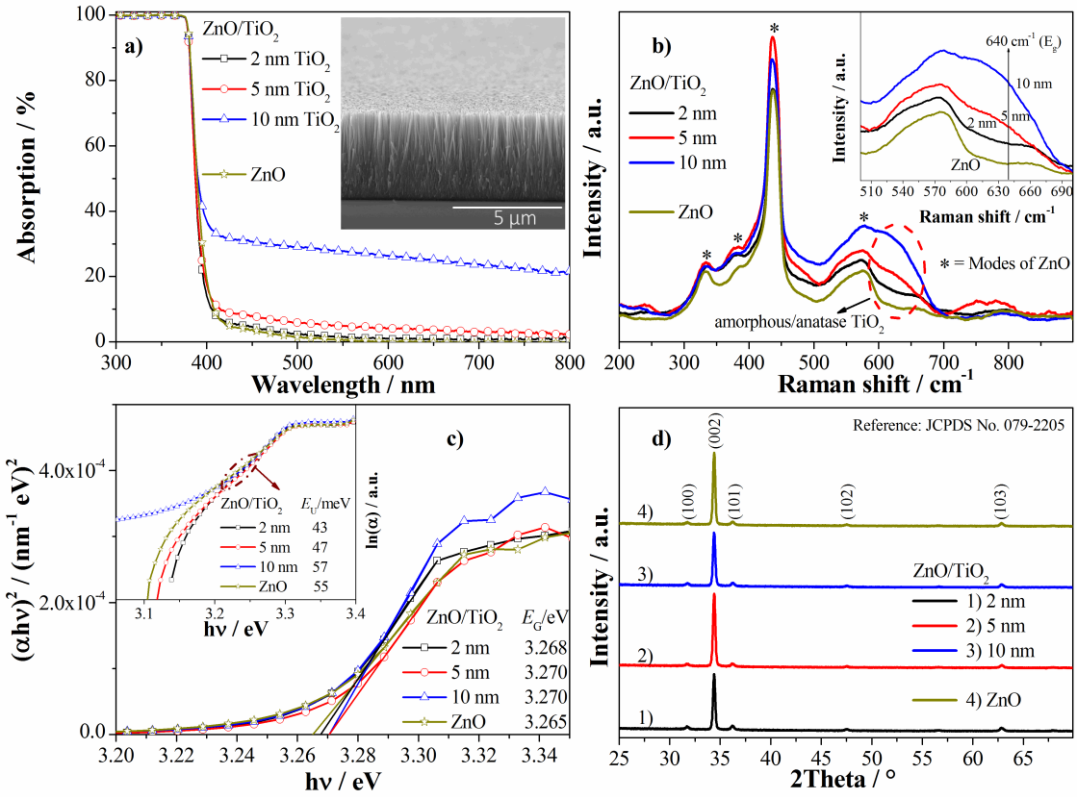

Figure 7-5: Material properties of ZnO-TiO_2 core-shell nanorod-arrays with varying TiO_2 layer thickness (2 nm, 5 nm, 10 nm): a) optical absorption spectra. Inset: SEM micrograph (ZnO), c) Tauc-plot for the estimation of the band gap energies E_G. Inset: estimation of the Urabach energy E_U, b) Raman spectra, d) XRD spectra.

all samples – including the ZnO reference – are very similar to each other giving rise to the conclusion that the electronic structure of the underlying ZnO has not been affected by TiO_2 deposition and that the increased visible-light absorption is most likely related to contamination. From the UV-Vis measurements the Urbach energies E_U for all samples were also estimated. The inset in Figure 7-5c shows the analysis of the logarithm of the absorption coefficients for the estimation of E_U (here the slopes of the linear part for photon energies $h\nu < E_G$ were taken for the determination). Interestingly the Urbach energy was found to increase for thicker TiO_2. When compared to the uncoated ZnO sample an over-layer of 2 nm or 5 nm TiO_2 E_U even decreased and a 10 nm thick layer reaches a comparable value in respect to the reference sample.

As the Urbach energy is commonly taken as a measure of structural disorder or energetic states near the band-edges (band-tail states) of a semiconductor a low Urbach energy corresponds to a material with low density of energetic states (e.g. structural or

surface defects) localized near the band-edges. For the TiO_2 coated samples it is thus obvious that the deposition of the protective layer did not lead to an increased density of these states. The reduction of same implies that the electronic properties of the coated samples (2 nm and 5 nm) may even have been improved.

As the 10 nm thick TiO_2 layer did not show an improvement of the Urbach energy compared to the uncoated sample, the heat treatment that occurred during the ALD process (180°C; i.e. annealing) cannot be responsible for the observed behavior. It is more likely that for thinner layers surface defects are passivated similarly to the findings of Liu et al.[66]

In order to gain some insight in the structural properties of the core-shell structures Raman and XRD measurements were carried out and are summarized in Figure 7-5b and d, respectively. The XRD measurements of the samples showed only ZnO related peaks with the response from the (002) plane as the most pronounced, confirming the good alignment of the grown ZnO nanorods – also visible in the SEM micrograph in Figure 7-5a. No TiO_2 related signals have been detected. Also the Raman spectra show mostly ZnO related peaks but significant differences can be seen between 600 cm^{-1} and 650 cm^{-1}. A more intense signal in this region was observed with increasing TiO_2 layer thickness. The inset in Figure 7-5b magnifies this range. It can be seen that especially for the 5 nm and 10 nm thick TiO_2 layers the features near 640 cm^{-1} become more prominent. It is noteworthy that the E_G mode of anatase TiO_2 occurs in this spectral region.[67] Since the feature is very broad and a clear peak is absent, the as-deposited TiO_2 possesses only a limited degree of long-range order as compared to the anatase phase.[67] Thus it appears likely that the TiO_2 films are an amorphous-anatase mixed phase.

Following the initial material characterization of the ZnO-TiO_2 core-shell structures, the photo-electrochemical performance of samples grown on FTO was evaluated. As an example, cyclic voltammetry (CV), LSV (both left panel) and chronoamperometry (CA, right panel) measurements for the unprotected and the core-shell samples with a TiO_2 layer thickness of 2 nm are shown in Figure 7-6.

In the dark both samples do not show a significant current for water oxidation. Interestingly the TiO_2 coated sample shows a higher reductive dark current as well as a sharp oxidative peak at -0.2 V vs. RHE (CV scans, left panel of Figure 7-6). Since

the CV measurements were recorded starting at 0 V vs. SCE scanning toward positive potentials (up to 1.35 V vs. SCE) and then sweeping back toward the negative end (-1 V vs. SCE), the observed behavior might result from a charging of the TiO_2 or the TiO_2/ZnO interface and subsequent rapid discharging in the potential range from -1 V – -0.640 V vs. SCE (-0.343 V – 0.017 V vs. RHE). In support of a possible charging/discharging effect – which would resemble the reduction/oxidation of TiO_2 – is the observation of the so called proton insertion Reaction (7.4) by other groups:[68-70]

$$Ti^{IV}O_2 + e^- + H^+ + \rightarrow Ti^{III}OOH \qquad (7.4)$$

A sufficiently high reductive potential leads thereby to the formation of Ti^{III} donor centers of which the charge is compensated by the proton. This reaction is frequently utilized as route for the doping of TiO_2. Interestingly it has been reported that this reaction manifests itself more strongly in acidic media.[70] If the observed CV behavior of the electrodes presented here is associated with the proton insertion reaction this might point toward a local pH difference at the electrode surface.

Under simulated sunlight both samples show an increase of the reductive current at low potentials vs. RHE as well as an oxidative photo-current toward more positive potentials as compared the non-illuminated case. The unprotected sample shows an earlier photo-current onset potential compared to the ZnO-TiO_2 core-shell structure. However, when more positive potentials are applied, the samples perform comparably with the protected, TiO_2 coated sample exhibiting an even steeper rise of the photo-current. It is also necessary to make the reader aware of the fact, discussed in a previous publication, that while measuring multiple ZnO-TiO_2 samples very early photo-current saturation has been observed for some samples.[71] However, after evaluating the data collected from multiple samples the core-shell structure presented here seems more representative.

The observed increase of the reductive current upon illumination is in fact the manifestation of back-reactions on the electrode surface. Since the oxidation of water involves multiple steps and intermediate products[72] illumination and subsequent rapid scanning toward positive potentials leaves oxidation intermediates in close proximity to the electrode surface. This is particularly true for the cell configuration used in this study, where the electrode is in a horizontal position and the electrolyte is

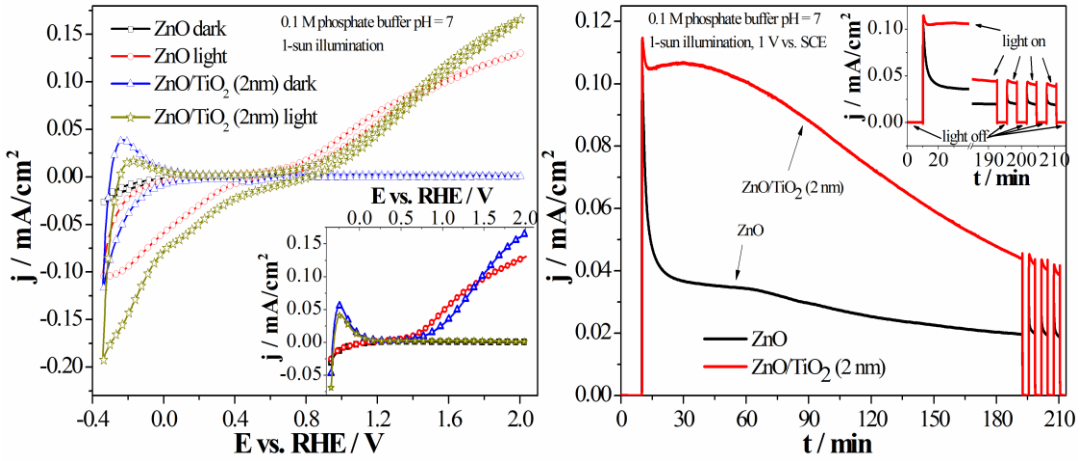

Figure 7-6: Left: Voltammograms (-1 V – 1.35 V vs. SCE, scan rate 50 mV/s) of uncoated ZnO and ZnO-TiO_2 (2 nm) core-shell nanorod-arrays grown on FTO in the dark and under illumination (1-sun). Inset: linear sweep voltammetry (LSV) spectra for the investigated samples (electrodes were hold at -1 V vs. SCE for 5 seconds before the sweeping to positive potentials). Right: Chronoamperometry measurements on the same samples at 1 V vs. SCE (1.66 V vs. RHE). 0.1 M phosphate buffer solution (pH = 7) has been the electrolyte for both measurements. Illumination: 100 mW/cm^2, AM 1.5G.

not agitated. An increased current when scanning to negative potentials is thus due to the back-reaction of these intermediates. Further proof of this can be found in the LSV scans of the samples (inset in the left panel of Figure 7-6). Here – when scanning from negative to positive potentials – no change of the reductive current is observed and the traces of the dark and light measurements on the respective samples are essentially the same for the reductive part of the spectrum. The earlier photo-current onset potential for the uncoated sample is also visible in the LSVs. This is an indication of a better initial catalytic charge transfer rate at the electrode surface for the plain ZnO sample. However, when the potential is increased and the catalytic hurdle for water oxidation is decreased charge carrier recombination becomes a major rate limiting factor. Here the photo-current for the ZnO sample increases steeply at the beginning but flattens toward higher potentials. In particular the flattening of the photo-current is not as dramatic for the ZnO-TiO_2 core- shell structure in the potential range examined. Thus it might well be that charge carrier recombination is reduced for the core-shell structure, similarly to the results of an earlier study.[66]

When biased at 1 V vs. SCE (1.66 V vs. RHE) for a longer period of time (CA measurements in right panel in Figure 7-6) a stabilization of the photo-current can be

observed for the ZnO-TiO_2 core-shell structure. The strong drop in the photo-current observed for the ZnO reference sample is not visible for this sample. The core-shell sample even shows an initial increase in photo-current (from ca. 5 min after the light is turned on) which then levels at ca. 0.107 mA/cm^{-2}. However, after 1 h the photo-current also decreases significantly for the protected sample.

The ultra-thin TiO_2 over-coating presented here is able to chemically protect the underlying ZnO as evidenced by the CA measurements. When evaluated over the entire measurement period of 3 h, the ZnO-TiO_2 core-shell structure generates more current than the ZnO reference. However, the initial increase in photo-current and the strong decrease of the current after ca. 1 h indicate that photo-corrosion processes still occur. These observations can be explained by arguing that the TiO_2 over-coating is not pinhole free leaving a small area of ZnO unprotected. Over the course of the measurement the exposed ZnO area gets bigger since the photo-corrosion process leads to removal of material in those areas where the TiO_2 layer exhibits pinholes. The removal of material may lead to the complete collapse of the TiO_2 protection layer. Due to the exposure of a greater area of ZnO to the electrolyte the photo-current initially increases. After prolonged measurement the photo-corrosion process therefore increases, resulting in the observed decrease in photo-current. Similar behavior could be observed for samples coated with thicker TiO_2 layers. These samples were able to protect the underlying ZnO for a longer time but the initial photo-current of these samples were found significantly reduced.

In order to evaluate the proposal that the protective layers were not entirely pin-hole free, ZnO-TiO_2 core-shell structures with varying TiO_2 thickness grown on glass were exposed to hydrochloric acid (pH = 2) and the optical transmission properties measured over time during this process. For these measurements the transmission of the samples in contact with water were taken as the baseline and the change in transmission was then recorded over time once the samples were put in contact with the acid. Finally, the transmission spectra recorded in this manner were weighted to the normalized spectrum of a plane glass slide in contact with the acid. The spectrum of the glass slide was taken after each long-term measurement on the respective sample. A loss of material due to possible chemical dissolution of ZnO should therefore be visible by a positive change of transmission.

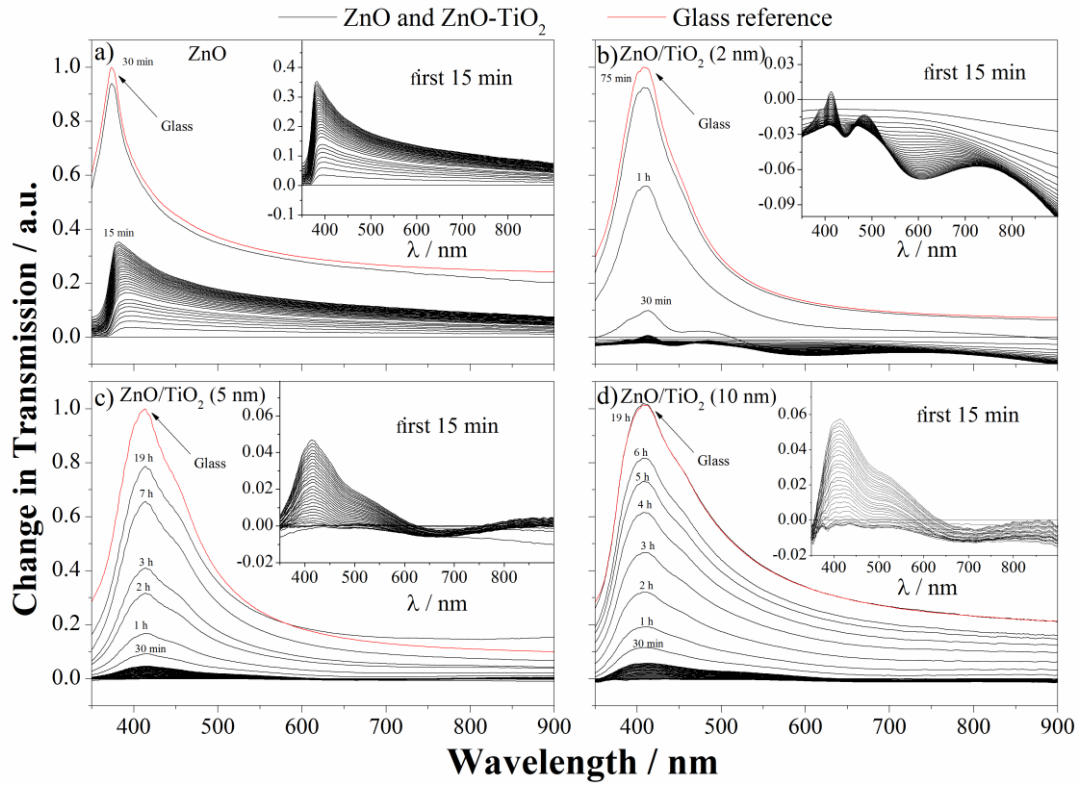

Figure 7-7: Change of optical transmission over time for samples being exposed to hydrochloric acid (pH = 2) – a) ZnO b) ZnO-TiO_2 with 2 nm TiO_2 c) ZnO-TiO_2 with 5 nm TiO_2 d) ZnO-TiO_2 with 10 nm TiO_2. A positive change in transmission represents possible dissolution of ZnO. Please note that the shape of the spectra (especially < 400 nm) cannot be correlated to electronic properties of the samples (e.g. band gap absorption) as the light source used is not intended for measurements in the UV range.

Figure 7-7 summarizes the optical measurements for the ZnO reference sample as well as for ZnO-TiO_2 structures with 2 nm, 5 nm and 10 nm TiO_2 layer thickness. The change in transmission for the unprotected sample is close to that of the glass slide after about 30 min. A significant delay of the change in transmission toward that of the glass slide is visible for all TiO_2 coated samples. For the 2 nm sample the transmission is close to the transmission of glass after ca. 75 min. However, for the samples with the thicker coatings, 5 nm and 10 nm, only slight differences are visible and the transmission for these samples approaches that of the glass slide after ca. 19 h. From the measurements of the change of transmission upon acid exposure it can be seen that protective layers consisting of 5 nm and 10 nm of TiO_2 protect the underlying ZnO well from the acid for a prolonged period of time. However some dissolution also occurs for these samples. During the measurements it was observed optically that the

nanorod-arrays were partly flaking off – especially for the 10 nm TiO_2 sample. Thus suggesting that the acid might be mainly attacking the bottom of the structures, leading to etching of the seed-layer. The 2 nm TiO_2 sample on the other hand did not exhibit flaking at the seed layer substrate interface. Nevertheless, the rapid dissolution of this core-shell structure verifies the proposal that a 2 nm thick TiO_2 layer most likely contains a larger number of pinholes. Interestingly this sample showed an initial negative change in transmission – especially during the first 15 min of the experiment. The recorded transmission curves for this period are shown in the inset of Figure 7-7b and differ significantly in their magnitude when compared to all other samples (insets in Figure 7-7a, c and d). When the photo-corrosion process described for this TiO_2 layer thickness (refer to Figure 7-6 and related comments) is taken as an explanation for the observed chemical dissolution in the acid exposure experiment, it is possible that the partial etching of the ZnO material in the pin-hole rich areas could lead to a micro-roughening of the surface of the core-shell structures. In turn, this might lead to an increased reflection in the visible range of the spectrum resulting in a decrease in transmission.

Indeed pin-hole rich TiO_2 layers could be observed in TEM measurements as the example-images for the 5 nm TiO_2 sample in Figure 7-8 show. The overview in Figure 7-8 a) shows that the TiO_2 layer along the edges of the rod is homogenous and the nominal layer thickness of 5 nm was achieved (Figure 7-8b). However, a closer view of the rod tips reveals an incomplete TiO_2 layer in this area (Figure 7-8c). As this phenomena has been observed on multiple rods (especially for the 2 nm TiO_2 sample)

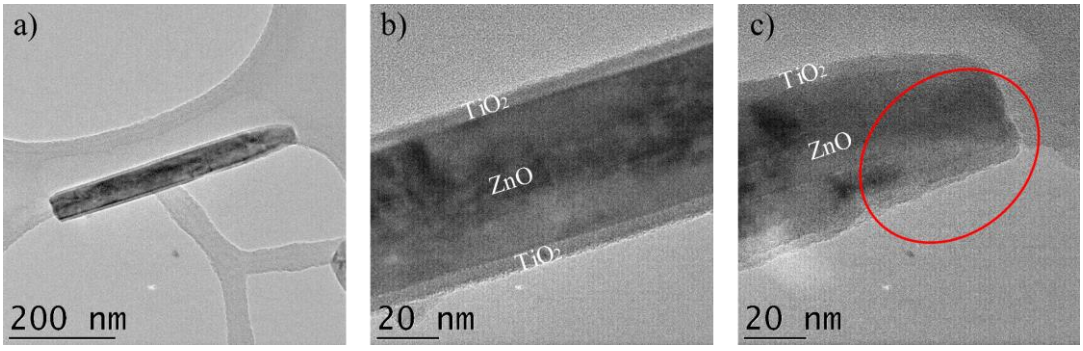

Figure 7-8: TEM images of a ZnO nanorod over-coated with 5 nm TiO_2 a) overview b) and c) magnification of the rod side-facets and the rod tip, respectively. The TiO_2 growth is non-conformal on the rod-tip.

it seems likely that TiO_2 nucleation and growth on the tip of the rod is somewhat inhibited. In particular a nucleation delay on the crystal facets of the tips seems likely. The non-conformal TiO_2 growth is thus making photo-corrosion as well as chemical dissolution of the underlying ZnO possible. Thus, future research will focus on improving the rod-tip coverage, possibly by optimizing the TiO_2 ALD.

7.5 Conclusions

Strategies for the minimization of the undesirable influences associated with the high rate of fast charge carrier recombination, low visible light absorption and photo-corrosion for ZnO nanorod-arrays grown from solution have been introduced.

It is demonstrated that careful defect-engineering may be used to increase the efficiency of photo-(electro)chemical reactions. Here, the specific focus was directed toward orange-luminescent defect-centers. Linear sweep voltammetry in neutral electrolyte solution revealed that ZnO nanorod-arrays exhibiting strong orange emission show a defect-promoted increase in photo-current under simulated sunlight of about 200% as compared to as-grown nanorod-arrays. Additionally, the effect of different seed layer deposition techniques has been compared and the results suggest a large influence on the material properties of the ZnO nanorod-arrays grown subsequently.

A doping strategy has been presented, which can be applied in order to shift the materials absorption into the visible region. As the large band gap energy of ZnO, some 3.3 eV (< 380 nm), limits the absorption of sunlight significantly, it is demonstrated that visible light absorption can be achieved by the incorporation of significant amounts of cobalt into the ZnO host lattice using a newly developed low-temperature solution-based growth method. It is shown that the visible-light absorption of the resulting material, which consists of ZnO:Co nanorod-arrays directly deposited onto seed-layer coated glass substrates, extends up to 700 nm by controlling the cobalt concentration in the growth solution.

Lastly, the issue of photo-corrosion of ZnO-based photo-electrodes was addressed. In order to produce effective and stable chemical barriers pin-hole free layers are essential. This requirement was approached using atomic layer deposition (ALD) which offers the advantage of controlled and nominally pin-hole free deposition of

ultrathin barrier layers even onto 3D-geometries. It has been shown that TiO_2 shells are able to chemically protect the ZnO core in acidic media. However, it was found that for some samples the TiO_2 barriers are not complete – especially at the rod tips – leading to a considerably lower etch rate as compared to uncoated nanorod-arrays. Photo-electrochemically, the core-shell structures with 2 nm TiO_2 coating showed a photo-current stabilization for several hours with a net gain in generated current over time.

7.6 References

[1] H. Morkoç and Ü. Özgür, "Optical Properties," in *Zinc Oxide - Fundamentals, Materials and Device Technology*: Wiley-VCH Verlag GmbH & Co. KGaA, 2009, pp. 131-244.

[2] A. B. Djurišić, A. M. C. Ng, and X. Y. Chen, "ZnO nanostructures for optoelectronics: Material properties and device applications," *Progress in Quantum Electronics,* vol. 34, no. 4, pp. 191-259, 2010.

[3] S. Xu and Z. L. Wang, "One-dimensional ZnO nanostructures: Solution growth and functional properties," *Nano Research,* vol. 4, no. 11, pp. 1013-1098, 2011.

[4] Y. Lu, Y. Lin, D. Wang, L. Wang, T. Xie, and T. Jiang, "A high performance cobalt-doped ZnO visible light photocatalyst and its photogenerated charge transfer properties," *Nano Research,* vol. 4, no. 11, pp. 1144-1152, 2011.

[5] Y. Mao, H. Yang, J. Chen, J. Chen, Y. Tong, and X. Wang, "Significant performance enhancement of ZnO photoanodes from Ni(OH)2 electrocatalyst nanosheets overcoating," *Nano Energy,* vol. 6, pp. 10-18, 2014.

[6] L. Cai *et al.*, "V ions implanted ZnO nanorod arrays for photoelectrochemical water splitting under visible light," *International Journal of Hydrogen Energy,* vol. 40, no. 3, pp. 1394-1401, 2015.

[7] W. C. Lee, G. E. Canciani, B. O. S. Alwhshe, and Q. Chen, "Enhanced photoelectrochemical water oxidation by ZnxMyO (M = Ni, Co, K, Na) nanorod arrays," *International Journal of Hydrogen Energy,* vol. 41, no. 1, pp. 123–131, 2015.

[8] J. Kaur, S. Bansal, and S. Singhal, "Photocatalytic degradation of methyl orange using ZnO nanopowders synthesized via thermal decomposition of oxalate precursor method," *Physica B: Condensed Matter,* vol. 416, pp. 33-38, 2013.

[9] J. Wang *et al.*, "Oxygen vacancy induced band-gap narrowing and enhanced visible light photocatalytic activity of ZnO," *ACS Appl Mater Interfaces,* vol. 4, no. 8, pp. 4024-4030, 2012.

[10] K. S. Ranjith, R. Pandian, E. McGlynn, and R. T. Rajendra Kumar, "Alignment, Morphology and Defect Control of Vertically Aligned ZnO Nanorod Array: Competition between “Surfactant” and “Stabilizer” Roles of the Amine Species and Its Photocatalytic Properties," *Crystal Growth & Design,* vol. 14, no. 6, pp. 2873-2879, 2014.

[11] F. Kayaci, S. Vempati, C. Ozgit-Akgun, N. Biyikli, and T. Uyar, "Enhanced photocatalytic activity of homoassembled ZnO nanostructures on electrospun polymeric nanofibers: A combination of atomic layer deposition and hydrothermal growth," *Applied Catalysis B: Environmental,* vol. 156-157, pp. 173-183, 2014.

[12] S. B. Ogale, "Dilute doping, defects, and ferromagnetism in metal oxide systems," *Adv Mater,* vol. 22, no. 29, pp. 3125-55, 2010.

[13] S. V. Bhat and F. L. Deepak, "Tuning the bandgap of ZnO by substitution with Mn2+, Co2+ and Ni2+," *Solid State Communications,* vol. 135, no. 6, pp. 345-347, 2005.

[14] S. Basu *et al.*, "Local Structure Investigation of Cobalt and Manganese Doped ZnO Nanocrystals and Its Correlation with Magnetic Properties," *The Journal of Physical Chemistry C,* vol. 118, no. 17, pp. 9154-9164, 2014.

[15] D. Y. Inamdar, A. D. Lad, A. K. Pathak, I. Dubenko, N. Ali, and S. Mahamuni, "Ferromagnetism in ZnO Nanocrystals: Doping and Surface Chemistry," *The Journal of Physical Chemistry C,* vol. 114, no. 3, pp. 1451-1459, 2010.

[16] V. Sharma, M. Dixit, V. R. Satsangi, S. Dass, S. Pal, and R. Shrivastav, "Photoelectrochemical splitting of water with nanocrystalline Zn1−xMnxO thin films: First-principle DFT computations supporting the systematic experimental endeavor," *International Journal of Hydrogen Energy,* vol. 39, no. 8, pp. 3637-3648, 2014.

[17] S. Benramache, B. Benhaoua, and H. Bentrah, "Preparation of transparent, conductive ZnO:Co and ZnO:In thin films by ultrasonic spray method," *Journal of Nanostructure in Chemistry,* vol. 3, no. 1, p. 54, 2013.

[18] R. Elilarassi and G. Chandrasekaran, "Influence of Co-doping on the structural, optical and magnetic properties of ZnO nanoparticles synthesized using auto-combustion method," *Journal of Materials Science: Materials in Electronics,* vol. 24, no. 1, pp. 96-105, 2012.

[19] V. Gandhi, R. Ganesan, H. H. Abdulrahman Syedahamed, and M. Thaiyan, "Effect of Cobalt Doping on Structural, Optical, and Magnetic Properties of ZnO Nanoparticles Synthesized by Coprecipitation Method," *The Journal of Physical Chemistry C,* vol. 118, no. 18, pp. 9715-9725, 2014.

[20] H.-J. Lee, S.-Y. Jeong, C. R. Cho, and C. H. Park, "Study of diluted magnetic semiconductor: Co-doped ZnO," *Applied Physics Letters,* vol. 81, no. 21, p. 4020, 2002.

[21] I. Djerdj, Z. Jaglicic, D. Arcon, and M. Niederberger, "Co-Doped ZnO nanoparticles: Minireview," *Nanoscale,* 10.1039/C0NR00148A vol. 2, no. 7, pp. 1096-1104, 2010.

[22] P. Koidl, "Optical absorption of Co2+ in ZnO," *Physical Review B,* vol. 15, no. 5, pp. 2493-2499, 1977.

[23] C. A. Johnson, T. C. Kaspar, S. A. Chambers, G. M. Salley, and D. R. Gamelin, "Sub-band-gap photoconductivity inCo2+-doped ZnO," *Physical Review B,* vol. 81, no. 12, p. 125206, 2010.

[24] J. W. May, J. Ma, E. Badaeva, and X. Li, "Effect of Excited-State Structural Relaxation on Midgap Excitations in Co2+-Doped ZnO Quantum Dots," *The Journal of Physical Chemistry C,* vol. 118, no. 24, pp. 13152-13156, 2014.

[25] C. A. Johnson, A. Cohn, T. Kaspar, S. A. Chambers, G. M. Salley, and D. R. Gamelin, "Visible-light photoconductivity of Zn1−xCoxO and its dependence onCo2+concentration," *Physical Review B,* vol. 84, no. 12, p. 125203, 2011.

[26] P. M. Aneesh, C. T. Cherian, M. K. Jayaraj, and T. Endo, "Co2+ doped ZnO nanoflowers grown by hydrothermal method," *Journal of the Ceramic Society of Japan,* vol. 118, no. 1377, pp. 333-336, 2010.

[27] M. Tortosa, M. Mollar, B. Marí, and F. Lloret, "Optical and magnetic properties of ZnCoO thin films synthesized by electrodeposition," *Journal of Applied Physics,* vol. 104, no. 3, p. 033901, 2008.

[28] C.-W. Liu *et al.*, "Enhancement in the structure quality of ZnO nanorods by diluted Co dopants: Analyses via optical second harmonic generation," *Journal of Applied Physics,* vol. 117, no. 8, p. 084315, 2015.

[29] W. Zang, P. Li, Y. Fu, L. Xing, and X. Xue, "Hydrothermal synthesis of Co–ZnO nanowire array and its application as piezo-driven self-powered humidity sensor with high sensitivity and repeatability," *RSC Adv.,* vol. 5, no. 102, pp. 84343-84349, 2015.

[30] P. P. Patel *et al.*, "Nitrogen and cobalt co-doped zinc oxide nanowires – Viable photoanodes for hydrogen generation via photoelectrochemical water splitting," *Journal of Power Sources,* vol. 299, pp. 11-24, 2015.

[31] M. Willander *et al.*, "Luminescence from Zinc Oxide Nanostructures and Polymers and their Hybrid Devices," *Materials,* vol. 3, no. 4, pp. 2643-2667, 2010.

[32] A. Janotti and C. G. Van de Walle, "Fundamentals of zinc oxide as a semiconductor," *Reports on Progress in Physics,* vol. 72, no. 12, p. 126501, 2009.

[33] A. B. Djurišić *et al.*, "Defect emissions in ZnO nanostructures," *Nanotechnology,* vol. 18, no. 9, p. 095702, 2007.

[34] K. H. Tam *et al.*, "Defects in ZnO Nanorods Prepared by a Hydrothermal Method," *The Journal of Physical Chemistry B,* vol. 110, no. 42, pp. 20865-20871, 2006.

[35] C. H. Ahn, Y. Y. Kim, D. C. Kim, S. K. Mohanta, and H. K. Cho, "A comparative analysis of deep level emission in ZnO layers deposited by various methods," *Journal of Applied Physics,* vol. 105, no. 1, p. 013502, 2009.

[36] K. Bandopadhyay and J. Mitra, "Zn interstitials and O vacancies responsible for n-type ZnO: what do the emission spectra reveal?," *RSC Adv.,* vol. 5, no. 30, pp. 23540-23547, 2015.

[37] D. Li *et al.*, "Different origins of visible luminescence in ZnO nanostructures fabricated by the chemical and evaporation methods," *Applied Physics Letters,* vol. 85, no. 9, p. 1601, 2004.

[38] J. Kegel, F. Laffir, I. M. Povey, and M. E. Pemble, "Defect-promoted photo-electrochemical performance enhancement of orange-luminescent ZnO nanorod-arrays," *Phys Chem Chem Phys,* vol. 19, no. 19, pp. 12255--12268, 2017.

[39] S. Chen and L.-W. Wang, "Thermodynamic Oxidation and Reduction Potentials of Photocatalytic Semiconductors in Aqueous Solution," *Chemistry of Materials,* vol. 24, no. 18, pp. 3659-3666, 2012.

[40] A. L. Rudd and C. B. Breslin, "Photo-induced dissolution of zinc in alkaline solutions," *Electrochimica Acta,* vol. 45, no. 10, pp. 1571-1579, 2000.

[41] S. G. Kumar and K. S. R. K. Rao, "Zinc oxide based photocatalysis: tailoring surface-bulk structure and related interfacial charge carrier dynamics for better environmental applications," *RSC Adv.*, vol. 5, no. 5, pp. 3306-3351, 2015.

[42] Y. W. Chen *et al.*, "Atomic layer-deposited tunnel oxide stabilizes silicon photoanodes for water oxidation," *Nat Mater*, vol. 10, no. 7, pp. 539-44, 2011.

[43] M. R. Shaner, S. Hu, K. Sun, and N. S. Lewis, "Stabilization of Si microwire arrays for solar-driven H2O oxidation to O2(g) in 1.0 M KOH(aq) using conformal coatings of amorphous TiO2," *Energy & Environmental Science*, vol. 8, no. 1, pp. 203-207, 2015.

[44] A. G. Scheuermann and P. C. McIntyre, "Atomic Layer Deposited Corrosion Protection: A Path to Stable and Efficient Photoelectrochemical Cells," *J Phys Chem Lett*, vol. 7, no. 14, pp. 2867-78, 2016.

[45] F. Kayaci, S. Vempati, I. Donmez, N. Biyikli, and T. Uyar, "Role of zinc interstitials and oxygen vacancies of ZnO in photocatalysis: a bottom-up approach to control defect density," *Nanoscale*, vol. 6, no. 17, pp. 10224-10234, 2014.

[46] F. Liu, Y. H. Leung, A. B. Djurišić, A. M. C. Ng, and W. K. Chan, "Native Defects in ZnO: Effect on Dye Adsorption and Photocatalytic Degradation," *The Journal of Physical Chemistry C*, vol. 117, no. 23, pp. 12218-12228, 2013.

[47] J. Al-Sabahi, T. Bora, M. Al-Abri, and J. Dutta, "Controlled Defects of Zinc Oxide Nanorods for Efficient Visible Light Photocatalytic Degradation of Phenol," *Materials*, vol. 9, no. 4, pp. 238-247, 2016.

[48] A. R. Bielinski, E. Kazyak, C. M. Schlepütz, H. J. Jung, K. N. Wood, and N. P. Dasgupta, "Hierarchical ZnO Nanowire Growth with Tunable Orientations on Versatile Substrates Using Atomic Layer Deposition Seeding," *Chemistry of Materials*, vol. 27, no. 13, pp. 4799-4807, 2015.

[49] A. R. Bielinski *et al.*, "Rational Design of Hyperbranched Nanowire Systems for Tunable Superomniphobic Surfaces Enabled by Atomic Layer Deposition," *ACS Nano*, vol. 11, no. 1, pp. 478-489, 2017.

[50] L. E. Greene *et al.*, "Low-temperature wafer-scale production of ZnO nanowire arrays," *Angew Chem Int Ed Engl*, vol. 42, no. 26, pp. 3031-4, 2003.

[51] J. Kegel, J. Halpin, F. Laffir, I. M. Povey, and M. E. Pemble, "Rapid low-temperature solution growth of ZnO:Co nanorod arrays with controllable visible light absorption," *CrystEngComm*, vol. 19, no. 14, pp. 1938-1946, 2017.

[52] L. Yanmei *et al.*, "Structure and photoluminescence of arrayed Zn1−xCoxO nanorods grown via hydrothermal method," *Journal of Physics D: Applied Physics*, vol. 40, no. 15, pp. 4592-4596, 2007.

[53] X. He, H. Yang, Z. Chen, and S. S. Y. Liao, "Effect of Co-doping content on hydrothermal derived ZnO array films," *Physica B: Condensed Matter*, vol. 407, no. 15, pp. 2895-2899, 2012.

[54] D. A. Schwartz, N. S. Norberg, Q. P. Nguyen, J. M. Parker, and D. R. Gamelin, "Magnetic Quantum Dots: Synthesis, Spectroscopy, and Magnetism of Co2+- and Ni2+-Doped ZnO Nanocrystals," *Journal of the American Chemical Society*, vol. 125, no. 43, pp. 13205-13218, 2003.

[55] S. Baruah and J. Dutta, "Hydrothermal growth of ZnO nanostructures," *Science and Technology of Advanced Materials,* vol. 10, no. 1, p. 013001, 2009.
[56] R. Xie *et al.*, "Enhancement and patterning of ultraviolet emission in ZnO with an electron beam," *Applied Physics Letters,* vol. 88, no. 13, p. 134103, 2006.
[57] C. G. Van de Walle, "Defect analysis and engineering in ZnO," *Physica B: Condensed Matter,* vol. 308–310, pp. 899-903, 2001.
[58] C. H. Patterson, "Role of defects in ferromagnetism inZn1−xCoxO: A hybrid density-functional study," *Physical Review B,* vol. 74, no. 14, 2006.
[59] A. Janotti and C. G. Van de Walle, "Native point defects in ZnO," *Physical Review B,* vol. 76, no. 16, p. 165202, 2007.
[60] D.-H. Kim, G.-W. Lee, and Y.-C. Kim, "Interaction of zinc interstitial with oxygen vacancy in zinc oxide: An origin of n-type doping," *Solid State Communications,* vol. 152, no. 18, pp. 1711-1714, 2012.
[61] Y.-S. Kim and C. H. Park, "Rich Variety of Defects in ZnO via an Attractive Interaction between O Vacancies and Zn Interstitials: Origin ofn-Type Doping," *Physical Review Letters,* vol. 102, no. 8, p. 086403, 2009.
[62] L. S. Vlasenko and G. D. Watkins, "Optical detection of electron paramagnetic resonance in room-temperature electron-irradiated ZnO," *Physical Review B,* vol. 71, no. 12, 2005.
[63] P. Cendula *et al.*, "Calculation of the Energy Band Diagram of a Photoelectrochemical Water Splitting Cell," *The Journal of Physical Chemistry C,* vol. 118, no. 51, pp. 29599-29607, 2014.
[64] Y. K. Gaudy and S. Haussener, "Utilizing modeling, experiments, and statistics for the analysis of water-splitting photoelectrodes," *J. Mater. Chem. A,* vol. 4, no. 8, pp. 3100-3114, 2016.
[65] J. Tauc, "Optical properties and electronic structure of amorphous Ge and Si," *Materials Research Bulletin,* vol. 3, no. 1, pp. 37-46, 1968.
[66] M. Liu, C.-Y. Nam, C. T. Black, J. Kamcev, and L. Zhang, "Enhancing Water Splitting Activity and Chemical Stability of Zinc Oxide Nanowire Photoanodes with Ultrathin Titania Shells," *The Journal of Physical Chemistry C,* vol. 117, no. 26, pp. 13396-13402, 2013.
[67] W. Ma, Z. Lu, and M. Zhang, "Investigation of structural transformations in nanophase titanium dioxide by Raman spectroscopy," *Applied Physics A,* journal article vol. 66, no. 6, pp. 621-627, 1998.
[68] M. Zukalova, M. Bousa, Z. Bastl, I. Jirka, and L. Kavan, "Electrochemical Doping of Compact TiO2Thin Layers," *The Journal of Physical Chemistry C,* vol. 118, no. 45, pp. 25970-25977, 2014.
[69] D. Liu, Z. Wei, Y. Shen, S. D. Sajjad, Y. Hao, and F. Liu, "Ultra-long electron lifetime induced efficient solar energy storage by an all-vanadium photoelectrochemical storage cell using methanesulfonic acid," *J. Mater. Chem. A,* vol. 3, no. 40, pp. 20322-20329, 2015.
[70] H. Pelouchova, P. Janda, J. Weber, and L. Kavan, "Charge transfer reductive doping of single crystal TiO2 anatase," *Journal of Electroanalytical Chemistry,* vol. 566, no. 1, pp. 73-83, 2004.
[71] J. Kegel, I. M. Povey, and M. E. Pemble, "(Invited) Tailoring Zinc Oxide Nanorod-Arrays for Photo-(electro)Chemical Applications," *ECS Transactions,* vol. 77, no. 4, pp. 43-60, 2017.

[72] R. L. Doyle and M. E. G. Lyons, "The Oxygen Evolution Reaction: Mechanistic Concepts and Catalyst Design," pp. 41-104, 2016.

Chapter 8

8 Conclusions and future work

The clean generation of fuels from sunlight presents a "*holy grail*" of chemical science and energy research [1]. Analogous to photosynthesis in plants, the solar splitting of water into hydrogen and oxygen resembles a key step on the way to store sunlight into chemical bonds. While plants store solar energy in form of carbohydrates every day since millions of years, research focusing on the generation of hydrogen as a fuel from water and light has only gained momentum since the early 1970s [2] and the technology has so far only been demonstrated on the lab-scale. Over the past decades the efficiency of devices generating hydrogen from sunlight as so called photo-electrochemical cells (PEC) has however increased substantially, with 16.2 % being achieved in 2017 [3]. From an economics point of view, the most efficient devices are unfortunately composed of relatively expensive III-V semiconductor materials [3-5]. Finding cost effective alternative materials that can meet the requirements of stable and efficient solar water splitting is thus of highest scientific importance. In this respect, semiconducting metal oxides are considered as promising candidates, especially due to their earth-abundant nature.

After discussing some basic PEC device configurations and underlying physical-chemical fundamentals, this thesis focused on the use of metal oxides – particularly zinc oxide (ZnO) – for solar water splitting. The technological importance of ZnO, not only for solar water splitting but also for other applications, was discussed on the basis of some important core material properties such as its wide direct bandgap, high charge carrier mobility, high binding energy and natural n-type character.

Derived from the same, the published literature dealing with possible routes to tailor ZnO for photo-(electro)chemical applications, namely photo-catalysis and as photo-anode material for the generation of oxygen, was reviewed. A first approach to increase the efficiency of these applications aims at controlling the structure of ZnO. The possibility to grow ZnO in various nano-geometries was found beneficial for increasing the active surface area of the materials and to control the portion of the polar basal plane, which is believed to be the catalytically most active plane. However, it was pointed out that structure alone may not necessarily be the only factor influencing the observed performance differences for different ZnO morphologies in various studies. This arises from the fact that the defect-chemistry of ZnO may be strongly

influenced by the deposition method and the morphology of the resulting structures. On the other hand, engineering of the intrinsic defects was presented as another possible route to influence the photo-(electro)chemical properties of ZnO. While intrinsic defects are found to be rather plentiful in ZnO, some defects are reported to aid photo-(electro)chemical reactions. In this respect, the majority of reports focus on the possible benefits that oxygen vacancies may have. The reporting literature elucidates different mechanisms for how these defects can improve the photo-(electro)chemical performance. A direct involvement as an active site is, for example, mentioned as a possible explanation for the observed phenomena. Another mechanistic possibility, which has been reported in the literature, is the absorption of visible light due to a high concentration of oxygen vacancies.

Visible light activity can also be induced by extrinsic impurities. A whole range of studies were found to deal with this topological research in respect to ZnO. Despite the fact that there are many possible extrinsic impurities/dopants, which may change the optical and electronic properties of ZnO, this thesis reports studies of this tailoring-route using nitrogen and cobalt as example dopants, since literature reports find that both aid photo-(electro)chemical reactions. Apart from engineering the morphology and intrinsic/extrinsic defects, some researchers focus on the functionalization of the ZnO surface. As part of this topic it was shown that over-coating of ZnO nanostructures can prove valuable in hindering photo-corrosion. However, the presented literature articles also point towards a synergetic effect of over-coatings that exhibit both a function as chemical barrier and as co-catalyst. Since a water oxidation catalyst may accept photo-generated holes, which then cannot degrade ZnO, this could furthermore aid the charge carrier separation and hence reduce charge carrier recombination.

The aforementioned fields of research identify important limitations of ZnO that hinder its use for PECs. These are: fast charge carrier recombination over intrinsic defects, low visible light absorption and the material`s (photo-)corrosion in aqueous solutions. The experimental studies presented herein tried to address these challenges and hence this thesis aimed at accelerating the use of ZnO in photo-electro(chemical) applications and at contributing to the general understanding of the material properties of functional ZnO nanostructures.

In this respect, a defect-engineering strategy was first applied (Chapter 3). Defect-rich ZnO nanorod arrays were synthesized and their material properties as well as their photo-electrochemical and photo-catalytic performance evaluated upon changing the defect-chemistry using rapid thermal annealing. Somewhat surprisingly, the emergence of strong orange-luminescence was observed from the nanorod arrays when annealed at temperatures around 450 °C, irrespective of the annealing atmosphere used (nitrogen, argon, oxygen, vacuum or forming gas). However, the orange emission was found to be temperature dependent, with higher and lower annealing temperatures (e.g. 350°C or 550°C) leading to no/weak orange luminescence. Based on a thorough materials characterization and on theoretical literature reports, the kinetic formation of the oxygen vacancy – zinc interstitial (V_O-Zn_i) defect-complex was identified as a possible origin for the orange luminescence in the bulk of the prepared ZnO nanorod arrays. Importantly, photo-anodes prepared with orange-luminescent nanorod arrays showed an improved photo-electrochemical performance, which the experiments suggested stemmed from a reduced charge carrier recombination. These findings were confirmed by a subsequent study of the defect-rich materials encompassing low-temperature photo-luminescence and photo-catalytic dye-degradation experiments (Chapter 4). It was shown that the orange-emission may involve a transition from states close to the conduction band edge (temperatures < 100 K) or from the conduction band (temperatures > 100 K) to a deep-level defect state, which is in line with the theoretical works on the V_O-Zn_i defect-complex by other authors. The photo-catalytic degradation of methylene blue under UV-irradiation was found to increase for orange-luminescent materials, when compared to ZnO nanorod arrays which did not appear to exhibit this emission. Thus, pointing again at a higher density of charge carriers participating in the photo-chemical reaction possibly caused due to the defect-complex acting as a slow photo-excited electron trap delaying the recombination with the photo-excited hole in the valance band. Moreover, detailed transmission electron microscopy and Raman spectroscopy measurements revealed the presence of structural defects and a graphitic surface-structure for some annealed samples. Despite the fact that the occurrence of these features was found to be independent of the orange-luminescent defects, they could be related to the rapid thermal annealing conditions. The structural defects were induced for all annealing temperatures used (350°C to 550°C, independent of the annealing atmosphere) and

evidence suggested that they correlate with the low-temperature PL emission observed at ca. 3.31 eV. In contrast, a graphitic surface structure was only observed by Raman measurements for ZnO nanorods that had been annealed in vacuum at temperatures ≥ 450 °C. Importantly, the presence of the carbon structure resulted in strong adsorption of methylene blue in the dark, which may have synergetic effects on the dye-degradation due to an increased attraction of the dye molecules towards the surface of the photo-catalyst. However, it was shown that cross-annealing in oxygen destroys the carbon structure and diminishes the dye-adsorption effect. Finally, the thorough characterization of the defect-engineered ZnO nanorod arrays exemplified the current difficulties when correlating particular defects to the photo-(electro)chemical reactions. For further studies in this field it was thus suggested that researchers need to carefully investigate and systematically adjust as many material properties as possible, in order to get real insight into the role of a particular defect state for photo-catalysis and solar water splitting.

Despite the thorough characterization of the orange-luminescent ZnO nanorods presented in this thesis, additional experiments regarding the nature and formation of the defect-center would be beneficial. Particularly (photo-)electron paramagnetic resonance measurements (EPR) may prove helpful to identify the exact recombination mechanism. One question that arises in this respect is whether the defect-complex may facilitate the presence of a V_O^+ (which is theoretically shown to be thermodynamically unstable but could exist upon photo-excitation). If these states are involved in the recombination mechanism, a signature EPR signal may be expected. Further rapid thermal annealing studies, including a change of the heating and cooling rates, and the overall annealing times, would also be valuable for the investigation of the kinetic formation of the defect-complex. Additionally, electrochemical studies of ZnO nanorod arrays exhibiting different intensities of orange-luminescence would be interesting, since it was theoretically shown that the defect-complex could contribute to the n-type character of ZnO. However, due to the high intensity of the observed orange emission at room temperature, future research may also depart from applications in photo-(electro)chemistry and could investigate the use of these materials as light emitting diodes, particularly when interfaced with gallium nitride (also wurtzite structure).

Generally, low-temperature solution-based growth techniques are very attractive for

the synthesis of ZnO, since the potential production costs would be low. Nonetheless, in regards to the doping of ZnO with cobalt for the increased absorption of visible light a lack of suitable low-temperature methods was identified. Thus, the growth of cobalt-doped ZnO (ZnO:Co) was investigated under highly alkaline conditions and by using monoethanolamine (MEA) as an organic growth modifier (Chapter 5). At a growth temperature of 85 °C – and potentially even lower – rapid growth of substitutionally cobalt-doped ZnO nanorods was achieved. Compared to undoped ZnO nanorods, these structures exhibit a clear shift of the absorption onset towards longer wavelengths and characteristic cobalt-related absorption in the visible range. Furthermore, it was shown that visible-light absorption of the material can be controlled by adjusting the cobalt precursor concentration in the growth solution. Moreover, the cobalt concentration – and therefore the visible light absorption – was found to increase when the films were grown at higher temperatures, which is related to the temperature dependent cobalt-solvation in ZnO. While in the initial growth studies the use of MEA was found to be crucial for the growth of ZnO:Co, a more detailed study of its role in the synthesis was need (Chapter 6). Hence, it was identified that MEA acts as complexing agent for zinc and cobalt. The respective complexes show different temperature stabilities with zinc being released into the solution at lower temperatures compared to cobalt. Additionally, as a result of the growth studies MEA can be assigned a growth directing function in the synthesis. When using a higher MEA concentration in the solution the rods where shown to grow longer but also thicker. UV-Vis measurements revealed that the resulting higher material volume leads to an increased visible light absorption. Thus, changing the MEA concentration in the growth solution was found to present another route to increase the overall visible light absorption of the ZnO nanorod arrays. A final and very important role of MEA is its effect as reducing agent in the synthesis. While reduction of Co^{3+} to Co^{2+} also occurs during the low temperature growth, it was observed that this effect becomes dominant when the growth temperature is raised during a second growth stage. Importantly, it could be demonstrated that the MEA concentration is crucial for the nature of the cobaltic decoration of the ZnO:Co nanorods that forms at higher temperatures. A high reducing capacity of the solution – achieved by a high MEA concentration – was shown to aid the growth of $Co(OH)_2$. On the other hand, Co_3O_4 decoration was observed when a lower MEA concentration was used. Hence, the developed one-pot two-stage growth method was found to enable

the deposition of ZnO:Co nanorod arrays, of which the visible light absorption can be controlled, decorated with catalytic $Co(OH)_2$ and/or Co_3O_4. As a result, the prepared anodes exhibited improved water oxidation kinetics with an overpotential of 0.55 V at 1 mA/cm^2. Additionally, it was demonstrated that the ZnO:Co nanorod arrays can utilise visible light, since a considerable photo-current was observed when the electrodes were illuminated with simulated sunlight of $\lambda > 400$ nm. Furthermore it is important to note that the proposed growth mechanism could potentially be adapted for other metal-oxide systems since the underlying growth mechanisms should be somewhat universal.

The studies conducted identify a big potential for the $Co(OH)_2$ and/or Co_3O_4 decorated ZnO:Co nanorod arrays to be used in PECs. However, more research on their photo-electrochemical performance is needed to answer open questions that arise from the studies presented herein. Firstly, the ZnO:Co nanorods alone need to be studied systematically for their photo-electrochemical properties and their dependency on the cobalt concentration in the films. Similarly, the growth parameters could be optimized in respect to some more general structural aspects of the ZnO:Co nanorods (length of the rods, aspect-ratio). Furthermore, additional work needs to be carried out in order to identify as to why nominally undecorated ZnO:Co nanorods showed relatively good water oxidation kinetics as well as cobalt-related redox features during the electrochemical characterization, which point towards a catalytic activity associated to the ZnO:Co nanorods alone. Building on these experiments the catalytic over-coating could then be optimized towards a thin but conformal layer-like structure. Different annealing treatments should be investigated in order to increase the photo-current of the resulting structures. Here, incorporation of nitrogen into the ZnO:Co nanorods over a thermal route is identified as an interesting route, since it might further increase the visible light absorption in the films. When accessing the photo-electrochemical properties of $Co(OH)_2$ and/or Co_3O_4 decorated ZnO:Co nanorod arrays, the focus must also be directed towards the investigation of their stability. The catalytic coating could act as an active protection against photo-corrosion, since photo-generated holes may oxidize the catalyst rather than the ZnO:Co. Additionally, Co_3O_4 decorated ZnO:Co nanorod arrays could also prove valuable for other applications such as electrode materials in batteries and in supercapacitors and the potential of the structures in these regards should be explored.

Lastly, it was attempted to address the photo-corrosion of ZnO by applying thin (2 – 10 nm) titanium dioxide (TiO_2) over-layers by atomic layer deposition (Chapter 7). The chemical stability of the resulting ZnO-TiO_2 core-shell structures was greatly enhanced when compared to unprotected ZnO nanorod arrays. However, when these structures were used as photo-anode materials, a decrease of the photo-current over time was nevertheless observed, indicating photo-degradation. Indeed, transmission electron microscopy confirmed that the TiO_2 over-coating was not homogenous. Pinholes were observed particularly at the rod tips and it is believed that these were responsible for the both the slow dissolution in acidic solution as well as the photo-current deterioration over time.

Also in regards to the ZnO-TiO_2 core-shell structures appropriate annealing conditions could lead to an improvement of the photo-electrochemical performance. Particularly changing the ALD TiO_2 crystal phase by increasing the annealing temperature (amorphous to anatase to rutile) and the resulting change of the energy band alignment between the ZnO and TiO_2 could have a strong influence on the anode performance. Furthermore, additional work must aim at the avoidance of pin-holes in the TiO_2 shell. Functionalization of the ZnO surface prior to the ALD growth is one possibility here but also the optimization of the ALD process should be considered. From the PEC applications point of view it may however be favourable to investigate catalytic over-layers, which also exhibit a protective function, more strongly.

In conclusion, the experimental studies presented in this thesis advanced the current understanding of the material properties of ZnO for photo-(electro)chemical applications and introduced synthetic approaches to overcome the material`s natural limitations in this respect. Atomic layer deposition was used to deposit functional thin films (seed- and barrier-layers) and hydrothermal growth methods were used to deposit defect-engineered or visible light absorbing ZnO nanorod arrays. These structures showed improved photo-electrochemical properties when used as photo-anode materials. A lower rate of charge carrier recombination was evidenced for the defect-engineered, strongly orange emitting ZnO nanorod arrays, which in turn increased the photo-current obtained. While these structures only capitalize on UV irradiation, cobalt-doped ZnO nanorod arrays were found to exhibit a visible light activated photo-

current. Additionally, the growth method developed for the deposition of cobalt-doped ZnO also enabled the decoration of the nanorod arrays with cobaltic structures, active to catalyze the oxygen evolution reaction. These coatings could potentially also inhibit photo-corrosion, a material shortcoming that was tackled in this work by the application of thin titanium dioxide shells. Thus, the results presented herein will help to further accelerate the use of ZnO for solar water splitting but will also facilitate future research in this respect, since the detailed discussion of the resulting material properties open up new routes to tailor ZnO towards photo-(electro)chemical applications.

8.1 References

[1] D. G. Nocera, "Solar Fuels and Solar Chemicals Industry," *Acc Chem Res*, vol. 50, no. 3, pp. 616-619, 2017.

[2] A. Fujishima and K. Honda, "Electrochemical Photolysis of Water at a Semiconductor Electrode," *Nature*, vol. 238, no. 5358, pp. 37-38, 1972.

[3] J. L. Young, M. A. Steiner, H. Döscher, R. M. France, J. A. Turner, and Todd G. Deutsch, "Direct solar-to-hydrogen conversion via inverted metamorphic multi-junction semiconductor architectures," *Nature Energy*, vol. 2, no. 4, p. 17028, 2017.

[4] M. M. May, H. J. Lewerenz, D. Lackner, F. Dimroth, and T. Hannappel, "Efficient direct solar-to-hydrogen conversion by in situ interface transformation of a tandem structure," *Nat Commun*, vol. 6, p. 8286, 2015.

[5] O. Khaselev and J. A. Turner, "A Monolithic Photovoltaic-Photoelectrochemical Device for Hydrogen Production via Water Splitting," *Science*, vol. 280, no. 5362, pp. 425-427, 1998.

Appendix 1: Supporting information for Chapter 3

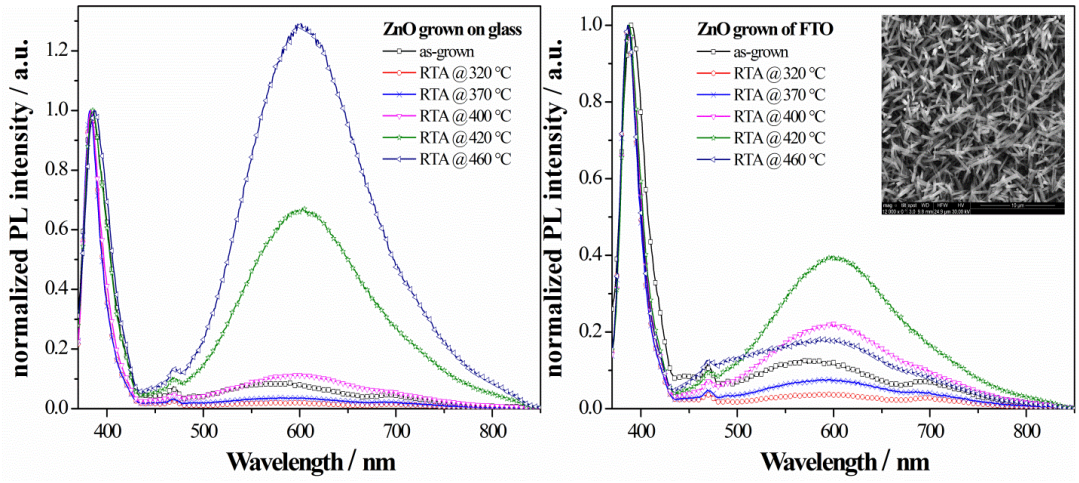

Figure A1- 1: Annealed ZnO nanorod-arrays grown on different substrates (same seed layer preparation used). Left) ZnO nanorod-arrays grown on ALD seed layer with glass as the substrate. Right) ZnO nanorod-arrays grown on ALD seed layer with FTO as the substrate. When FTO is used as the substrate the orange emission is generally less and occurs/peaks at ca. 30 °C lower temperatures compared to the sample grown on glass. The inset shows a top-view SEM micrograph of the photo-electrode, revealing that the alignment and density is lower for nanorod-arrays grown on FTO/seed layer (compare Figure 3-1 of Chapter 3). This may point towards a structural influence on the obtained photo-luminescence spectra.

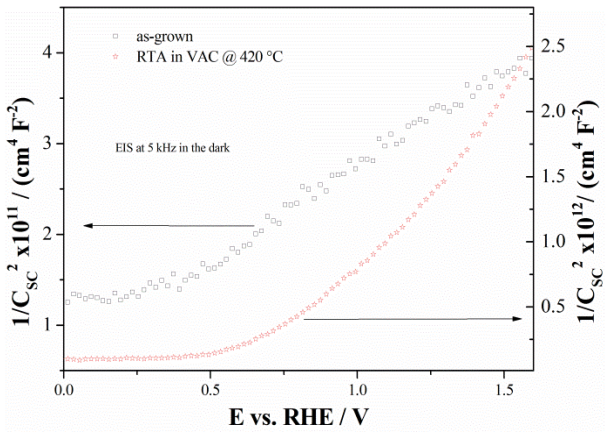

Figure A1- 2: Examples of Mott-Schottky plots obtained in the dark at 5 kHz of as-grown and RTA treated (vacuum 420 °C) ZnO nanorod-arrays. The frequency of 5 kHz was chosen to reduce the influence of the double-layer capacitance in the electrolyte and slow charge transfer processes (slower time domain). For the as-grown sample a linear dependence of $1/C^2$ from the applied potential is observed, indicating that the band-edges are "pinned" at the semiconductor-electrolyte interface.[1, 2] The Mott-Schottky plot for the sample annealed at 420 °C (strong orange-emission) does not show a linear increase of $1/C_{SC}^2$ with the applied potential. To a lesser extend this behavior has also been observed for the sample annealed at 350 °C (strong band-band recombination and little orange emission – see Chapter 3). A non-linear behavior might indicate that the Fermi-level is "pinned" to surface states.[1] Generally the non-linearity reveals that the charge transfer at the semiconductor-electrolyte is more complex than in the case of the as-grown sample. Different charge carrier transfer routes (e.g. holes from the conduction band oxidizing the electrolyte, electron transfer from the electrolyte into defect states) are thereby possible and might contribute to the curved slope in the figure. For the as-grown sample the flatband potential E_{FB} and the donor concentration N_D^+ were estimated from the x-axis intercept and the slope of the linear extrapolation (range used for fit 0.5 V – 1.5 V vs. RHE), respectively. The Mott-Schottky equation was used: $1/C_{SC}^2 = (2/(\varepsilon_0 \varepsilon_r q N_D^+ A^2))(E_a - E_{FB} - kT/q)$. Where ε_0 is the permittivity of vacuum, ε_r the relative dielectric constant of ZnO (taken as 8.15)[3], q the electron charge, E_a the applied potential, and kT/q the thermal energy ≈ 26 mV. The in this manner calculated donor density and flat-band potential – $7.76 \cdot 10^{19}$ cm^{-3} and -0.27 V vs. RHE, respectively – agree well with literature reports.[3-5] Due to the non-linear behavior a meaningful fit was not possible for the sample exhibiting strong orange emission.

Discussion of the energy barrier associated with the kick-out process for the formation of the V_O-Zn_i defect-complex

Based on theoretical calculations of Kim *et al*., the energy barrier E_B for the kick-out process was calculated to be around 1.3 eV.[6] Following the approach presented by Janotti and Van de Walle, the required annealing temperature T to overcome this

energy barrier can be calculated using (A1.1):

$$f = f_0 \exp\left(\frac{-E_b}{kT}\right) \quad \text{(A1.1)}$$

Where f is the frequency a defect can travel with (jump of an atom to a near vacancy site or jump of an interstitial to the next interstitial; in good approximation f can be taken as 1 s^{-1}), f_0 is a prefactor (in good approximation f_0 can be taken as 10^{13} s^{-1}) and k is the Boltzmann constant.[7] An energy barrier of 1.3 eV therefore corresponds to an annealing temperature of *ca*. 231 °C. Table A1- 1 lists estimated energy barriers based on the annealing temperatures used throughout Chapter 3. As can be seen in Figure 3-5 and Figure 3-9 of Chapter 3, orange emission occurs for some samples already to a minor degree at temperatures of about 350 °C. The energy barrier associated with this temperature is *ca*. 1.61 eV, suggesting that the real energy barrier related to the kick-out process leading to the formation of the defect-complex might be higher than was calculated theoretically by Kim *et al*.[6] When the temperature range from 350 °C to 550 °C is taken as the "window" for the stabilization of the defect-complex an energy higher than 1.6 eV + 0.51 eV (energy difference between 550 °C and 350 °C) results in the annihilation of the defect-complex. The energy of 0.51 eV is hereby in good agreement with the binding energy of the complex reported in the literature (0.5 – 0.6 eV).[6, 8]

Table A1- 1. Estimated energy barriers E_b from some annealing temperatures T used throughout the study.

T in °C	E_b in eV	Comments
350	1.61	Start of defect formation – minor orange emission for some samples (e.g. Figure 3-5 and Fig 3-9 of Chapter 3)
450	1.86	Peak of orange emission around this temperature
550	2.12	Temperature at which no orange emission is clearly observed anymore
636	2.37	Annealing temperature associated with the neutral oxygen vacancy[7]

Influence of Xe flash lamp artefacts on photo-luminescence measurements

The fluorescence spectrometer used to record PL and excitation PL spectra includes different pre-set filters for the excitation as well as for the emission port. Whereas

different emission filters (e.g. cut off filter 360 nm) were found to have negligible influence, the selection of the excitation filter crucially effects the spectra. Figure A1-3 shows the spectrum of the used xenon (Xe) flash lamp as well as PL spectra taken on a defect-rich ZnO sample and on a microscope glass slide. The PL spectra were taken with different excitation filter settings: Filter1 = band-pass filter 250 – 395 nm; Filter 2 = band-pass filter 335 – 620 nm; a combination of Filter 2 and an additional 450 nm short-pass filter. When exciting with *e.g.* 370 nm the PL spectra of both the microscope glass slide as well as the defect-rich sample show significant differences in the emission recorded between 400 nm and 600 nm depending on the filter selected. Especially when Filter2 is selected the emission spectra show strong artefacts in the range 400 nm – 550 nm originating from the Xe flash lamp. However, at 600 nm the differences between the signals recorded with different filter setting are marginal indicating that artefacts have little or no influence in this wavelength range.

By inserting an additional 450 nm short-pass filter into the excitation beam the artefacts for wavelengths > 450 nm can be dramatically reduced. This leaves only a small wavelength range where artefacts can be present (395 nm – ca. 450 nm). This knowledge is essential when examining the entire emission spectra of a sample upon illumination with different excitation wavelengths, as has been done in Figure A1- 4. The near-band emission (NBE, left panel in Figure A1- 4) has been recorded using Filter1 and varying the excitation wavelength from 315 nm to 395 nm. Additionally the use of a 400 nm short-pass filter was found helpful in reducing the artefcts around 400 nm. Apart from the NBE associated with the band-band transition and recombination over shallow defects no additional radiative recombination processes could be observed, even when the sample was excited with $h\nu < E_G$ (385 nm and 395 nm).

The deep-level emission (DLE; right panel in Figure A1- 4) was recorded using Filter1 for excitation wavelengths between 315 nm and 365 nm. Thereafter Filter2 and an additional 450 nm short-pass filter have been used. For the latter filter setting a Xe flash lamp artifact is visible between 450 nm and 470 nm (see also Figure A1- 3 and related comments). However, the emission shape does not change until 375 nm and is clearly dominated by the orange emission. For 385 nm ($h\nu < E_G$) the orange emission is significantly reduced and diminishes when longer excitation wavelengths are used

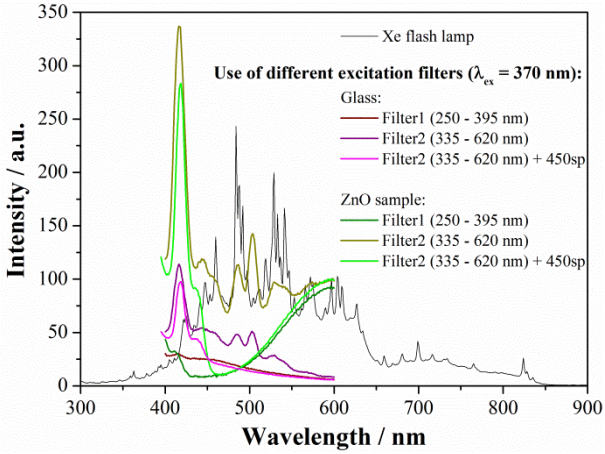

Figure A1- 3: Comparison of PL spectra recorded with different excitation filter settings showing strong influence of Xe flash lamp artefacts in dependence of the selected excitation filter. An additional 450 nm short-pass filter (450sp) has been used to examine the suppression of artefacts for wavelengths > 450 nm. Note that the artefact visible around 400 nm can be further reduced when an additional 400 nm short-pass is used to filter the excitation beam (not shown).

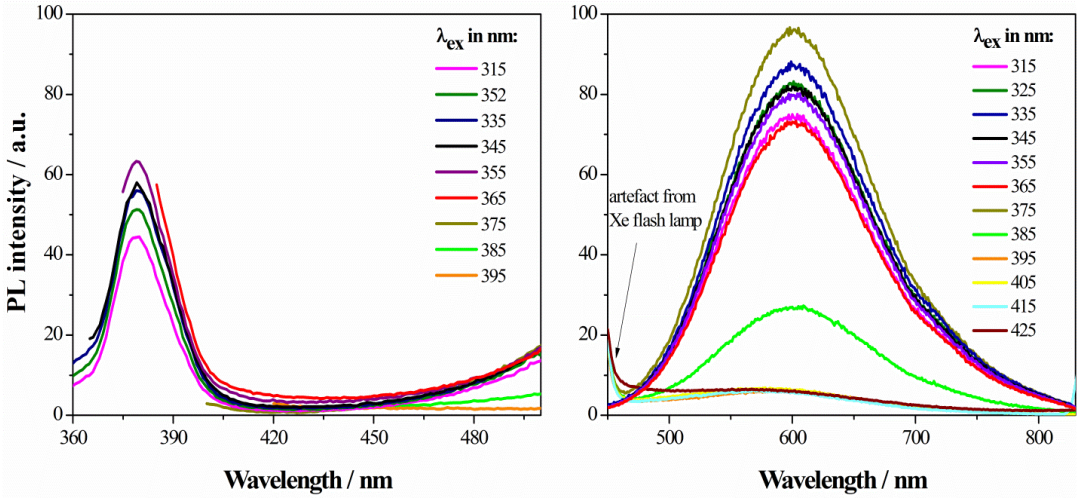

Figure A1- 4: Near-band emission (left; NBE) and deep-level emission (right; DLE) of defect-rich ZnO nanorod-arrays upon excitation with various wavelengths. Due to the excitation filter settings (see Figure A1- 3 and related comments) the NBE could only be examined until 395 nm (excitation Filter1). The DLE was recorded using excitation Filter1 until 365 nm and excitation Filter2 and a 450 nm short-pass filter from 375 nm onwards. For the latter filter settings Xe flash lamp artefacts are present at the beginning of the spectra (450 nm - 470 nm)

(≥ 395 nm). The emission shape of the spectra with hν < E_G does however not show any additional features.

It is important to note that when using a single excitation wavelength (345 nm in Chapter 3) the influence of artefacts is insignificant as the combination of the 250 –

395 nm band-pass excitation filter and the 360 nm cut-off emission filter (i.e. 360 nm long-pass filter) provides good control over unwanted reflections of the Xe flash lamp. Furthermore the effect of Xe flash lamp artefacts is also low when carrying out excitation PL measurements fixing the emission wavelength to 600 nm (as done in Figure 3-7 of Chapter 3). However, a minor influence in these measurements can stem from the characteristic intensity changes/peaks of the Xe flash lamp (e.g. 363 nm, 393 nm, 405 nm, 421 nm, 441 nm *etc*. – see Figure A1- 3).

References

[1] Y. K. Gaudy and S. Haussener, "Utilizing modeling, experiments, and statistics for the analysis of water-splitting photoelectrodes," *J. Mater. Chem. A*, vol. 4, no. 8, pp. 3100-3114, 2016.

[2] A. Nakamura, M. Sugiyama, K. Fujii, and Y. Nakano, "Comparison of Semiconductor–Electrolyte and Semiconductor–Metal Schottky Junctions Using AlGaN/GaN Photoelectrochemical Electrode," *Japanese Journal of Applied Physics*, vol. 52, no. 8S, p. 08JN20, 2013.

[3] J. Z. Bloh, R. Dillert, and D. W. Bahnemann, "Ruthenium-modified zinc oxide, a highly active vis-photocatalyst: the nature and reactivity of photoactive centres," *Physical Chemistry Chemical Physics*, vol. 16, no. 12, pp. 5833-5845, 2014.

[4] I. n. Mora-Seró *et al.*, "Determination of carrier density of ZnO nanowires by electrochemical techniques," *Applied Physics Letters*, vol. 89, no. 20, p. 203117, 2006.

[5] V. Sharma, M. Dixit, V. R. Satsangi, S. Dass, S. Pal, and R. Shrivastav, "Photoelectrochemical splitting of water with nanocrystalline Zn1−xMnxO thin films: First-principle DFT computations supporting the systematic experimental endeavor," *International Journal of Hydrogen Energy*, vol. 39, no. 8, pp. 3637-3648, 2014.

[6] D.-H. Kim, G.-W. Lee, and Y.-C. Kim, "Interaction of zinc interstitial with oxygen vacancy in zinc oxide: An origin of n-type doping," *Solid State Communications*, vol. 152, no. 18, pp. 1711-1714, 2012.

[7] A. Janotti and C. G. Van de Walle, "Native point defects in ZnO," *Physical Review B*, vol. 76, no. 16, p. 165202, 2007.

[8] Y.-S. Kim and C. H. Park, "Rich Variety of Defects in ZnO via an Attractive Interaction between O Vacancies and Zn Interstitials: Origin ofn-Type Doping," *Physical Review Letters*, vol. 102, no. 8, p. 086403, 2009.

Appendix 2: Supporting information for Chapter 4

Dye-degradation rates

The rate of dye-degradation k was estimated for each experiment from the first "light on" stage using the slope of the ln(C/C0) vs. t plot in this section. Where C is the dye concentration at a given time t. However, it is important to note that the exact surface area could not be determined. In turn, sample comparison based on the degradation rates are troublesome and should be avoided. Since each sample was measured multiple times (e.g. before and after RTA; surface area is equal) the change of the rates of a single samples is indeed meaningful and can be taken to evaluate changes of the photo-catalytic performance upon RTA. The dye-degradation rates determined for the samples shown in Figure 4-1b - d are presented in Table A2- 1 and for the samples of Figure 4-5 are listed in Table A2- 2. Additionally, the sample size (not surface area) of each sample is given below the sample name. As expected, the samples with smaller sample size exhibit a smaller degradation rate (e.g. compare the two RTA treated samples in). While in some cases (e.g. smooth layers) it may be appropriate to normalize the dye-degradation rates to the individual sample size, this approach is not followed here since it might evoke the impression that sample comparisons are then meaningful. In the present study these comparisons would only be meaningful if the exact surface area would be known.

Table A2- 1: Dye-degradation rates for samples from Figure 4-1b - d in Chapter 4. The size of each sample is given in brackets. However, this does not reflect the actual surface area - which could not be measured for the samples. The rates are given in h^{-1}.

Figure 4-1	**As-grown (2.13 cm^2)**	**RTA in O_2 450 °C (1.81 cm^2)**	**RTA in VAC 450 °C (2.10 cm^2)**
as-grown h.i. MB	-	-0.54	-0.71
MB h.i.	-0.80	-0.67	-0.93
MO h.i.	-0.30	-0.26	-0.29
MB l.i.	-0.58	-0.59	-0.81
Mo l.i.	-0.20	-0.14	-0.21

Table A2- 2: Dye-degradation rates for samples from Figure 4-5 in Chapter 4. The size of each sample is given in brackets. However, this does not reflect the actual surface area - which could not be measured for the samples. The rates are given in h^{-1}.

Figure 4-5	**RTA @ 350 °C (1.87 cm^2)**	**RTA @ 450 °C (2.06 cm^2)**	**RTA @ 550 °C (2.06 cm^2)**	**RTA in VAC @ 450 °C + O2 380 °C (2.13 cm^2)**
as-grown	-0.65	-0.79	-0.75	
RTA in VAC	-0.79	-1.03	-0.92	
RTA in VAC + O_2 380 °C	-0.69	-0.92	-0.77	-0.92

Action spectra of ZnO, MO and MB

Figure A2- 1 shows the absorbance spectra of a representative ZnO nanorod-array as well as the absorbance spectra of methylene blue and methyl orange (concentrations as given in Chapter 4). Methylene blue was taken for most photo-catalytic tests since it does not show significant absorption at 365 nm. Due to the small absorption at 365 nm methyl orange was mainly used to investigate the surface properties (e.g. charge) of the ZnO materials. However, in both cases the possible drawbacks associated with light absorbing dyes (see Chapter 4) could be dramatically minimized.

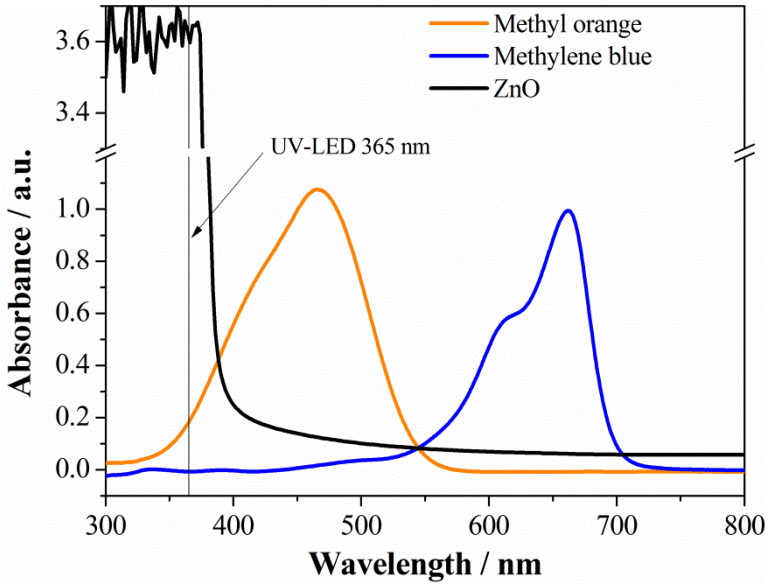

Figure A2- 1. Absorbance spectra of a representative ZnO nanorod-array and methylene blue and methyl orange (concentrations as given in Chapter 4).

Characterization of as-grown samples

Room-temperature PL, XRD and SEM measurements were carried out on as-grown samples. The examples shown in Figure A2- 2 represent the different sample sets used in the Chapter 4 and Appendix 2. They can therefore be seen as representative examples of all samples grown for this study. All PL spectra (normalized to their maximum) in the upper left panel of Figure A2- 2 exhibit two characteristic features. A near-UV peak centered at ca. 380 nm and a broad feature in the visible region centered at ca. 575 nm. The near-UV peak represents the near-band emission (NBE) originating from defect states close to the valence/conduction band and the band-band recombination. The broad PL emission in the visible region can be attributed to defect states as well as surface adsorbents (especially at around 575 nm). For further discussion on the nature of the PL features and the involvement of surface absorbents the reader is referred to an earlier study on similarly deposited samples.[1] Importantly the emission shape of all samples is similar and the spectra only differ in their intensity. This is an indication for comparable defect chemistry after the growth of the samples. Likewise the XRD spectra in the upper right panel of Figure A2- 2 confirm the comparability of the as-grown samples. For all samples only ZnO (JCPDS card No. 79-2205) related peaks were observed and the intensities of same are similar. The inset in the plot exemplifies this behavior on the basis of the (002) peak of the samples (note the absolute intensity given in counts). Since the (002) peak intensity is an indication for the alignment of the samples, it can be concluded that the as-grown nanorod arrays do not differ significantly structurally in terms of their alignment. Additionally the peak position of the (002) peak does not exhibit any significant shift between the samples, which is an evidence for the same level or stress/strain in the samples. Finally the SEM images in the lower part of Figure A2- 2 further confirm the XRD results in terms of the alignment of the rods. Furthermore it can be seen that the density, length and width is somewhat comparable with only a small variance between the samples. Overall it can be concluded that the samples presented in this study do not strongly differ regarding their structural and defect-chemical properties. This finding is crucial since, as mentioned in Chapter 4, the evaluation of the influence of a particular defect on the photo-catalytic properties demands as little as possible variance among these other material properties.

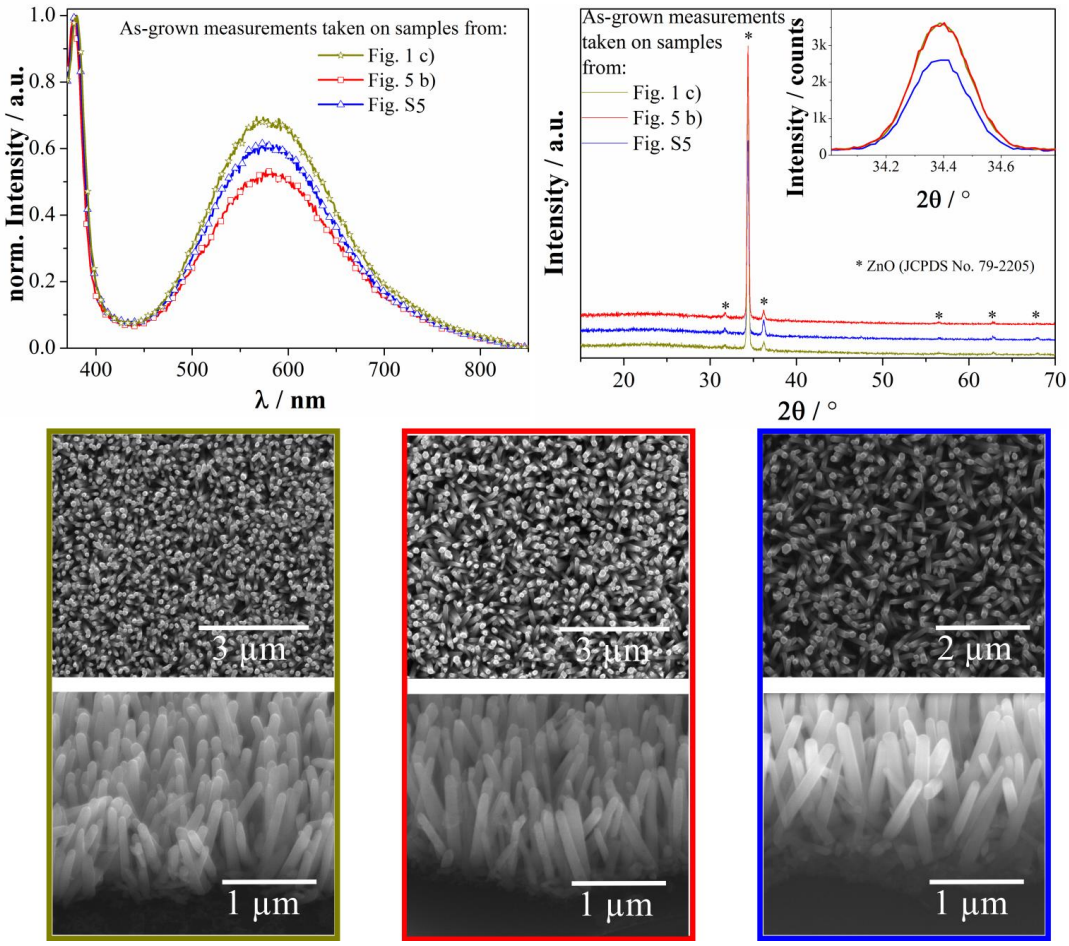

Figure A2- 2: Materials characterization of as-grown samples. The sample examples shown here are from different sample sets used in Chapter 4 and in the appendix. Upper left panel: room temperature PL measurements. Upper right panel: XRD spectra. The inset shows the dominating (002) peak magnified. The lower half shows the respective (color online) SEM top-view (upper row) and tilted view (40°) images for each sample.

Example of a fitted low-temperature PL spectrum

Figure A2- 3 shows a low-temperature PL spectrum of a ZnO NR array annealed in argon at 450°C. In order to de-convolute the NBE emission peak for the peak position of the FX_A and D_0X contribution, a part of the spectrum has been fitted with two Gaussian peaks. The resulting fit is shown in red and the two contributions can be recognized in green and blue. A good fit (red curve) to the sample DLD-related emission can be achieved using three Gaussian peaks centered at around 2.4 eV, 2.2 eV and 1.9 eV. Based on the area of the peaks the 1.9 eV peak accounts for more than 90 % of the total DLD intensity. It is important to note that the annealing atmosphere is different to the RTA atmospheres presented in Chapter 4. This was done

in order to show that the orange emission, which is only observed that clearly at annealing temperatures around 450 °C, is independent of the RTA atmosphere (see also Figure A2- 5 for RTA in forming gas).

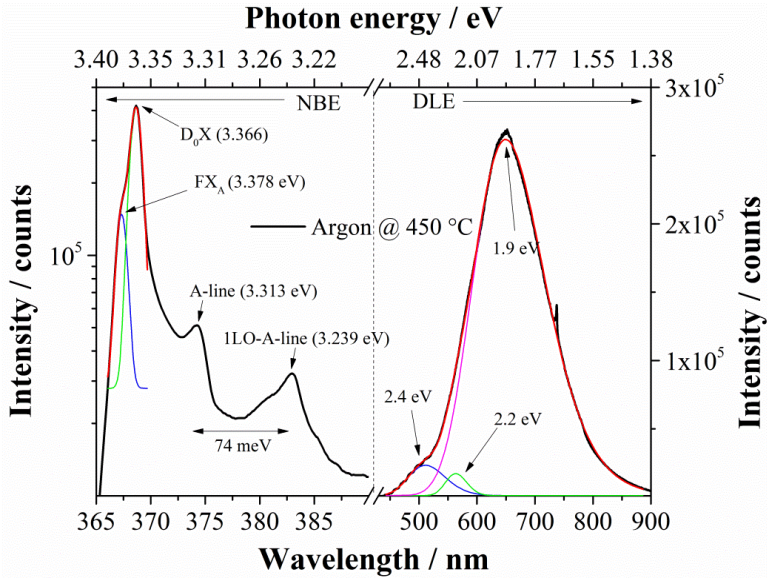

Figure A2- 3. Low temperature PL spectrum with de-convoluted NBE and DLD emission (DLE) of a ZnO NR array annealed in argon at 450°C.

XPS spectrum of an orange-luminescent ZnO NR array

A typical XPS spectrum (survey scan and high-resolution O 1s and C 1s scans) of an annealed ZnO NR array is shown in Figure A2- 4. The spectrum was taken after prolonged (300 s) argon bombardment in order to minimize the influence of naturally occurring carbon contaminations. A strong carbon response (17.5 %at) is nevertheless still visible after the argon bombardment. This finding supports the hypothesis that the nanorods are indeed carbon rich. The C 1s peak is hereby found to exhibit three components which may arise from “free” carbon or carbon from a graphitic structure (C 1s_1), carbon that may be attributed to doping (C 1s_2) and carbon residues from the growth process (C 1s_3). Additionally it is worth pointing out the high oxygen deficiency, visible due to the big shoulder towards the high binding energy end of the O 1s peak. For further discussion of the peaks and XPS analysis of samples annealed in different atmospheres and temperatures the reader is referred to Ref [1].

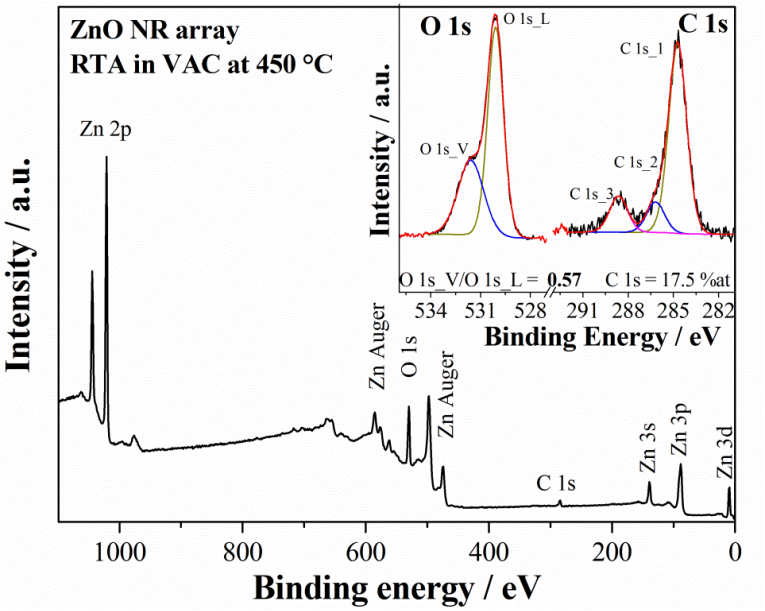

Figure A2- 4: XPS spectrum of a ZnO NR array annealed in vacuum at 450 °C. The inset shows the high-resolution scans of the O 1s and C 1s peaks. Adapted from Ref [1] by permission of the PCCP Owner Societies.

Influence of long-term annealing and RTA in forming gas on the structural and PL properties of ZnO NRs

Recently Bora et al. reported an increase of PL emission in the range 500 – 600 nm upon annealing of ZnO NRs in air at 250 °C.[2] They attributed the rise of the defect-related PL in this range (especially green) to the diffusion of oxygen vacancies towards the rod-surface. In Figure A2- 5 high-resolution XRD patterns and PL spectra (a) and b), respectively) of a sample subject to an annealing sequence are presented. The annealing sequence consisted of long-term annealing in air prior and after a RTA step in forming gas at 450 °C. The initial long-term annealing lead to an increase of the NBE peak centered around 380 nm (e.g. improved band-band recombination) and to a reduction of the defect-related emission in the range 500 – 600 nm alongside with a shift of the broad peak-centre from 575 nm to ca. 590 nm. The overall reduction of the defect emission upon annealing at 250 °C is believed to stem from the removal of surface adsorbents.[1, 3] An increase of the emission as observed by Bora et al. could not been detected. However, this does not mean that the diffusion of oxygen vacancies towards the surface did not occur. In fact the peak shift towards longer wavelengths may indicate this process. For the samples presented here it is thus likely that both, the

desorption of surface-groups and the diffusion of oxygen vacancies, occur as a result of long-term annealing in air. It is also important to note that annealing in air for 1h at 250 °C (not shown) led to a comparable emission pattern as presented here. In turn it can be concluded that the duration during the long-term annealing at 250 °C has no significant influence on the intensity of the defect emission and does not lead to strong orange emission centred around 600 nm.

The RTA step then increases the NBE further and leads to the appearance of strong orange emission (please refer to Ref [1] for discussion, especially in regards to the increases NBE upon RTA in forming gas). These characteristic features are also observed for a sample that was not subjected to a long-term annealing step prior to RTA (black traces in Figure A2- 5). These results further confirm the discussion in Chapter 4 and regarding Figure A2- 3, which find the appearance of strong orange emission annealing atmosphere independent. If the NRs are then annealed in air at 250 °C for 8 h (pink traces) the overall emission (NBE + DLD) is further increased. Here it is important to point out that the orange emission still remains after this treatment (i.e. the emission is stable and the responsible defects cannot be annealed out or saturated). Finally the long-term low temperature annealing treatments before/after RTA further confirm a possible temperature-dependent kinetic defect-formation mechanism, as presented and discussed in detail in Ref [1].

Importantly, the RTA treatment does not have significant influence on the structural properties of the samples. This is revealed by the XRD patterns in Figure A2- 5a as well as the insets (SEM micrographs) in Figure A2- 5b. The peak position for example changes only very little upon the annealing treatments. As a result, the lattice parameters a and c calculated after each annealing step differ only slightly from each other. Furthermore the lattice parameters of the annealed samples move closer to the parameters of the JCPDS reference card no. 79-2205, which is an indication of improved crystal quality and thus reduced strain in the film. Also the calculated crystallite sizes are comparable (calculated from the (101) peak using the Scherrer equation). The insets of Figure A2- 5b show the same spot on the sample subjected to the annealing sequence before and after RTA. These images reveal that the structure also does not change significantly on a microscopic level (e.g. the overall surface area of a sample can be expected to be comparable before and after RTA).

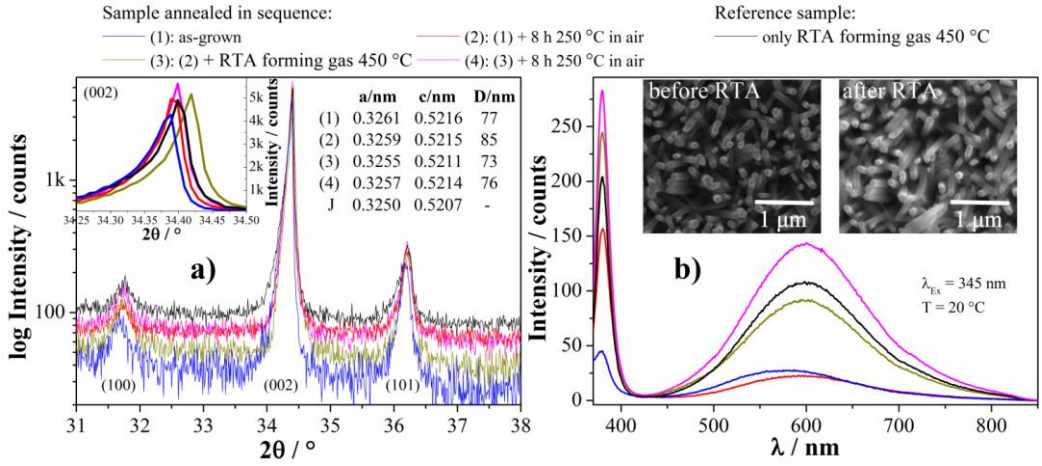

Figure A2- 5: High-resolution XRD patterns (a)) and room-temperature PL spectra (b)) of a sample subjected to an annealing sequence (first 8h 250 °C, then RTA in forming gas at 450 °C and lastly 8h 250 °C). The inset in a) magnifies the (002) XRD peak. Additionally the lattice parameters (a and c) and the crystallite size D of the sample subjected to the annealing sequence are given in a). Please note that "J" stands for the lattice parameters obtained from the JCPDS reference card no. 79-2205. The high-resolution XRD patterns were recorded as 2θ-ω scans. The insets in b) are SEM micrographs of the same spot on the sample before and after the RTA step.

Temperature dependent PL measurements

Figure A2- 6 shows the temperature dependent PL measurements (left panel) of a ZnO NR array sample which had been annealed at 450 °C in vacuum. Both the NBE- and DLD-emission (DLE) related peak intensities increase with decreasing temperature. Furthermore a shift of the peak positions of the NBE peaks is visible. These shifts and the change of the intensity as a function of the inverse temperature (Arrhenius) have been analyzed in the right panel of the figure. Based on the Arrhenius fit of the data the activation energy E_A for the orange-luminescent defect centre is estimated to be 7.9 meV. For the NBE peaks the centre positions decrease (red shift) with increasing temperature. For the A-line the recorded peak intensity-values were also thermally corrected ($E_{A\text{-line}} - k_BT/2$) in order to evaluate the possibility of a free-to-bound (FB) origin of this emission.[4] A similar slope compared to the FX_A would thus be an indication for a FB transition. However, also after correcting the data the peak position of the A-line shifts significantly less than the FX_A transition (17.2 meV and 21.4 meV, respectively; between 11.5 K and 120 K).

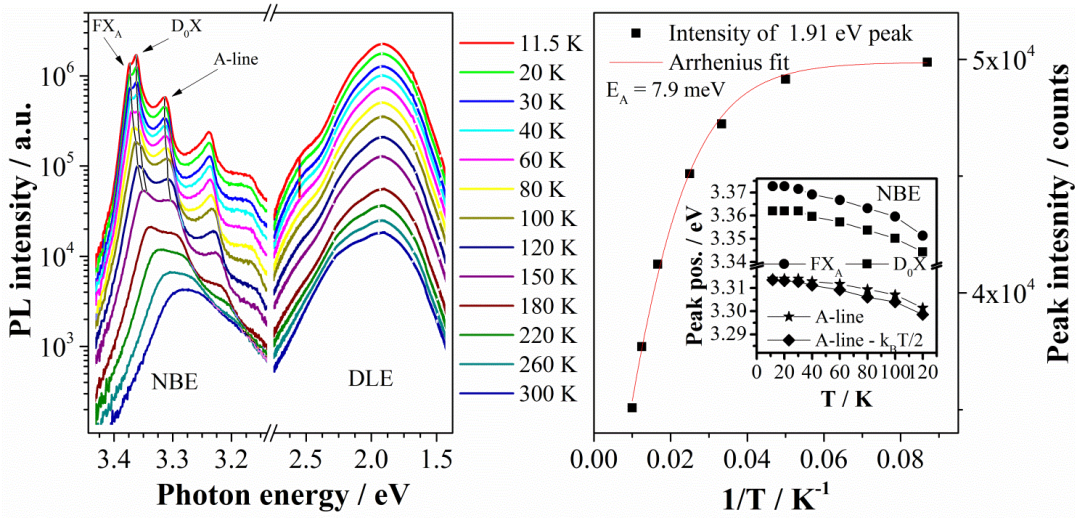

Figure A2- 6. Left) Temperature dependent PL spectrum of a ZnO NR array annealed at 450 °C in vacuum (color online; spectra have been offset for better visibility). Right) Arrhenius plot for the 1.91 eV peak in the temperature range 11.5 K – 100 K. The inset shows the peak positions for the characteristic features in the NBE peak (i.e. FX_A, D_0X and A-line) as a function of temperature.

Integrated PL intensity and PL peak position of the orange emission (1.9 eV) as a function of the inverse temperature

Figure A2- 7 shows the integrated PL intensity and PL peak position of the orange emission (1.9 eV) as a function of the inverse temperature. A typical decrease of the intensity with increasing temperature has been observed. No negative thermal quenching (NTQ) – as observed for the DLD emission of ZnO by others[5, 6] – of the

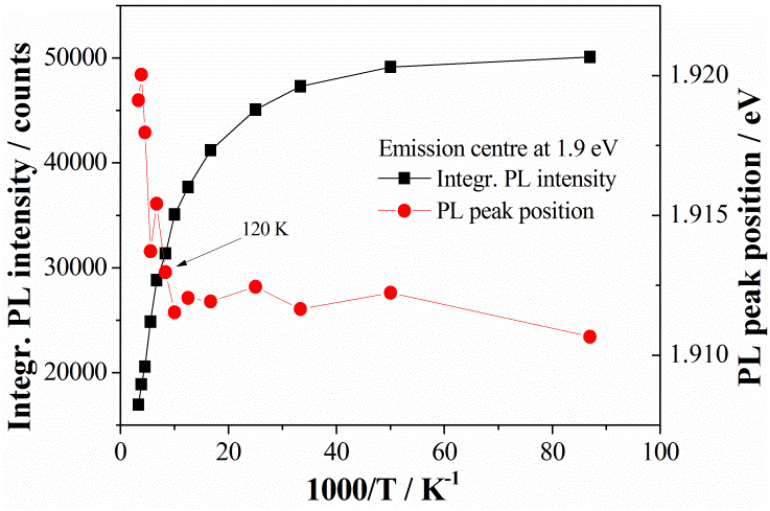

Figure A2- 7. Integrated PL intensity and PL peak position of the orange emission (1.9 eV) as a function of the inverse temperature.

PL intensity could be detected. The peak position of the 1.9 eV emission shows a blue-shift at elevated temperatures (> 100 K). At lower temperatures (< 100 K) the peak position does not change significantly. The sudden shift of the peak position may be an indication of a transition from donor-acceptor to a free-to-bound recombination.

Rate of dye-degradation of an orange-luminescent ZnO NR array in MO – influence of cross-annealing in oxygen

The rate of dye-degradation was evaluated for a sample annealed in vacuum at 450 °C (trace (2)) and subsequent cross-annealing in oxygen at 380 °C (trace (3)) and is depicted in Figure A2- 8 . Methyl orange was used as a dye and the catalytic experiments were performed under low intensity UV-irradiation (1 mW/cm^2). The dye-degradation rate is strongly improved after RTA in vacuum at 450 °C (induction of orange-luminescent defects). However, similarly to the dye-degradation curves in Chapter 4, cross annealing in oxygen leads to a slower dye-degradation. Nevertheless an overall improvement of the dye-degradation rate (compare (1) and (3)) is still observed for this sample. The inset magnifies the change of the dye concentration during the first dark stage (10 to 100 min). No significant dark dye-adsorption could be observed. In this regard it can be expected that possible synergetic effects, which a strong dye-adsorption could present for the dye-degradation, do not exist. Hence, the improved dye-degradation is more likely to be somewhat correlated to the defects induced during RTA (i.e. mainly orange-luminescent defects). The slight decrease of the dye-degradation rate upon cross-annealing in oxygen might indicate that oxygen vacancies could be involved to some extend as well (see discussion in Chapter 4). However, since annealing in oxygen also leads to an improved dye- degradation rate (see. Figure 4-1c in Chapter 4) this contribution is believed to play a minor role.

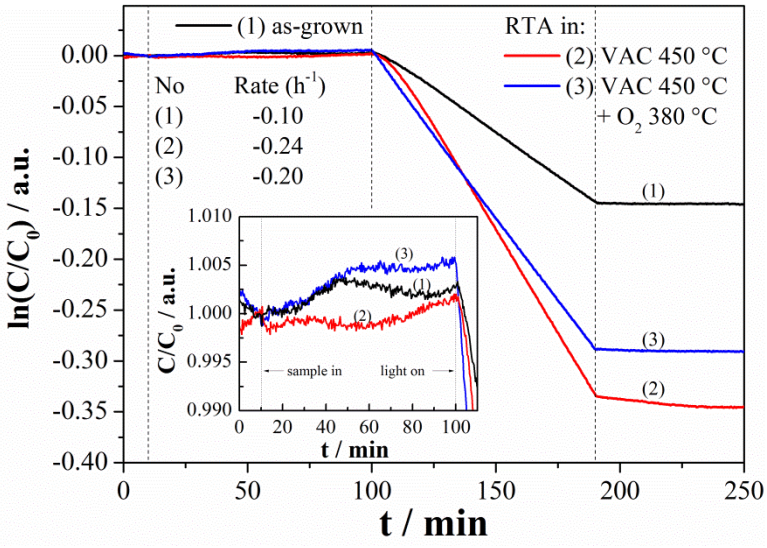

Figure A2- 8. Determination of the rate of dye-degradation for a sample annealed in vacuum at 450 °C (trace (2)) and subsequent cross-annealing in oxygen at 380 °C (trace (3)). Methyl orange was used as a dye and the catalytic experiments were performed under low intensity UV-irradiation (1 mW/cm^2). Sample size = 1.74 cm^2.

Experimental methods

UV-Vis diffuse-spectroscopy was conducted using a Shimadzu UV-2401PC spectrometer (range 300–800 nm). A Cary Eclipse spectrophotometer was used to record room-temperature PL spectra (excitation wavelength = 345 nm, interval = 1 nm). XRD spectra were taken using a Panalytic X'Pert X-ray diffractometer (Cu Kα radiation λ = 0.1541874 nm). The high-resolution XRD patterns presented in Figure A2- 5 were recorded in a triple-axis experiment as 2θ-ω scans (step size = 0.01°). For calculation of lattice constants and crystallite size the raw peak data was analyzed. XPS measurements were performed (after prolonged argon sputtering of 300 s) using a Kratos Axis ULTRA spectrometer equipped (monochromatic Al Kα radiation, energy 1486.6 eV; performed at University of Limerick) – see Ref [1].

References

[1] J. Kegel, F. Laffir, I. M. Povey, and M. E. Pemble, "Defect-promoted photo-electrochemical performance enhancement of orange-luminescent ZnO nanorod-arrays," *Phys Chem Chem Phys*, vol. 19, no. 19, pp. 12255--12268, 2017.

[2] T. Bora, P. Sathe, K. Laxman, S. Dobretsov, and J. Dutta, "Defect engineered visible light active ZnO nanorods for photocatalytic treatment of water," *Catalysis Today*, vol. 284, pp. 11-18, 2017.

[3] A. B. Djurišić *et al.*, "Defect emissions in ZnO nanostructures," *Nanotechnology,* vol. 18, no. 9, p. 095702, 2007.
[4] Q. X. Zhao, M. Willander, R. E. Morjan, Q. H. Hu, and E. E. B. Campbell, "Optical recombination of ZnO nanowires grown on sapphire and Si substrates," *Applied Physics Letters,* vol. 83, no. 1, pp. 165-167, 2003.
[5] H. He, Q. Yang, C. Liu, L. Sun, and Z. Ye, "Size-Dependent Surface Effects on the Photoluminescence in ZnO Nanorods," *The Journal of Physical Chemistry C,* vol. 115, no. 1, pp. 58-64, 2011.
[6] L. Hu *et al.*, "Dual-donor (Zn(i) and V(O)) mediated ferromagnetism in copper-doped ZnO micron-scale polycrystalline films: a thermally driven defect modulation process," *Nanoscale,* vol. 5, no. 9, pp. 3918-30, 2013.

Appendix 3: Supporting information for Chapter 5

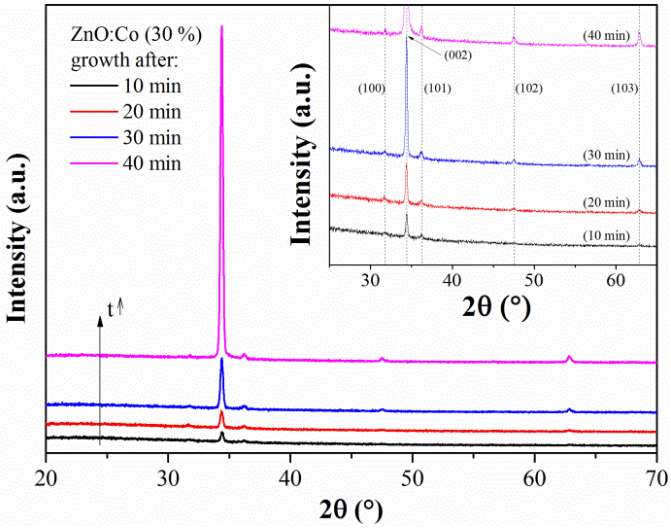

Figure A3- 1: XRD spectra of ZnO:Co nanorod-arrays with 30 % Co/Zn concentration ratio in the growth solution measured at different stages of the growth process. Inset: magnified view on the range 2θ = 25 - 65°. For all samples only ZnO related XRD peaks were detected.

Appendix 4: Supporting information for Chapter 6

Additional growth/XRD experiments designed to resolve the nature of a detected secondary phase

Figure A4- 1 shows the XRD spectra of undoped ZnO NR arrays grown to help evaluate the nature of the material deposited from the appearance of the peaks visible at angles of 2θ ca. 31°, 32.9° and 37.7°. Firstly, one sample was grown using the recipe outlined in the methods section (green trace) but with another OH^- precursor (4M KOH). Secondly, a sample was synthesized using the method outlined in the methods section but without addition of MEA and with double the precursor concentration. Lastly, ZnO NRs deposited from zinc nitrate (ZnN) instead of ZnAc and without the addition of MEA (precursor concentrations were also doubled). For all spectra in Figure A4- 1 the ZnO (002) peak is the dominant XRD feature. However, additional smaller features were recorded at the angles mentioned above and additionally at 37.1°. Interestingly the appearance of these peaks is independent of the addition of MEA and of the OH^- source (NaOH or KOH) or zinc precursor used. In turn, this excludes MEA as well as carbon (growth from ZnN + NaOH is carbon free) as being responsible for the observed secondary phases. Also it is important to note that the recorded peaks are observed for both NaOH and KOH as OH^- sources.

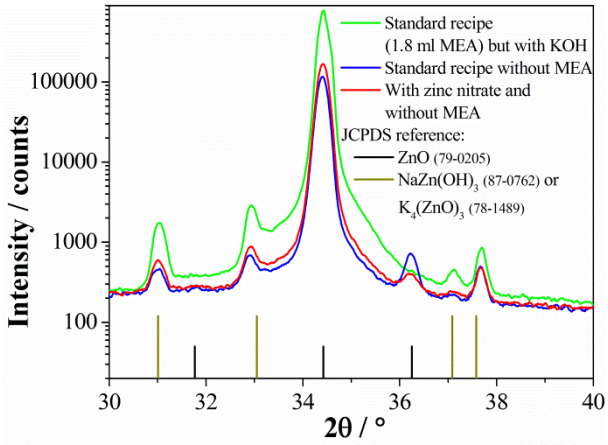

Figure A4- 1: XRD spectra of undoped ZnO NR arrays grown from: green trace) the recipe outlined in the methods section but with 4M KOH instead of 4M NaOH; blue trace) the recipe outlined in the methods section but without the addition of MEA; red trace) a zinc nitrate (ZnN) precursor and NaOH. Please note that for the latter two growths the concentrations were doubled (e.g. 0.1 M ZnAC/ZnN and 15 ml NaOH) in order to evaluate possible changes due to higher precursor availability. However, no significant effect on the XRD patterns has been observed.

However, additional phases that could exists from these growth experiments, such as $NaZn(OH)_3$ and $K_4(ZnO)_3$ (JCPDS references 87-0762 and 78-1489, respectively), both have peaks at the 2θ angles mentioned. Hence, it is believed that under the growth conditions presented (hydrothermal and strong alkaline) the formation of these phases may occur and this in turn leads to the recorded XRD pattern. Furthermore it is important to note that the intensity of the peaks is somehow correlated to the alignment of the NRs. It has been observed that better aligned samples (i.e. stronger (002) response as compared to the other planes) also exhibit stronger responses of the secondary peaks. The peaks also remain after annealing.

Top-view SEM images of samples subjected to a second growth stage (2GS)

Figure A4- 2 shows the top-view images (overview and detail) of the samples subjected to a second growth stage (2GS; refer to Figure 6-4 for tilt-view SEM images). Additionally, SEM images of a sample grown with $R_{MEA/M} = 3$ in a 100 ml autoclave (all other samples grown in 200 ml autoclave) are included in the figure. For samples grown from a high MEA concentration the 2GS leads to the formation of larger surface structures on the top of the rods (see overview images). These structures are believed to be $Co(OH)_2$. The density and size of these surface structures scales with the deposition time. A dense coverage of the rod tips is only observed for the sample for which the 2GS had a duration of 4.5h.

This is in contrast to the samples grown from a low MEA concentration ($R_{MEA/M} = 3$). Here the rod-tips are already densely covered with a thick Co_3O_4 over-coating after 1.5 h. Furthermore, the $R_{MEA/M} = 3$ samples do not show larger structures on the sample surface. However, when the synthesis is performed in a 100 ml autoclave, instead of in a 200 ml autoclave, surface structures can be observed (see bottom line of Figure A4- 2). This growth behaviour is in line with the proposed growth mechanism, where the available oxygen during the second growth stage may be in competition with the reduction of Co^{3+} to Co^{2+}. A lower oxygen volume in the autoclave (i.e. 50 ml air volume instead of 150 ml) would favour the reduction of Co^{3+} to Co^{2+} rather than the formation of CoOOH. Hence, it is possible to obtain over-coatings that may contain both $Co(OH)_2$ and Co_3O_4.

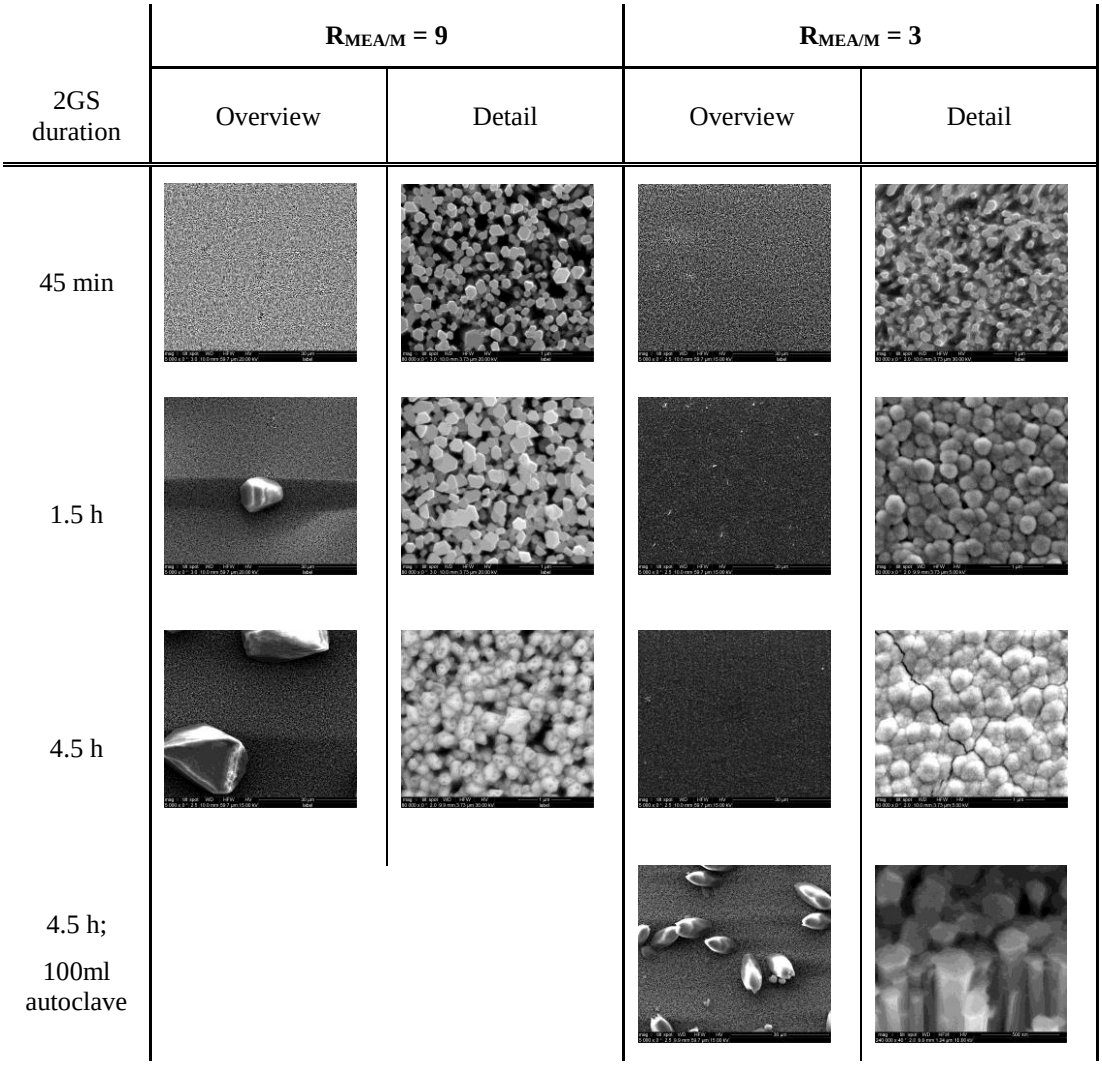

Figure A4- 2 SEM top-view images of samples subjected to a second growth stage (2GS; 150 °C). The samples were grown from varying MEA concentrations ($R_{MEA/M}$ = 9 or 3) and the duration of the 2GS was 45 min, 1.5 h or 4.5 h. Furthermore, one sample was grown in a 100 ml autoclave (all other growths in 200 ml autoclave). Overview and detail images were taken at a magnification of x5k and x80k, respectively (detail of 4.5 h in 100 ml autoclave at x240k).

Description of the starting conditions and proposed nanorod growth during the 1GS

Using the growth recipe presented in Chapter 6, the solution prior to heating may be described as follows. The dissolution of the cobalt- and zinc acetate results in the presence of hexaaquazinc (II) and hexaaquacobalt(II) ions. However, in order to simplify matters the water molecules are omitted hereafter, leading to the following equations (A4.2) and (A4.3):

$$Zn(CH_3COO)_2 \rightarrow Zn^{2+} + 2CH_3COO^- \quad \text{(A4.2)}$$

$$Co(CH_3COO)_2 \rightarrow Co^{2+} + 2CH_3COO^- \quad \text{(A4.3)}$$

If NaOH is added to the metal salt solution the respective metal hydroxides form (eq. (A4.4-A4.9)):

$$Zn^{2+} + 2OH^- \leftrightarrow Zn(OH)_2 \quad \text{(A4.4)}$$

$$Zn(OH)_2 + OH^- \leftrightarrow [Zn(OH)_3]^- \quad \text{(A4.5)}$$

$$Zn(OH)_2 + 2OH^- \leftrightarrow [Zn(OH)_4]^{2-} \quad \text{(A4.6)}$$

$$Co^{2+} + 2OH^- \leftrightarrow Co(OH)_2 \quad \text{(A4.7)}$$

$$Co(OH)_2 + OH^- \leftrightarrow [Co(OH)_3]^- \quad \text{(A4.8)}$$

$$Co(OH)_2 + 2OH^- \leftrightarrow [Co(OH)_4]^{2-} \quad \text{(A4.9)}$$

When the pH > 13 (here ca. 13.6) the most probable metal species have been reported to be tetrahedral $[Zn(OH)_4]^{2-}$ and octahedral $Co(OH)_2$ and/or $[Co(OH)_3]^-$ (note the omission of water molecules).[1-4] Immediately after the NaOH is added to the metal salt solution the color changes from pink to blue, indicating the formation of α-$Co(OH)_2$. Upon stirring of the solution the more stable β-$Co(OH)_2$ is formed. This was visible due to a gradual color change to a rose/pale pink slurry (complete after ca. 5 min).[4] Furthermore, another very slow color change to brown was noticed when stirred for 24 h. In strong alkaline solutions Co(III) is more stable and thus the formation of the brown cobalt(III) oxy-hydroxide (CoOOH) is favoured.[5-8] Likewise, the brown cobalt(III)oxide-hydrate ($Co_2O_3 \cdot nH_2O$) may be formed upon prolonged stirring due to reaction with dissolved oxygen.[6] However, at the time when MEA is added to the solution (1.5 min) the formation of significant amounts of CoO(OH) and/or $Co_2O_3 \cdot nH_2O$ is unlikely. Also a colour change back to blue (without addition of MEA; indicative of $[Co(OH)_4]^{2-}$) could not be observed after prolonged stirring. Furthermore, no back-reaction of $[Zn(OH)_4]^{2-}$ to $Zn(OH)_2$(s) occurred (white precipitation), which can be attributed to the high alkalinity.

Upon addition of MEA to the solution MEA-metal complexes are formed of the type ($[Zn(MEA)_m]^{2+}$ and ($[Co(MEA)_m]^{2+}$).[5, 9] Additionally, the excess of OH^- groups may also enable the formation of MEA-Co-OH ($[Co(MEA)_m(OH)_x]^{2-x}$) complexes,

which has also been observed by others.[10] In the case of cobalt, the complex formation goes in conjunction with a change of the oxidation state from (II) to Co(III) and accompanying color change to black (faster with higher MEA concentration).[5, 6]

During the first stage, ZnO:Co nanorod growth occurs upon heating the solution to a low temperature (here 90 °C). In addition to any free $[Zn(OH]_4]^{2-}$, the Zn-MEA complex releases Zn^{2+} into the solution (A4.10), forming more $[Zn(OH)_4]^{2-}$ following equations (A4.4-A4.6). The $[Zn(OH)_4]^{2-}$ growth units then lead to the ZnO deposition (A4.11):

$$[Zn(MEA)_m]^{2+} \leftrightarrow \ Zn^{2+} + mMEA \tag{A4.10}$$

$$[Zn(OH)_4]^{2-} \ \leftrightarrow ZnO + 2OH^- + H_2O \tag{A4.11}$$

The nanorod growth appears along the c-axis of the wurtzite ZnO crystal. This implies an increased growth rate along the polar basal plane ((002)). While $[Zn(OH]_4]^{2-}$ contributes to the growth along [002] direction due to its preferred adsorption on the surface of the ZnO nuclei,[9, 11] it was also suggested that growth on the alternatingly Zn^{2+} or O^{2-} terminated (002) plane involves the formation of ZnO_2^{2-} from the $[Zn(OH)_4]^{2-}$ growth units, with fast adsorption of these groups onto the basal plane (A4.12-A4.14):[3, 12]

$$[Zn(OH)_4]^{2-} \ \leftrightarrow {ZnO_2}^{2-} + 2H_2O \tag{A4.12}$$

$${Zn^{2+}}_{surface} + \ {ZnO_2}^{2-} \leftrightarrow 2ZnO \tag{A4.13}$$

$${O^{2-}}_{surface} + \ {ZnO_2}^{2-} + 2H_2O \leftrightarrow ZnO + 4OH^- \tag{A4.14}$$

In regards to the growth-directing role of MEA, somewhat competing mechanisms may be involved: When the MEA concentration is high, the likelihood of the MEA (as a polar molecule) interacting with/adsorbing to the basal plane of the ZnO crystal is increased. Thus, the adsorption of the precursor molecules ($[Zn(OH)_4]^{2-}$ and ZnO_2^{2-}) and subsequent growth along the c-axis may be hindered. However, MEA is reported to exhibit a sol stabilizing function.[13, 14] Hence, a high MEA concentration in the solution may also favour the slower formation of $[Zn(OH)_4^{2-}]$ growth units due to a more controlled release of Zn^{2+}. In turn, this could result in less ZnO precipitating out

of the solution, enhancing the possibility of the rod formation. Finally, the combination of both effects may contribute to the observed lengthening and thickening of the rods.

Other potential influences on the growth of $Co(OH)_2/Co_3O_4$ decorated ZnO:Co nanostructures

Despite MEA`s crucial role during the growth of the $Co(OH)_2/Co_3O_4$ decorated ZnO:Co nanostructures other factors may influence the growth as well. The high alkalinity, for example, does increase the reduction capacity of the solution.[7] Hence higher NaOH concentrations could in turn lead to more favourable $Co(OH)_2$ deposition conditions. Also the initial cobalt acetate concentration has an influence on the growth of $Co(OH)_2/Co_3O_4$ decorated ZnO:Co nanorods. During the first growth stage the amount of cobalt in the films may scale with the initial cobalt acetate concentration in the solution.[15] Since the deposition of $Co(OH)_2/Co_3O_4$ happens fast, a lower cobalt acetate concentration could allow a more controllable deposition of smaller/thinner structures during the second growth stage. Furthermore, additional growth experiments revealed that the length of the rods – and therefore the overall visible light absorption – can be influenced by changing the metal precursor concentration, with higher concentrations leading to longer rods (while keeping the metal/OH^- ratio as well as the MEA concentration constant), somewhat similar to the results of a recent study.[16] Also the seed-layer was found to influence these structural parameters.

Cyclic voltammetry of ZnO/ZnO:Co and ZnO/ZnO:Co-$Co_3O_4/Co(OH)_2$ structures in ferri/ferrocyanide

In addition to the CV scans presented in Chapter 6, voltammograms were also recorded in ferro/ferricyanide (aqueous solution of 10 mM potassium ferricyanide and 10 mM potassium ferrocyanide trihydrate in 1 M potassium chloride). These measurements were performed immediately after the CV and EIS experiments in 1 M KOH (after thorough rinsing of the cell with Millipore H_2O) on the same measurement spot. The CV scans were recorded at a scan rate of 50 mV/s and a step size of 5 mV in a potential window of -0.2 V – 0.7 V vs. Ag/AgCl.

Figure A4- 3 shows voltammograms of ZnO/ZnO:Co and ZnO/ZnO:Co-$Co_3O_4/Co(OH)_2$ structures recorded in ferro/ferricyanide solution. Whereas the as-

grown samples show no clear Fe^{2+}/Fe^{3+} redox features, annealing leads to the appearance of same. Since the Fe^{2+}/Fe^{3+} redox-couple can be readily oxidized/reduced these measurements can aid the evaluation of how good the electrode is in terms of charge transfer. In the ideal case (completely reversible) the peak-to-peak splitting of the Fe^{2+}/Fe^{3+} redox-couple would be 59 mV. For the electrodes presented here, the redox features are either absent (no annealing) or exhibit a peak-to-peak of ca. 140 mV +-10mV (after annealing; note that this is independent of the presence/absence of a cobaltic coating). The discrepancy from the ideal case is the manifestation of additional resistances/impedances on the current path.[17] Under the assumption that the charge transfer resistance at the electrolyte interface is not rate limiting (i.e. fast oxidation/reduction of the Fe^{2+}/Fe^{3+} redox-couple), losses inherent to the charge transfer within the structure may be responsible for an increased peak-to-peak splitting. For example, Scheuermann et al. observed an increasing peak-to-peak splitting for $Si/SiO_2/TiO_2/Ir$ photo-anodes scaling with the TiO_2 thickness, which they attributed to an increasing impedance of the TiO_2 layer.[17, 18] In this respect, the electrode quality

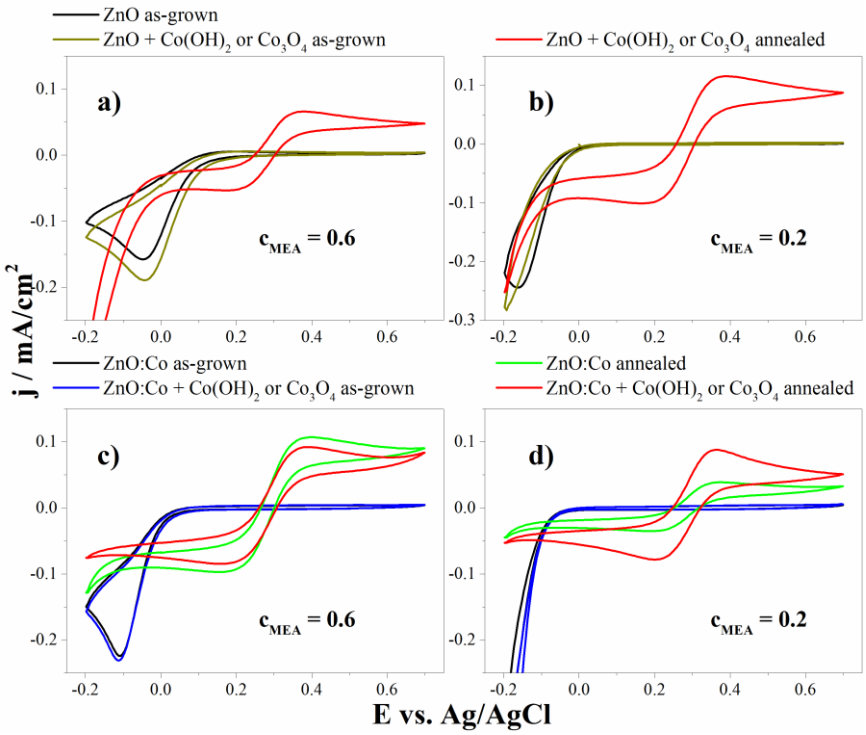

Figure A4- 3. Cyclic voltammograms in ferro/ferricyanide solution of a) and b) undoped ZnO NR arrays without/with $Co(OH)_2$ or Co_3O_4 over-growth, respectively; c) and d) cobalt doped ZnO:Co NR arrays without/with $Co(OH)_2$ or Co_3O_4 over-growth, respectively. Annealing was carried out at 400 °C for 3h. The scan rate was 50 mV/s.

may be expected as rate determining here. Hence, the absence of the Fe^{2+}/Fe^{3+} redox features for as-grown samples, may be indicative of a relatively poor electrode quality and charge transfer within the structures. This may result from e.g. recombination processes over defect states. Annealing of the samples dramatically improves the charge carrier transport within the structures, probably by improving the overall quality of the films. In turn a higher density of charge carriers can be expected at the interface. These are then available to participate in the Fe^{2+}/Fe^{3+} redox-reactions.

Bode plots of annealed decorated/undecorated ZnO:Co NR arrays grown from c_{MEA} = 0.6

Figure A4- 4 shows the Bode plots of the annealed decorated/undecorated ZnO:Co NR arrays samples grown from c_{MEA} = 0.6 ($R_{MEA/M}$ = 9). These correspond to the Nyquist plots presented in Figure 6-8c. While the discussion regarding the Nyquist plots is mainly focused on the overall charge transfer resistance of the structures, the representation of the data in the Bode plot allows a more distinguished interpretation of charge transfers at different time scales. Focusing on the undecorated ZnO:Co NR array first (black traces), it is recognized that the phase spectra consists of one main peak slightly stretched toward higher frequencies (ca. 10^3 Hz) and a rather small additional capacitive component at high frequencies (> 10k Hz). In contrast, the

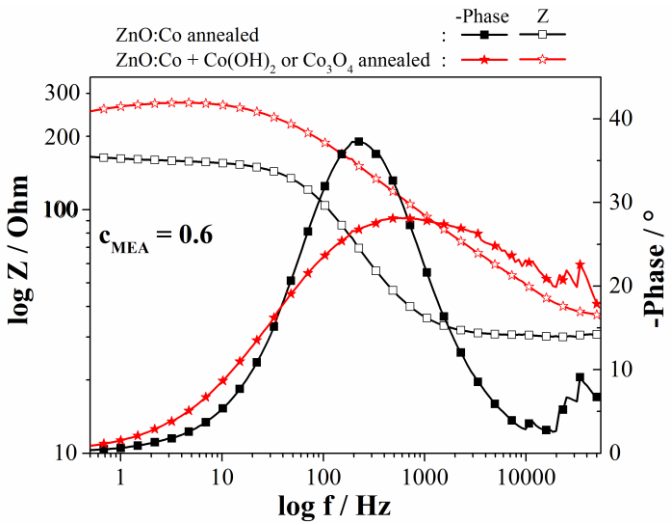

Figure A4- 4. Bode plots of annealed decorated/undecorated ZnO:Co NR arrays grown from c_{MEA} = 0.6 ($R_{MEA/M}$ = 9). Annealing was carried out at 400 °C for 3h – please note that $Co(OH)_2$ (decoration of the as-grown sample) was thus converted to Co_3O_4.

decorated ZnO:Co NR array (red traces) exhibits a broad feature over the high- and mid-frequency range. Since the processes involved in the oxygen evolution reaction at the semiconductor-electrolyte interface are relatively slow, the main peak seen for the undecorated sample can be assigned to this charge transfer (ca. f < 200 Hz). On the other hand, the capacitive components at higher frequencies are fingerprints of charge transfers taking place within the structures (e.g. NR-seed layer interface, NR-Co_3O_4 interface). It is in this frequency domain where the Bode plot reveals significant losses for the decorated ZnO:Co NR array, resulting in a higher impedance and pointing towards a higher internal recombination rate. However, when focusing on the mid-frequency domain it becomes visible that the phase – and therefore the capacitance of the sample – is lower than that obtained from the undecorated sample. This may imply a smaller charge build up at the interface and thus indicate improved charge mitigation over the semiconductor-electrolyte interface as a result of the catalytic over-coating.

CV and EIS measurements for ZnO:Co NR arrays grown with different growth-durations during 1GS

Figure A4- 5 shows the EIS spectra (left panel) and cyclic voltammograms (right panel) of annealed ZnO:Co NR arrays that were kept in the growth solution for between 10 h and 24 h during the first growth stage (1GS; note that 10 h led to complete NR growth in terms of rod-length and thickness). These samples were not subjected to an additional second growth stage. The annealed undecorated ZnO:Co NR array sample presented in Figure 6-7c and 8c (red traces) was grown using the same growth conditions (i.e. c_{MEA} = 0.6 ml, no 2GS) and was added to Figure A4- 5 for comparison (here sample "16 h"). The overall charge transfer resistance, visible by the width of the semicircle, is comparable for all of the samples with the samples grown for 16 h and 24 h exhibiting almost the same overall charge transfer. This translates into quite similar CV characteristics of the water oxidation results as shown in the right panel of Figure A4- 5. Again, all samples show comparable oxidation currents. The inset of the right panel of Figure A4- 5 shows the pre-OER potential range magnified. Here the 16 h sample shows a well resolved oxidation peak (at ca. 1.32 V vs. RHE; see Chapter 6 for explanation). Also the other samples show this feature, but less pronounced. However, the CV scans of the 10 h and 24 h samples show an increased

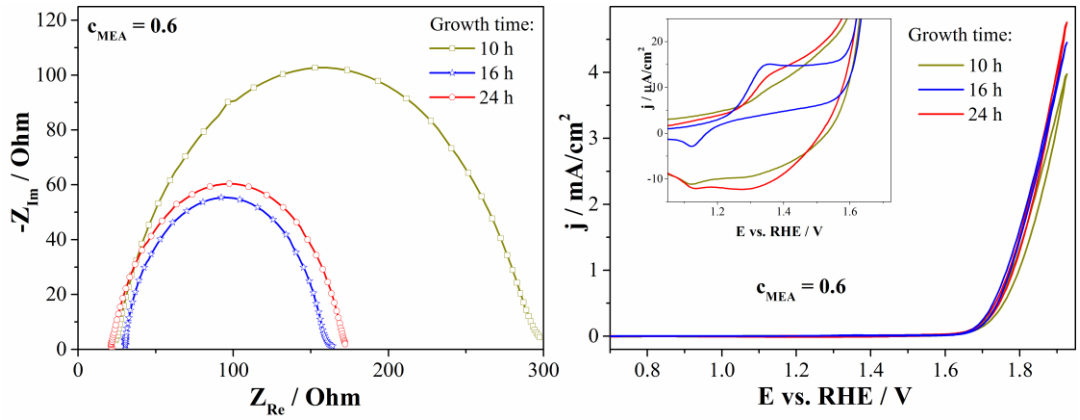

Figure A4- 5. Left) EIS spectra for ZnO:Co NR arrays kept in the growth solution for 10 h, 16 h and 24 h during the first growth stage (1GS). Right) Cyclic voltammograms for ZnO:Co NR arrays kept in the growth solution for 10 h, 16 h and 24 h during the first growth stage (1GS). The inset shows the pre OER potential range magnified. All samples were grown from a solution containing c_{MEA} = 0.6. No second growth stage was carried out. Electrolyte: 1M KOH. CV scan rate = 50 mV/s. EIS: E_{appl} = 1.7 V vs. RHE, E_{AC} = 10 mV, f = 50k – 0.5 Hz.

current in the range 1.4 – 1.5 V vs. RHE, which may be attributed to an increased Co^{3+} → Co^{4+} charge transfer. In turn, in the reverse direction these samples exhibit a small additional dip (compared to the 16 h sample) at ca. 1.3 V which may be taken as a fingerprint of the reduction of Co^{4+} back to Co^{3+}. However, these slight differences in the pre-OER potential range do not translate into significant changes for the water oxidation. It is also noted that a similar analysis as carried out for the Figure A4- 4 revealed an increased capacitive component in the higher frequency range for the 10 h sample. This may contribute to the slightly increased overall charge transfer resistance for this sample as compared to the other samples. However, in light of the question as to whether 16 h of growth during the 1GS leads to ultrathin cobaltic decoration, the measurements show no significant differences among the samples.

SEM micrographs of ZnO:Co nanorods before and after the photo-electrochemical (PEC) characterization

Figure A4- 6 shows the top-view SEM micrographs of an undecorated ZnO:Co NR sample before (left) and after (right) PEC measurements. Prior to the LSV measurements in the dark/under illumination, the sample was also tested in the dark by means of CV and EIS measurements. No structural changes were observed.

Furthermore it is important to note that ZnO may be chemically unstable in highly alkaline solutions, even in the dark.[19] However, no structural changes were observed for ZnO:Co NR samples that were in contact with 1M KOH for 2-3 hours.

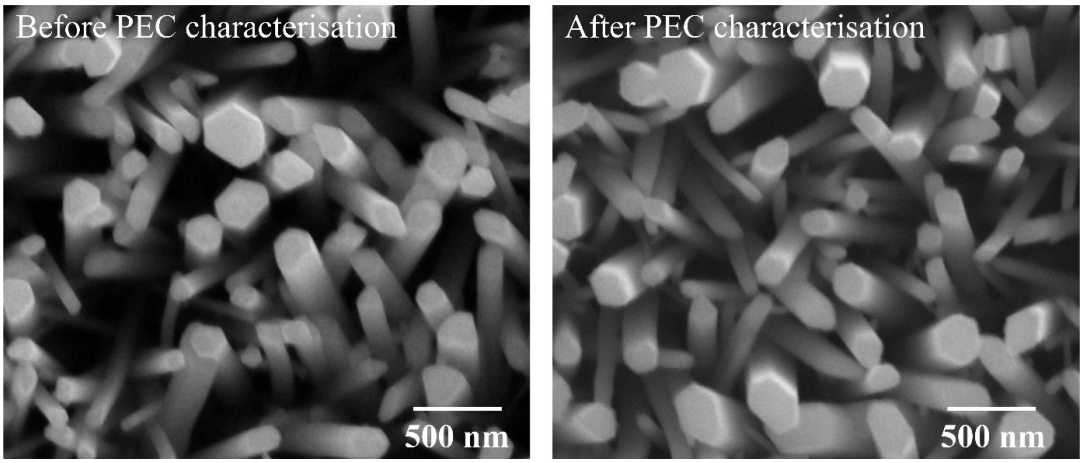

Figure A4- 6. SEM micrographs of undecorated ZnO:Co nanorods grown from c_{MEA} = 0.6 before (left panel) and after (right panel) photo-electrochemical measurements.

References

[1] J. Chivot, L. Mendoza, C. Mansour, T. Pauporté, and M. Cassir, "New insight in the behaviour of Co–H2O system at 25–150°C, based on revised Pourbaix diagrams," *Corrosion Science*, vol. 50, no. 1, pp. 62-69, 2008.

[2] K. Govender, D. S. Boyle, P. B. Kenway, and P. O'Brien, "Understanding the factors that govern the deposition and morphology of thin films of ZnO from aqueous solution," *Journal of Materials Chemistry*, vol. 14, no. 16, p. 2575, 2004.

[3] S. Xu and Z. L. Wang, "One-dimensional ZnO nanostructures: Solution growth and functional properties," *Nano Research*, vol. 4, no. 11, pp. 1013-1098, 2011.

[4] Z. Huang *et al.*, "Study on the oxidation process of cobalt hydroxide to cobalt oxides at low temperatures," *RSC Advances*, vol. 6, no. 83, pp. 80059-80064, 2016.

[5] P. W. Atkins, T. L. Overton, J. P. Rourke, M. T. Weller, and F. A. Armstrong, *Inorganic Chemistry*, 5th ed. Oxford University Press, 2010.

[6] E. Riedel and C. Janiak, *Anorganische Chemie*, 8th ed. Walter de Gruyter, 2011.

[7] Y. Cao, F. Yuan, M. Yao, J. H. Bang, and J.-H. Lee, "A new synthetic route to hollow Co3O4 octahedra for supercapacitor applications," *CrystEngComm*, vol. 16, no. 5, pp. 826-833, 2014.

[8] V. Pralong, A. Delahaye-Vidal, B. Beaudoin, B. Gerand, and J. M. Tarascon, "Oxidation mechanism of cobalt hydroxide to cobalt oxyhydroxide," *Journal of Materials Chemistry*, vol. 9, no. 4, pp. 955-960, 1999.

[9] X. Wang, Q. Zhang, Q. Wan, G. Dai, C. Zhou, and B. Zou, "Controllable ZnO Architectures by Ethanolamine-Assisted Hydrothermal Reaction for

Enhanced Photocatalytic Activity," *The Journal of Physical Chemistry C*, vol. 115, no. 6, pp. 2769-2775, 2011.

[10] R. S. Subrahmanya, "Polarographic behaviour of metals in ethanolamines," *Proceedings - Mathematical Sciences*, journal article vol. 45, no. 3, pp. 195-203, 1957.

[11] Y. Zhang, T. Bian, J. Gu, X. Zheng, and Z. Li, "Controllable ZnO architectures with the assistance of ethanolamine and their application for removing divalent heavy metals (Cu, Pb, Ni) from water," *New Journal of Chemistry*, vol. 42, no. 5, pp. 3356-3362, 2018.

[12] L. N. Demianets, D. V. Kostomarov, I. P. Kuz'mina, and S. V. Pushko, "Mechanism of growth of ZnO single crystals from hydrothermal alkali solutions," *Crystallography Reports*, journal article vol. 47, no. 1, pp. S86-S98, 2002.

[13] P. Hosseini Vajargah, H. Abdizadeh, R. Ebrahimifard, and M. R. Golobostanfard, "Sol–gel derived ZnO thin films: Effect of amino-additives," *Applied Surface Science*, vol. 285, pp. 732-743, 2013.

[14] P. Sagar, P. K. Shishodia, and R. M. Mehra, "Influence of pH value on the quality of sol–gel derived ZnO films," *Applied Surface Science*, vol. 253, no. 12, pp. 5419-5424, 2007.

[15] J. Kegel, J. Halpin, F. Laffir, I. M. Povey, and M. E. Pemble, "Rapid low-temperature solution growth of ZnO:Co nanorod arrays with controllable visible light absorption," *CrystEngComm*, vol. 19, no. 14, pp. 1938-1946, 2017.

[16] K. Govatsi, A. Seferlis, S. G. Neophytides, and S. N. Yannopoulos, "Influence of the morphology of ZnO nanowires on the photoelectrochemical water splitting efficiency," *International Journal of Hydrogen Energy*, vol. 43, no. 10, pp. 4866-4879, 2018.

[17] A. G. Scheuermann, C. E. D. Chidsey, and P. C. McIntyre, "Understanding Photovoltage in Insulator-Protected Water Oxidation Half-Cells," *Journal of The Electrochemical Society*, vol. 163, no. 3, pp. H192-H200, 2016.

[18] A. G. Scheuermann, J. D. Prange, M. Gunji, C. E. D. Chidsey, and P. C. McIntyre, "Effects of catalyst material and atomic layer deposited TiO2 oxide thickness on the water oxidation performance of metal–insulator–silicon anodes," *Energy & Environmental Science*, vol. 6, no. 8, p. 2487, 2013.

[19] C.-F. Liu, Y.-J. Lu, and C.-C. Hu, "Effects of Anions and pH on the Stability of ZnO Nanorods for Photoelectrochemical Water Splitting," *ACS Omega*, vol. 3, no. 3, pp. 3429-3439, 2018.